Curso 2010/11
CIENCIAS Y TECNOLOGÍAS/5
I.S.B.N.: 978-84-15287-23-0

NORBERTO CASTRO RODRÍGUEZ

Estudio de estrellas masivas extragalácticas

Director
ARTEMIO HERRERO DAVÓ

SERVICIO DE PUBLICACIONES
UNIVERSIDAD DE LA LAGUNA

SOPORTES AUDIOVISUALES E INFORMÁTICOS
Serie Tesis Doctorales

Thesis supervisor:
Prof. Dr. Artemio Herrero Davó.

ISBN: xx-xxx-xxxx-x
Depósito legal: TF-xxxx/2010

Some of the material included in this document has been already published in *Astronomy & Astrophysics*.

A mi madre
y a mi hermana.

Abstract

AMONG all shining sources in the night sky, massive blue stars are the rarest in number, but also the main engines in the chemical and dynamical evolution of the Universe. Their violent ending and strong stellar winds enrich and ionize the interstellar medium, reaching far galactic distances from where the stars were born. They are also among the brightest objects in the Universe, property that gives the opportunity of carrying out their detailed study beyond the Milky Way boundaries, even at the Virgo cluster distance, rendering their analysis in different environments, and so this work.

This thesis work is mainly focused on the quantitative analysis of a large massive blue star sample in NGC 55, a galaxy situated at $\sim 1.9\ Mpc$ away. The observed spectra were taken with the multi-object spectrograph VLT-FORS2 in the optical range ($\sim 3900 - 6000\ \AA$) at resolution $R \sim 1000$. In spite of the low resolution and the weakness of the sources it is possible to perform deep analyses. The stellar parameters determination relied on the comparison with synthetic FASTWIND atmosphere models.

We have introduced a new silicon model atom designed for the stellar code DETAIL into the FASTWIND environment. The similarities between both codes make the process relatively straightforward. The new model atom was evaluated and compared to the old one through different tests on synthetic spectra and Galactic stars, provided by the IACOB spectroscopic database.

The quantitative analysis, carried out in this work, required the development of several tools. A new FASTWIND grid was designed for studying supergiant stars with spectral types between $\sim O8$ and $A1$, which stellar parameters were efficiently selected, saving computational time. The match between the observed spectra and the synthetic grid was performed through an automatic χ^2 minimization method. As a result of the differences introduced by data quality and resolution, we have provided two alternative paths for an accurate quantitative analysis.

The detailed analysis on NGC 55 presented in this work gives the first census

of blue massive stars analyzed in NGC 55. From 204 observed stars, the spectral classification criteria reduced the sample to 164 supergiants with spectral type earlier than F0. Using this catalog as reference, we selected 75 objects with spectral types between $B9 - O8$ and, through the tools developed in this work, provided the stellar parameters and chemical compositions with an accuracy according to the signal-to-noise ratio of each star.

The results brought a characterization of the stars analyzed: stellar parameters, chemical abundances, physical parameters (mass, radius and luminosity), and information about their evolution. Even so, the sample allows us to derive important properties of the host galaxy, as well as the dynamical structure and chemical distribution along NGC 55.

Resumen

LAS as estrellas masivas azules son raras en número comparadas con otras estrellas de menor masa, y sin embargo son los motores químicos y dinámicos del Universo. Su violento fin, así como los fuertes vientos estelares que sufren durante sus vidas, enriquecen e ionizan el medio interestelar que las rodea. Llegando su influencia a recónditos lugares de la galaxia, lejos de su lugar de nacimiento. Estos objetos se encuentran entre los más brillantes que pueblan el Universo, propiedad que facilita su análisis más allá de los límites de nuestra Galaxia, incluso a distancias tan lejanas como el cúmulo de Virgo, permitiendo su estudio en diferentes medios, y el trabajo presentado en esta memoria de investigación.

Nuestro trabajo se centra en el estudio cuantitativo de una larga muestra de estrellas masivas azules observadas en la galaxia NGC 55, a una distancia $\sim 1.9\ Mpc$. El análisis se realizó sobre una muestra obtenida con el espectrógrafo multi-objeto VLT-FORS2, en el rango óptico ($\sim 3900 - 6000\ \AA$) a resolución $R \sim 1000$. A pesar de la baja resolución y de la débil magnitud aparente de los mismos, es posible llevar a cabo su análisis y determinar parámetros físicos. El estudio fue acometido mediante la comparación con espectros sintéticos generados con el código de atmósferas estelares FASTWIND.

Durante este trabajo se incorporó un nuevo modelo atómico de silicio, diseñado para el código DETAIL, dentro de la estructura de FASTWIND. Las similitudes entre ambos códigos en el tratamiento de la información atómica facilitaron el proceso. El nuevo modelo de silicio fue evaluado y comparado con la versión previa mediante diferentes pruebas, haciendo uso de espectros sintéticos y estrellas Galácticas.

El estudio cuantitativo de una forma objetiva, requirió del desarrollo de ciertas herramientas. Con este fin, una nueva red de modelos FASTWIND fue diseñada específicamente para el estudio de estrellas supergigantes azules con tipos espectrales comprendidos entre $\sim O8$ y $A1$. Los parámetros estelares fueron seleccionados de una forma eficiente en la zona de interés para nuestro estudio, salvando así tiempo de computación. Evitando una comparación puramente visual entre los espectros

observados y los modelos sintéticos, implementamos un método automático basado en el cálculo y minimización de la distribución de χ^2. En función de la resolución y calidad de los datos, diferentes estrategias han sido propuestas para alcanzar el resultado más exacto posible.

El análisis de la muestra condujo al primer censo de estrellas masivas azules desarrollado en la galaxia NGC 55. De la muestra de 204 objetos observados, su clasificación espectral redujo la cifra a 164 estrellas supergigantes con tipos espectrales más tempranos que F0. A través de este primer catálogo, seleccionamos 75 estrellas supergigantes con tipos espectrales comprendidos entre *B*9 y *O*8, las cuales fueron sometidas a un estudio detallado. A través de las herramientas desarrollados durante este trabajo determinamos los parámetros estelares y abundancias químicas, con una precisión de acuerdo a la señal-ruido de cada objeto.

El análisis desarrollado durante esta tesis proporcionó la primera y más extensa caracterización de una muestra de estrellas masivas azules a la distancia de NGC 55. Facilitando información no sólo acerca de las propiedades de los objetos estudiados (temperatura efectiva, gravedad superficial, masa, luminosidad, composición, etc.), sino también de la propia galaxia que las aloja, como su estructura dinámica o la distribución de abundancias a lo largo de NGC 55.

Conclusiones del Trabajo de Tesis

Las modelos teóricos actuales aún presentan importantes dudas acerca de la evolución de las estrellas masivas azules, y su paso a través de etapas tan complejas como, por ejemplo, la de LBV. Una mayor comprensión de su evolución requiere el desarrollo de detallados análisis cuantitativos a través de los más avanzados códigos de atmósferas estelares, modelos atómicos actualizados, y extensas muestras de candidatos observados en diferentes condiciones (metalicidad, edad, etc.). Los esfuerzos invertidos en esta tesis han tenido como objetivo la mejora de dicho conocimiento mediante la adaptación de un nuevo modelo atómico en el código FASTWIND, el desarrollo de diversas herramientas de análisis automático y el estudio de una muestra de estrellas masivas azules en la galaxia NGC 55.

Actualización del Modelo de Silicio en FASTWIND

Contar con información atómica exacta y detallada en el estudio de estrellas masivas azules fuera del equilibrio termodinámico es indiscutible. En base a recientes datos mecánico cuánticos, un nuevo modelo atómico de los iones de Si II, Si III y Si IV fue desarrollado bajo la filosofía y estructura del código estelar DETAIL, buscando

resolver ciertos problemas asociados a una falta de precisión en el modelo atómico previo. Durante este trabajo hemos tomado el modelo de silicio diseñado por el Dr. N. Przybilla y lo hemos transferido a los requisitos del código FASTWIND. Los puntos principales de la transferencia del modelo atómico y posteriores pruebas fueron:

- Ambos modelos estelares, DETAIL y FASTWIND, comparten una estructura similar en el tratamiento de la información atómica, facilitando la transferencia de uno al otro sin necesidad de tocar el código fuente. Solamente las transiciones radiativas ligado-libre (con información mecánico cuántica de su sección eficaz de fotoionización) requirieron modificaciones en el código.

- El nuevo modelo atómico presenta una detallada descripción de la estructura de niveles de los iones Si III y Si IV, aunque similar en el caso de Si II. En cambio, el tratamiento de las transiciones radiativas y colisionales muestran cambios sustanciales en los tres iones respecto al modelo previo.

- Comparaciones entre perfiles sintéticos obtenidos con ambas versiones muestran las mayores diferencias en las líneas de Si II estudiadas. Importantes transiciones, como son Si III 4552 $\AA$ y Si IV 4116 $\AA$, presentan menores divergencias. El impacto en la temperatura efectiva, dependiendo del modelo y del tipo espectral del objeto analizado, ronda entre $\Delta T_{eff}\,500 - 1000\ K$. No obstante, las diferencias en otras líneas (por ejemplo Si II 3853 $\AA$) pueden llegar a ser importantes. Normalmente estas transiciones son débiles en estrellas supergigantes, pero su papel en estrellas enanas es relevante.

- El análisis de seis estrellas Galácticas, usando ambos modelos atómicos, mostraron resultados dependientes de cada objeto. Cuatro de ellas eran lo suficientemente frías como para mostrar transiciones de Si II, Si III y Si IV. Por otro lado, mientras dos presentaron una clara mejoría en los valores de $T_{eff} - log\,(g)$ obtenidos mediante diferentes balances de ionización y la nueva versión del modelo de silicio, los otras dos exhibieron un comportamiento opuesto. A altas temperaturas (sólo disponible transiciones de Si III y Si IV), el resto de estrellas analizadas devolvieron un mejor acuerdo con el balance de ionización de helio a través del nuevo modelo atómico.

  La determinación de las abundancias de silicio siguió un comportamiento similar. Únicamente dos de las estrellas analizadas mostraron un mejor resultado mediante el modelo antiguo de silicio; la falta de acuerdo en el balance de ionización acaba propagándose al análisis de abundancias.

  La transición de Si III 4813 $\AA$ muestra una mejor correlación con el resto de líneas mediante el nuevo átomo de silicio.

Técnicas de Análisis Automáticas

Las últimos surveys desarrollados en el campo de estrellas masivas azules demandan un estudio sistemático, objetivo y reproducible, evitando técnicas de ajuste visual. El análisis de cientos de estrellas es un proceso complejo, pero necesario y posible. Siguiendo esta idea:

- Implementamos una nueva red de modelos FASTWIND centrada en el análisis cuantitativo de estrellas masivas azules con tipos espectrales entre $\sim A1$ y $O8$. Los parámetros involucrados en los modelos de atmósfera estelares fueron seleccionados de forma eficiente, salvando tiempo de computación y simplificando la comparación con datos observados.

- El mejor conjunto de parámetros estelares (junto a sus respectivos errores) que reproducen el espectro fueron determinados mediante la minimización de la distribución de χ^2. La técnica se basó en el cotejo directo de transiciones relevantes (de acuerdo con cada tipo espectral) y la red de espectros sintéticos generada durante este trabajo. Las diferentes pruebas pusieron de manifiesto la fiabilidad del método, remarcando los problemas del mismo, los cuales deben ser tenidos en cuenta para evitar fuentes adicionales de error.

- Hemos seguido el método de *'Síntesis Espectroscópica'*, propuesto por otros autores, para el estudio de espectros a baja resolución ($R \sim 1000 - 2000$). Se evitó el análisis visual de los espectros mediante la minimización de la función χ^2, recuperando los parámetros estelares de una manera rápida y precisa.

  Las diferentes pruebas sobre modelos sintéticos mostraron un buen acuerdo entre los perfiles de entrada y los recuperados. Pruebas similares en estrellas Galácticas, degradadas a baja resolución y señal ruido, dieron resultados equivalentes a los calculados a alta resolución siguiendo procedimientos estándares.

- Siguiendo la misma filosofía que a baja resolución, la técnica fue adoptada a alta resolución como una primera estimación de los parámetros estelares. El resultado final fue obtenido mediante la metodología estándar (i. e. la relación entre los balances de ionización disponibles y las alas de la serie Balmer, junto con el método de *'Curvas de Crecimiento'*). Las diferentes pruebas ilustraron la fiabilidad del procesos de análisis. El estudio se llevó a cabo buscando la mínima interacción por parte del usuario.

- La creación y mejora de varios programas, adaptando el análisis bajo los criterios de CONDOR, acelera notablemente el cálculo. A través de este sistema de paralelización hemos mejorado el proceso de creación de extensas redes de

modelos en un corto periodo de tiempo, además de facilitar la comparación entre los perfiles sintéticos y los observados.

NGC 55, Análisis Cuantitativo

Extender el estudio de estrellas masivas azules más allá de la Vía Láctea es fundamental para un mayor ahondamiento en su conocimiento y en el papel desempeñado por importantes factores como la metalicidad. Su estudio proporciona importantes herramientas para una detallada caracterización de la composición química y dinámica de la galaxia que las hospeda. Además, son potenciales referencias de distancia, con una precisión comparable a la obtenida mediante estrellas variables. Mediante las herramientas desarrolladas en este trabajo hemos llevado a cabo el estudio de una sub-muestra de estrellas masivas azules pertenecientes a la galaxia NGC 55. Los principales resultados alcanzados pueden resumirse en:

- Hemos presentado el primer censo de estrellas masivas azules en la galaxia NGC 55. La clasificación espectral llevada a cabo sobre 204 espectros redujo la muestra a 164 estrella, pertenecientes a la galaxia, con tipos espectrales más tempranos que F0. El catálogo engloba siete objetos peculiares, probablemente estrellas azules en un alto estado evolutivo (WR o candidatas a LBV).

- La larga muestra analizada permitió estudiar la distribución dinámica de la galaxia, obteniendo velocidades radiales en concordancia con estudios previos en regiones H I. La distribución 2-D de velocidades medida mediante nuestra muestra de estrellas azules, mostró un patrón similar al estimado por otros medios. El centro dinámico, ligeramente desplazado con respecto al óptico, se corresponde con el obtenido a partir de estudios en hidrógeno neutro y detecciones en el infrarrojo medio. Sin embargo, los errores en nuestra medidas impiden un estudio estructural más detallado de NGC 55.

- Partiendo del catálogo presentado, 75 estrellas supergigantes azules fueron sometidos a un detallado escrutinio, estimando parámetros estelares y abundancias químicas, convirtiendo este estudio en el más amplio desarrollado a esta distancia. La muestra analizada comprende objetos con temperaturas efectivas entre $\sim$ 12000 y 32000 K, ilustrando el potencial y eficacia de las herramientas presentadas en este trabajo.

- La distribución de abundancias a lo largo de NGC 55 no apuntó a una clara tendencia, con un contenido en metales similar a la Gran Nube de Magallanes. Los patrones de abundancias 2-D de silicio, magnesio y oxígeno, a lo largo de la galaxia, muestran un ligero incremento en la parte noroeste, sin embargo los

errores son demasiado grandes para sostener la existencia de un gradiente. A pesar de la crudeza de los mapas, cabe destacar el valioso papel del estudio de abundancias en 2-D, principalmente en galaxias que presentan un morfología compleja, y donde un simple análisis radial podría enmascarar tendencias o zonas puntualmente relevantes en la galaxia.

- Las concentraciones de nitrógeno, carbono y oxígeno (este último en menor medida) pueden encontrarse contaminados por la evolución estelar del objeto. De esta forma los cocientes de [N/C] y [N/O] son usados comúnmente como diagnósticos del envejecimiento de las estrellas. La distribución de [N/O] muestra una mayor dispersión en el sureste de la galaxia, que decrece en la parte norte. Sin embargo, los errores y la falta de una muestra estadísticamente representativa, evitan poder llegar a una afirmación clara acerca del grado de evolución en la galaxia.

- Desafortunadamente problemas en la calibración de la fotometría impidieron un correcto cálculo de los radios y masas de las estrellas analizadas. Asumiendo una extinción promedio, hemos estimado un valor preliminar para los parámetros físicos. El estudio sitúa las estrellas en el diagrama HR con una masa comprendida entre $\sim 20 - 50\ M_{\odot}$ evolucionando hacia la parte roja del mismo.

Contents

Abstract **v**

Resumen **vii**

1 Introduction **1**

2 Modeling Massive Blue Star Atmospheres **11**
2.1 Numerical Approach 12
2.2 State-Of-The-Art Stellar Atmosphere Codes 16
2.3 Fast Analysis of STellar atmospheres with WINDs (FASTWIND) 18

3 A New Silicon Model in Town **21**
3.1 The Need of a New Silicon Model 21
3.2 Atomic Model Description: FASTWIND and DETAIL Philosophy . . 22
3.2.1 Atomic Structure and Energy Levels 23
3.2.2 Statistical Equilibrium 24
3.3 Silicon Model: A Detailed Description 27
Energy Levels 27
Collisional and Radiative Transitions 30
3.4 *Old versus New* Silicon: On Synthetic Profiles 33
3.4.1 Comparison Tests 33
3.4.2 Tests at Low Resolution 43
3.5 Silicon *Old versus New*: On Galactic Stars 46
3.5.1 Selection of Candidates: The IACOB Spectroscopic Database 46
3.5.2 Quantitative Comparison 47
Stellar Parameters 47
Chemical Abundances 49

3.5.3 General Remarks . . . 57
3.6 Summary . . . 59

4 Quantitative Analysis of Massive Blue Stars 63
4.1 Building a FASTWIND Grid . . . 64
4.1.1 Stellar Parameters . . . 64
4.1.2 Atomic Models . . . 71
4.1.3 Through CONDOR . . . 73
4.1.4 Convergence Criteria . . . 73
4.2 Automatic Stellar Parameters Determination . . . 75
4.2.1 Low Resolution: *Spectroscopy Synthesis Method* . . . 77
Stellar Parameters: How to Proceed... . . . 77
Stellar Parameters: Tests . . . 84
Chemical Abundances . . . 89
4.2.2 High Resolution: *Spectroscopy Synthesis Method* + *Curves of Growth* . . . 92
Stellar Parameters: How to Proceed... . . . 92
Stellar Parameters: Tests . . . 100
Chemical Abundances . . . 100
4.2.3 Issues in the Quantitative Analysis . . . 106
4.2.4 High Resolution versus Low Resolution . . . 108
4.2.5 Completing the Fundamental Parameters: Radius, Luminosity and Mass . . . 109
4.2.6 Other Automatic Methods . . . 112
4.3 Summary . . . 114

5 Massive Blue Stars in NGC 55 115
5.1 The Sculptor Group Galaxy NGC 55 . . . 115
5.2 Observations and Data Reduction . . . 118
5.2.1 Multi-Object Spectroscopy: FORS2 . . . 119
5.2.2 Data Reduction . . . 122
5.3 Spectral Classification . . . 123
5.3.1 Classification Criteria for Massive Blue Stars . . . 125
O-type Stars . . . 125
B-type Stars . . . 126
A- and later type Stars . . . 126
***Exotic* Stars** . . . 129
5.3.2 Results for NGC 55 Objects . . . 129
OBA-type Stars . . . 130
WRs & LBV candidates . . . 131

Contamination **of the Sample** 135
5.4 Radial Velocity Distribution 135
5.5 Quantitative Analysis 138
5.5.1 Stellar Parameters 138
5.5.2 Chemical Composition 141
5.5.3 Comments on individual targets 148
5.5.4 Chemical Spatial Distribution 152
5.5.5 CNO Evolution Status 154
5.5.6 Fundamental Parameters 156
5.6 Summary 159

6 Conclusions and Future Research **165**

A NGC 55 Catalog **171**

B NGC 55 B-type Stars: Quantitative Analyses **177**

1

Introduction

To fly would be folly,
To stay would be jolly
And listen and hark
Till the end of the dark
to our tune
The Hobbit, J.R.R. Tolkien

In the dark night a simple glance above our heads reveals the astonishing show that the Universe brings to us. A black background full of twinkling lights that has inspired our imagination since the beginning of humankind. Our knowledge about what they really are has hugely evolved from the Aristotelian concept of eternal static objects fixed to an stellar sphere propelled by an unmoved mover, which transfers the inertia to the rest of the Universe. However, this theory was partly right. Stars are the engines of the Universe; the dynamical and chemical evolution of the cosmos is driven by stars.

Massive blue stars, center of this thesis work, (young objects with $M_* \geq 8-9M_\odot$) are rare in number, in comparison with lower mass stars (Salpeter 1955). However their influence on the interstellar medium and on galactic evolution is remarkable. The mass lost via stellar winds (in early B-type star $\sim 10^{-6}$ $M_\odot yr^{-1}$, see for instance Repolust et al. 2004, even larger in evolved stages) together with their end in a supernova explosion inject a huge amount of energy, momentum and material (processed and unprocessed) into the surrounding interstellar medium, changing its dynamics, composition and, in certain cases, triggering new star formation (Elmegreen 1980). Nevertheless, their influence is not restricted to the nearby medium. Their impact and enrichment can propagate across the entire galaxy forming *'chimneys'* and

'fountains' of material which may afterwards fall back to the galactic plane (Corbelli & Salpeter 1988).

Evolution in the Upper Hertzsprung–Russell Diagram

Their high masses and brightnesses place these stars in the upper part of the Hertzsprung–Russell (HR) diagram (see Fig. 1.1). This area is populated by O-, B- and A-type stars, together with exotic objects which are also massive stars in different evolutionary stages, as Red Supergiants (RSG), Wolf-Rayets (WR) or Luminous Blue Variables (LBV). As we explain below, the evolution and the path followed by massive blue stars across the HR diagram is still uncertain, with several issues than theoretical evolutionary models have not been able to explain so far.

The formation of objects with large masses is still puzzling. According to the classical view (Larson 2003), it would be impossible to reach such stellar masses from a cold molecular cloud since the energy released during the process would stop the gravitational collapse, avoiding the formation of objects with 83 $M_{\odot}$ which in turn, have been observed by Rauw et al. (2005). Even the upper limit of the initial mass function (i. e. how massive is the most massive star) is still unknown, particularly due to the lack of understanding of star formation and the incompleteness in surveying the Galaxy (see Figer 2005). Several hypotheses try to explain their formation involving rotation or magnetic fields, merge of smaller objects or angular momentum release by gravitational interaction with surrounding stars (Larson 2010).

Our knowledge of the subsequent evolution after the hydrogen burning phase also presents some gaps. During the main sequence stage, these stars feed themselves by burning hydrogen in their core via the CNO cycle (more efficient than proton-proton chain cycle at these temperatures), producing helium. Because of their high stellar mass, the pressure, and temperature in the core are higher than for lower mass stars. In these conditions the nuclear reactions are quite efficient, burning the fuel faster than in less massive stars. Thus, massive stars have remarkably short lives ($\sim 10^7$ *yr*) compared with solar types ($\sim 10^{10}$ *yr*), according to their typical nuclear time scales.

Once they run out of hydrogen, the radiative pressure decreases and the star collapses until the density and temperature are again high enough to start a new nuclear reaction, this time using helium as fuel. At the same time the outer layers expand, and the surface cools down, bringing the star to the supergiant area in the HR diagram. Hydrogen burning continues in concentric shells, increasing the amount of helium in the core while the star is evolving towards the red side of the HR diagram. When the helium supply is over, the core collapses again until it is able to ignite the helium-burning residuals, carbon. This process is repeated each time with heavier elements, each of them burning faster than the previous one, until the star forms an iron core. At this point, fusion is not longer exothermic and the star collapses into its end producing

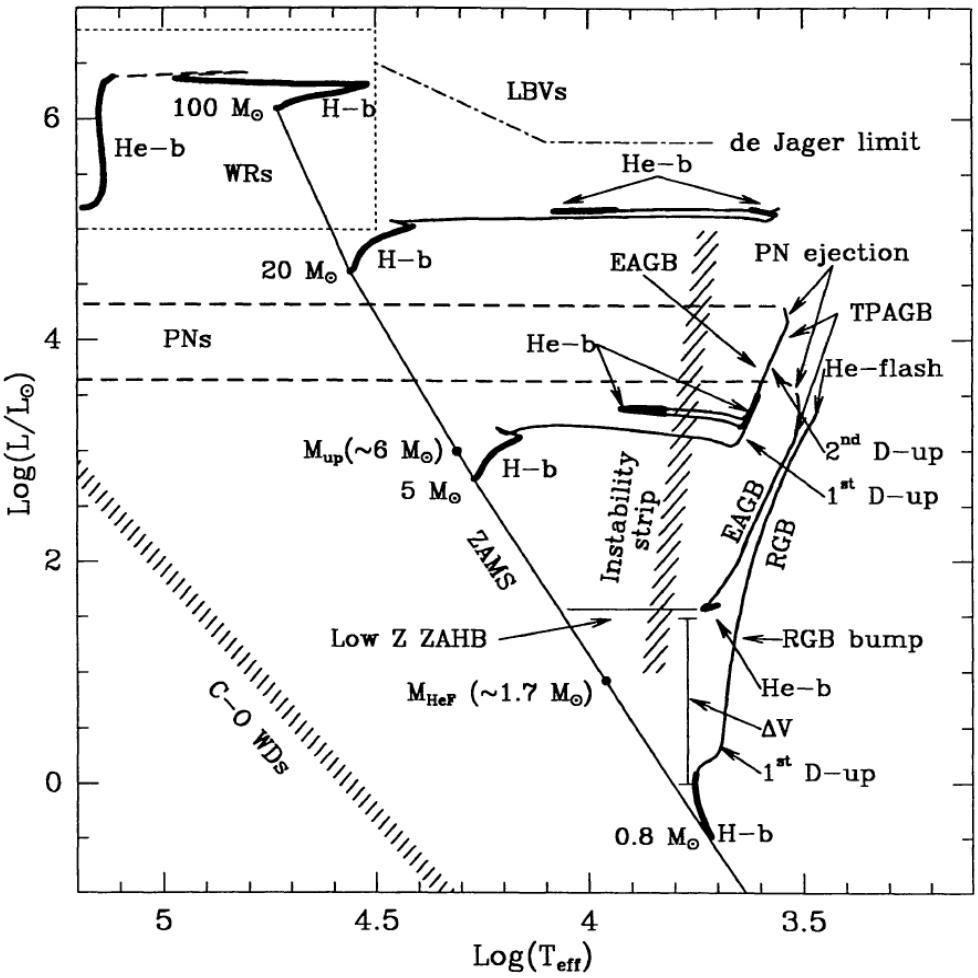

FIGURE 1.1— Detailed Hertzsprung–Russell diagram from Chiosi et al. (1992). The different evolutionary paths followed by stars, according to their masses, are displayed together with certain important events during their evolution. The hydrogen burning phases are marked by *'H-b'*, while the helium burning stages by *'He-b'*. This thesis work focuses on the most massive stars ($M > 8M_{\odot}$) and their evolution across the upper part of the HR diagram. The locus of exotic stars, intermediate and possibly final pre-supernova steps in their evolution (WRs and LBVs), are also indicated in the diagram.

a supernova explosion.

However, we still do not understand the stages experienced by massive stars after they leave the main sequence. Conti (1976) suggested a possible evolutionary pattern for these objects and the connection between the O-type stars and the WR phases. The *'Conti Scenario'*, although reviewed ever since (Massey 2003), is still a good first

order reference the evolution of massive stars:

- Stars more massive than $M_* > 40\ M_\odot$ experience strong winds which sweep away the external layers removing hydrogen. Without hydrogen for burning in shells and an additional helium source supply, these stars never reach the RSG phase. Their high luminosity sets them near the Humphreys-Davidson limit (Humphreys & Davidson 1979), an observational upper limit for stellar luminosities related to the Eddington limit. The most massive stars can enter the LBV stage ($M_* \geq 85\ M_\odot$). Eventually they end their lives with a supernova explosion after undergoing a WR period. See, for instance, the theoretical path followed by a star of initial mass of 100 $M_\odot$ in Fig. 1.1.

- Stars with masses $20 \leq M_*/M_\odot \leq 40$ evolve until they reach the RSG stage. When the stars return to the blue side of the HR diagram they enter the WR stage and end as supernova.

- Finally, stars with $10 \leq M_*/M_\odot < 20$ reach the RSG and return to the blue supergiant (BSG) regime through the instability strip (see Fig. 1.1) before their lives end as supernovae. They do not reach the WR status before perish.

This scenario provides the basic ideas about massive blue star evolution, but it does not take into account important factors, such as rotation (Meynet & Maeder 2003), which can modify the internal structure and enhance the mass loss rate, changing considerably the final evolution of the star.

Several observational issues still remain unexplained by theoretical models. Thus, theory does not match the observed BSG/RSG ratio. Due to their fast BSG evolution a lower ratio would be expected, while the empirical data show a large number of BSGs. That could be a consequence of stars returning to the BSG phase once the objects have reach the RSG phase, the so-called *blue-loops*, already proposed in the *'Conti Scenario'*. However its existence has not been definitely proved.

Metallicity plays a fundamental role in the stellar evolution. The mass loss rate or the internal convection structure also depend on the metal content. Nonetheless, the observed relationship between the BSG/RSG ratio and metallicity (the ratio increases steeply with the metal content, Cowley et al. 1979), cannot be reproduced by the theory (Langer & Maeder 1995). Although the incorporation of stellar rotation in the theoretical models improves the results (Eggenberger et al. 2002).

The presence of processed CNO material at the stellar surface is also a hot topic in blue massive star evolution. The relative abundances of carbon, nitrogen and oxygen in the stellar interior change and they can be brought to the stellar surface by different processes, mainly by the convective dredge-up in the RSG phase, hence becoming an age indicator. In the Milky Way, the group of BSG encloses objects with a wide variety

of surface abundances suggesting different evolutionary stages (Herrero 2003). This could hint that the population is a mixture of objects evolving towards the RSG stages and objects returning back after a blue loop. Other mechanisms can also bring nuclear burning products to the stellar surface, being rotation the main candidate (Heger & Langer 2000; Maeder & Meynet 2001; Lennon et al. 2003). Nonetheless, some authors have pointed out that rotation alone cannot explain the entire nitrogen enhancement observed in some stars and have proposed magnetic fields as an additional source of enrichment (Hunter et al. 2008a).

In order to understand the evolution of massive blue stars, the quantitative analysis of a large sample (statistically significant) is needed. With this aim, several collaborations have been established to gather more observational information, not only in our Galaxy but also in nearby ones (see for instance the FLAMES collaboration described by Evans et al. 2005b or the IACOB spectroscopic database presented by Simón-Díaz et al. 2010, in prep.).

Extragalactic Studies

The bright intrinsic luminosity of massive blue stars enables us to go farther than the Milky Way boundaries and extend the research to resolved individual stars in nearby galaxies, even beyond the Local Group (Kudritzki 2010). The last generation of large telescopes together with more efficient instruments have played an important role in these studies, allowing us to obtain spectra with enough quality to carry out a detailed quantitative analysis.

Although this kind of studies represents a challenging task compared to analyses in the Milky Way, as these stars are fainter than their Galactic counterparts, the opportunity of studying blue stars in very different metallicity environments makes it rewarding. In addition, massive blue stars can be used as tools for the chemical analysis of the host galaxy. Abundance gradients in galaxies provide an important reference for understanding galactic evolution (Stasińska 2002).

The chemical composition of galaxies used to be probed with H II regions. Their quantitative study allows us to measure abundances of several chemical species seen in their spectrum (mainly nitrogen, oxygen, sulfur, neon and argon). The analysis of H II regions can be carried out at large distances, where it is not possible to resolve individual stars. However, the accuracy of the results is limited by our ability to determine the electronic temperature in the nebula. If collisional excited lines are present in the nebular spectrum, temperature can be derived from their relative equivalent widths, for instance using the [O III] $(4959+5007)/4363$ $\AA$ ratio. Nevertheless, the O III 4363 $\AA$ transition required for the temperature determination, is usually very weak. When this transition is not detected (either because the distance to the target or because its metal content) an empirical calibration for the electronic

temperature must be used. The abundances derived are strongly dependent on the calibration used (Pagel et al. 1979; Stasińska 2004). They can change by 0.5 *dex* in the worst case, depending on the calibration employed (Trundle et al. 2002; Kennicutt et al. 2003).

Massive blue stars offer an alternative way to analyze the chemical composition and the distribution of metals in the host galaxies. Moreover, these objects are rich in many other chemical species not available in H II regions, such as silicon, magnesium or iron, plus the elements commonly detected in nebulae (e. g. oxygen and nitrogen). Note that although free from the use of empirical calibrations, the results from massive blue stars analyses suffer from uncertainties inherent to the method, associated to the atomic data and approximations imposed in the stellar atmosphere models for reaching a self-consistent solution.

Abundances derived from B-type stars have allowed us to probe the chemical composition of the Solar Neighborhood (Przybilla et al. 2008) or to constrain the recent star formation history of nearby regions such as Orion (Cunha & Lambert 1992; Simón-Díaz 2010). Outside the Milky Way, the spectra have usually lower signal-to-noise ratios (S/N) making the analysis challenging, but still possible. Some examples of recent work done in the Magellanic Clouds, the most targeted due to their proximity and their different metallicity from the Milky Way, are: Korn et al. (2005); Lennon et al. (2005); Trundle & Lennon (2005); Trundle et al. (2007); Hunter et al. (2008b, 2009). Farther away, with increasing difficulty, similar studies have been presented for M 31 (Venn et al. 2000; Trundle et al. 2002), M 33 (Monteverde & Herrero 1998; Monteverde et al. 2000; Urbaneja et al. 2005b; U et al. 2009), NGC 6822 (Muschielok et al. 1999; Venn et al. 2001), NGC 3109 (Evans et al. 2007), WLM (Venn et al. 2003; Bresolin et al. 2006; Urbaneja et al. 2008) or IC 1613 (Bresolin et al. 2007). The studies extend to the Sculptor group, NGC 300 (Bresolin et al. 2002; Urbaneja et al. 2003, 2005a) where iron-group elements have been studied for the first time outside the Local Group (Kudritzki et al. 2008). At a distance of 6.7 Mpc, Bresolin et al. (2001) managed to determine global metallicities for A-type supergiants in NGC 3621.

Figure 1.2 displays an example of the oxygen gradient found in M 33 by Urbaneja et al. (2005b) from the detailed analysis of massive blue stars. Their work also showed good agreement with previous H II analyses (Vilchez et al. 1988), within the uncertainties that both methods carry. The studies developed by Trundle et al. (2002) and Urbaneja et al. (2005a) in M 31 and NGC 300 respectively illustrated that the match between massive blue stars and H II studies is strongly dependent on the empirical calibration used in the H II analyses. Other examples in the nearby Magellanic Clouds can be seen in the works performed by Korn et al. 2002 and Trundle et al. 2004.

Another advantage of using massive blue stars is the capability of measuring abundances in the external areas of galaxies where H II regions are too faint, but the

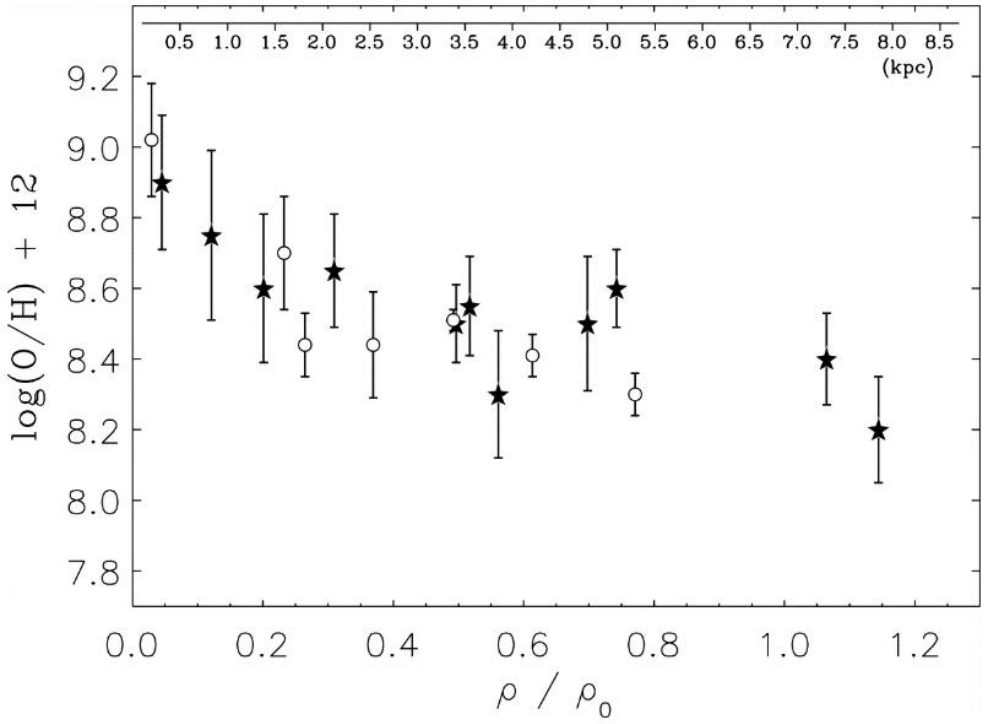

FIGURE 1.2— Oxygen gradient across M 33 (Urbaneja et al. 2005b) derived from the quantitative analysis of massive blue stars (black stars). The trend found by the authors matches the results from H II regions obtained by Vilchez et al. (1988) (open circles).

massive blue stars are not.

Finally, massive blue stars constitute accurate standard candles by means of the calibration of their luminosity with their wind momentum (Kudritzki et al. 1995) or their flux-weighted gravity g/T_{eff}^4 relationships (Kudritzki et al. 2003). Once well calibrated, these techniques bring distance estimates to the Virgo and Fornax clusters as an alternative distance diagnostic to Cepheids, and with comparable accuracy (see Kudritzki et al. 1999). The analyses of massive blue stars present a remedy to the dependence of the derived distances on environmental properties, such as metallicity, reducing the largest contribution to the systematic uncertainties in the determination of accurate absolute distances to nearby galaxies. The ARAUCARIA project (Gieren et al. 2005), where part of this work is included, focuses its efforts on establishing a reliable calibration between different distance and the properties of the interstellar medium.

Stellar Atmosphere Modeling

The accuracy in stellar parameters and chemical determinations lies in the correct simulation of all the processes that lead to the observed spectrum. The light emitted from the star contains all the information that we can gather from it. Modeling all the physical phenomena occurring in the atmosphere of the stars is a challenging task, involving non-local thermodynamical equilibrium processes, and strong stellar winds in a spherically extended atmosphere (Kudritzki & Puls 2000). To fully characterize the system would require to solve simultaneously a set of coupled equations, for which we do not have an analytical solution. Instead, we make some assumptions regarding the physics of the atmosphere, although we still reach a realistic solution. Even so, a huge computational effort is required. Since the first stellar models developed by Unsold (1955) the improvements have been remarkable with current models, being more complex and giving a more reliable representation of the observed spectral flux (see for instance the work by Santolaya-Rey et al. 1997 or Hillier & Miller 1998). This is due to the improvement of computational systems, our better understanding of the atmosphere of massive blue stars. State-of-the-art mathematical algorithms have also enabled us to solve the involved equations in a faster and more efficient way.

A realistic representation of the stellar atmosphere is not the only requirement when performing analyses in a non-thermodynamic equilibrium scenario. The stellar atmosphere model must be supported by the correct implementation of all processes, radiative and collisional, that can have an impact on the level population of the chemical species considered in the stellar atmosphere. Thus, reliable atomic models with accurate data are fundamental for achieving realistic results. The improvement of the observation techniques and the refinement of the stellar codes have shown the lack of accuracy in the atomic data used so far. This fact, together with updated quantum mechanical data, have led to the development of new detailed atomic models (see, for instance, the review by Rauch & Deetjen 2003 and the work by Nieva 2007 in the design of a new model of carbon). Nonetheless, the simplifications in our representation of the atmospheres of massive blue stars, and the atomic models used, introduce intrinsic systematic errors in the analysis.

An accurate quantitative analysis entails a large computational and human effort. The stellar code reproduces, to the best of our current understanding, the observed spectra according to several free parameters, such as effective temperature, surface gravity, etc. The features in the spectrum (mainly hydrogen and helium plus several metallic transitions, depending of the spectral type and luminosity class) will react in a different ways to variations of these parameters, which allows us to constrain the stellar properties (McErlean et al. 1999). The accuracy in this *quest* for the set of stellar parameters that best reproduces the observations is strongly linked to the stellar code used, the model atoms and, in many cases, to subjective personal considerations.

All these factors introduce undesirable systematic effects, adding *noise* to the derived stellar parameters. Careful analyses have shown the impact and changes in the results due to these systematic errors (see for instance Przybilla et al. 2008 or Simón-Díaz 2010).

Multi-object spectroscopy together with large surveys of massive blue stars have driven the production of large databases, which analysis would require a large amount of time. These projects call for objective analyses with automatic procedures. Besides speeding up the analysis, automatic methods avoid the systematic errors attached to a human stellar parameter determination. Several projects have addressed this point, looking for an optimum way to analyze extend samples in the shortest time (Mokiem et al. 2005; Lefever 2007; Urbaneja et al. 2008).

Thesis Outline

The lack of large systematic quantitative analyses is one the main obstacles to improving the general theory of evolution in the upper side of the HR diagram. The use of heterogeneous methods for the analyses also add an important uncertainty source that can burden the results and cause mismatches with theoretical models. Thus, a consistent and systematic study of large homogeneous samples is a fundamental requirement to improve the theory involved in the description of these stars. Extending this study to galaxies, as far as current technology permits, completing the survey with essential information such as the environmental role in their formation, evolution and impact on the host galaxy.

The work presented here is mainly focused on the detailed quantitative analysis of a large sample of stars in the galaxy NGC 55 ($\sim 1.9\ Mpc$ away). This study will allow us to characterize the galaxy massive blue population (i. e. stellar parameters, chemical composition and evolutionary status) and chemical history. The tool built for this study will prove extremely useful not only in extragalactic fields, but also in detailed analyses of galactic stars. This work has been structured in three main blocks. They can be summarized as follows:

- **Improvement of the silicon model atom .-** A new silicon model atom is available with more accurate quantum mechanical data and a detailed description of the energy level structure. Chapter 3 presents its integration in the FASTWIND stellar code and the different tests carried out to compare the new and old silicon atomic models. A description of the effects on the main lines normally used in the analysis plus several examples on Galactic stars are provided in this chapter.

- **Techniques for automatic quantitative analysis .-** The search for objective techniques and their automation is tackled in this work. A new grid of

FASTWIND stellar models has been developed, together with the adequate tools for carrying out an automatic quantitative analysis at high and low resolution. A full description of the new FASTWIND grid and the methods can be found in Chapter 4.

- **Analysis of NGC 55 massive blue stars .-** Finally, we used the tools built in this study and the new silicon model atom implemented to perform a quantitative analysis of a sample of 75 supergiant stars with spectral types $\sim O8 - B9$ in NGC 55. This is the largest set of massive blue stars ever analyzed belonging to a galaxy as distant as NGC 55. The results show the reliability of our techniques and provide a characterization of NGC 55 through its massive blue stellar population. The detailed study is compiled in Chapter 5.

The dissertation is completed with an introduction to stellar atmosphere modeling with state-of-the-art codes available for massive blue star analyses, provided in Chapter 2. Chapter 6 ends this work with a final review, the main conclusions and the future applications of the techniques developed in this thesis work. Complementary information is compiled in the appendixes.

2

Modeling Massive Blue Star Atmospheres

Yes, I know, it's not the truth,
but in a great history little truths
can be altered so that the greater
truth emerges.
Baudolino, Umberto Eco

THE light received from the stars keeps many secrets about their atmospheres and winds. Physical properties and chemical composition can be determined through the correct modeling of all phenomena produced in the stellar atmospheres, a challenging but possible task. In the last decades the techniques developed in this field have experienced a huge evolution, and nowadays state-of-the-art stellar atmosphere models are capable of recovering the observed spectra with high accuracy.

Reproducing the stellar behavior for atmospheres in the upper part of the HR diagram is not trivial. The basic assumptions used for low mass stars, such as a stellar plasma in local equilibrium with the radiative field, do not apply to O- and B-supergiants. The first model of a massive blue star (τ-Sco) was developed by Unsold (1955) through a simple code in plane-parallel geometry and hydrostatic equilibrium, assuming local thermodynamic equilibrium (LTE). However, Auer & Mihalas (1972) were the first in reaching a successful solution for the optical spectra of an OB-star by a non local thermodynamic equilibrium (NLTE) stellar code. Nonetheless their models

were strongly limited by the small number of frequencies and atomic levels that they handled, which resulted in a poor description of the relevant atomic processes.

In this chapter we present an outline about the stellar atmosphere numerical approach in massive blue stars, gathering a brief description of the main stellar codes developed in this field so far. Finally we center the discussion on FASTWIND keystones, the code used in this work.

2.1 Numerical Approach

A correct atmosphere simulation involves the solution of a system of coupled equations, tightly interdependent. An *exact* atmosphere description would require the simultaneous solution at all frequencies and along the entire atmosphere of the hydrodynamics equations, the energy equation, the rate equations for all the ions, and the radiative transfer equation under the correct geometry. This set of equations cannot be directly solved due to the dependencies between all of them. To simplify the calculations and reach a solution it is necessary to use certain approximations. However, we have to keep in mind when these *'shortcuts'* apply.

The first analysis developed by Unsold (1955) was hampered by the computational resources available at the time, which were insufficient to generate a reliable OB atmosphere model. Thus, the assumptions used (plane-parallel, hydrostatic and LTE atmosphere) are far from being realistic. Even today, coping with a detailed analysis requires a large computational effort and several constraints must still be considered. In this section we present an overview of the common approximations used in the model atmosphere with the goal of finding a way to solve the system of equations.

Geometry

Plane-parallel geometry simplifies the analysis. However it is only adequate under certain conditions. Depending on the scale-height of the photosphere and the stellar radius (R_*) the effect of the atmospheric curvature can be relevant in the analysis. The characteristic length in the photosphere (H, the pressure scale height) can be estimated, assuming hydrostatic equilibrium, a pure hydrogen atmosphere and an equation of state (an ideal gas, for instance). According to the temperature (T) and the effective gravity (g_{eff}), H reads:

$$H = \frac{kT}{\mu\, m_H\, g_{eff}} \tag{2.1}$$

where k is the Boltzmann constant, m_H the hydrogen atomic mass and μ the mass weight for free particles in the atmosphere. In those cases where $H/R_* \ll 1$ and low dense winds the extension of the atmosphere is negligible and the plane-parallel

approximation can be considered. On the other hand, if H is comparable to R_* and the wind is strong, lines can formed in external layers. Under these conditions, effects of the atmospheric curvature must be considered.

The plane-parallel approach is usually suitable for B and late O dwarf stars. Evolved stars with dense winds (supergiants and WRs) need the spherical geometry treatment for reliable results.

Velocity Structure

The solution of the hydrodynamic equations yields the velocity and density stratification of the stellar atmosphere. If magnetic fields are not considered, the momentum equation reads:

$$\rho \frac{\partial \vec{\upsilon}}{\partial t} + (\rho \vec{\upsilon} \vec{\nabla}) \vec{\upsilon} = -\nabla P - \rho \vec{g} + \rho \vec{g}_{rad} \tag{2.2}$$

the variations in the velocity field ($\vec{\upsilon}$) are governed by the gas pressure (P), the gravity force ($\vec{g}$) and the radiative pressure on the material ($\vec{g}_{rad}$), being the latter the hardest to quantify. The description of $\vec{g}_{rad}$ must consider the electronic scattering and the momentum transfer from continuum and lines. These last two terms are specially difficult to calculate since they result from the contribution of a huge number of transitions. This is usually parametrized in a compact way, making easier the global computational process (see the work by Castor et al. 1975, Abbott 1982 and Pauldrach et al. 1986).

Even so, deriving a consistent solution for the velocity stratification is highly expensive in computational time. In those cases where the wind can be neglected it is assumed a hydrostatic atmosphere. If it is not possible, the velocity structure is usually described with an analytical expression for the photosphere plus the stellar wind characterized with several free parameters, consistently with numerical calculations (see for instance Pauldrach et al. 1986).

Once the velocity stratification is known, the density along the atmosphere can be obtained from the continuity equation:

$$\dot{M} = 4\pi r^2 \rho(r) \upsilon(r) \tag{2.3}$$

where ($\dot{M}$) is the mass loss rate and $\rho(r)$ is the density structure of the atmosphere.

Recent findings hint that the velocity pattern of the stellar wind differs from a monotonically and smooth flow. The presence of shocks and structures in the wind can change the stellar evolution (Puls et al. 2008). The incorporation of these events is mandatory to reproduce observed phenomena like X-ray emissions (Harnden et al. 1979), attributed to shocks in the wind, or to bring different observed wind diagnostics

into agreement (e. g. between UV profiles and H_α, see Sundqvist et al. 2010). However, they have no significant impact on the optical lines.

Temperature Structure

A correct description of the collisional and radiative processes (see chapter 3) in the plasma of the stellar atmospheres requires an accurate temperature stratification (Auer & Mihalas 1972). Assuming the conservation of energy through the entire atmosphere and that it is only transferred by radiation it is possible to build the temperature stratification across the atmosphere under the radiative equilibrium approximation. In a no hydrostatic, spherical and stationary medium the full description of the conservation of energy is defined as:

$$\rho \upsilon \frac{\partial \varepsilon}{\partial r} + \frac{P}{r^2}\frac{\partial (r^2 \upsilon)}{\partial r} = \int_0^\infty \chi_\nu (J_\nu - S_\nu) d\nu \tag{2.4}$$

where ε is the internal energy, χ_ν is the absorption coefficient, J_ν the mean intensity (zero moment of the radiation field, see Mihalas 1978), and S_ν the source function.

However, solving this equation is again very time consuming, and some approximations are often made to speed up the process. A faster alternative consists on using a grey atmosphere in LTE (Mihalas 1978). In this way the temperature can be determined independently from the rest of the equations involved in the radiative transfer system, simplifying the calculations. The grey LTE atmosphere approximation, however, is not a realistic description of massive blue star atmospheres, where the radiation field is strong and the LTE condition does not hold. In addition, this simplification does not ensure the energy conservation and it must be checked between the atmosphere boundaries. Some codes rely on a complete solution of the temperature structure, like CMFGEN (see section 2.2), with the consequent increases in the computational time; while others are based on LTE approximations, for instance using Hopf functions as in FASTWIND (see section 2.3).

Radiative Transfer and Statistical Equilibrium Equations

The behavior of the radiation field across the plasma and its interaction with the particles are described by the radiative transfer equation:

$$\mu \frac{\partial I_\nu}{\partial r} + \frac{1-\mu^2}{r}\frac{\partial I_\nu}{\partial \mu} = \eta_\nu - \chi_\nu I_\nu \tag{2.5}$$

In this equation, the variations of the spectral intensity (I_ν) along the atmosphere (where $\mu = cos(\theta)$ is the angle between the ray and the radial direction in spherical geometry), assuming an stationary approach, is equal to the amount of energy absorbed

($\chi_\nu I_\nu$) and emitted (η_ν, emission coefficient) by the medium in each volume element. These two coefficients are determined by the composition and electronic configuration of the plasma, and depend also on the radiation field.

It is possible to solve analytically Eq. 2.5 using the LTE approximation. The emission and absorption coefficients are then easily calculated, since the occupation number in the plasma can be described by the Saha and Boltzmann equations (Mihalas 1978). Instead, in NLTE conditions the Saha and Boltzmann expressions are no longer valid and the thermodynamic state must be described by a more elaborated expression, taking into account both collisional and radiative transitions through the statistical equilibrium equations (see section 3.2.2 for more details). The latter are coupled with the radiative transfer equations (note that there is one equation for each frequency and ray direction), and the set of equations cannot be solved directly.

This system can be treated in several ways, trying to separate the determination of the radiation field and the atomic populations. The mean intensity can be expressed as an operator (Λ) acting the source function:

$$J_\nu = \Lambda[S_\nu]. \tag{2.6}$$

Although an analytical solution cannot be achieved, it is possible to solve Eq. 2.6 with an iterative procedure. Starting from initial population of atomic levels (which can be estimated in a grey LTE atmosphere, for instance), the radiation field is calculated. The results can be used to re-calculate the populations, starting the cycle again and so forth until convergence is reach. This procedure is the core concept of the $\Lambda - iteration$ method (Mihalas 1978). However, it has a big drawback: each step is equivalent to transfer the information between points separated by one mean free path of the photons. Solving the problem for the entire atmosphere is therefore unfeasible.

Several methods have been developed to overcome this problem. The *Accelerated Lambda Iteration (ALI)* is one of the most powerful and commonly used. Based on Cannon (1973)'s work and extended by Scharmer (1981), the method introduces a perturbation in the Λ operator, producing a new approximated Λ^*. The perturbation could be arbitrary, but it must guarantee the convergence. This technique has been widely used in multidimensional and multilevel atom systems (Auer et al. 1994) and also in the development of codes to simulate expanding stellar atmospheres (Hamann 1985; Pauldrach & Herrero 1988; Puls 1991; Santolaya-Rey et al. 1997).

Blocking and Blanketing Effects

In their way from the stellar interior to the surface, photons interact with matter. The UV flux (the bulk of the radiation field in hot massive stars) will be absorbed by hundreds of transitions (chiefly from metallic elements) which block the radiation.

As a result, the opacity of the medium increases, making the temperature of the inner layers higher (backwarming or blanketing effect). This temperature change affects the ionization stratification in the line formation region of several important diagnostic lines (as He I lines). The blocking of UV radiation also reduces the Lyman continuum flux and enhances the infrared and radio emission. This effect has a strong impact on the derived stellar parameters, and in the ionization of the surrounding environment. The effective temperature can change by as much as 5000 K with the incorporation of this effect (Herrero & Najarro 2005).

A full description of all the metallic lines involved in the UV blocking effect, although essential to accurately model the atmospheres of massive blue stars, is computationally expensive. Different codes usually rely on different approximations, like considering the effect of all the transitions using Opacity Distribution Functions (ODF, Kurucz 1993a).

2.2 State-Of-The-Art Stellar Atmosphere Codes

In the last twenty yeas, different groups have tackled the analysis of massive blue stars. Each group has used different numerical approaches and simplifications, according to the targets and goals of their projects. Several codes have been developed since the first estimations of the stellar parameters of OB stars by Unsold (1955). In these section we present an overview of the main state-of-the-art stellar atmosphere codes used nowadays for quantitative analyses of massive blue stars.

- **TLUSTY** [1] (Hubeny 1988; Hubeny & Lanz 1995) is a plane-parallel hydrostatic and stationary code. Departures from LTE are allowed. The opacity and blanketing treatment are performed according to either ODFs or Opacity Sampling (OS, Kurucz 1993a).

  The strength of TLUSTY is its detailed treatment of metallic transitions. However, the code does not consider the stellar winds of OB stars, and can only be used to derive photospheric parameters and abundances for stars with weak or moderate winds.

  TLUSTY has been used in several massive blue star analyses. Some recent examples are the works by Trundle et al. (2007) and Hunter et al. (2008b). A large TLUSTY grid oriented to the quantitative analysis of O- and B-type stars is available by Lanz & Hubeny (2003) and Lanz & Hubeny (2007).

- **DETAIL & SURFACE** (Butler & Giddings 1985) stellar codes determine the level population and the formal solution, respectively, under NLTE conditions, plane-parallel geometry and hydrostatic equilibrium. The blanketing is treated

[1] http://nova.astro.umd.edu/

with the ODF approximation (Kurucz 1993a). These codes do not solve the stellar atmosphere structure and require an initial atmosphere model to work with. This atmosphere model can be generated, for instance, with the code ATLAS9 (Kurucz 1993b), which relies on plane-parallel and LTE approximations.

This combination of stellar codes (ATLAS9+DETAIL+SURFACE) gives a fast and efficient way of obtaining realistic results, as long as the assumption of LTE is valid for the atmosphere structure (dwarf and giant B stars, but not supergiants). The method is based on a hydrostatic approximation and it does not include any stellar wind treatment.

This hybrid NLTE method has been applied to several quantitative analyses, see for instance the works by Przybilla et al. (2006), Nieva & Przybilla (2008) and Irrgang et al. (2010).

- **WM-basic**[2] (Pauldrach et al. 2001) provides a complete NLTE line blanketed treatment on the entire atmosphere, from the photosphere to the wind. It is based on the assumption of homogeneous, stationary and spherical symmetric radiation driven wind. The code was developed to reproduce UV fluxes and profiles through a consistent description of the opacity and blanketing. The lack of a correct Stark broadening treatment prevents its use to analyze the photospheric hydrogen and helium lines in optical wavelengths.

  Some quantitative analyses carried out with WM-basic to determine stellar and wind parameters are compiled in Bianchi & Garcia (2002) and Garcia & Bianchi (2004).

- **CMFGEN**[3] (Hillier & Miller 1998) produces a sophisticated NLTE, spherically symmetric wind treatment. The introduction of detailed atomic models for all the chemical elements (even iron) allows an accurate treatment of the opacity and blocking/blanketing effects without using approximate techniques (as ODF or OS). An undesired disadvantage of this accuracy is the huge computational time required to reach a solution. It does not solve the hydrodynamics equation, so the velocity and density structure must be provided as input parameters.

  This code has been used in many quantitative analysis of O- and B-type stars (Crowther et al. 2006; Searle et al. 2008). It was designed to reproduce the expanded atmosphere of evolved objects, like LBVs (see for instance the works by Najarro et al. 1997 and Herrero et al. 2010).

[2] http://www.usm.uni-muenchen.de/people/adi/Programs/Programs.html
[3] http://kookaburra.phyast.pitt.edu/hillier/web/CMFGEN.htm

- **FASTWIND** (Santolaya-Rey et al. 1997; Puls et al. 2005) was developed to calculate NLTE model atmospheres with line blanketing, spherical symmetry and a robust stellar wind treatment in a short period of time. The code was designed for the analysis of O-, B- and A-type stars in the optical and infrared wavelength ranges. Thanks to the implemented approximations, mainly in the opacity treatment, the code is able to generate a reliable stellar model atmosphere of similar quality to CMFGEN, which can take hours, in minutes (see the comparisons between both stellar models presented by Puls et al. 2005). However, the approximations introduced make FASTWIND suitable for optical and infrared analyses, but not UV ones (where CMFGEN or WM-basic, for example, shall be used).

  FASTWIND has been widely used in quantitative analyses of massive blue stars in the Milky Way (Repolust et al. 2004; Simón-Díaz et al. 2006; Simón-Díaz 2010) and also in nearby galaxies (Trundle & Lennon 2005; Urbaneja et al. 2005b).

2.3 Fast Analysis of STellar atmospheres with WINDs (FASTWIND)

The pillar of this work and the subsequent quantitative analyses, compiled in the next chapters, is the FASTWIND stellar code. The speed of the code, which generates realistic models in minutes, is its best feature and the goal for which it was designed. Thanks to this, we can build large grids of models in a short period of time (see chapter 4). In this section we illustrate the main approximations employed in code to reach this fast performance.

Temperature Structure

FASTWIND avoids the rigorous solution of the radiative equilibrium to save computing time. Instead, the temperature stratification was implemented using a modified NLTE-Hopf function (Mihalas 1978). In the first versions of the code, the temperature was defined with three initial parameters (Hopf parameters) manually introduced as input in the model. This approximation means that the energy conservation is not guaranteed, and the Hopf parameters are actually selected to achieve the flux conservation along the atmosphere. The temperature treatment was updated in subsequent FASTWIND versions (Puls et al. 2005) allowing a more self-consistent treatment. A correction based on the thermal balance of electrons was implemented, similar to the one used by Kubát et al. (1999). This increases slightly the final computing time, but gives a more user-independent temperature stratification, a smaller error in the flux conservation, and an improved description of the stellar wind.

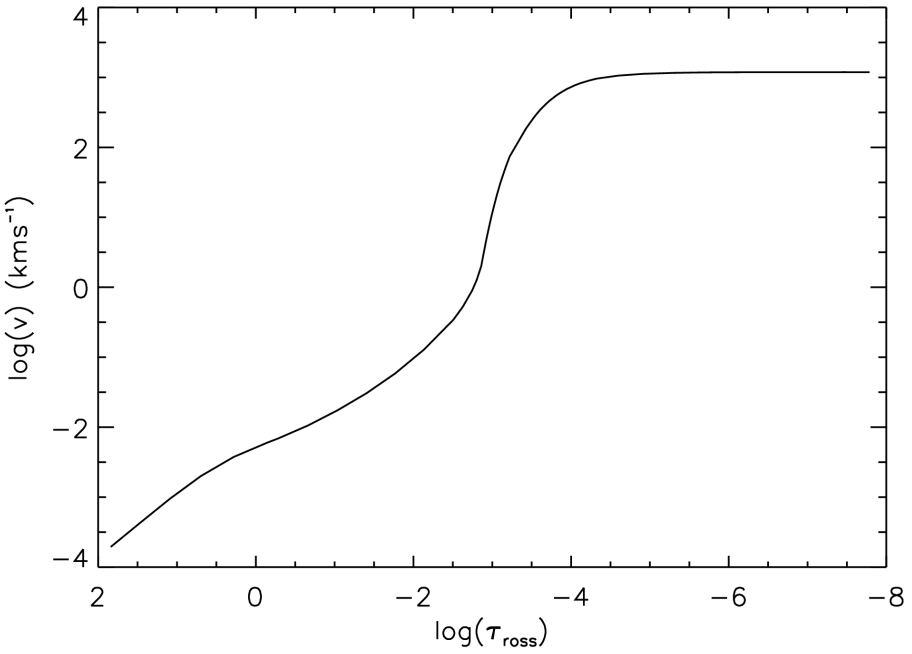

FIGURE 2.1— Example of the velocity stratification of a FASTWIND model (see Eq. 4.3). See the smooth transitions from the photosphere to the wind at $log\,(\tau_{ross}) \sim -3$

Velocity Structure

Consistently with the philosophy of a fast procedure, FASTWIND does not solve the hydrodynamic equations either. The code follows the concept of Unified Model Atmosphere (Gabler et al. 1989) where the photosphere and the stellar wind are treated together through a smooth transition of the velocity structure. FASTWIND calculates the velocity field using a semi-empirical expression proposed by Hamann & Schmutz (1987). An exponential behavior is assumed in the inner part of the photosphere and a β-law function describes the wind layers:

$$v(r) = \begin{cases} v_\infty(1-b/r)^\beta & if\ r > r_c \\ v_{min}\, exp[(r-R_*)/H] & if\ r < r_c \end{cases} \tag{2.7}$$

where v_∞ is the wind terminal velocity, which together with β determine the slope of the wind velocity stratification. v_{min} is the minimum velocity in the inner photosphere. The parameters b and r_c are calculated to force a smooth transition between photosphere and wind. Figure 4.3 shows an example of the velocity

stratification along the atmosphere generated by FASTWIND for a model with an effective temperature 30000 K, a surface gravity 3.00 dex, $v_\infty = 1200\ kms^{-1}$ and $\beta = 1.00$.

Model Atoms Treatment

The calculation of model atmospheres in NLTE requires a full description of the atomic elements included, as we mentioned before (see also chapter 3 for more details). It is necessary to include not only the transitions present in the observed spectrum, but also all the metallic lines that constrain the opacity and the blocking/blanketing effect. However, a complete characterization of the entire atomic species requires a huge computational time, as seen in CMFGEN models. This is not in the quickness spirit of FASTWIND.

To handle the atomic treatment in a fast and accurate way, FASTWIND separates metals in *explicit* and *implicit* elements. The elements included *explicitly* in the code require a detailed description of the structure of energy levels and all the interactions that populate/depopulate them (see chapter 3). Hydrogen and helium (the most abundant atoms in the stellar structure) together with the elements whose transitions the user wants to reproduce (and include in the formal solution) are managed in this way. The rest of chemical species will play a fundamental role in the opacity treatment (as it is the case of iron), but they are not included in detail. FASTWIND considers the occupation of these elements by approximated NLTE rate equations. The needed information is provided by WM-basic data (Pauldrach et al. 2001). This alternative way speeds up hugely the spectral synthesis. If an element is introduced *explicitly* it is automatically evicted from the background approximated calculation.

The exceptionally fast performance of this stellar code has allowed us to carry out quantitative studies and develop the tools presented in the next chapters (see chapters 4 and 5). The development of a grid of models in a reasonable amount of time without a loss of realism in the optical range, and subsequent sub-grids for refining the stellar parameters in almost no additional time underlines its potential.

3

A New Silicon Model in Town

Dr. Hibbert: "Yes, is the alien carbon-based or silicon-based?"
Homer: "Uh, the second one. Zillophone. Next question..."
The Simpsons

MODELING chemical species in stellar atmospheres is crucial for a correct interpretation of blue supergiant spectra. Progress in observational facilities has enhanced the need for a better atomic data giving an accurate representation of the observed stellar line profiles. While in cold and dense objects it is possible to describe the atomic behavior in terms of local properties of the medium (temperature and particle density), in the domain of blue supergiant stars this is no longer possible due to a strong radiation field that cannot be neglected, forcing a detailed description of the atomic structure and rendering the effects on the level occupation number is mandatory.

This chapter is centered on the incorporation into the FASTWIND stellar code (key tool of this work) of a new silicon atomic model, originally designed for DETAIL+SURFACE, besides different comparison tests with the atomic model used previously.

3.1 The Need of a New Silicon Model

Silicon is a key element in the quantitative analysis of massive blue stars, mainly in early B- and late O-type stars. At these temperatures the optical spectra show transitions of different silicon ionization stages (Si II-III-IV), an invaluable tool for determining the effective temperature of the stars through the ionization balances available according to their spectral type. In addition, the silicon abundance hardly

suffers any modification through the stellar evolution and hence it is a good indicator of silicon abundance in the interstellar medium, where the stars were born.

Nevertheless several studies have revealed some limitations in the commonly used silicon atomic model (Becker & Butler 1990) that remain unsolved.

- In stars with spectral type around B3 there are lines of the three ionization states included in the model (Si II-III-IV). This allows us to determine the effective temperature using different ionization balances, which results in discrepancies larger than the typical errors ($\sim 500 - 1000\,K$) (Urbaneja 2004).
- In objects with spectral type O9-B0 the effective temperature can be estimated either from the ionization balance of the He II/He I or from the Si IV/Si III one. These ways do not give the same temperatures, and differences $\geq 1000\,K$ are common (Simon-Diaz 2005).

Atomic models are neither perfect nor complete and these problems may be traced to a lack of accuracy of the atomic silicon model. Obviously, we do not have all the information required for a *perfect* description of the silicon atomic structure, notwithstanding we rely on modern and more accurate quantum mechanical data. An initial effort to improve the silicon model atom, introduced by Becker & Butler (1990), was performed by Dr D. Lennon and Dr. C. Trundle using the updated Si II version implemented in the TLUSTY stellar code (see Allende Prieto et al. 2003). Although this first revision partly solved the problems indicated in the first item above, a more extensive modification was needed also in the other two silicon ions (Si III and Si IV). Dr. N. Przybilla (Priv. communication 2007) developed a new model for these three silicon ions oriented to DETAIL using the latest calculation of atomic structure and scattering processes.

The atomic model structures and the way in which FASTWIND and DETAIL handle this information present strong similarities, making the transfer to FASTWIND relatively easy. It is fundamental to be aware that the model was designed for DETAIL and calibrated mainly with dwarf and giant stars. The inclusion of an expanding atmosphere with spherical symmetry, as done in FASTWIND, can introduce differences in the profiles that DETAIL cannot reproduce (see chapter 2 for a description of each stellar code).

3.2 Atomic Model Description: FASTWIND and DETAIL Philosophy

Following the idea of DETAIL, FASTWIND is a data-driven code. This means a complete independence between the source code and the atomic models used with it, a huge simplification in the introduction and modification of new atomic models. The similarities between both stellar codes also offer the option of transferring atomic

models from one to the other with only certain adaptations. Since the codes have *evolved* separately, there are processes that require more effort than others (see section 3.3). The DETAIL+SURFACE manual by K. Butler[1] and the work by Przybilla et al. (2001) are fundamental sources for a detailed understanding of atomic model construction for DETAIL.

A reliable atomic model demands a description of the atomic structure (energy levels) and information about all the interaction processes (collisional and radiative) that play a role in the population of each energy level. Several approximations have been followed to achieve a reliable atomic energy structure together with an ionization and excitation description, based either on ab-initio quantum mechanical considerations or following approximate computations. A more complete description can be consulted in Nahar & Pradhan (2003); Nahar et al. (2003) (see also the dissertations of Przybilla 2002 and Nieva 2007).

3.2.1 Atomic Structure and Energy Levels

The structure of the atom and the effects that it can suffer by the interaction with photons or other charged particles (mainly electrons) are described, in quantum mechanics, through the Schrödinger equation. Its solution provides the energy levels and characterizes the scattering processes. However, in the case of multielectron systems it is no possible to reach an exact solution, and approximated techniques have to be followed. Several methods have been developed to reach an alternative way through effective potentials, as done for instance it in the case of the code SUPERSTRUCTURE (Eissner 1974).

The demand of a complete description of the atomic structure and the need of knowing the radiative and collisional ratios motivated several collaborations in order to provide this information for astrophysics studies. The Opacity Project (OP, Seaton 1987; Seaton et al. 1994) and the Iron Project (IP, Hummer et al. 1993) are probably the main sources through detailed ab-initio calculations. Also, not to forget, the extensive semi-empirical atomic database provided by Kurucz (1992) (and references therein). These works, together with the information provided by the NIST Atomic Spectra Database[2] or VALD[3] (Vienna Atomic Line Database) archives, are the main sources for the energy levels and their atomic properties considered in the atomic model.

The atmosphere model is calculated using the atomic structure obtained under the LS-coupling formalism. The formal solution and the final spectra are computed paying attention to the fine structure of the levels involved in the transitions. Their implementation in the atomic model must be done bearing in mind that a small number

[1] http://ccp7.dur.ac.uk/Docs/detail.pdf

[2] http://www.nist.gov/physlab/data/asd.cfm

[3] http://vald.astro.univie.ac.at/ṽald/php/vald.php

of levels considered may produce an inaccurate result, but increasing their number will increase the calculation time as well. To save computation time the highest energy levels can be packed (the so-called superlevels), i. e. all the levels with the same principal quantum number (n) are considered as single energy state with an effective statistical weight. That is possible since the differences in the energy between them are small enough. Most of the silicon levels presented in this work have experimental energies; when they are not available, theoretical values have been adopted.

3.2.2 Statistical Equilibrium

The electronic configuration of an atom (or ion) embedded in a plasma is continually modified by the different radiative or collisional transitions with the rest of particles. Basically, we have interactions with photons or electrons (ions or neutral particles are usually neglected since their densities and velocities are lower compared with electrons for metallic species) that populate o depopulate each state conforming to their energy, density, cross-section, etc.

The behavior of the atom and its population in a plasma depend of the assumed thermodynamic state of the atmosphere. In cold and dense stars, considering the atmosphere in LTE is plausible. Under this approximation all the processes are dominated by collisions and the influence of the radiative field in the atomic populations can be neglected. The particle mean-free-path (i. e. the average distance that a particle moves between interactions) is short enough to assume that only local properties, temperature and particle density, determine the energy level population/depopulation rates. In a thermalized environment like that, developing an atomic model is simple; since the level populations will be described by the Saha and Boltzmann expressions, providing the enough information for solving the radiative transfer equation (see section 2.1) .

On the other hand, in *hot*-type stars and low density atmospheres (A-, B-, O-supergiant) assuming LTE is equivalent to neglecting the impact of the radiative coming from different regions of the atmosphere on the excitation and ionization of the atoms, a naive approach to the problem. At this low density environment the collisional mean-free-path is not so short and the radiation emitted in different areas can affect the atomic properties. The Saha and Boltzmann equations are no longer valid and a more general approach is required. The statistical equilibrium equations, in which all the processes that populate/depopulate each level are taken into account, shall be considered under the NLTE state. The equations read:

$$n_i \sum_{j \neq i} (R_{ij} + C_{ij}) = \sum_{j \neq i} n_j (R_{ji} + C_{ji}) \tag{3.1}$$

where R_{ij} and C_{ij} are the radiative and collisional rate respectively, for transitions from level i to level j; n_i and n_j the occupancy number densities for the respective level. Left side represents the transitions (radiative and collisional) that depopulate the level i, while the right part of the equation shows state population.

The radiative rates (assuming $i < j$) are given as:

$$R_{ij} = 4\pi \int_0^\infty \alpha_{ij} \frac{J_\nu}{h\nu} d\nu \tag{3.2}$$

$$R_{ji} = 4\pi \left(\frac{n_i}{n_j}\right)^* \int_0^\infty \frac{\alpha_{ij}}{h\nu} \left(\frac{2h\nu^3}{c^2} + J_\nu\right) e^{(-h\nu/kT)} d\nu \tag{3.3}$$

α_{ij} is the cross-section, usually assumed equal in both expressions; h is the Planck constant; and c the speed of light. Both equations are functions of the temperature (T) and the frequency (ν). The downward rate (Eq. 3.3) contains the spontaneous emission in the first term of the sum and the stimulated one in the second. $\left(\frac{n_i}{n_j}\right)^*$ refers to the LTE level population ratio.

The collisional rates are given by:

$$C_{ij} = n_e \int_0^\infty \sigma_{ij} f(v) v dv \tag{3.4}$$

$$C_{ji} = \left(\frac{n_i}{n_j}\right)^* C_{ij} \tag{3.5}$$

σ_{ij} is the collisional cross-section and $f(v)$ the velocity distribution of the colliding particles (chiefly electrons).

These set of equations for each atomic level give a linearly dependent system. To close it we add the total number conservation equation over all levels and ions for a given species:

$$\sum_i n_i = N_{elem} \tag{3.6}$$

This set of equations must be solved together with the radiative transfer equation for a reliable description of the stellar atmosphere under the NLTE assumption. The resolution of this non-linear equation system is not trivial an requires a great numerical effort (see section 2.1).

The OP and IP, together with work by Kurucz (1992), are fundamental sources for the radiative and collisional ratios, including an extensive set of ions. Measuring collisional rates is not easy and there are only quantum mechanical data for a limited number of levels, the rest of them being based on *the gaunt factor approximations*. van Regemorter (1962) and Seaton (1962) introduced two formulae for these situations. Seaton's expression gives the collision ionization cross-section, while the van Regemorter's applies for collisional excitations in interactions allowed by the electric dipole selection rules. In the case of forbidden transitions, the semi-empirical formula by Allen (1973) is used.

All the relevant phenomena that affect the atom state must be taken into account and a complete description, as far as possible, of all the collisional and radiative ratios must be presented in the atomic model to solve Eq. 3.1. These interactions can be listed as:

- **Collisional bound-bound (CBB)** $e + X^{+Z} \leftrightarrows e' + X^{+Z*}$

  Only the collisions with electrons are considered since they are the most probables. The lowest excited levels rely on ab-initio cross-sections calculations. The rest are treated either by the van Regemorter (1962) approximation, which requires information about the transition oscillator strength (allowed transitions) or by the Allen (1973) approximation (rest of them).

- **Collisional bound-free (CBF)** $e + X^{+Z} \leftrightarrows e' + X^{+Z+1} + e''$

  The ionization cross-section due to collision is calculated by the Seaton (1962) formula. The ionization thresholds are obtained from ab-initio data or (chiefly for highly excited levels) the hydrogenic approximation (Mihalas 1978), if there is no any other source.

- **Radiative bound-bound (RBB)** $h\nu + X^{+Z} \leftrightarrows X^{+Z*}$

  The input parameter needed for their characterization is the oscillation strength (f_{ij}). They are usually taken from ab-initio results (dipole-allowed transitions). The line cross-section of RBB transitions is given by:

  $$\alpha_{ij} = \frac{\pi e^2}{m_e c} f_{ij} \phi_\nu \tag{3.7}$$

  The line profile (ϕ_ν) is simplified in the population calculation assuming only Doppler effect, due to thermal motions, plus the microturbulence (for metallic

elements). Instead, the formal solution and the subsequent synthetic spectrum is built accounting for natural, collisional, Doppler effect and microturbulence broadening in the transitions, the so-called Voigt profile.

- **Radiative bound-free (RBF)** $h\nu + X^{+Z} \leftrightarrows e + X^{+Z+1}$

  The lowest lying levels (normally until $n \sim 4$) have accurate quantum mechanic data for the photoionization cross-section. The OP provides a detailed description of the photoionization cross section for the first excited levels over an ample catalogue of ions studied. Again, the hydrogenic simplification is used for the rest.

- **Dielectronic recombination** $e + X^{+Z} \rightarrow (X^{+Z-1})^{**} \rightarrow X^{+Z-1} + h\nu$

  This mechanism is not explicitly implemented in the atomic model due to the complexity of quantifying it. Nevertheless, in those levels that have a RBF treatment by means of OP data the dielectronic recombination is treated indirectly through the *resonances* in the photoionization cross section (see below).

  The omission of these processes in the atomic model poses a serious problem for treating some important lines, as the N III transitions around $4630 - 4640\,\AA$.

- **Collisional and radiative free-free (CFF and RFF)**

  They are indispensable for a reliable treatment of the atmosphere continuous opacity (together with the bound-free transitions). However, they are only explicitly implemented for the hydrogen and helium atoms since they are the most abundant and their contribution to opacity cannot be ignored. Ions less abundant in the atmosphere, like silicon, do not include free-free transitions in the atomic model, their contribution is negligible.

3.3 Silicon Model: A Detailed Description

In this section we summarize the main characteristics of the two atomic models considered in this study and the sources of atomic data used by each one of them. The atomic model designed by Dr. Przybilla and transferred by us to FASTWIND is labeled as *'NEW'*, while the model previously used is marked with *'OLD'* in next sections.

Energy Levels

Both silicon models comprise a detailed description of Si II, Si III and Si IV ions plus the fundamental level of Si IV.

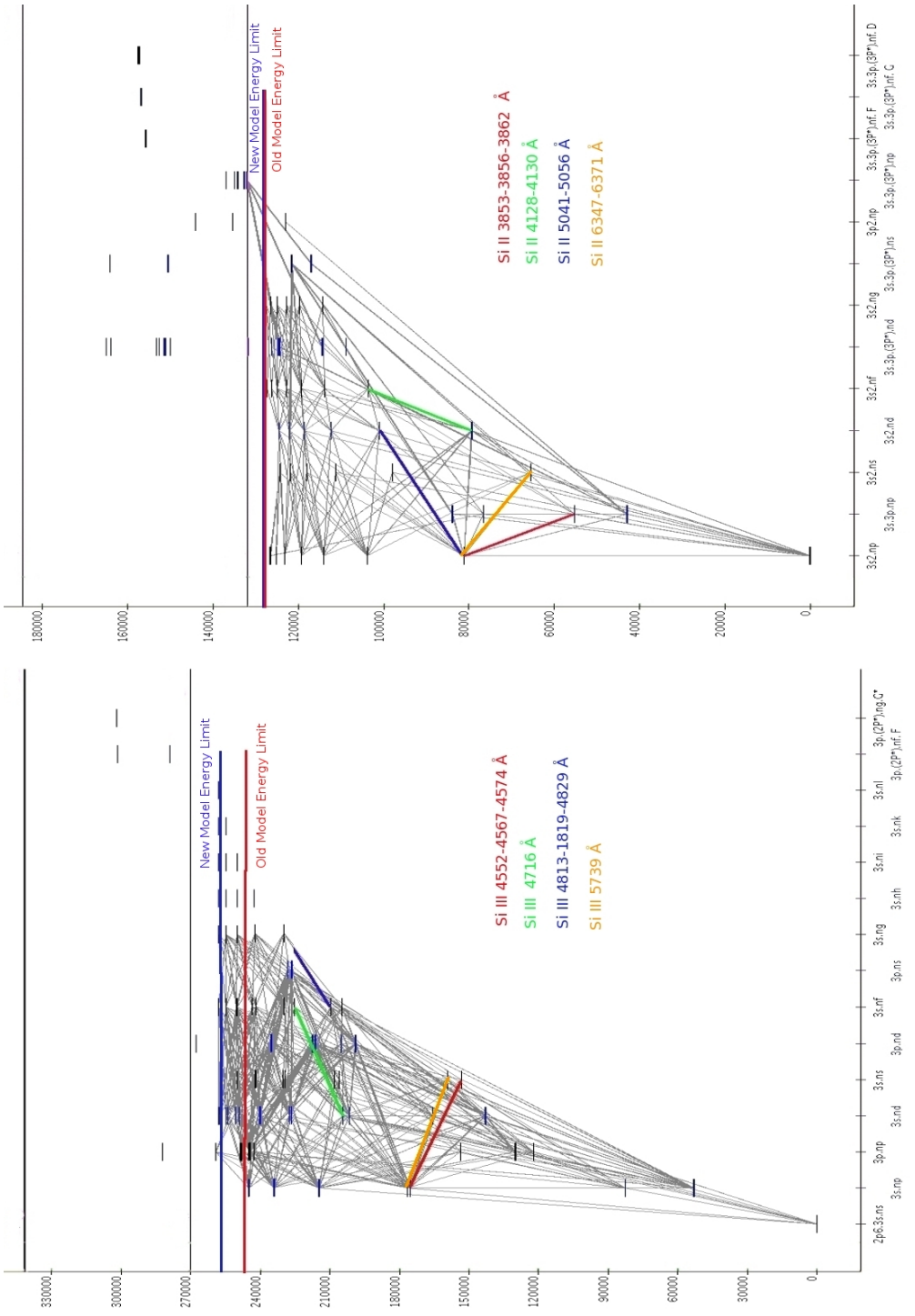

FIGURE 3.1— Grotrian diagrams for Si II (top), Si III (bottom). They were generated by the NIST database (Ralchenko et al. 2008). Only the allowed electric dipole transitions are shown in the charts. The main optical lines in O- and B- type are marked in color. The maximum energy level considered in each atomic model is also indicated.

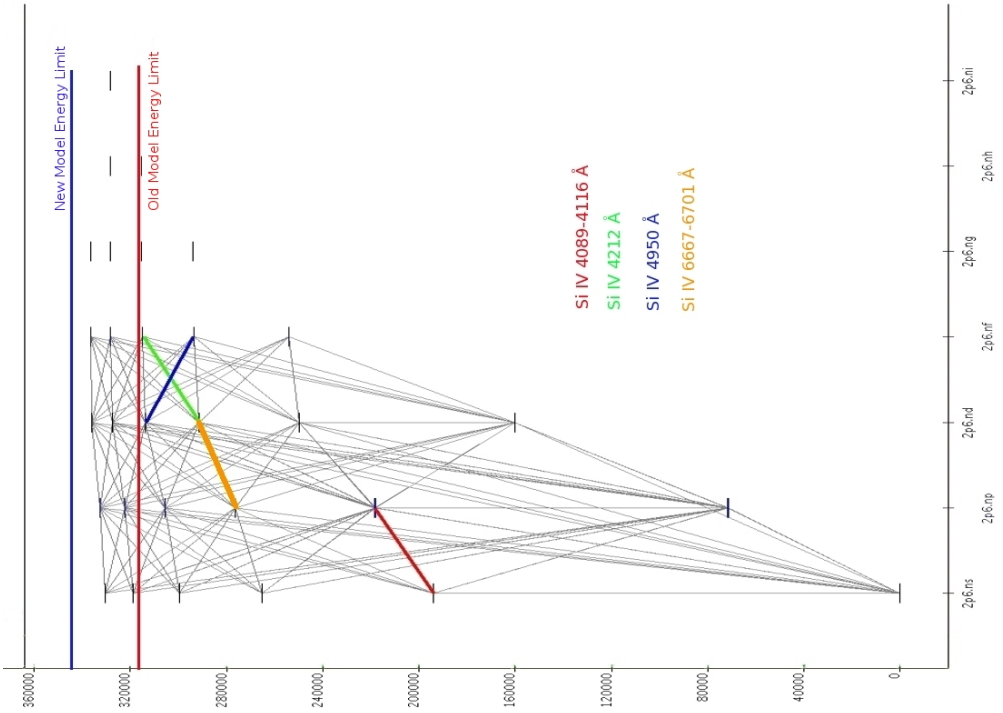

FIGURE 3.2— Grotrian diagrams for Si IV, see Fig. 3.1.

Figures 3.1 and 3.2 show the Grotrian diagrams (Ralchenko et al. 2008) for the three ions included in the atomic model, along with those radiative transitions allowed by the electric dipole mechanism. The upper energy limit considered by each atomic model is also marked, together with the main transitions used in the analysis of B-type stars in the optical wavelength range ($\sim 3800-7000$ Å). The upper energy edge will mark the reliability of some transitions, thus if the stages involved in a transition are strongly populated/depopulated from/to a level no considered in the atomic model the resultant profile will not be reliable enough to compare with observations.

Table 3.1 illustrates the main differences between both silicon atomic models. The Si IV and Si III implemented in the new atomic model rely on a more complete level structure compared with the old ions built by Becker & Butler (1990), reaching levels with higher principal quantum number (*'n'*). This shift in the upper limit energy boundary introduces a higher accuracy in the atomic description, however it also increases the computational time. Trying to simplify the calculation as much as possible, high energy levels were packed in single levels according to n (superlevels). In the Si III ion, they were also split according to the triplet and singlets systems.

		Si II		Si III		Si IV	
		OLD	NEW	OLD	NEW	OLD	NEW
Number of Levels		34	39	28	70	18	35
Maximum *'n'* Included		10	10	6	9	6	10
Superlevels *'n'*		9,10	8,9,10	–	8,9*	–	9,10
Maximum Energy (cm^{-1})		127312	127104	242471	257631	315099	346191
Collisional Transitions	CBB_{ab}	0	171	66	190	0	21
	CBB_{Van}	174	249	40	487	45	202
	CBB_{All}	354	387	153	1755	103	402
	CBF_{Sea+h}	34	39	28	69	18	35
Radiative Transitions	RBB	174	298	114	506	52	242
	RBF_{ab}	0	35	0	57	0	23
	RBF_{h}	34	4	28**	12	18**	12

TABLE 3.1— Energy levels and transitions stratification in the old silicon model and the new atomic version. The transitions are split in radiative and collisional, and in subgroups depending of the treatment used: (ab), ab-initio data; (h) hydrogenic approximation, see Mihalas (1978) ; (Van), van Regemorter (1962) formula; (All), Allen (1973) expression; and (Sea), Seaton (1962) equation. Superlevels for Si III (*) are split in singlets and triplets. Not all the RBF transition (**) in the old model are calculated by the hydrogenic approximation, see text for more details.

The Si II designed by Becker & Butler (1990) was notably improved by Dr. Lennon and Dr. Trundle (Priv. communication) based on the silicon atomic model incorporated in the stellar code TLUSTY (see Allende Prieto et al. 2003). The issues cited by Urbaneja (2004), clearly due to the lack of detail in the atomic model, were solved in part with this improvement. The energy structure proposed by the new atomic model is rather similar to the TLUSTY version: both atomic models share almost the same number of elements and the upper energy limit (see Tab. 3.1).

The new energy levels are based on the work of G. A. Martin and R. Zalubas developed by the NIST 3.1.0 (Ralchenko et al. 2008). The old model use the energy levels measured by Moore (1965), except for Si II which takes the information from the atomic model implemented in TLUSTY (Allende Prieto et al. 2003).

Collisional and Radiative Transitions

The radiative transitions allowed by the electric dipole mechanism are shown in Figs. 3.1 and 3.2. However, these are not the only ones to be taken into account in a detailed atomic model: collisions, forbidden transitions or ionization/recombination have to be also accounted for a reliable NLTE computation. Some of them are not straightforward to be quantified (e. g. the intercombination transitions between levels with different spin stages, forbidden by electric dipole selection rules, that contribute to the Si III triplet at $\sim 4820\ \AA$).

In the subsequent, we describe briefly the treatment applied to collisional and radiative processes in the new silicon atomic model and the main data sources. The old atomic model follows similar approximations as it is listed in Tab. 3.1. It also

summarizes the number of transitions considered in the old and the new atomic model, along with the approximation employed in their treatment.

Collisional Processes

All the states treated for both atomic models are coupled by CBB transitions but only the low ionization states have accurate quantum mechanical data. There are several studies concerning collisional strengths for the silicon ions. The new atomic model uses recent computations by Butler et al. (in Prep.) for Si II, Griffin et al. (1999) for Si III and the work by Kimura et al. (1998) on Si IV.

In those cases in which directly computed data are not available the approach suggested by van Regemorter (1962) is employed, using the oscillator strengths provided by Froese Fischer & Tachiev (2004). Forbidden transitions and those without information of the oscillator strength were considered with Allen (1973)'s semi-empirical expression. Generally this approximation uses a collision strength (related with the collisional cross-section) equal to one for all of them. High excited levels can be coupled with the continuum through collisions. Thus, using a collisional strength equal to one in these cases has not much sense, since they can be easily excited and coupled to the next ion fundamental stage by collisions. Several of these transitions were fitted empirically until an appropriate match to the observations[4] was obtained (see Nieva 2007).

The CBF transitions were carried out either using Seaton (1962) formula with OP data or through the hydrogenic approximation in the high ionization states (Mihalas 1978).

In the old atomic model there are only precise CBB data for the lowest term of Si III. The rest of the transitions follow the same approximated rules than in the new atomic model.

Radiative Processes

RBB transitions are described by the oscillator strength in the case of the allowed transitions, represented in the Grotrian diagrams of Figs. 3.1 and 3.2. The sources are the same that in CBB collisional cases, (Froese Fischer & Tachiev 2004).

RBF processes use photoionization cross-sections provide by the OP. Again, the hydrogenic approximation is required for high ionization states when no further information is available (Mihalas 1978).

While introducing the OP photoionization cross-section in DETAIL does not present any major issue, in FASTWIND it is more challenging because it does not

[4]Note that these calibrations were done with giant stars by the stellar code DETAIL. They should be tested for the case of supergiant objects analyzed with FASTWIND

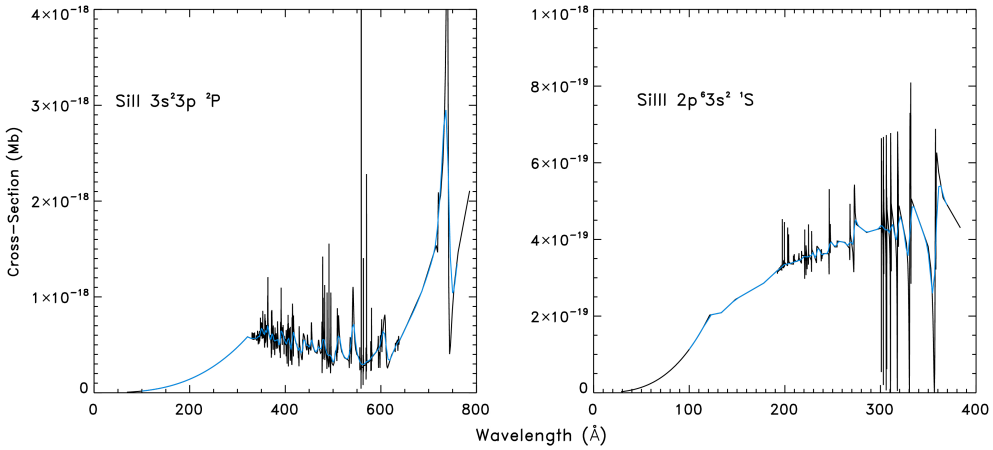

FIGURE 3.3— Photoionization cross-section for the Si II (left) and Si III (right) fundamental states obtained from OP (black). The blue curve represents the *smoothed* version of the original OP data and the input for FASTWIND (see the text for more details).

calculate a hydrostatic model as DETAIL does. The cross-section must be evaluated in all atmospheric layers and since the material movements introduce a Doppler effect on the OP frequency grid a new one must be defined at each height in the atmosphere. If we try to use a mesh of frequencies so accurate as the OP provides, although possible in DETAIL, in FASTWIND would represent a huge amount of computational time. To avoid this, the cross-section is smoothed by a Gaussian function ($R = 100$) to a coarse frequency grid, but keeping the integral and then the same radiative rate (Eq. 3.5). Figure 3.3 displays two examples of the photoionization cross-section from the fundamental states of Si II and Si III. In spite of the lost of resolution due to the smoothing process, the resonances are still present in the calculation. The autoionization and dielectronic recombinations, although not explicitly treated in the model, are accounted through the resonances in the cross-section. The use of OP data was employed in other elements adapted for FASTWIND, nevertheless the old silicon does not count on them. This new incorporation required certain modifications of the FASTWIND source code for accepting OP data in a similar way as the last version of DETAIL does. This was done with the help of Dr. J. Puls. As it was pointed by Bautista et al. (1998), this average cross section is also expected to minimize errors in the derived ionization rates that could result from small uncertainties in computed positions of resonances.

The introduction of the OP photoionization cross-section is a big improvement in the description enclosed in the atomic models with respect to the previous version, treating the RBF transitions by means of a hydrogenic approximation with the

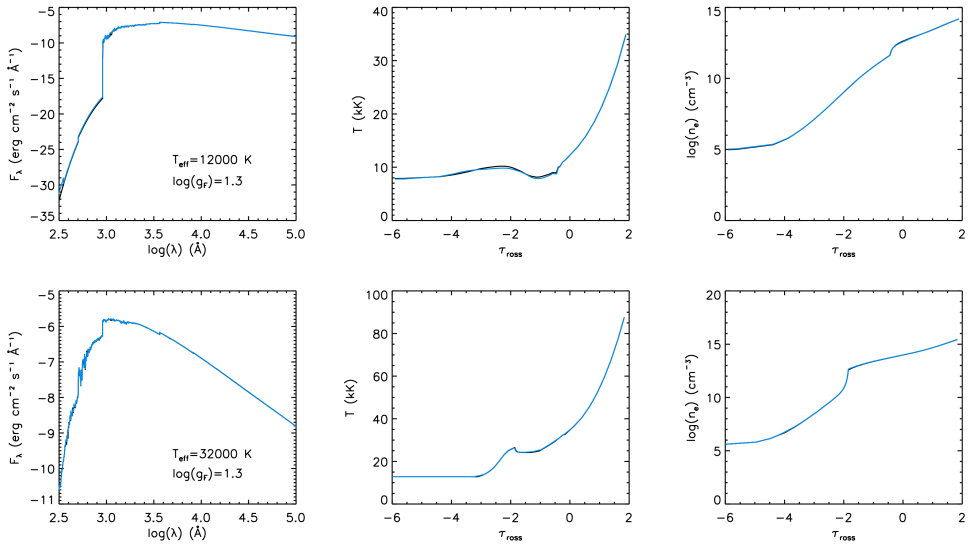

FIGURE 3.4— Atmospheric structure -flux (left), temperature (middle) and electronic density distribution (right)-, for two different temperatures -12000 (top) and 32000 K (bottom)- with the same flux-weighted gravity ($log\,(g_F) = 1.3\ dex$, see Eq. 4.1). The old atomic model is plotted in black, while the new one is in blue.

exception of the lowest energy states of Si III and Si IV, which relies on a linear least-square procedure for fitting the cross-section.

3.4 *Old versus New* Silicon: On Synthetic Profiles

The new atomic model was evaluated through two tests. In the first one a comparison between the synthetic spectra generated by the old model and the new one was performed. Secondly, we analyzed a set of good quality supergiant optical spectra and studied the stellar parameters derived with each silicon atom.

3.4.1 Comparison Tests

The synthetic comparisons were performed over the whole $T_{eff} - log\,(g)$ plane comprised in the grid described in section 4.1. The microturbulence was fixed to 15 $km\,s^{-1}$ and the abundances to solar values, reducing the computational time required. Nonetheless, the complete mesh in $T_{eff} - log\,(g)$ provides us with a clear view of where the differences are, and what is their impact.

Stellar Atmosphere Comparison

Figure 3.4 shows emergent the flux, temperature and electronic density of two models with effective temperature 12000 K and 32000 K, both with the same flux-weighted gravity ($log(g_F) = 1.3$ dex, see Eq. 4.1). The effects of the new silicon model atom on the stellar atmosphere structure are practically negligible. As we have already commented, the main sources in the opacity and the atmosphere stratification are due to hydrogen, helium and other chemical elements, such as iron, implicitly considered in the atmosphere model for a correct treatment of the line blanketing, which are identical in both. The differences when using one or the other silicon model are practically null. The small jumps displayed in the temperature and density structure are in the joint of the photosphere and wind regimes.

Synthetic Profiles Comparison

Nine models covering three temperatures, $12000 - 22000 - 32000$ K, and three flux-weighted gravities, $1.1 - 1.3 - 1.5$ dex were selected to study the impact of the new model ions on the profiles of three important silicon optical lines: Si II 4128 $\AA$, Si III 4552 $\AA$ and Si IV 4116 $\AA$. Figures 3.5, 3.6 and 3.7 present the line profiles resulting from FASTWIND computations using the two atomic models.

The Si IV 4116 $\AA$ transition (Fig. 3.5) does not show any clear difference between the two versions. At low temperatures slight differences in the line core begin to appear, making the new profiles weaker than the older. The Si III 4552 $\AA$ line (Fig. 3.6) is practically identical in the cases considered, except at high temperatures where the line becomes stronger when using the new model. On the other hand, the Si II 4128 $\AA$ line (Fig. 3.7) predicted by the new atomic model is clearly weaker, even when the line starts to vanish at 22000 K. Therefore, the derived T_{eff} when this line is used is expected to depend on the atomic model. All the figures display the difference equivalent width percentage between both atomic models

$$\Delta EW = \frac{EW_{new} - EW_{old}}{EW_{old}}. \tag{3.8}$$

We have established a limit of 10 $m\AA$ in the equivalent width to consider the lines strong enough for the comparison. Lines smaller than this (in absorption or emission) are hard to measure and their results are not reliable even with high S/N. The typical error is around ± 5 $m\AA$. In those cases where this condition is not fulfilled we have omitted the ΔEW value (see Figs. 3.5, 3.6 and 3.7).

While Si IV and Si III lines present differences $\leq 10\%$ (with the exception of Si III 4552 $\AA$ at 32000 K), the differences for Si II can be up to 30% for same cases. This is to be expected since Si II is the ion which has suffered the most important updates in

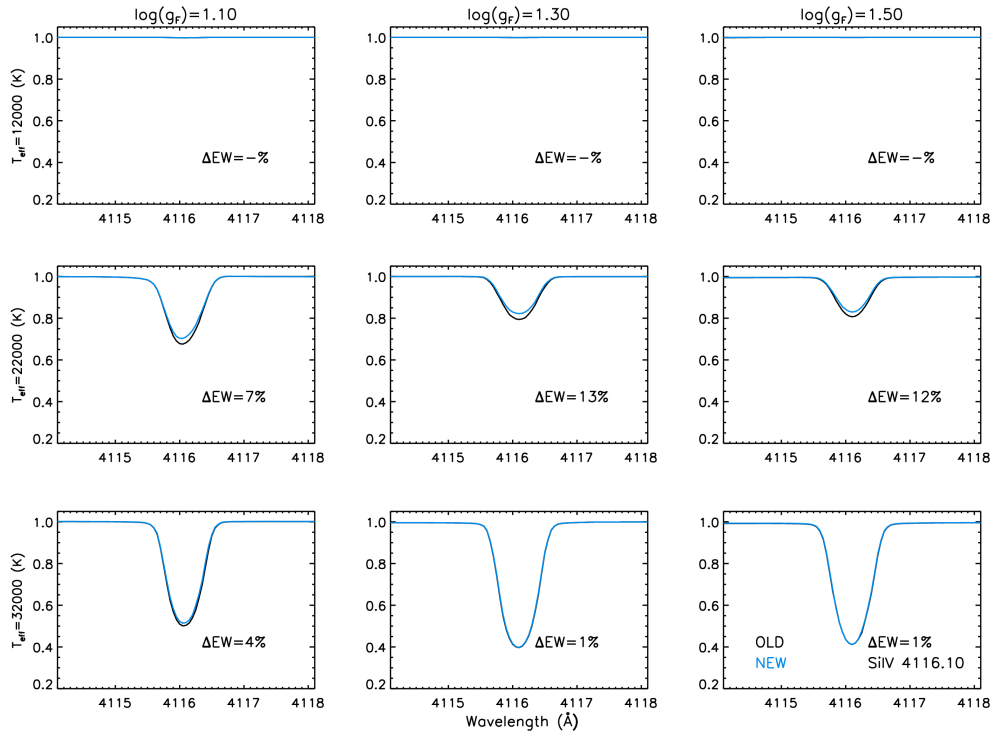

FIGURE 3.5— Profiles of Si IV 4116 $\AA$ obtained with the old model (black) and the new one (blue) for a sub-grid of nine models with different T_{eff} and $log\,(g_F)$. In those cases where differences exist the new one produces weaker profiles than the old one. A quantification of the differences is shown in each chart through $\Delta EW = \frac{EW_{new}-EW_{old}}{EW_{old}}$, but just in those cases where the EW is ≥ 10 $m\AA$ (see text for additional details).

the transitions treatment. The new collisional rates, summarized in Tab. 3.1, are one of the main causes of the differences in the profiles.

Synthetic Equivalent Width Comparison

Looking for a detailed description, a comparison between the equivalent widths of the main optical silicon lines in both models is displayed in Figs. 3.8-3.13 covering the entire $T_{eff} - log\,(g)$ mesh calculated in section 4.1. This test was performed over those lines whose equivalent width were equal or larger than 10 $m\AA$, as in the previous section.

To make a visual interpretation of the result easier a common scale was used for all the figures. They are ranged between -100 and $+100$ %, those values larger than these edges are *saturated* in the figures, and forced to $\pm 100\%$. The isocountours show

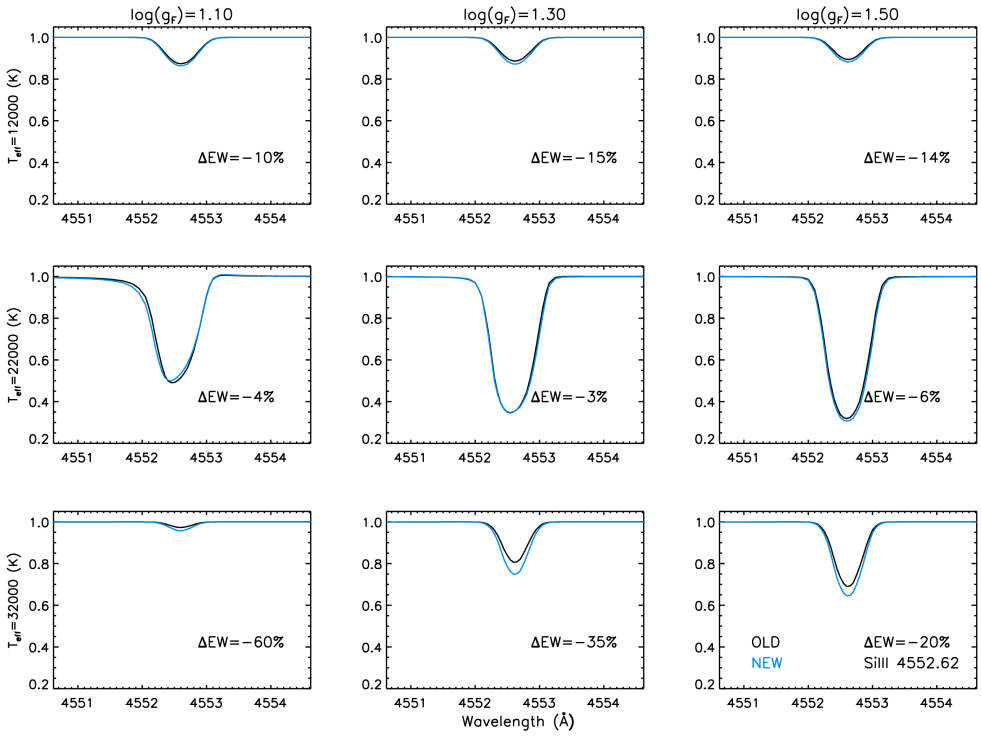

FIGURE 3.6— Si III 4552 $\AA$ line generated with the old (black) and new (blue) atomic model using the same grid as in Fig. 3.5. Differences are important at the highest T_{eff} considered, where the resulting lines are stronger.

punctual strong mismatches compared with the surrounding points in the $T_{eff} - log\,(g)$ plane, likely either spots where the code does not behave correctly (see section 4.1.4) or cases where the line is already weak and the ratio can return odd results. Those $T_{eff} - log\,(g)$ cases resulting in lines weaker than 10 $m\AA$ are not displayed.

The transitions shown in Figs. 3.8-3.13 are marked in the Grotrian diagrams (see Figs. 3.1 and 3.2), showing the levels involved. The lines plotted in the figures are representative of the multiplet to which they belong. For instance, the differences between the profiles generated by both atomic versions for Si III 4552 $\AA$ are similar for the other transitions of the same triplet (Si III $4567 - 4574$ $\AA$).

Main Lines for Temperature Determination

Si II 4128 $\AA$, Si III 4552 $\AA$ and Si IV 4116 $\AA$ are the main silicon transitions involved in the temperature determination (in the optical range) through the different ionization balances, according to the spectral type. The differences in the line profiles generated

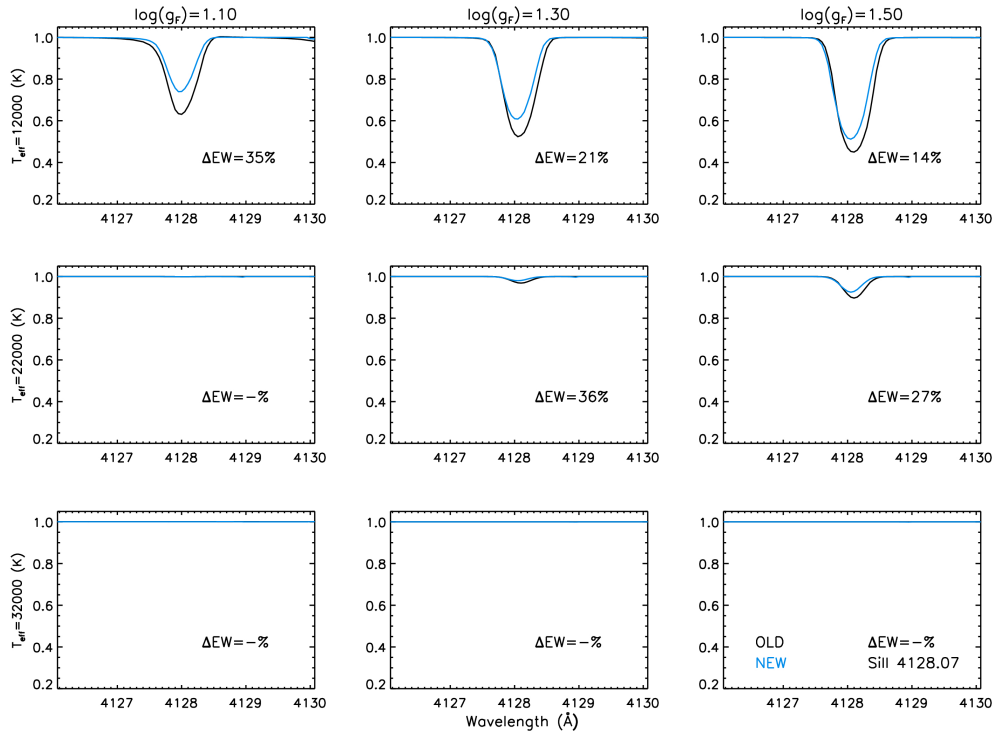

FIGURE 3.7— Si II 4128 Å shows the largest differences compared with the two lines presented before in Figs. 3.5 and 3.6. The new atomic model (blue) displays weaker profiles compared with the old model (black).

for each silicon atomic model across the $T_{eff} - log\,(g)$ grid are displayed in Fig. 3.8.

The $\Delta EW\%$ color-map shown in the figure, together with its projection in temperature and gravity display the main differences in the final equivalent widths recovered for each atomic model.

- The Si II 4128 $\AA$ line shows the largest differences at high temperatures, reaching differences around 40% in ΔEW at $\sim$ 20000 K. At this temperature the Si II profiles start to faint.
- The new model produces a slightly intense Si III 4552 $\AA$ line than the previous one, and it is in the supergiant area where this effect is larger. Note also that the major differences are at temperatures where Si III loses strength. Nonetheless, they are barely larger than 20%.
- At high temperature the new Si IV 4116 $\AA$ line is weaker than the one from the old version. Differences increase at mid temperatures, but it is under 10% for

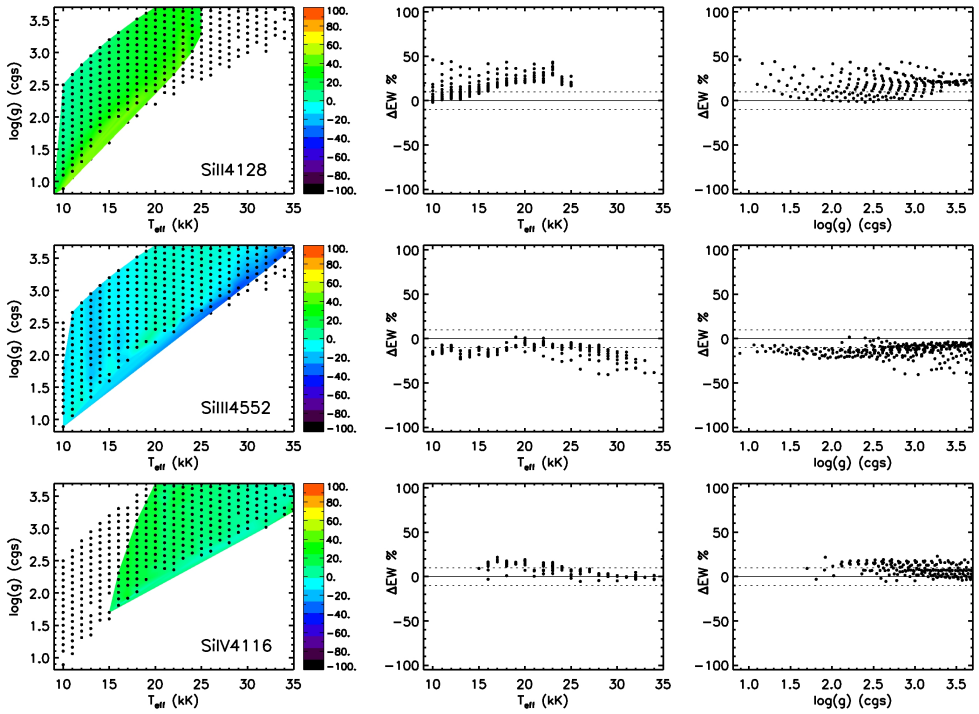

FIGURE 3.8— Comparison between the equivalent widths of the main optical silicon lines, used for temperature determination, calculated with the old and new atomic models. The isocountours of $\Delta EW = \frac{EW_{new}-EW_{old}}{EW_{old}}$ are plotted in the $T_{eff} - log\,(g)$ plane (left). The projections with respect to T_{eff} (middle) and surface gravity (right) are also displayed for each silicon line (identified in the charts). The match was only performed in those $T_{eff} - log\,(g)$ points where the equivalent width of the line was equal or larger than 10 $m\AA$. With the aim of giving an uniform distribution for all the plots they were scaled between -100 and $+100$ % those values that go beyond were *saturated* to these limits. Additionally, the $\pm 10\%$ variation is drawn in the individual temperature and gravity panel (dotted black lines).

almost all the parameters considered.

Impact on the Ionization Balances

These differences will have an impact on the effective temperature, but how important could it be? Trying to answer this question Figs. 3.9 and 3.10 plot the ratios of Si III 4552/Si II 4128 and Si IV 4116/Si III 4552 (typical temperature diagnostics) for the old and new atomic models respectively. Only those cases in which both lines have $EW \geq 10\ m\AA$ are displayed.

- **Si** III4552**/Si** II4128**.-** The new atomic model predicts a ratio, $\sim$ 20%–40%

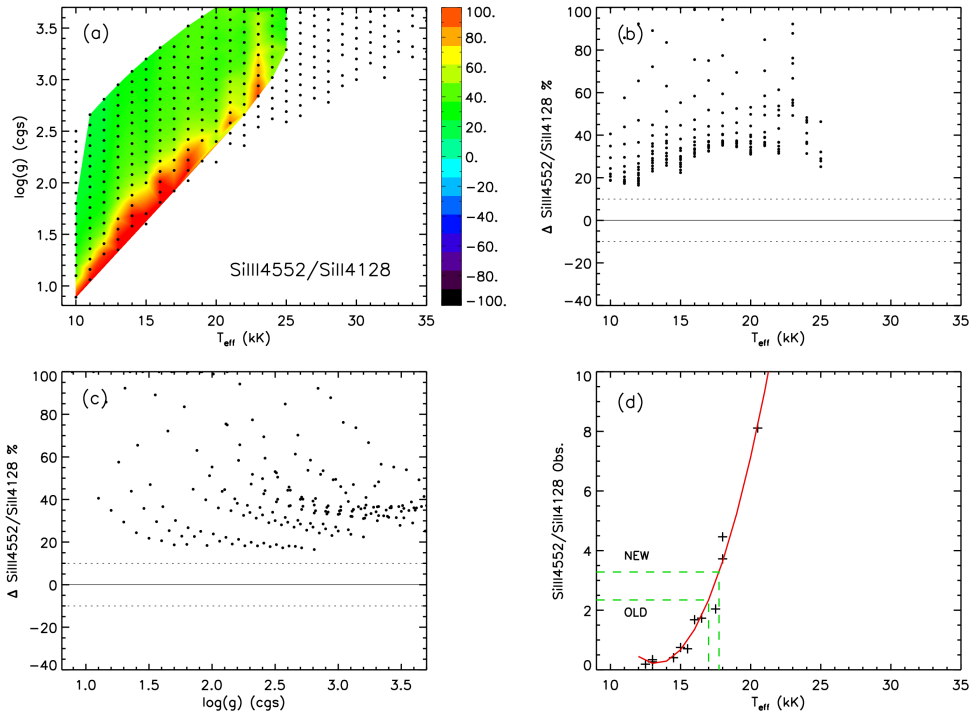

FIGURE 3.9— Differences in Si III 455/Si II 4128 ratio due to the atomic model employed. From upper left: (a) Δ Si III 4552/Si II 4128 isocountours in the $T_{eff} - log\,(g)$ plane; (b) and (c) projection of Δ Si III 4552/Si II 4128 against the temperature and gravity respectively; (d) the effect of these discrepancies is tested over the relationship estimated by empirical measurements of Lennon et al. (1993) and the respective quantitative analyses taken from the literature (Takeda & Takada-Hidai 1998; Kudritzki et al. 1999; Repolust et al. 2004; Crowther et al. 2006; Searle et al. 2008) (red solid line). The effect of the percentage was checked at 17000 *K* (green dashed lines).

higher than the old one (Fig. 3.9). In the supergiant area this difference increases notably.

With the goal of translating these percentages to temperatures and, based on the work by Lennon et al. (1993), we have related their empirical equivalent widths with the temperature estimated for several authors on the same stars (Takeda & Takada-Hidai 1998; Kudritzki et al. 1999; Repolust et al. 2004; Crowther et al. 2006; Searle et al. 2008). With a simple smooth fit to this tendency we have estimated the shift in temperature introduced by the new atomic model. Thus, these variations in the Si III4552/Si II4128 ratio are equivalent to 700 *K* at 17000 *K* (green dashed lines at the right-bottom chart in Fig. 3.9).

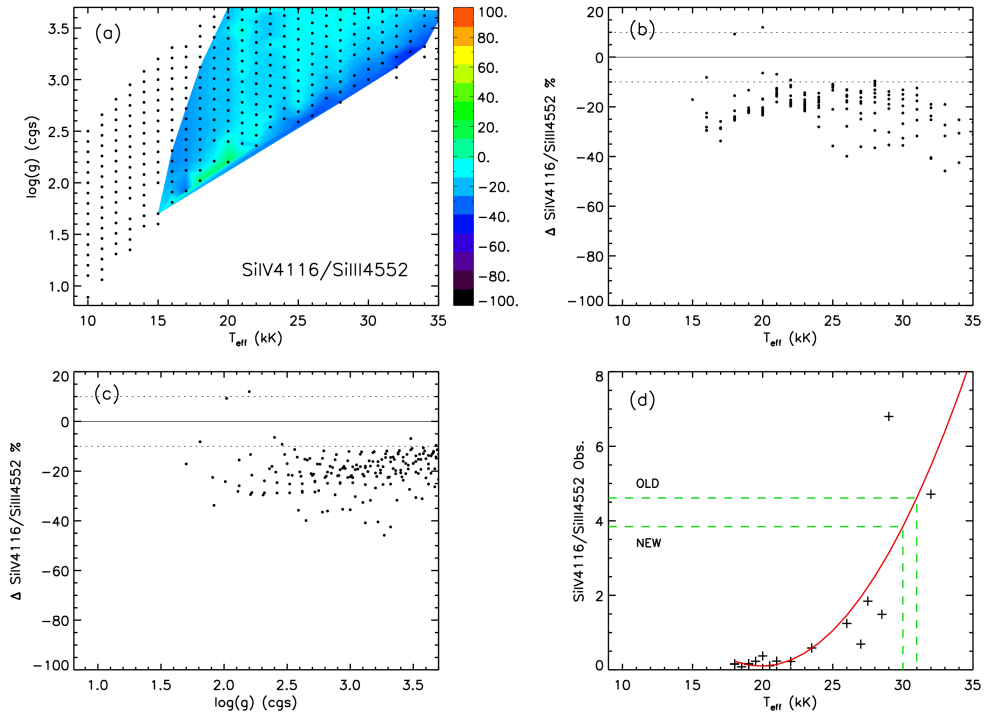

FIGURE 3.10— Continuation of Fig. 3.9, in this case applied to Si IV4116/Si III4552 ratio. The test gathers in chart (d) was performed at 30000 *K* (green dashed lines).

- **Si** IV4116/**Si** III4552**.-** The new model gives a smaller ratio, which drives the solution to cooler temperatures. Nonetheless, the difference between both atomic models is small, around 20% in the ratio.

  This percentage is equivalent to a temperature variation of $\sim$ 1000 *K* around 30000 *K* (green and dashed lines at the right-bottom chart in Fig. 3.10).

The largest differences with respect to these two ratios are in the supergiant zone. This can solve some of the issues discussed for the previous silicon model. We would like to remind the reader that models close to the grid border (i. e. near the Eddington Limit) can be compromised by FASTWIND convergences (see section 4.1.4).

Other Interesting Lines for Abundance Analyses

Additionally, there are other important silicon features in the optical range considered. Though they are not usually considered during the temperature determination process they play an important role in the silicon abundance determination and constraining

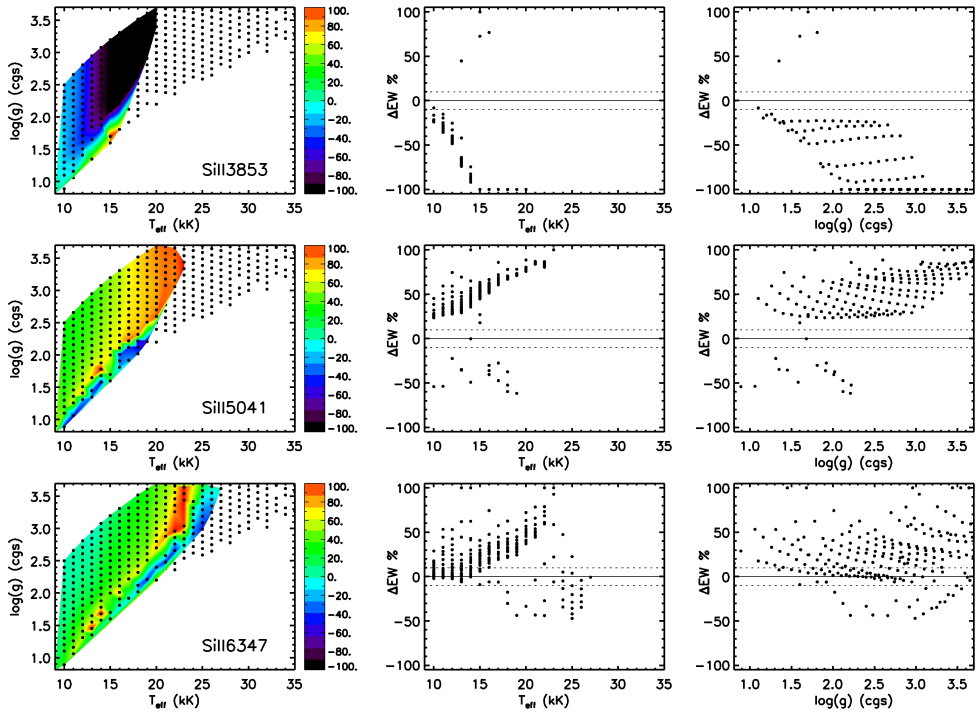

FIGURE 3.11— Comparison between the equivalent widths of three Si II transitions using the old and new atomic models. See Fig. 3.8 for more details.

the microturbulence. Figs. 3.11, 3.12 and 3.13 show the differences for some representative lines of Si II, Si III and Si IV respectively.

- Figure 3.11 gathers three different Si II transitions. They show the strongest differences at mid temperatures. In contrast to Si II 4128 $\AA$, they can reach more than 100%. Thus Si II 3853 $\AA$ shows a clear trend through the giant with the temperature increases (see color-map in Fig. 3.11). The other two lines evaluated show a similar pattern although less abrupt than in the previous one. A note of caution must be taken for the models close to the grid edges since at these points the stellar atmosphere model convergence is challenging.

- The differences of three Si III transitions are gathered in Fig. 3.12. Si III 4716 $\AA$ shows remarkable differences, mainly in the supergiant region, however this transitions is weak at this temperature and gravity, and it is not commonly used. The other two lines analyzed in Fig. 3.12 display more subtle changes along the parameters space, being them in most cases lower than 10% in ΔEW. Only in

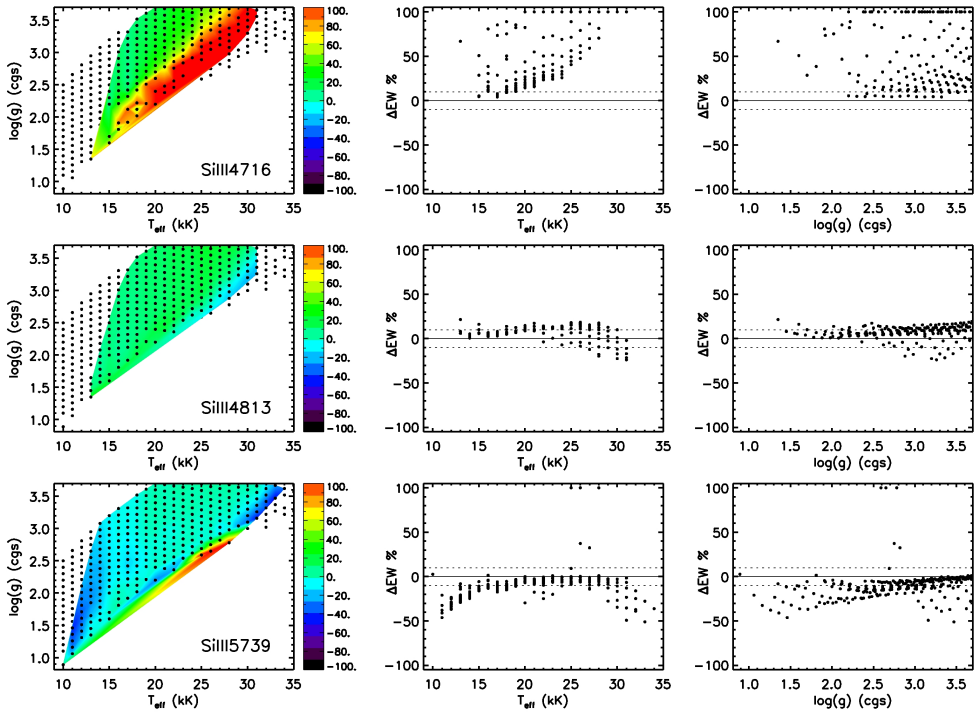

FIGURE 3.12— Comparison between the equivalent widths of three Si III transitions using the old and new atomic models.

extreme $T_{eff} - log\,(g)$ cases, close to the grid edges, the differences increase.

- In the temperature and wavelength ranges covered by our grid models the Si IV transitions (with the exception Si IV $4116 - 4089$ $\AA$) are weak. It is at higher temperatures where their role gains relevance. The differences shown by Si IV 4631 $\AA$ are small, lower than 10% (see Fig. 3.13), while the other two lines display an average of $\sim 25\%$.

Impact on the Stellar Wind

The previous tests were performed without paying attention to the role played by the stellar wind. Although the model was created for a hydrostatic code (DETAIL), the atomic information is independent of the atmospheric characterization. The only point to bear in mind is the set of collisional bound-free transitions empirically fitted using dwarf stars. Figure 3.14 displays the ratio of line equivalent widths for the old and new models versus the Q-parameter (see section 4.1.1 for Q-parameter definition), for

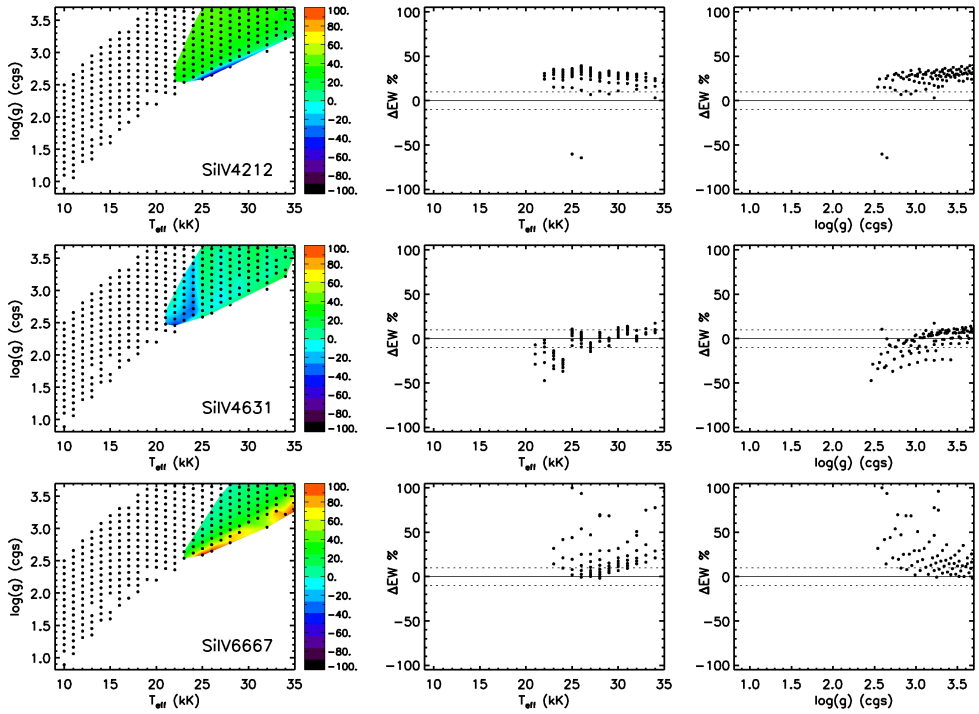

FIGURE 3.13— Comparison between the equivalent widths of three Si IV transitions using the old and new atomic models.

three silicon lines. The three plots show a correlation of the ratio with the Q-parameter, more relevant for Si II 4128 *Å*. Again, the large differences are produced at high mass loss rates which, in this grid, is equivalent to high temperatures (see section 4.1) where this line faint. Despite of this fact, the effect on the wind cannot be neglected and performing a quantitative analysis with a wrong wind estimation will be reflected in the temperature and gravity obtained. The other two lines plotted in Fig. 3.14 do not show a clear trend as in the case of Si II 4128 *Å*.

3.4.2 Tests at Low Resolution

The previous tests have revealed small shifts in the effective temperature and surface gravity inferred when the new silicon atom is considered compared to the old one[5]. An important part of our work resides in the quantitative analysis of low resolution spectra (see chapter 5). To evaluate the implications of using a different atomic model,

[5]Note than temperature and gravity are correlated so we have to consider both parameters at the same time

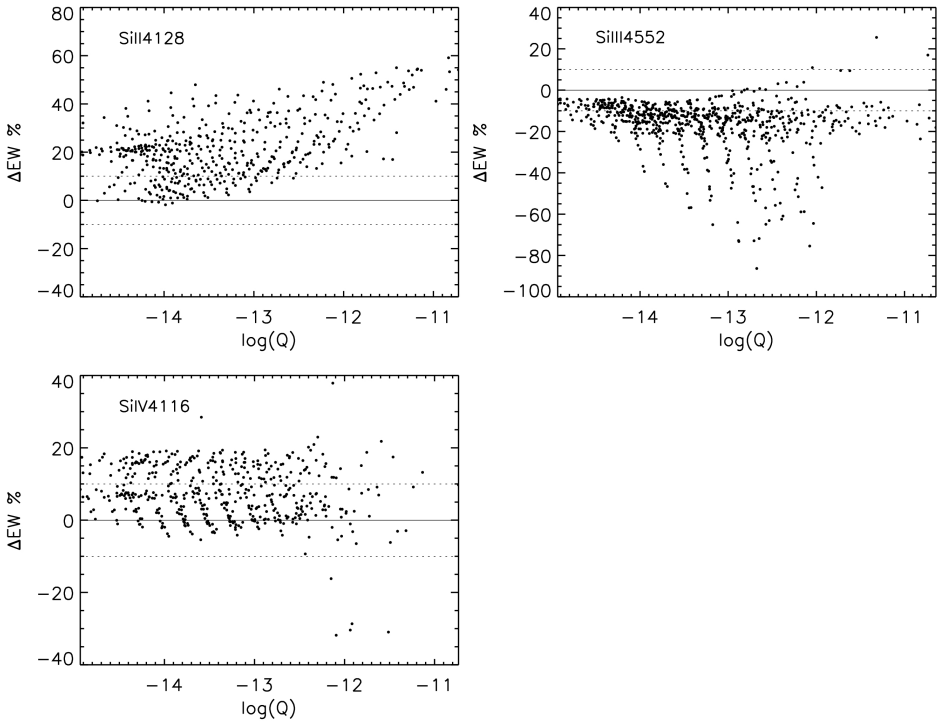

FIGURE 3.14— Dependence of ΔEW ratio with the stellar wind through the Q-parameter for Si II 4128 $\AA$, Si III 4552 $\AA$ and Si IV 4116 $\AA$.

a comparison was developed taken three synthetic spectra with temperatures 12000, 22000 and 32000 K and the same flux-weighted gravity ($log\,(g) = 1.3\ dex$). For consistency with our low resolution data, the spectra were degraded to low resolution ($R = 1000$) and $S/N = 150$.

The match for the three temperatures is presented in Fig. 3.15. The differences highlighted in previous sections are almost diluted by the low resolution and noise. Only at low temperatures the Si II lines show an appreciable discrepancy, larger than 1σ, between both atomic models, however, it is still very small. The different percentages shown for each plot are almost noise; small variations are present but they have a negligible impact on the derived stellar parameters.

The grid designed for this work and the quantitative analysis at low resolution on extragalactic stars is based on the new atomic model. Nonetheless the influence of using one or another atomic model, discussed in this chapter, is barely significant. We have to add, as we will see in this work, that the errors derived in our quantitative analysis are usually larger than the shifts previously quoted because of the atomic

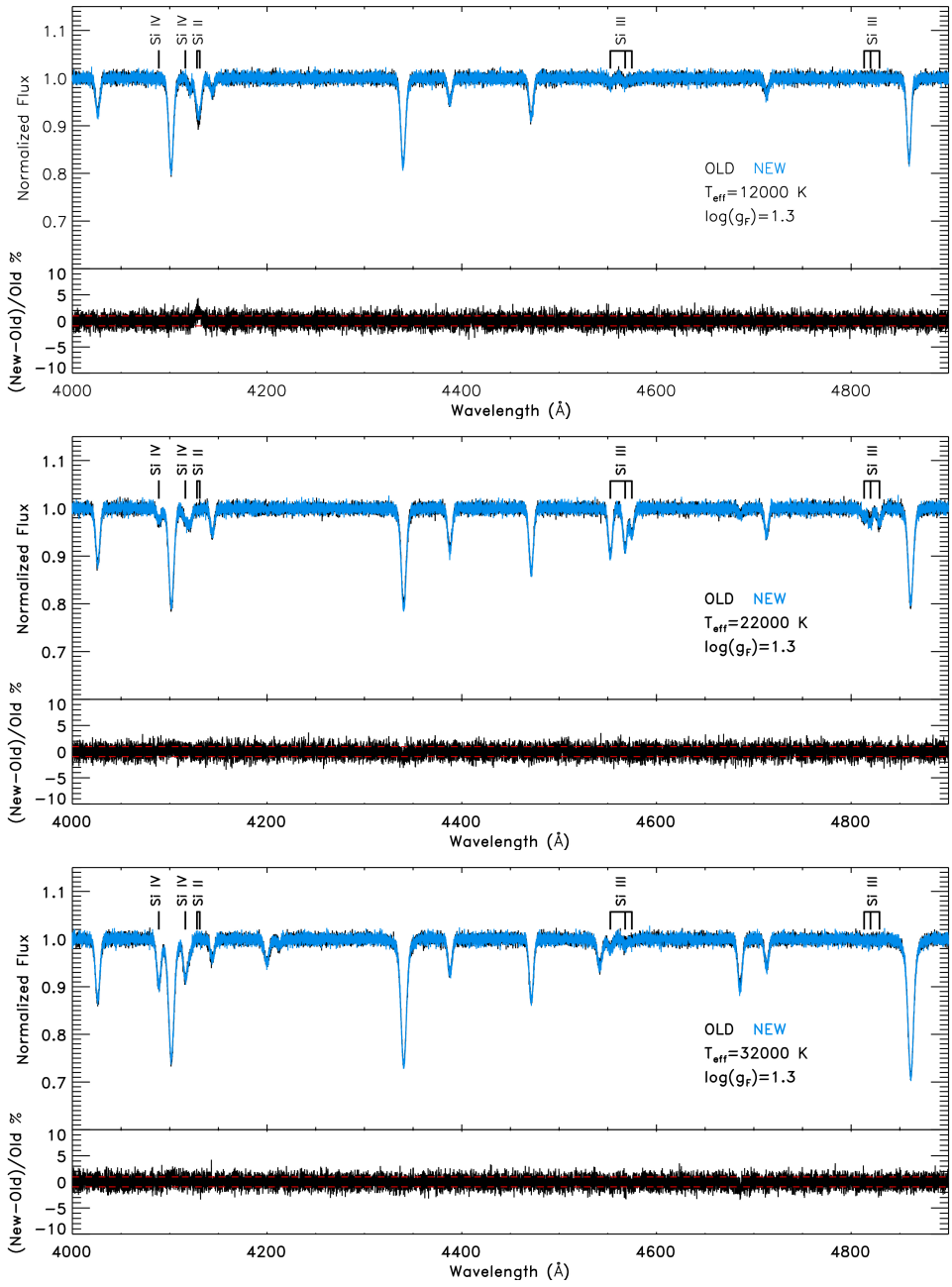

FIGURE 3.15— Comparison between the new (blue) and old (black) atomic model for three different synthetic models with different effective temperatures -12000 K (top), 22000 K (middle) and 32000 K (bottom)- and the same flux-weighted gravity ($log\,(g_F) = 1.3\ dex$). The percentage of the difference is plotted at the bottom of each chart. The spectra were degraded to $R = 1000$ and $S/N = 150$.

HD	RA(J2000)	DEC(J2000)	m_U	m_B	m_V	SpT
HD 31327	$04^h56^m20.09^s$	+36°10'06.73"	6.03	6.41	6.10	B2Ib
HD 206165	$21^h37^m55.22^s$	+62°04'54.98"	4.49	5.01	4.79	B2Ib
HD 14818	$02^h25^m16.03^s$	+56°36'35.36"	5.91	6.50	6.27	B2Iae
HD 24398	$03^h54^m07.92^s$	+31°53'01.09"	2.19	2.97	2.88	B1Iab:
HD 204172	$21^h25^m47.02^s$	+36°40'02.59"	4.89	5.86	5.94	B0Ib
HD 36822	$05^h34^m49.24^s$	+09°29'22.48"	3.28	4.23	4.40	B0III

TABLE 3.2— List of OB stars selected from the IACOB survey for quantitative analyses. The coordinates, apparent magnitudes and spectral types (SpT) were obtained from the SIMBAD Astronomical Database (*http://simbad.u-strasbg.fr/simbad/*).

model used.

3.5 Silicon *Old versus New*: On Galactic Stars

A comparison with high quality Galactic spectra is mandatory for evaluating the differences between results obtained with the new silicon model and the previous atomic version. We have selected six stars from the IACOB spectroscopic database (Simon-Díaz et al. in prep.) with spectral types between B2 and B0, covering the effective temperature range where transitions of the three ionization stages included in the atomic models are present.

We concentrate in the following main results from the quantitative spectroscopic analysis: (1) stellar parameters (viz. effective temperature and surface gravity); (2) silicon abundances; and (3) the microturbulence derived from the silicon transitions. A detailed description of the techniques applied in the quantitative analyses can be revised in section 4.2.2.

3.5.1 Selection of Candidates: The IACOB Spectroscopic Database

The *IACOB spectroscopic database of Galactic O and B stars* (Simon-Díaz et al. in prep.) is an homogeneous set of high quality spectra (high resolution and S/N) of northern Galactic O- and B-type stars with apparent magnitude $m_V \leq 7$. The spectra were observed with the Nordic Optical Telescope (NOT) situated in La Palma (Spain) by the echelle spectrograph FIES. The survey was obtained at high resolution ($R = 46000$), covering an optical spectral range $\sim 3800 - 6800\,\AA$.

The good data quality and the ample survey provided for the IACOB database give an excellent source for the selection of candidates suitable for testing the silicon atomic models on Galactic stars. The selected candidates are indicated in Tab. 3.2. These stars, due to their proximity and brightness, have also been studied by other authors. A summary of these previous studies is presented in Tab. 3.3. We have only

cited the most recent works where a quantitative analysis was performed.

3.5.2 Quantitative Comparison

The comparison analyses were performed on the main silicon features present in the spectra. The stellar parameters -effective temperature and surface gravity- were determined from the intersections between the silicon Si IV 4116/Si III 4552, Si IV 4116/Si II 4128 and Si III 4552/Si II 4128 ratios and the average obtained from H_γ and H_δ profile fitting. At high temperatures, the Si II 4128 line is no longer available, nonetheless the He II 4541 / He I 4387 ratio can be also used as a complementary temperature diagnostic (see section 4.2.2).

The silicon abundances were estimated based on Si II $4128-4130$ $\AA$, Si III $4552-4567-4575-4813-4819$ $\AA$ and Si IV 4116 $\AA$. Obviously, the presence of the lines will be conditioned mainly by the spectral type of the stars. A description of the techniques followed for the silicon abundance determination and the microturbulence derived through *curves of growth* is described in section 4.2.2.

Stellar Parameters

The objects selected allow us to test the silicon atomic model in the temperature range $\sim 18000-32000$ K for supergiant stars. Figure 3.16 displays the results obtained for the six stars using the new and old silicon atomic models. We have determined the $T_{eff} - log\,(g)$ pair through the ionization balances available for each particular star. The values recovered are compiled in Tab. 3.4.

The analyses of these stars using the new atomic model result in an almost perfect agreement for some of the stars but with certain issues for others. Thus, the parameters recovered for HD 31327 and HD 206165, from different line ratios, show a good match with the new atomic model (see Fig. 3.16). In contrast, the values predicted by the old atomic model show a scatter of ~ 1000 K and 0.8 dex (see Tab. 3.4) for temperature and gravity, respectively (though these differences are within the intrinsic uncertainties associated with the equivalent width measurements). On the other hand, HD 14818 and HD 24398 point to the opposite results. Now, it is the old silicon model which gives the best match between the ionization ratios, while the new atomic model displays discrepancies within the normal error bars.

At ~ 30000 K (the approximated temperature of HD 204172 and HD 36922) the diagnostics are restricted to Si IV / Si III and He II / He I. Our tests show a common behavior indistinctly of the atomic model used. Even though, the discrepancies obtained with the new atomic model are slightly smaller, practically within the errors. The match found in HD 36922 between the two ratios used is almost impeccable. It is not the case of HD 204172, where a discrepancy of ~ 1000 K is found (a bit larger for the old atomic model).

Name	$T_{eff}(K)$	log (g) (cgs)	ξ (kms^{-1})	He/H	$\dot{M}$ $(10^{-6}M_{\odot}yr^{-1})$	v_{∞} (kms^{-1})	β	$\varepsilon_C{}^a$	ε_N	ε_O	Ref.
HD 31327	21500	2.90	15.0	–	–	–	–	–	–	–	McErlean et al. (1999)
HD 206165	18000	2.50	15	–	0.50	640	1.5	7.96	8.15	8.43	Searle et al. (2008)
	19300	2.50	–	0.10-0.20	0.27	640	1.5	–	–	–	Markova & Puls (2008)
	20000	2.50	25	0.10	0.06	700	2.5	–	–	–	Kudritzki et al. (1999)
	20000	2.50	15	–	–	–	–	–	–	–	McErlean et al. (1999)
	–	–	–	–	–	640	–	–	–	–	Prinja et al. (1990)
HD 14818	18000	2.38	15	–	1.00	625	1.5	7.66	8.72	8.90	Searle et al. (2008)
	18500	2.40	20	0.20	0.55	565	2.0	7.65	8.35	8.45	Crowther et al. (2006)
	20100	2.40	17	0.15	0.30	650	1.9	7.65	8.45	8.65	Urbaneja (2004)
	–	–	–	–	–	600	–	–	–	–	Evans et al. (2004)
	20000	2.40	–	0.10	0.30	650	2.0	–	–	–	Kudritzki et al. (1999)
	20000	2.38	10	–	–	–	–	–	–	–	McErlean et al. (1999)
	–	–	–	–	–	465	–	–	–	–	Prinja et al. (1990)
HD 24398	23000	2.73	12	–	–	–	–	–	–	–	McErlean et al. (1999)
	–	–	–	–	–	1270	–	–	–	–	Prinja et al. (1990)
HD 204172	28500	3.13	15	–	0.57	1685	1.0	7.66	7.71	8.66	Searle et al. (2008)
	28500	3.02	9	–	–	–	–	–	–	–	McErlean et al. (1999)
	–	–	–	–	–	1630	–	–	–	–	Prinja et al. (1990)
HD 36822	–	–	–	–	–	–	–	–	–	–	

TABLE 3.3— Quantitative studies performed on the stars selected for our tests between the new and old silicon atomic model. The respective references of each analysis are gathered in the last column. Unfortunately there is not recent quantitative study for HD 36822.

[a] $\varepsilon_X = log(X/H) + 12$ (by number)

The issues in the new silicon model seem to be related to the Si II transitions involved. Effect that does not appear in the stars with temperature $\sim 18000\ K$ but only in the two examples at $\sim 21000\ K$, finding again an improved match at the highest temperatures considered. Nevertheless, with only six objects analyzed it would be reckless to suggest a relation with the temperature. The analysis of a large sample, covering different spectral types and luminosity classes, is recommended for tuning the silicon atomic model. Note that Si II $4128 - 4130\ \AA$ could also be affected by O II transitions or even by a lack of accuracy in the wind determination (see section 3.4.1).

Chemical Abundances

Once the impact of the new atomic model has been evaluated on the stellar parameters, the next step is checking the effects on the silicon abundance and microturbulence determinations.

The abundances and microturbulences recovered for the analyzed stars, using both silicon models, are displayed in Figs. 3.17–3.22. To clarify the comparison, we have split the lines plotted in two groups. The first one gathers the main optical Si III lines available, normally used for constraining the microturbulence that recovers the same silicon abundance in all the transitions. The second group displays Si II and Si IV transitions plus Si III 4552 $\AA$ (used as a reference with the first group).

In general, the Si III transitions show a better convergence using the new silicon atomic model rather than the old version, though the differences are small. Nevertheless, we would like to remark the notable improvement of the Si III 4813 $\AA$ line, obtaining in all the examples a better agreement in the new atomic model with the common behavior. Issues with this transition were already pointed out by other authors (see for instance Simón-Díaz 2010). Si III 4574 $\AA$ shows a strong divergence in HD 31327, which is present for both atomic models. The average abundance and microturbulence derived from both cases are similar, with the exception of HD 31327. Notwithstanding, we have to keep in mind that these results are linked to the temperature and gravity determined before.

The match of Si II and Si IV with Si III lines is quite good in HD 31327 (with the exception of Si III 4574 $\AA$) and HD 206165 (Figs. 3.17–3.18) using the new atomic model. The differences are slightly larger in the old model. We saw above how the silicon ionization ratios did not converge properly in these two examples, which is reflected in the abundance determination as well. The divergences found in HD 14818 and HD 24398 are considerable (see Figs. 3.19 and 3.20), likely related to the issues in the temperature determination. In these two examples a better consistency is achieved with the old model, however there are still problems with Si II 4130 $\AA$. The two stars analyzed with the highest temperature show a good match between all the lines considered indistinctly of the atomic model used (Figs. 3.21–3.22).

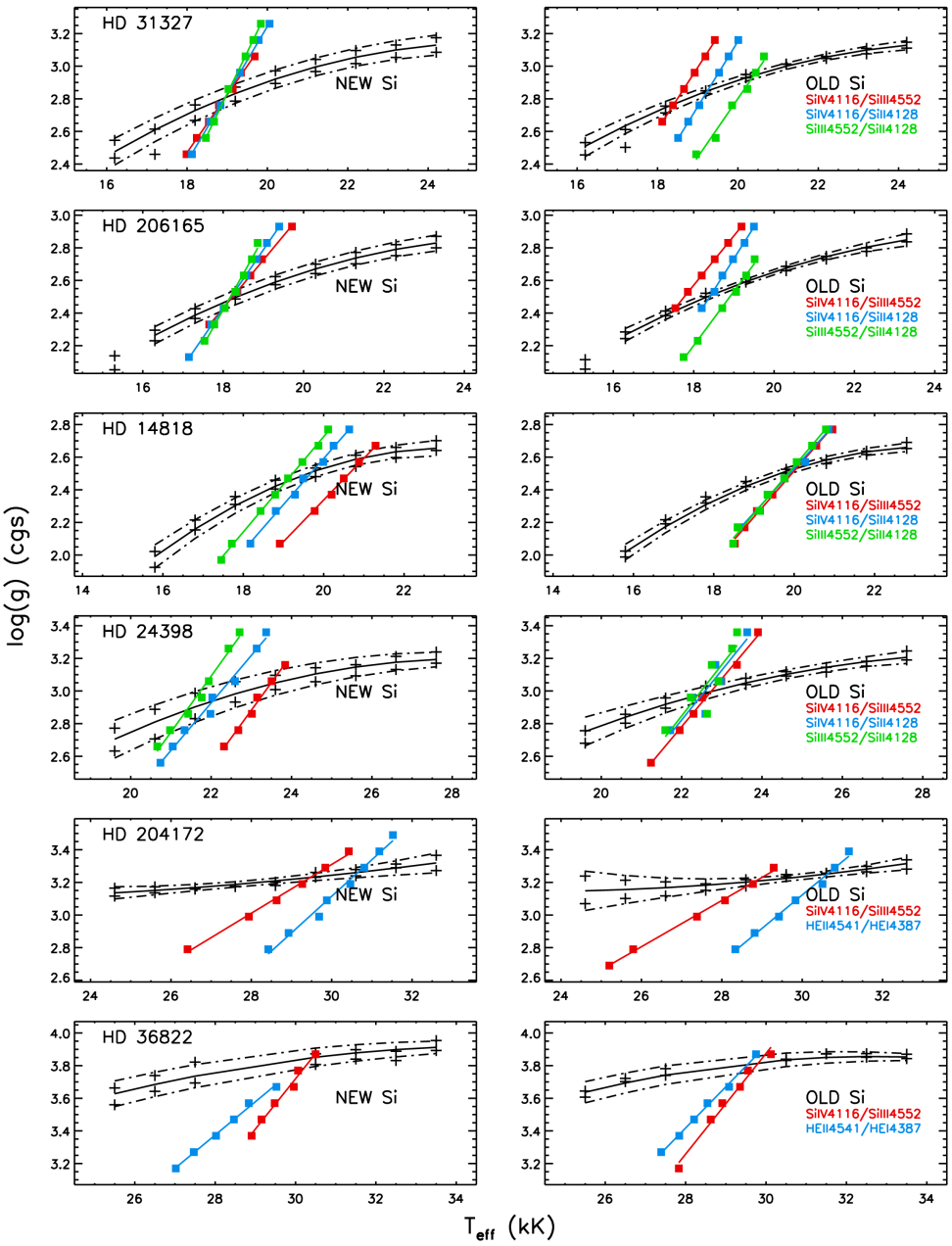

FIGURE 3.16— Diagnostic diagrams used to derived T_{eff} and $log\,(g)$ in the six stars tested. The stellar parameters were determined as a result of the intersection between the ionization balances according to each spectral type and the average trend given by H_γ and H_δ best modeling (see section 4.2.2 for more details). Left panel, new silicon atomic model; right panel, old silicon atomic model.

Ratios	NEW		OLD	
	T_{eff} (K)	$log\,(g)$ (cgs)	T_{eff} (K)	$log\,(g)(cgs)$
HD 31327				
SiIV 4116/SiIII 4552	18954±1090	2.81±0.08	18411±1049	2.77±0.05
SiIV 4116/SiII 4128	18947±705	2.81±0.08	19244±812	2.85±0.04
SiIII 4552/SiII 4128	18953±529	2.81±0.08	20400±497	2.94±0.03
Mean	18951±809	2.81±0.08	19352±818	2.85±0.04
Standard Deviation	4	0.00	999	0.08
HD 206165				
SiIV 4116/SiIII 4552	18182±1066	2.48±0.07	17456±1010	2.41±0.04
SiIV 4116/SiII 4128	18136±670	2.48±0.06	18421±753	2.51±0.03
SiIII 4552/SiII 4128	18130±373	2.48±0.06	19133±310	2.58±0.03
Mean	18149±758	2.48±0.06	18337±749	2.50±0.03
Standard Deviation	28	0.00	842	0.08
HD 14818				
SiIV 4116/SiIII 4552	21031±947	2.60±0.05	20068±898	2.53±0.03
SiIV 4116/SiII 4128	19711±572	2.51±0.05	19998±593	2.53±0.03
SiIII 4552/SiII 4128	19054±420	2.45±0.06	19931±427	2.52±0.03
Mean	19932±683	2.52±0.05	19999±668	2.53±0.03
Standard Deviation	1007	0.07	69	0.00
HD 24398				
SiIV 4116/SiIII 4552	23474±630	3.04±0.09	22733±620	3.00±0.05
SiIV 4116/SiII 4128	22045±643	2.94±0.13	22529±820	2.98±0.05
SiIII 4552/SiII 4128	21399±857	2.88±0.13	22409±905	2.98±0.05
Mean	22306±718	2.95±0.12	22557±791	2.99±0.05
Standard Deviation	1062	0.08	164	0.01
HD 204172				
SiIV 4116/SiIII 4552	29465±230	3.23±0.03	28833±193	3.21±0.03
HeII 4541/HeI 4387	30653±515	3.26±0.04	30631±466	3.25±0.03
Mean	30059±399	3.25±0.04	29732±357	3.23±0.03
Standard Deviation	840	0.02	1271	0.02
HD 36822				
SiIV 4116/SiIII 4552	30420±562	3.85±0.06	29826±538	3.82±0.05
HeII 4541/HeI 4387	30311±465	3.85±0.07	29572±411	3.81±0.05
Mean	30366±516	3.85±0.07	29699±479	3.82±0.05
Standard Deviation	77	0.00	180	0.00

TABLE 3.4— Stellar parameters derived for the different silicon ratios analyzed on the six stars tested and represented in Fig. 3.16 for both silicon atomic models. The average temperature and gravity plus the standard deviation from the different diagnostic ionization balances are also indicated.

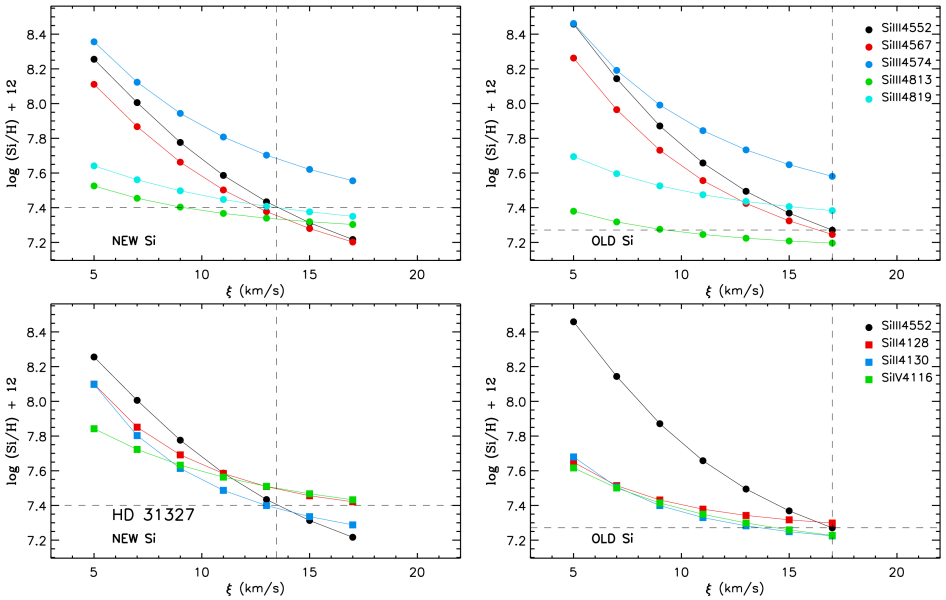

FIGURE 3.17— Silicon abundance determination for HD 31327. The lines used in the analysis and the respective color and symbol code are codified in the figure. For the sake of clarity we have split the lines in two different groups. The Si III transitions are plotted at the top, while Si II and Si IV plus Si III 4552 *Å* (used as reference with the first group) are at the bottom. The left panels show the results obtaining with the new atomic model and the right those with the old one. The average abundance and microturbulence obtained using all the lines are marked by dashed black lines.

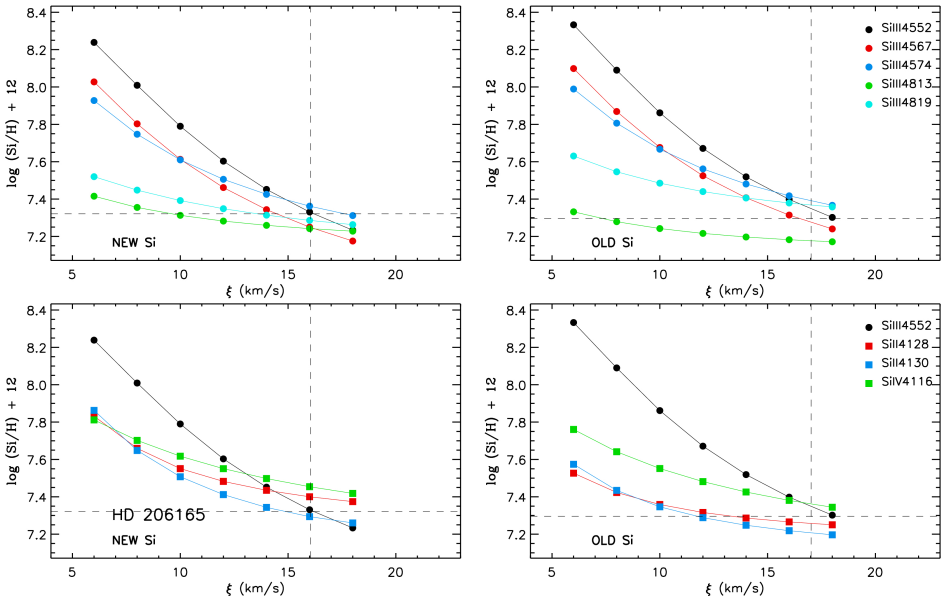

FIGURE 3.18— Silicon abundance determination for HD 206165 (see Fig. 3.17 for details)

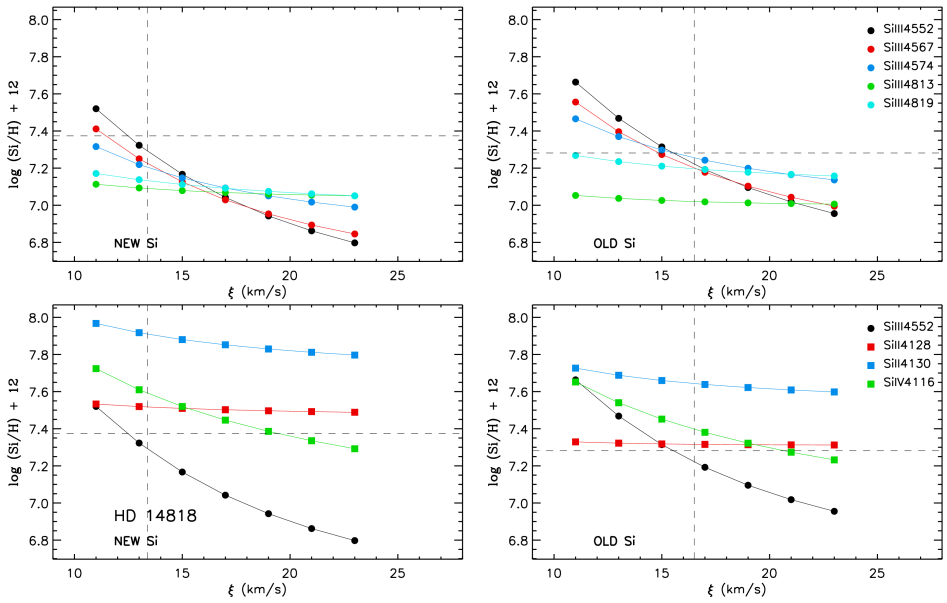

FIGURE 3.19— Silicon abundance determination for HD 14818 (see Fig. 3.17 for details)

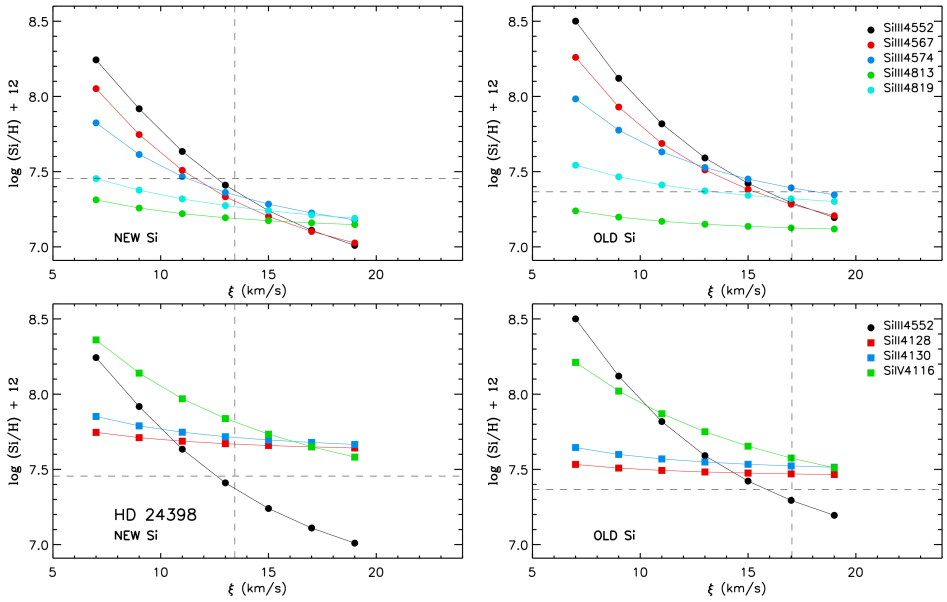

FIGURE 3.20— Silicon abundance determination for HD 24398 (see Fig. 3.17 for details)

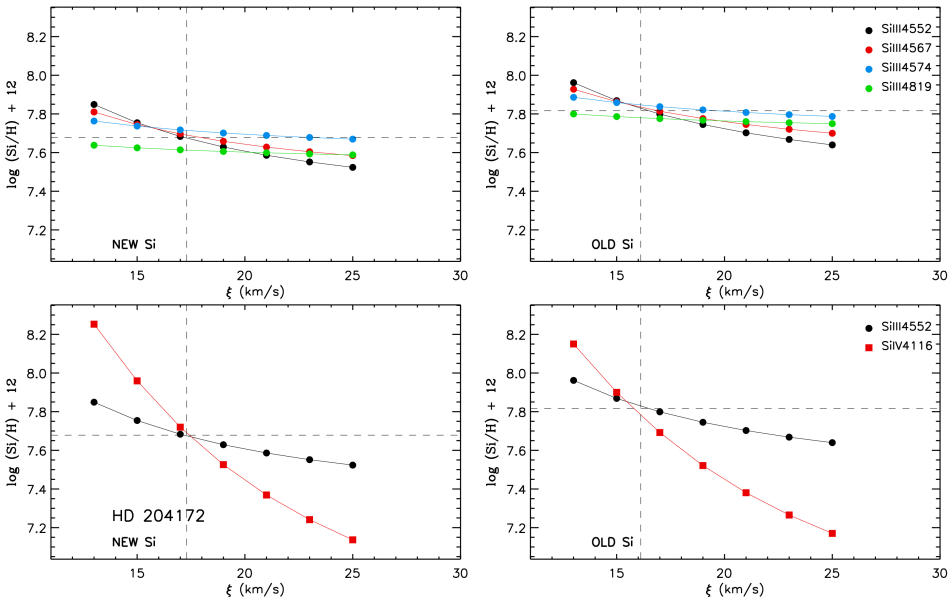

FIGURE 3.21— Silicon abundance determination for HD 204172 (see Fig. 3.17 for details)

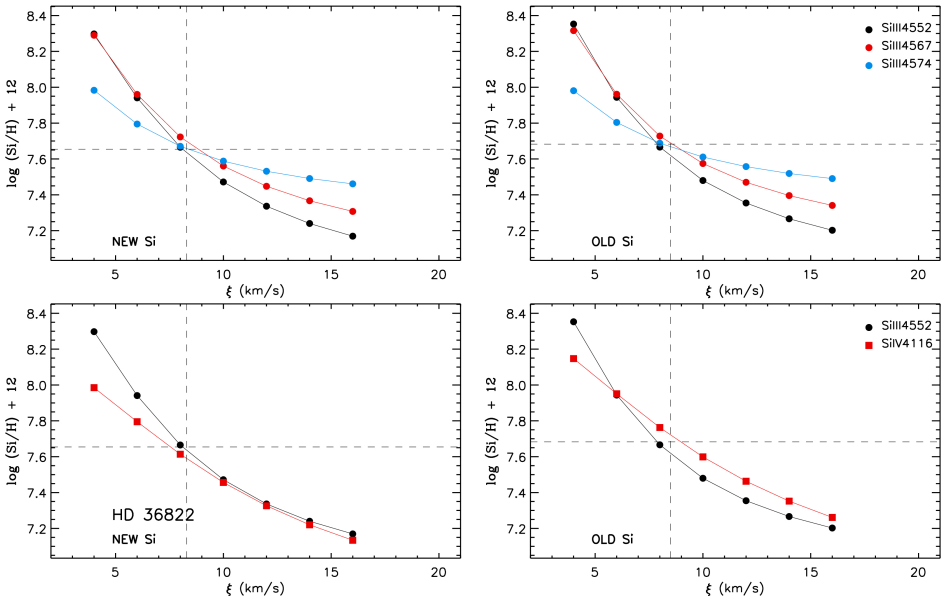

FIGURE 3.22— Silicon abundance determination for HD 36822 (see Fig. 3.17 for details)

Lines (*Å*)	log (Si/H)+12 (by number)	
	NEW	OLD
HD 31327		
SiII 4128	7.48±0.07	7.31±0.14
SiII 4130	7.36±0.22	7.24±0.14
SiIII 4552	7.40±0.12	7.28±0.10
SiIII 4567	7.34±0.09	7.26±0.07
SiIII 4574	7.67±0.13	7.59±0.12
SiIII 4813	7.33±0.23	7.20±0.21
SiIII 4819	7.40±0.15	7.39±0.14
SiIV 4116	7.49±0.48	7.23±0.45
Mean	7.43±0.19	7.31±0.17
Standard Deviation	0.11	0.13
Microturbulence ($km\,s^{-1}$)	13.5±2.5	17.0±2.1
HD 206165		
SiII 4128	7.39±0.20	7.26±0.11
SiII 4130	7.28±0.05	7.21±0.14
SiIII 4552	7.33±0.09	7.34±0.08
SiIII 4567	7.24±0.07	7.27±0.07
SiIII 4574	7.35±0.08	7.39±0.08
SiIII 4813	7.24±0.21	7.18±0.20
SiIII 4819	7.28±0.07	7.37±0.07
SiIV 4116	7.45±0.48	7.36±0.50
Mean	7.32±0.16	7.30±0.16
Standard Deviation	0.07	0.08
Microturbulence ($km\,s^{-1}$)	16.0±1.8	17.0±0.9
HD 14818		
SiII 4128	7.52±0.19	7.32±0.15
SiII 4130	7.91±0.22	7.64±0.17
SiIII 4552	7.30±0.04	7.22±0.10
SiIII 4567	7.23±0.04	7.20±0.09
SiIII 4574	7.21±0.09	7.25±0.08
SiIII 4813	7.09±0.17	7.02±0.16
SiIII 4819	7.13±0.09	7.20±0.09
SiIV 4116	7.60±0.42	7.40±0.40
Mean	7.37±0.16	7.28±0.16
Standard Deviation	0.28	0.18
Microturbulence ($km\,s^{-1}$)	13.4±1.2	16.5±1.4

TABLE 3.5— Chemical abundances obtained for each silicon line considering an average microturbulence, according to all the lines involved in the analysis (see Fig. 3.17). The average abundance plus the standard deviation are also indicated in the table, reflecting the accuracy of each silicon atomic model in the stars considered during this test.

Lines (*Å*)	log (Si/H)+12 (by number)	
	NEW	OLD
HD 24398		
SiII 4128	7.67±0.32	7.47±0.26
SiII 4130	7.71±0.22	7.52±0.18
SiIII 4552	7.37±0.09	7.28±0.08
SiIII 4567	7.30±0.09	7.27±0.07
SiIII 4574	7.34±0.07	7.38±0.06
SiIII 4813	7.19±0.13	7.12±0.11
SiIII 4819	7.26±0.10	7.32±0.09
SiIV 4116	7.81±0.27	7.57±0.23
Mean	7.46±0.16	7.37±0.14
Standard Deviation	0.24	0.15
Microturbulence (km s^{-1})	13.4±1.0	17.0±2.1
HD 204172		
SiIII 4552	7.68±0.08	7.83±0.08
SiIII 4567	7.69±0.15	7.84±0.16
SiIII 4574	7.71±0.10	7.85±0.11
SiIII 4819	7.61±0.22	7.78±0.23
SiIV 4116	7.70±0.23	7.79±0.22
Mean	7.68±0.16	7.82±0.16
Standard Deviation	0.04	0.03
Microturbulence (km s^{-1})	17.3±2.5	16.1±2.3
HD 36822		
SiIII 4552	7.65±0.14	7.63±0.09
SiIII 4567	7.71±0.11	7.70±0.10
SiIII 4574	7.67±0.08	7.67±0.07
SiIV 4116	7.59±0.19	7.72±0.20
Mean	7.66±0.13	7.68±0.12
Standard Deviation	0.05	0.04
Microturbulence (km s^{-1})	8.30±1.6	8.50±1.4

TABLE 3.6— Table 3.5, continued.

Results of a 'Blind' Analysis

In addition to the divergences observed between the different lines, we have performed a *'blind'* test and determined the average silicon abundance and best microturbulence, that tries to get a common solution for all the lines. These results, together with the abundances line by line (according to the best microturbulence), are summarized in Tabs. 3.5 and 3.6. This average is also illustrated in Figs. 3.17–3.22.

The largest discrepancies in microturbulence are found in HD 31327, HD 14818 and HD 24398. Again the issues in the ionization balance seem to be the problem. In spite of the small role played by the microturbulence in the ionization ratios (Villamariz & Herrero 2000), if the value changes with respect to the one used during the temperature determination, it is recommended to repeat the first step with the new microturbulence velocity until convergence, avoiding the introduction of any additional systematic error.

This effect is also reflected in the abundances predicted by each one of the individual lines. The standard deviation in the worst cases (HD 14818 and HD 24398) reaches values of ~ 0.25 *dex* in the new atomic model. Though better when using the old atomic model, ~ 0.17 *dex*, it is still large. The other four stars analyzed show a good match in both silicon atomic configurations (≤ 0.1 *dex*). The differences in the average abundance between both atomic models are within the typical errors of ~ 0.1 *dex*.

3.5.3 General Remarks

The different tests carried out have shown the main differences between the silicon atomic models when applied to the Galactic stars analyzed. The performance found for each atomic model depends on the particular star under consideration. We have found objects where the new atomic model brings a better match than the old model and vice versa.

This effect is observed both in the effective temperature and surface gravity calculations, and also in the silicon abundance determination. It is in these last analyses where the differences between both atomic models are more noticeable. Nonetheless, the global results are similar. Figure 3.23 shows the final temperatures and gravities derived using each atomic model. The differences are small and the results are bracketed by their respective errors. The comparison with previous quantitative analyses on these stars shows strong discrepancies with some of them. This is not really odd, as they were obtained as a result of different atmosphere codes with different assumptions. For instance the study developed by McErlean et al. (1999) does not include blanketing effects in the stellar atmosphere model. The new atomic model results in slightly lower temperatures than the old atomic model, with the exception of hotter objects, where the opposite trend is found.

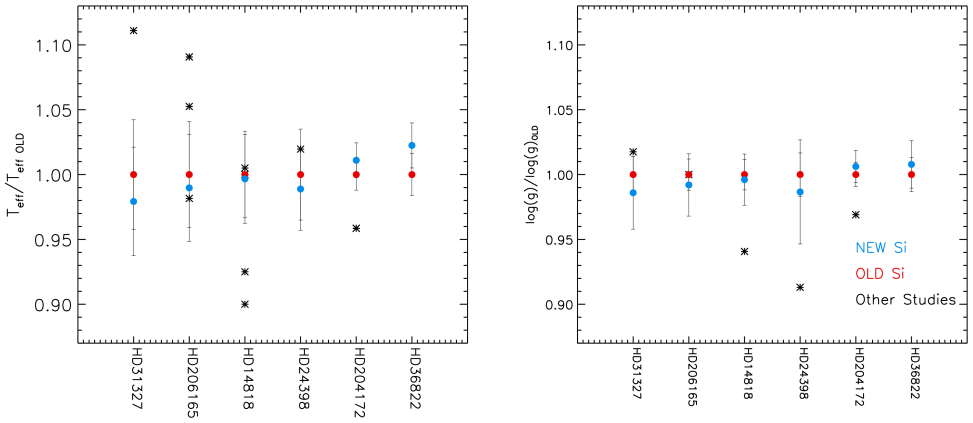

FIGURE 3.23— Effective temperatures (left panel) and surface gravities (right panel) derived during the tests for both silicon atomic models. They are normalized to the old atomic values to bring all them to a common reference system. The stars are sorted in temperature being the coolest object at the left side (HD 31327). Previous studies developed by other authors are plotted (black asterisks) for comparison (see Tab. 3.3).

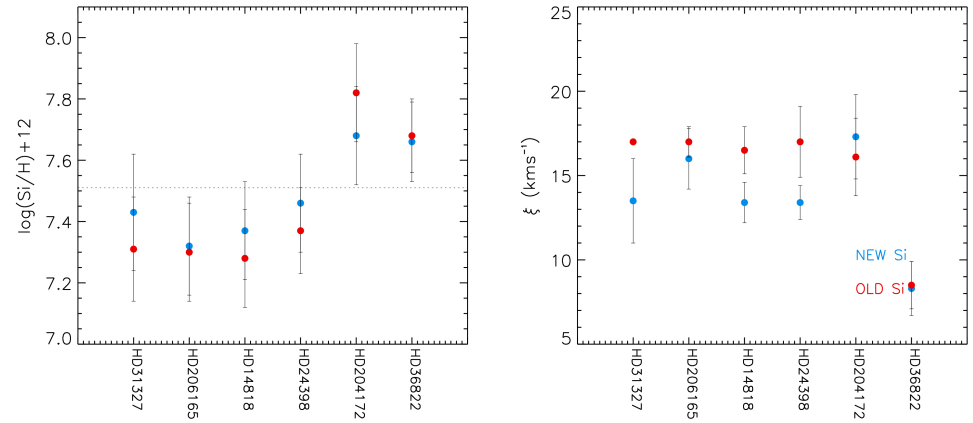

FIGURE 3.24— Silicon abundances (left panel) and microturbulences (right panel) obtained using both atomic model versions. The solar abundance (7.51 *dex*, Asplund et al. 2009) is marked (dotted line).

The average silicon abundances determined are displayed in Fig. 3.24. In the previous section, we have already shown the issues of some of the lines in the most conflicting examples considered in this chapter. Nevertheless, the mean gives compatible values for both models, within the errors. In the cooler objects treated, the new model produces higher abundances, while in hotter stars it results in lower ones. The same relation was already observed in the temperature, which is not odd

since these parameters are coupled. The microturbulences obtained are smaller in the new atomic model. In general, the new model produces abundances closer to the solar value (Asplund et al. 2009).

Figure 3.25 displays the final profiles obtained as a results of the best parameters derived from the new and old atomic models. In these six stars, where we have focused our tests, the final synthetic spectra are almost indistinguishable, in spite of the high resolution and S/N in the data. At this accuracy level, there is a clear degeneration in all the stellar parameters involved in the analyses. Thus, the increase in temperature, for instance, is compensated by the rest of free parameters involved in the study, obtaining quasi similar synthetic profiles.

Some of the lines are affected by blends as Si IV 4089 $\AA$ mixed with a O II transition. The oxygen atomic model is not included in the synthetic spectra displayed in Fig. 3.25 which explains the differences in some of the stars. The lack of this element in the modeling could have certain impact on the Si II $4128-4130\,\AA$. Even at high resolution the observed spectra plotted in the figure show the possible influence of nearby O II transitions on these two lines. This fact may explain part of the discrepancies observed previously.

3.6 Summary

A new silicon atomic model has been transferred from DETAIL and tested in FASTWIND. The model presents a detailed treatment for the Si II, Si III and Si IV ions, with a description of the energy structure and updated information on the radiative and collisional processes. Due to the similarities between DETAIL and FASTWIND (handling the atomic data in a similar way) the transference was straightforward. Only RBF transitions with OP data required modifications in the stellar code source.

To check the differences and the reliability of the new atomic models in contrast to the previous version used so far, we developed several tests with synthetic and Galactic optical spectra. The comparison between the profiles resulting for both atomic models showed the largest differences in the Si II ion. Although the Si II level description is similar in both, the processes treatment has suffered drastic changes.

The differences showed by the equivalent widths in the main optical lines (those normally used for the effective temperature) are small, reaching temperature corrections of up to $\sim 1000\,K$ under certain conditions. Instead, the changes in other important transitions, those normally used to the chemical abundance determination, are larger. The work developed by Simón-Díaz (2010) in dwarf stars indicated divergences in some of these lines, avoiding to reach a common solution for all the transitions. The new silicon atomic model could be the key to solve this problem at low luminosity classes.

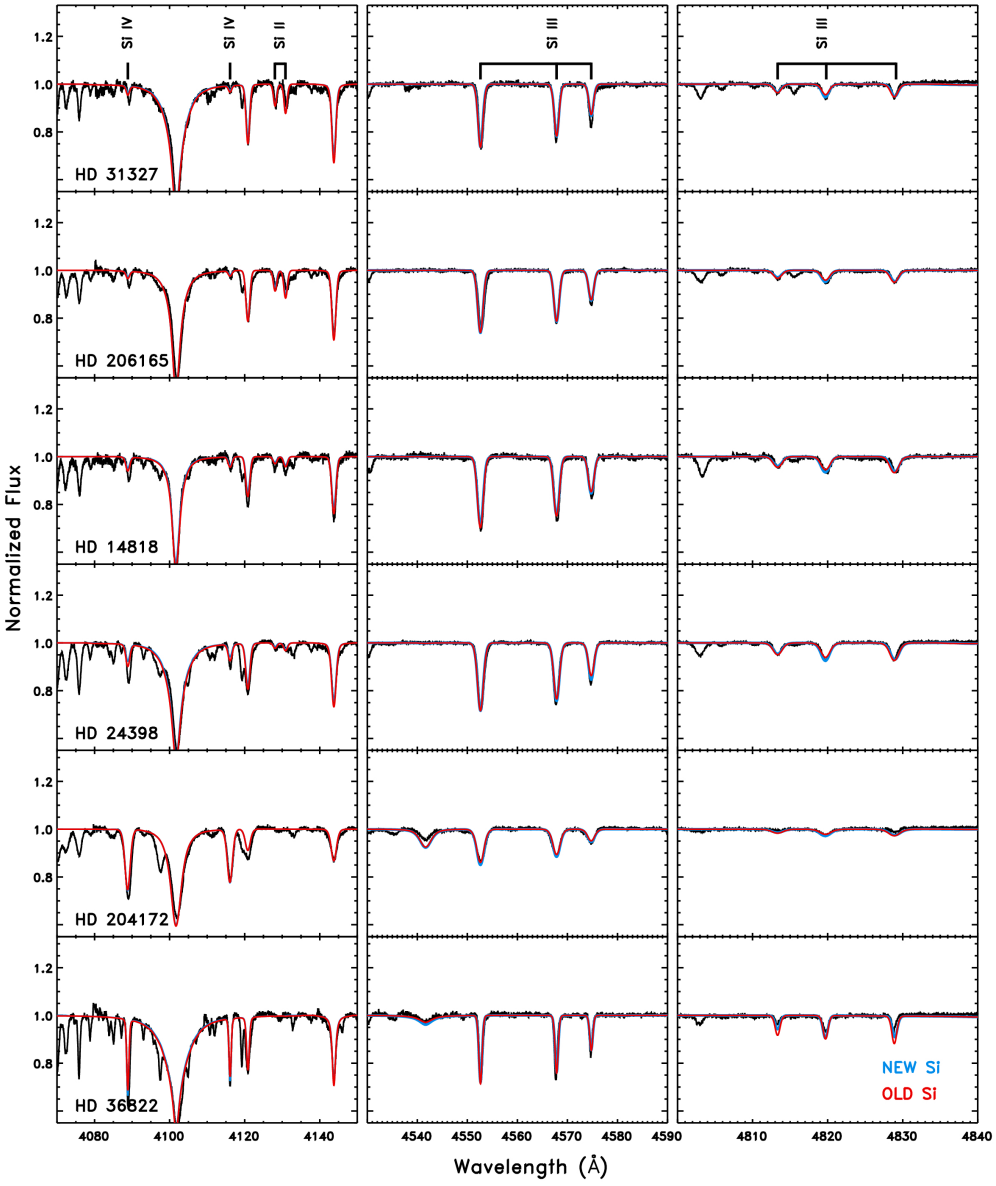

FIGURE 3.25— High resolution spectra from the IACOB database used for testing both silicon atomic model. The figure is centered in the most relevant silicon features in the optical range at these temperatures (marked in the figure). Both models give a good agreement with the observed spectra. Note that Si IV 4089 $\AA$ is blended with an O II transition not included in the synthetic spectra.

The quantitative analyses carried out on six Galactic supergiant stars showed overall better agreement between the different ionization balances and the lines used in the chemical and microturbulence determination when using the new atomic model. There are, however, two exceptions (HD 14818 and HD 24398) where the old model gave a better match between the ionization ratios. In the other four stars the deviations presented for the new atomic model were smaller, and even the transitions Si III 4813 $\AA$ showed a notable improvement.

The problems found in HD 14818 and HD 24398 can be attributed to several factors: unsolved problems in the atomic model at this temperature and gravity range, likely in the Si II ion; a contamination due to O II transitions in the Si II $4128-4130$ $\AA$ lines; or the effect of the wind and microturbulence in the ionization ratios (though they should be small, it is advisable to take them into account to avoid systematic errors). An extensive quantitative study on a large database covering different temperatures and gravities is highly recommended to evaluate the atomic model across the whole parameter space and refine it. Thanks to the completeness of the IACOB database we already have enough information for carrying out this study in future work.

4

Quantitative Analysis of Massive Blue Stars

Then the traveller in the dark,
Thanks you for your tiny spark,
He could not see which way to go,
If you did not twinkle so.
The Star, Jane Taylor

THE analysis of massive blue stars is a challenging and time consuming task, even for a single star. Thanks to multiobject spectroscopic instruments, we add the option of obtaining hundreds of stars in a single observational campaign, a huge amount of time is required for fulfilling a detailed quantitative analysis. In an attempt to reduce this effort we have implemented a semi-automatic technique. The method is based on a χ^2 minimization procedure, following the work of Lefever (2007), and takes advantage of the short time needed to calculate a FASTWIND model, crucial for generating extensive model grids.

The completeness of the grid, the range of the considered parameters, and the steps between them are fundamental issues for the accuracy of stellar parameters. However, we have to bear in mind the limitations of a large model grid: the cost in computational time, which urges an efficient parameter selection, and the difficulty in managing a huge number of models and matching them with observed data.

The grid and the method presented here were firstly conceived for low-resolution analyses, as those typically found in many extragalactic observations. Nevertheless, the method could also be applied to high resolution spectra and we have developed the

necessary tools to use it on Galactic stars.

This chapter summarizes the development of the methodology and the different steps in the semi-automatic quantitative analysis. We describe the construction of the grid and the selection of its stellar parameters, customized for our study of supergiant blue stars. Once a robust grid is ready, we explore the different ways to proceed at low and high resolution.

4.1 Building a FASTWIND Grid

The stellar atmosphere model constitutes the basic pillar in a quantitative analysis. Section 2.2 gave a summary of the main codes available for massive blue stars. In this work the atmosphere/line formation stellar code FASTWIND (Santolaya-Rey et al. 1997; Puls et al. 2005) was selected, because of its high computational efficiency. Its main characteristics fulfill all the requirements for carrying out reliable model atmosphere simulations in short periods of time (see section 2.3), invaluable for building large sets of synthetic spectra.

The atomic models included in the code represent the second crucial part in the calculation of a reliable model out of the LTE domain. Enough detail must be provided for reproducing the different spectral transitions, taking into account that these features may depend on many different atomic levels and processes. In the temperature range considered in this study ($\sim 14000 - 29000\ K$) lines from different metallic species (mainly silicon, oxygen, carbon, nitrogen and magnesium) together with important transitions of hydrogen and helium are accounted for (see section 4.1.2).

Each FASTWIND model is described by nine main parameters. Ideally, all of them would vary in our model grid. However, because of the large parameter space covered some of them were fixed, saving a significant amount of time, but without introducing any limitation in our analysis. Some parameters (e. g. radius) can be updated in a later step of the analysis, provided that the information can be recovered from the observations at hand (for instance, apparent magnitude, distance and reddening). We briefly describe in this section the constraining criteria and range of values adopted for each parameter.

4.1.1 Stellar Parameters

The stellar atmosphere is defined as a function of the effective temperature, surface gravity, radius, microturbulence, helium abundance, metallicity, and the parameters that govern the stellar wind (mass loss rate, terminal velocity, and β). All of them must be properly taken into account in the calculation of an atmosphere model.

- **Effective Temperature (T_{eff}).-** Our study is aimed at late-O and early-B supergiant stars. We have consequently built the grid for a range of temperatures

between 9000 and 35000 K, in steps of 1000 K. This covers objects with spectral types $\sim A1 - O8$. This ample range of temperatures was purposely adopted to avoid any star being too close to the grid limits.

- **Surface Gravity ($log\,(g)$).-** Although the goal of this work is the analysis of supergiant stars, we have extended our calculations to higher gravities, again avoiding that observed objects lie too close to the grid edges. We adopted an upper limit of $log\,(g) = 3.7$ *dex*.

  In order to select the gravities for each temperature, we decided to do so according to the flux-weighted gravity, defined as:

$$log\,(g_F) = log\,(g) - 4 \cdot log\,(T_{eff} \cdot 10^{-4}) \tag{4.1}$$

  Kudritzki et al. (2008) presented a linear tight relationship between this parameter and the absolute bolometric luminosity of the star (FGLR). In regular blue supergiants, it reads:

$$M_{bol}^{FGLR} = (3.41 \pm 0.16) \cdot (log\,(g_F) - 1.5) - (8.02 \pm 0.04) \tag{4.2}$$

  where M_{bol}^{FGLR} is the bolometric magnitude estimated through the FGLR.

  The $log\,(g_F)$ allows us to perform the gravity selection at constant luminosity steps, in concordance with the effective temperature, as it is shown in Fig. 4.1. The evolution of supergiant stars is predicted at almost equal luminosity in their travel to the red supergiant side of the HR diagram, therefore our criteria give an efficient sampling of the supergiant area.

  Supergiants of luminosity classes Ia and Ib span a range in $log\,(g_F)$ between 1.0 and 1.5 *dex*, which for objects with an effective temperature of 25000 K means $log\,(g)$ 2.6 and 3.1 *dex* respectively. Our models were calculated wrapping the $log\,(g_F)$ range from 0.9 to 2.5 *dex*, with the $log\,(g)$ limit specified before. As we will show later in section 4.1.4, those models with 0.9 *dex* hardly converge since they are too close to the Humphreys–Davidson limit (see Fig. 4.1).

  Figure 4.1 shows the position of the grid models in the HR diagram overplotted on the evolutionary tracks with rotation (300 kms^{-1}) calculated by Meynet & Maeder (2003). This selection enables the study of evolutionary stages with an initial mass in the range $\sim 8 - 60\ M_{\odot}$ at constant luminosity steps.

- **Radius (R_*).-** For each given pair $T_{eff} - log\,(g)$ (or $log\,(g_F)$) the radius is calculated according to the FGLR (see Eq. 4.2). From the temperature and the gravity of each model we can obtain an estimated bolometric magnitude and

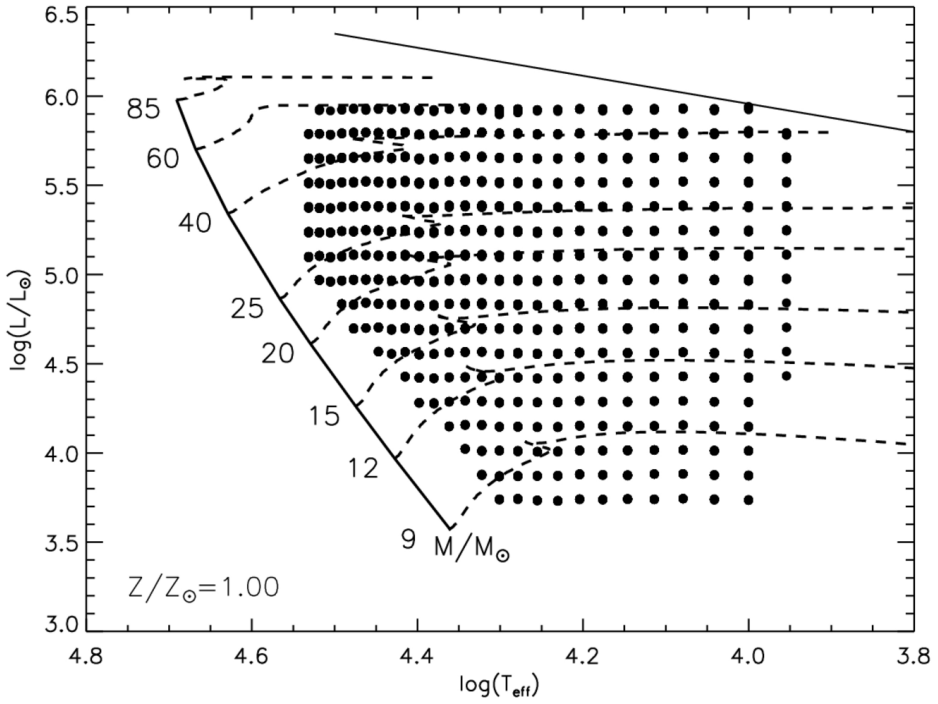

FIGURE 4.1— Distribution of the grid models in the $log\,(T_{eff}) - log\,(L/L_{\odot})$ plane (black dots). To have an idea of the kind of stars that the grid allows to analyze, the evolutionary tracks with rotation obtained by Meynet & Maeder (2003) are plotted for different masses. The Humphreys–Davidson Limit (Humphreys & Davidson 1979) is also drawn in the upper part of the diagram (solid line), delimiting the approximated convergence area at high luminosity.

therefore the model radius (see section 4.2.5). Although this relationship was established for supergiants, evolving at constant luminosity, we have also used it for objects that do not entirely fulfill this condition. The values in the model grid will be considered as a first approximation for the radii of the analyzed stars. The real radius will be obtained from the apparent magnitude corrected from extinction (section 4.2.5).

Figure 4.2 displays a comparison between values collected from the literature (Martins et al. 2005; Crowther et al. 2006; Kudritzki et al. 2008) and the radii that would be obtained for these objects by applying our criterion, using the temperature and gravities provided in the previous references. The area of supergiant stars shows a good match with the FGLR estimation, however in dwarf objects the radius proposed for the FGLR is slightly lower than the values

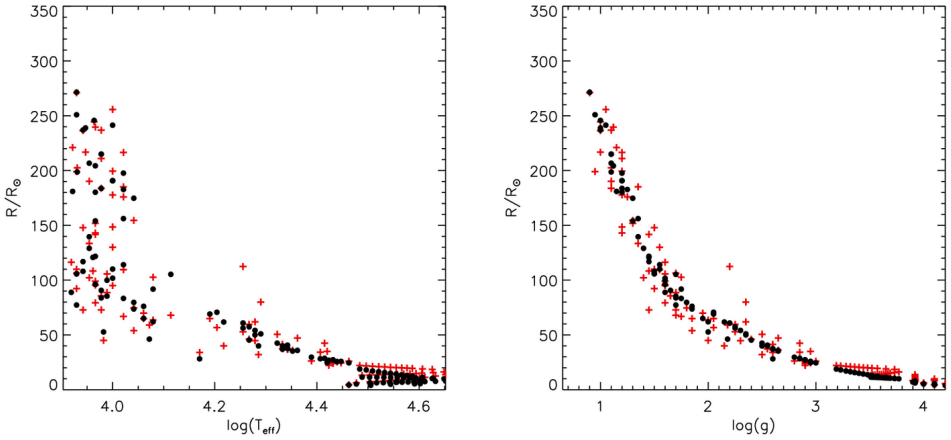

FIGURE 4.2— Radius versus $log\,(T_{eff})$ (left panel) and $log\,(g)$ (right panel). Red crosses represent T_{eff}, $log\,(g)$ and radius obtained by Martins et al. (2005); Crowther et al. (2006); Kudritzki et al. (2008). Black dots have the same T_{eff} and $log\,(g)$, but the radius was calculated from the FGLR.

estimated by Martins et al. (2005), as expected, since the FGLR was obtained for supergiant stars.

- **Microturbulence (ξ).-** The atmosphere was modeled with three different values for the microturbulence 7, 17 and 27 kms^{-1}. Nevertheless, during the calculation of the formal solution it is possible resort to a richer set of values, always taking into account that they must be close to the one used in the model atmosphere (otherwise the final spectrum will not be reliable). The grid was completed with $\xi_{\,FORMAL\ SOLUTION} = 5$, 7, 10, 12 (for $\xi_{\,MODEL} = 7\ kms^{-1}$), 15, 17, 20, 22 (for 17 kms^{-1}), 25, 27 and 30 kms^{-1} (for 27 kms^{-1}).

- **Helium abundance.-** The abundance of helium relative to hydrogen (He /H), by number, was sampled with four points 0.05, 0.1 (solar), 0.15 and 0.2. Although 0.05 is unrealistically low it was used to avoid the solar value in the edge of the grid and to detect peculiar objects.

- **Metallicity (Z).-** Five values of metallicity were used, from $Z/Z_{\odot} = 0.25$ to 1.25 in steps of 0.25. The abundances of all the chemical elements included, either in an explicit or implicit way (see section 2.3), were scaled by the metallicity value. The solar references were taken from Asplund et al. (2009).

  In the subsequent, we refer the metallicity and the silicon abundance (solar value scaled by $Z/Z_{\odot}$) as similar parameter in the analysis. Obviously this is an approximation, nonetheless silicon transitions (together with magnesium at

low temperatures, $\sim 15000\ K$) are the only features available in our data that are not altered by stellar evolution, and should reflect the stellar metal content.

The role of the wind cannot be ignored in the stellar evolution of massive blue stars. FASTWIND is a unified code which includes a stellar wind treatment by considering a beta velocity law (see Puls et al. 2008), and by ensuring a smooth transition between the pseudostatic photosphere and the wind (see section 2.3). Three free parameters are required to include the wind in this way into the calculation (neglecting any kind of clumping):

- **Terminal velocity (v_∞).-** Terminal velocities were fixed by considering the observed relationship between the escape velocity (v_{esc}) and the wind terminal velocity. Following the studies of Lamers et al. (1995) and Vink et al. (1999) this relationship is defined as a bimodal function separated by the so-named *'bi-stability jump'*. Crowther et al. (2006) argued that this *jump* is, actually, a smooth transition around 20000 K.

  The v_∞ estimation that we propose is based on different studies and references therein (Kudritzki & Puls 2000; Crowther et al. 2006; Markova & Puls 2008) and tries to reproduce its behaviour in the *bi-stability* transition region. With the goal of emulating the empirical values, a monotonous trend was used in the range of temperatures where the *jump* takes place. Figure 4.3 shows a compilation of published v_∞ and v_{esc} from the literature, cited before, with those used for our grid. The latter are calculated with the empirical T_{eff} dependence described in Eq. 4.3.

$$\frac{v_\infty}{v_{esc}} = \begin{cases} 1.10 & T_{eff} \leq 15kK \\ 11.65 \cdot log\,(T_{eff}) - 47.62 & 15kK < T_{eff} < 24kK \\ 3.41 & T_{eff} \geq 24kK \end{cases} \tag{4.3}$$

  v_∞ depends on the metallicity of the stars. We accounted for the metal content by introducing a power-law dependence as derived by Leitherer et al. (1992) (see the review by Kudritzki & Puls 2000, but also Vink et al. 2001 and Kudritzki 2002).

$$v_\infty(Z) \propto Z^{0.12} \tag{4.4}$$

- **Exponent of the wind velocity law, β.-** We used a linear relationship between β and T_{eff}, based on empirical data (Urbaneja 2004 and Crowther et al. 2006,

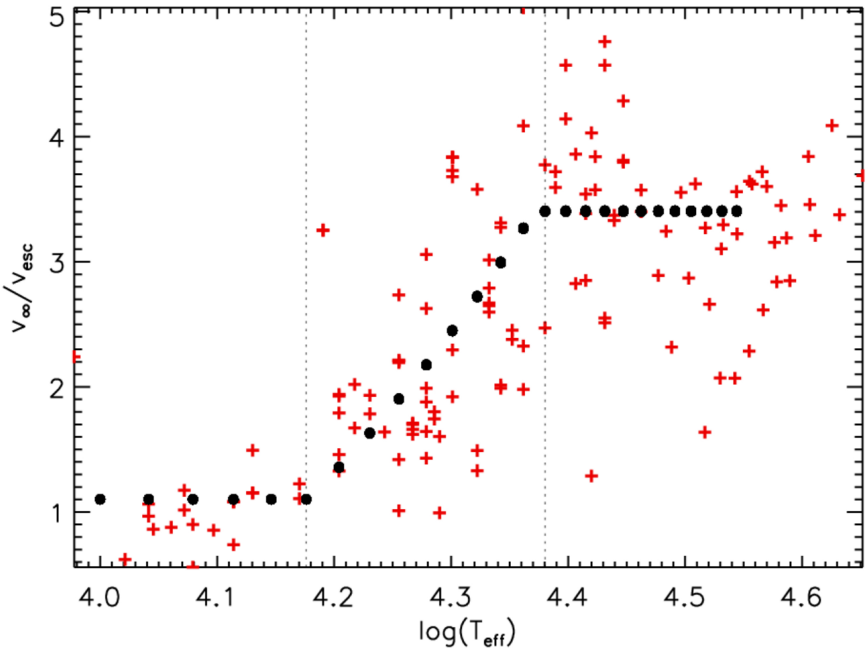

FIGURE 4.3— Calibration of (v_∞/v_{esc}) versus T_{eff} (black dots). We preferred a smooth transition in the area of $15000-24000\,K$ (dashed lines), following empirical studies (red crosses, Kudritzki & Puls 2000; Crowther et al. 2006; Markova & Puls 2008), instead of an abrupt jump.

see Fig. 4.5). This linear regression was established for supergiants with temperatures between $10000\,K$ and $31000\,K$. Beyond those limits fixed values were adopted:

$$\beta = \begin{cases} 3.60 & T_{eff} \leq 10kK \\ -1.40\cdot(T_{eff}10^{-4})+5 & 10kK < T_{eff} < 31kK \\ 0.70 & T_{eff} \geq 31kK \end{cases} \tag{4.5}$$

- **Mass loss rate ($\dot{M}$).-** Puls et al. (1996) showed that there exists a degeneration of the stellar wind parameters, so that different combinations of mass loss, terminal velocity and radius can produce the same emergent profiles. For the case of recombination dominated lines (e. g. H_α) an *'optical depth invariant'* parameter *(Q)* was defined (see also Puls et al. 2008, for more details) as:

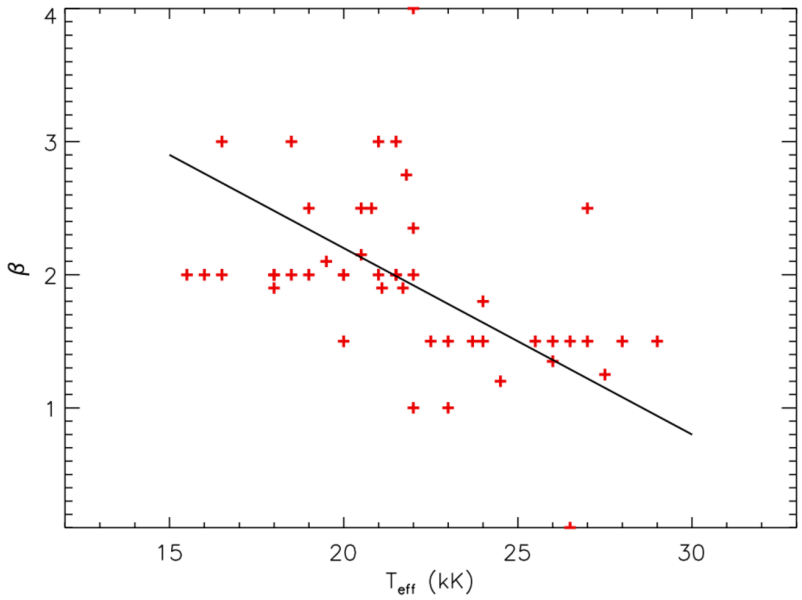

FIGURE 4.4— Distribution of β parameter with T_{eff}. The fit used in the grid (black line) was done based on the values proposed by Urbaneja (2004) and Crowther et al. (2006) (red crosses).

$$Q = \frac{\dot{M}}{(R_* v_\infty)^{1.5}} \tag{4.6}$$

Since R_* and v_∞ are already defined by other stellar parameters, the basic idea is to define the mass loss through Q, allowing certain freedom. In other words, for models with fixed v_∞, R_*, we vary the Q-parameter to account for different wind densities. To avoid a too large number of models and unrealistic values, we have used the wind-momentum luminosity relationship (WLR) to define the central Q-value for each luminosity. The *'modified stellar wind momentum'* is defined as:

$$D_{mom} = \dot{M} v_\infty \sqrt{\frac{R}{R_\odot}} \tag{4.7}$$

According to the WLR (Kudritzki et al. 1995; Kudritzki & Puls 2000):

$$\begin{aligned} log\,(D_{mom}) &\cong x\,log\,(L_*/L_\odot) + D_o \\ &\cong 2.31 log\,(L_*/L_\odot) + 15.94 \end{aligned} \tag{4.8}$$

The values for x and D_o quoted in Eq. 4.8 were obtained from a linear regression based on previous studies by Crowther et al. (2006), Lefever et al. (2007), Mokiem et al. (2007) and Markova & Puls (2008). For each set of parameters, three models with different Q were created, using the value derived from Eq. 4.7 and Eq. 4.8 plus ± 0.5 *dex*. Those models with $\dot{M} < 10^{-8}\ M_\odot yr^{-1}$ were calculated with $\dot{M} = 10^{-8}\ M_\odot yr^{-1}$, since at this low mass loss rate the effects on the analyzed profiles are negligible. With this imposition, redundant spectra and a waste of computational time are avoided (note that this restriction should be relaxed at IR or UV wavelengths). That criterion was fixed at $log\,(L/L_\odot) \sim 4.4$. Fig. 4.5 displays the WLR for the grid at $Z = Z_\odot$. As a result of our lower limit for $\dot{M}$, there is a flattening of D_{mom} below $log\,(L/L_\odot) \leq 4.4$.

We accounted for the metallicity impact on the mass loss rate as we did for the wind terminal velocity, by introducing a power-law dependence:

$$\dot{M}(Z) \propto Z^m \tag{4.9}$$

By combining Galactic, LMC and SMC stars, Mokiem et al. (2007) derived an exponent of $m = 0.83$.

Let us make a remark about the role played by the stellar radius in the calculation of $\dot{M}$ from Q (see Eq. 4.6). If a better estimation of the radius exists, a new mass loss rate must be calculated to reproduce the same Q-parameter.

4.1.2 Atomic Models

The atomic models used in the calculations play a fundamental role, not only in the subsequent determination of stellar parameters, but also in the computational time required. The aim of this work is to obtain first the stellar parameters, leaving the detailed abundance analysis for a second step. Atomic models for H I, He I-II, Si II-III-IV and O II-III were explicitly included in the code. We introduced the O II-III ions because at low resolution the Si IV 4116 $\AA$ and Si II $4128 - 4130$ $\AA$ lines are blended with several O II transitions. For the chemical abundance study, C II-III,

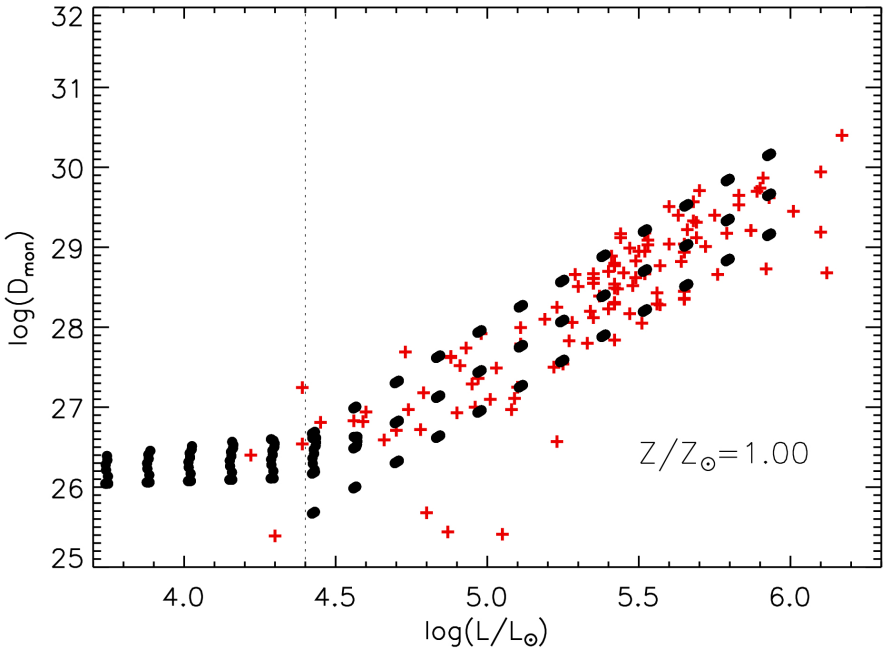

FIGURE 4.5— WLR relationship used to estimate Q values (hence mass loss rates) for the grid models, as a function of their luminosity. The relationship was established according to data obtained by Crowther et al. (2006), Lefever et al. (2007), Mokiem et al. (2007) and Markova & Puls (2008) (red crosses). For a given luminosity, the corresponding Q is used to calculate a model, plus two additional atmosphere models with $log\,(Q) \pm 0.5\ dex$ (black dots). Models with luminosity lower than $log\,(L_*/L_\odot) \sim 4.4$ (dotted black line) have the mass loss rate fixed to $10^{-8}\ M_\odot yr^{-1}$.

N II-III and Mg II ions were also included. Models have been usually imported from the DETAIL code with several updates (Urbaneja 2004). The chemical species used and their principal references and sources are listed below:

- **Hydrogen:** Jokuthy (2002)
- **Helium:** Jokuthy (2002)
- **Silicon:** N. Przybilla (2007, private communication). As it was commented in chapter 3, the implementation in FASTWIND of an updated version of silicon model ions was an important part of this work and a more detailed description of the silicon atomic structure can be consulted in that chapter.
- **Oxygen:** O II, Becker & Butler (1988); O III, D. Kunze (1998, private communication)

- **Nitrogen:** N II, Becker & Butler (1989); N III, Butler (1984)
- **Carbon:** C II, Eber & Butler (1988); C III, Eber (1987)
- **Magnesium:** K. Butler (1998, private communication)

The rest of chemical species were treated in an implicit way (for further details, see section 2.3) which speeds up the time spent in each model, while keeping the required accuracy in the background opacity.

4.1.3 Through CONDOR

This careful selection has led to more than 45900 models. In a regular computer (2 Gb RAM, 2 GHz CPU) each model can take around 40 minutes, which means several years for the entire grid. Thus, it is nearer impossible to complete the project with a single computer or a small network, but it can be managed with the aid of CONDOR[1] in a month. CONDOR creates a High-Throughput Computing environment and utilizes the computing power of workstations over a network when the machines are idle, parallelizing the whole process.

To carry out the grid calculation through CONDOR, several programs were updated, while others were built from scratch, speeding up the whole process as much as possible. The philosophy of parallel processing of CONDOR, together with the PC network of the Instituto de Astrofísica de Canarias, allows us to reach more than 200 CPUs, computing 200 models at the same time (it depends on the number of the users requesting CONDOR or their own machines). This tool not only makes the creation of huge grids easier, but also provides a way to rapidly build a small set of models, for abundance analyses, or for fine tuning the stellar parameters in the same time than a couple of models with a single processor.

4.1.4 Convergence Criteria

Not all models described before will finish successfully. For some models at the grid edges, FASTWIND has difficulties to reach convergence. For instance, at low gravities and high temperatures the code cannot generate a stable atmosphere, as radiative pressure is too high to be compensated by gravity.

An end without *crashing* in a model run does not mean a reliable atmosphere spectrum. Three criteria are demanded for considering a model as converged:

- FASTWIND follows an iterative path searching for a self-consistent solution of the radiative and statistical equilibrium equations. Thus, the code will stop (if it does not so before for any other reason) when reaching the maximum number of

[1] http://www.cs.wisc.edu/condor/

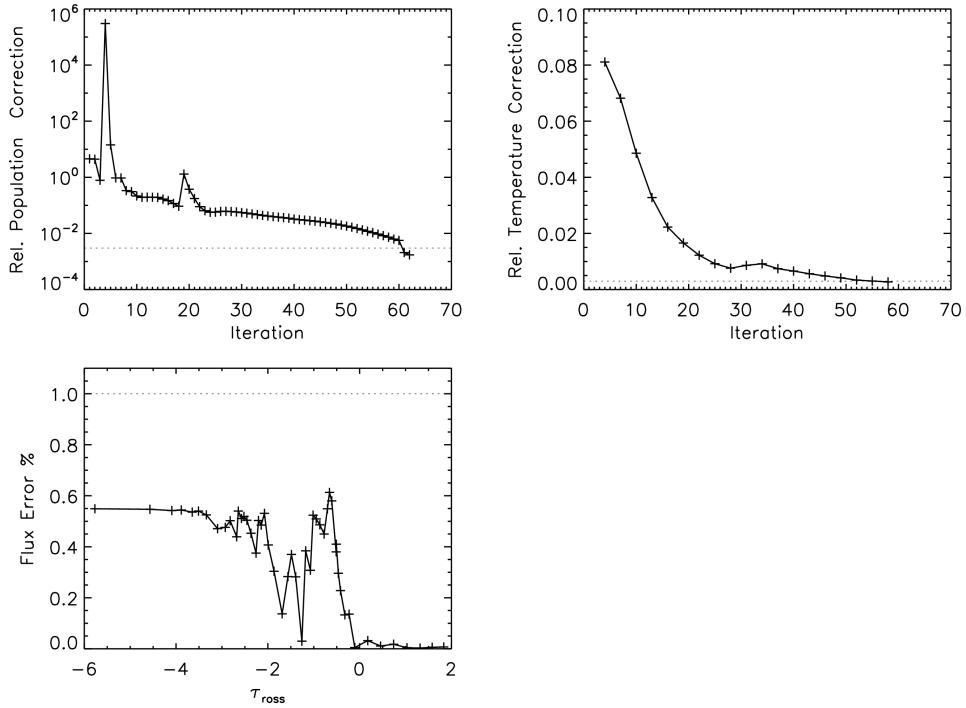

FIGURE 4.6— Convergence criteria mandatory for a reliable model. Top-left panel, maximum relative population correction in each one of the iterations carried out by FASTWIND. Top-right panel, maximum relative temperature correction in each 2-3 (set by user) FASTWIND iteration. Bottom-left chart, flux error percentage across the atmosphere stratification in the resulting model. The limits imposed are marked by a dotted line in each diagram.

iterations imposed by the user, or if the maximum relative correction in the level populations is less than $3x10^{-3}$. Models that do not stop fulfilling this second limit are not considered. The top-left plot in Fig. 4.6 illustrates this criterion. This particular FASTWIND model in Fig. 4.6 stops near the 62nd iteration since it reached the threshold in the population correction.

- Urbaneja (2004) (see also Puls et al. 2005) introduced a similar iterative process in the code, but now applied to the temperature stratification. Each two or three iterations of the code (value set by the user) a correction in the temperature was done. The maximum of the relative temperature change at all depths must be also smaller than $3x10^{-3}$ to accept the model. The top-right chart in Fig. 4.6 shows the temperature correction in each iteration until the model converged, before the relative population correction reaches its proper limit.

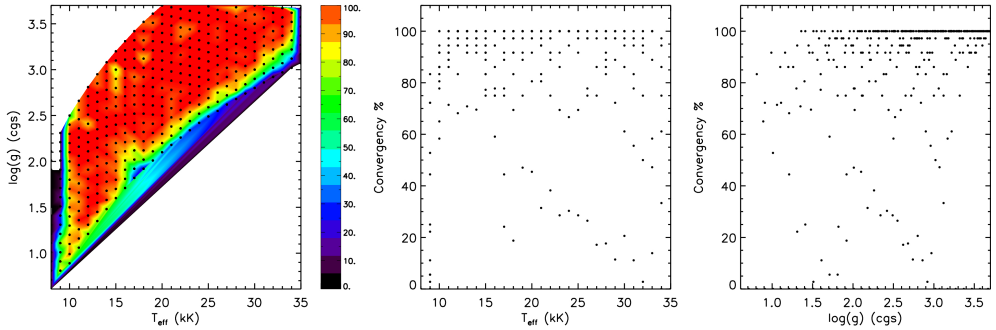

FIGURE 4.7— Percentage convergence color-map (being red a convergence of 100%) for the grid with solar metallicity over the $T_{eff} - log\,(g)$ plane (left panel), together with its projection in the temperature (middle panel) and gravity (right panel) axis respectively. For each $T_{eff} - log\,(g)$ par there are 36 models with different helium abundance, microturbulence, etc.

- Eventually, the maximum error in the flux of the final model must be lower than 1%. With this last criterion the flux conservation in each depth point of the atmosphere is checked. Bottom-left panel in Fig. 4.6 displays the absolute values of the flux error across the atmosphere. This particular model shows a maximum in the flux conservation error around 0.6%.

Only those models that fulfill these criteria are considered in the final grid for quantitative analyses. For each metallicity $\sim$ 12000 models are calculated, around 1000 of them do not pass this sieve. Figure 4.7 explores the convergence percentage $\left(\frac{N_{converged}}{N_{NOconverged}}\right)$ map in the $T_{eff} - log\,(g)$ plane for the solar metallicity grid and its projection in the temperature and gravity axes. As it was mentioned above, most of these non-converged models are situated close to instability regions. Some punctual spots in the grid show a slight decreasing in the convergence percentage, mainly due to precision errors that do not allow to accomplish the imposed criteria. The atomic models will also affect convergence. Adding a complex atomic model with a detailed level structure will result in a larger set of equations to be solved and more time needed for reaching a solution.

4.2 Automatic Stellar Parameters Determination

The spectral resolution dictates the best approach to proceed with the quantitative analysis. Depending of the information available, two ways have been proposed in this work. These are not new techniques, nonetheless we are going to automatize them as much as possible using the grid described in this chapter as a starting point.

Depending on the spectral resolution we are going to follow two different paths. Although data obtained at low resolution give limited information about the stellar

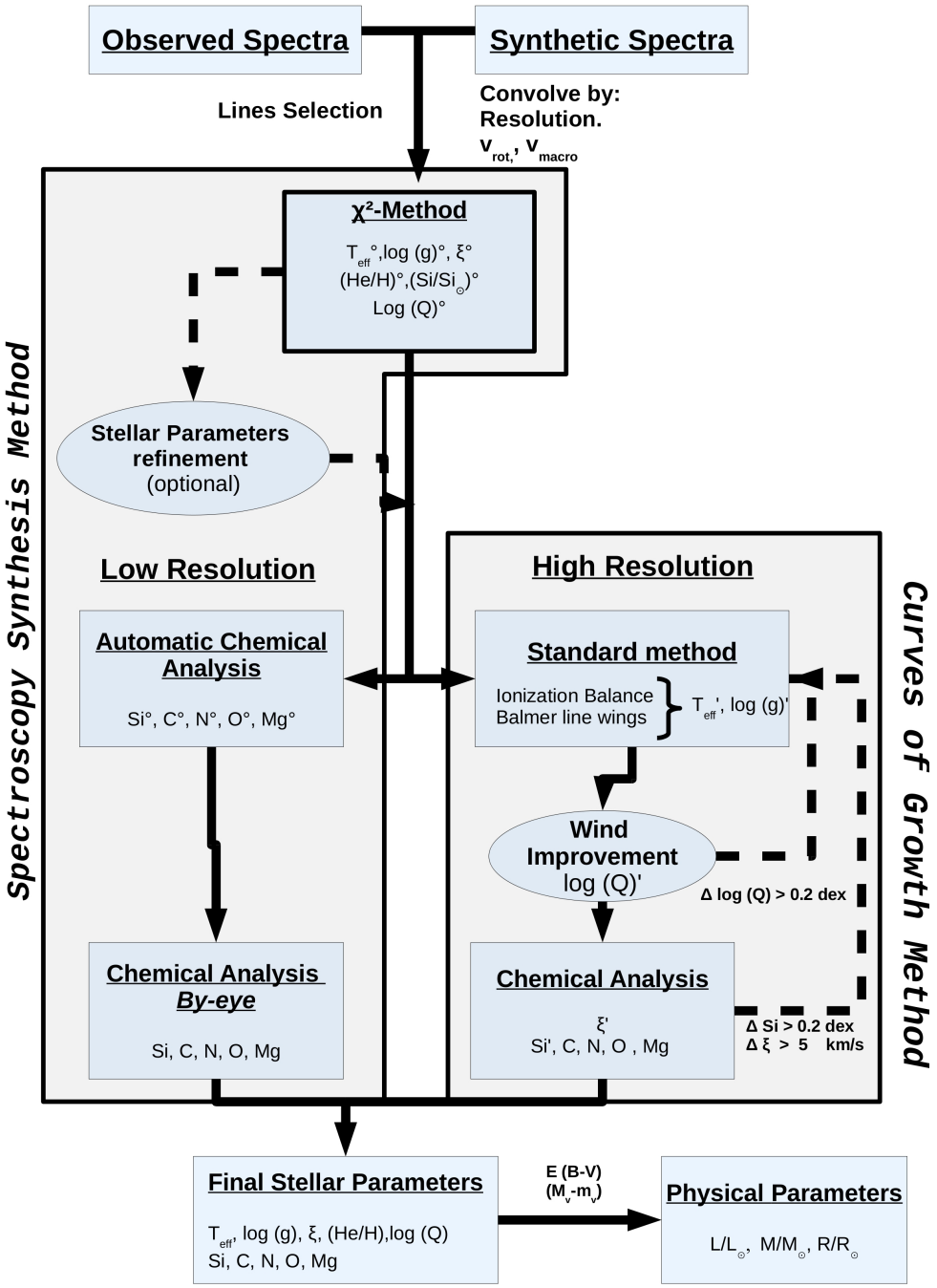

FIGURE 4.8— Schematic flowchart of the methodology apply at low and high resolution in this work.

parameters and part of the information might be lost, it is possible to carry out a quantitative analysis. On the other hand, higher resolution data offer the option of a more detailed analysis with better final accuracy. We are going to describe both methods, starting with the analysis at low resolution (since the extragalactic studies are the main goal of this work) and following with the high resolution technique. Briefly:

- At low resolution we require a similar method to the one employed by Urbaneja et al. (2005a) for the analysis of NGC 300's stars, and later by Evans et al. (2007) in their work on a NGC 3109 sample, the so-called *'Spectroscopy Synthesis Method'*. The idea is focused on reproducing all main spectral features at the same time, constraining as much as possible the stellar parameters with all the information achievable in the spectrum.

- High resolution and S/N spectra provide enough information to obtain the stellar parameters using individual features and not the entire spectrum as in the previous case, following the standard quantitative procedure described by other authors (e. g. Villamariz & Herrero 2000). Notwithstanding the philosophy, described in next sections, is the result of mixing both methods, the *'Spectroscopy Synthesis Method'* plus the standard way or *'Curves of Growth'*.

A flowchart of the different ways used in this work is displayed in Fig. 4.8. In the following sections we are going to center the discussion on each one of these paths, giving a detail description of the stellar parameters, errors and limitations of the methods employed.

4.2.1 Low Resolution: *Spectroscopy Synthesis Method*

Although the different ways proposed before can be handled independently, we have established a first common block for both methods (see Fig. 4.8). This section describes the χ^2-method developed for the low resolution analysis.

Stellar Parameters: How to Proceed...

To avoid a subjective *'by-eye'* method and also to allow the analysis of large datasets, we have implemented a straightforward χ^2 technique, similar to the Lefever et al. (2007)'s scheme.

The method is based on the comparison of the observed spectrum and our grid of synthetic models, in a number of spectral ranges covering relevant optical lines. Although the user can chose those spectral windows more interesting for each analysis, we have centered our study on the most relevant lines in the optical range between $4000 - 5000$ $\AA$ plus H_α (at massive blue stars typical temperatures), listed in Tab. 4.1. The method was designed to carry out the quantitative analyses in NGC 55 (see

Ion	$\lambda(\AA)$	Ion	$\lambda(\AA)$
HI	6562.85	HeI	4921.93
HI	4101.74	HeII	4542.80
HI	4340.47	SiII	4128.07
HI	4861.33	SiIII	4552.62
HeI	4026.19	SiIII	4567.84
HeI	4387.93	SiIII	4574.76
HeI	4471.48	SiIV	4116.10

TABLE 4.1— Lines used in the match between the observed spectrum with the stellar model atmosphere grid. At low-resolution the lines of Si II and Si IV can be blended with O II transitions.

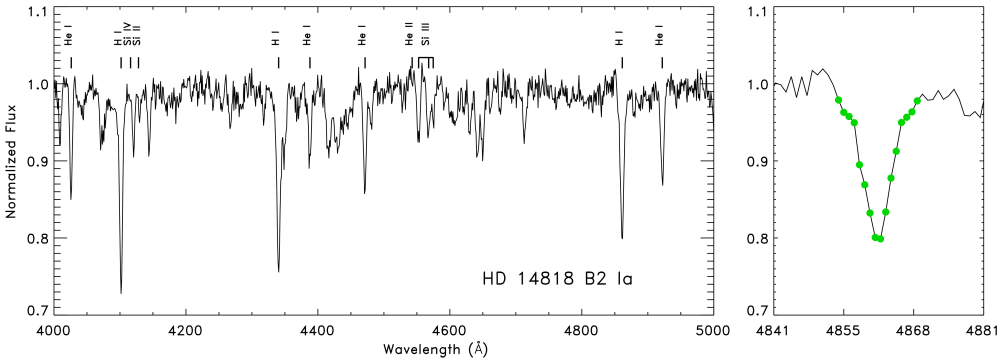

FIGURE 4.9— The lines employed in the χ^2 calculation are marked on the HD 14818 spectrum, degraded to $R = 1000$ and $S/N = 100$. The right panel shows an example of the wavelengths (green dots) used for the comparison with the synthetic data, in this example the line of H_β.

chapter 5) and it is constraint to the wavelength available, therefore the technique and tests developed in this section are orientated to this study.

Figure 4.9 shows an example of a Galactic star, HD 14818, observed with high resolution and S/N, but degraded to $R \sim 1000$ and $S/N = 100$. The lines compiled in Tab. 4.1 are marked in the plot, except H_α. In the right hand side of the image a zoom around the H_β line shows the wavelengths used for the match between the synthetic models and the observed profile. This range selection was made paying extra attention to the continuum rectification and the central line positions. It is fundamental to ensure that a shift in the line, for instance due to a wrong radial velocity correction, is not introducing any *bias* in the final results.

The spectral range covers other features that we do not have taken into account for this analysis. Mainly lines of carbon, nitrogen and oxygen, used later in the

determination of abundances. Besides, a set of hydrogen, helium and silicon lines have also been ignored because of different reasons: they are blended, like He II 4200 $\AA$ which overlaps with a N II transition; they are too weak (at this S/N), for instance the silicon triplet around 4820 $\AA$; or there are still doubts about their correct modeling, as in the case of He II 4686 $\AA$, that in principle, should react to wind properties in the same way as H_α does, but it has a more complicate and uncertain behavior (Puls et al. 2008).

Performing a comparison with the entire set of models a global χ^2 was calculated.

$$\chi^2_i = \frac{1}{n_{lines}} \sum_{j=0}^{n_{lines}} \frac{1}{n_{points}} \sum^{n_{points}} (y_{ij} - y_{obs})^2 \tag{4.10}$$

where n_{points} is the number of wavelengths used to compare the observed (y_{obs}) and synthetic data (y_{ij}), for model i and line j. Eventually, all the lines are considered with the same weight in the calculation.

Selecting Models and Constraining Errors.

Due to the uncertainties introduced by the limited S/N there is a sample of models around the minimum χ^2 that must be considered as candidates to reproduce the observed spectrum. Moreover, the uncertainties from the model grid distribution have also to be considered. The use of a discrete distribution of models drives to interpolations between the grid points, introducing an additional error that has to be considered.

The final parameter selection plus its errors were determined through two steps trying to cope with the two errors sources already mentioned:

- From the χ^2 distribution generated by the comparison of the observed spectrum with the model grid, through Eq. 4.10, we have selected all those models with a χ^2 value below the minimum plus 15%. This percentage was not chosen arbitrarily, but using a sample of twelve high resolution stars with S/N larger than 150 obtained as part of the IACOB spectroscopic database (see section 3.5.1). We carried out their analyses by the χ^2-method and fixed the percentage value at which expected errors for high resolution are obtained. Figure 4.10 shows how the errors of the different stars increase when the threshold is relaxed. We set the limit at 15% which in the test is equivalent to an mean error in the effective temperature of $\sim 700\ K$. Typical errors estimated for other authors are between $500 - 1000\ K$.

Figure 4.11 illustrates the results of this technique on HD 14818. Thus, those models with a χ^2 that accomplish the criterion are selected to derived the stellar parameters, marked on red dots in the figure. The final stellar parameters and their errors are calculated by averaging all these models, weighted by $e^{-0.5\chi^2}$ (normal distribution probability), and their standard deviations respectively. Figure 4.11 displays the average (solid black line) and the standard deviation (dotted black lines) resulting for each one of the stellar parameters considered.

In next sections, the different test performed using this criterion will return reliable results and errors in the stellar parameters according to the data quality of each spectrum. However, the fact of defining this threshold as a result of high quality data broke the self-consistence of the method. In future version of the method we will improve this constraint.

The errors obtained are constrained by the step used in the parameters selection. Thus, with a step of 1000 K in temperature an error lower than 500 K make no sense, and it must be fixed at this edge.

- Looking for a robust methodology in the stellar parameters determination together with their errors, the procedure commented above was complemented with a Monte Carlo simulation. This simulation allows us to estimate the systematic errors introduced by the continuum rectification and the S/N measured in each star. Given the S/N of the spectrum, we generate a random array of 100 elements around the continuum position limited by the noise $(1/(S/N))$. These positions were used as continuum references for a new re-rectification of the star. For each one of this 100 analyses, the stellar parameters and their errors were re-calculated (using the procedure described above), evaluating the S/N and the continuum rectification impact.

The methods described before produce a set of errors in the final stellar parameters. We are aware that they are not independent and both estimations are linked to the spectral S/N and the uncertainties introduced by the grid design. Our final estimation is forged as the sum of these two uncertainty sources.

$$\sigma^2_{total} = \sigma^2_{15\%} + \sigma^2_{MC} \tag{4.11}$$

An example to illustrated the entire process is displayed in Fig. 4.12. The plot represents the analysis on the Galactic B-type supergiant HD 14818 degraded to $R = 1000$ and $S/N = 100$. The top-left panel shows the χ^2 distribution as a result of the comparison with the entire grid. Those models with χ^2 below the minimum plus its 15% are marked in red dots. The rest of panels are focused on the results returned from the Monte Carlo simulation for the individual parameters. In each step of the

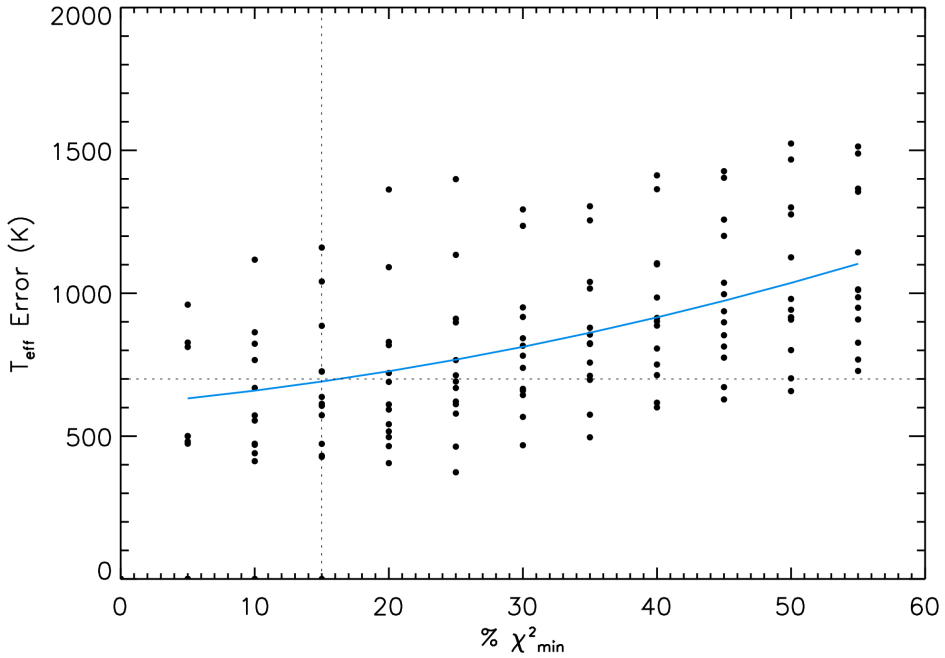

FIGURE 4.10— The χ^2-method was applied to twelve stars with high resolution ($R = 46000$) and S/N larger than 150 from the IACOB survey. The results allow us to fix the threshold used for selecting those models compatibles with the analyzed spectrum. The figure shows that typical errors for the effective temperature are recovered within a 15% of the minimum χ^2 (dotted lines) . See the text for more details.

Monte Carlo simulation the values of the stellar parameters and their errors where determined using the 15% limit commented before. The error estimated from the standard deviation are marked in red dashed lines while the dispersion due to the Monte Carlo simulation is marked with blue dashed lines. In this example the errors are of the same order.

The good match obtained by the stellar parameters derived from the HD 14818 spectrum is shown in Fig. 4.13. The lines used in the analysis display a remarkable match with the observed spectrum. Note that during the stellar parameters determination we considered the hydrogen, helium, silicon, oxygen and magnesium atomic models and only the transitions marked in the figure were analyzed in detail, explaining the mismatch in other transitions shown in Fig. 4.13. During the subsequent chemical analysis those other transitions will be handled (see section 4.2.1).

The silicon abundance, linked to the stellar metallicity (see section 4.1), is considered in this step as a first estimation. It will be improved during the chemical

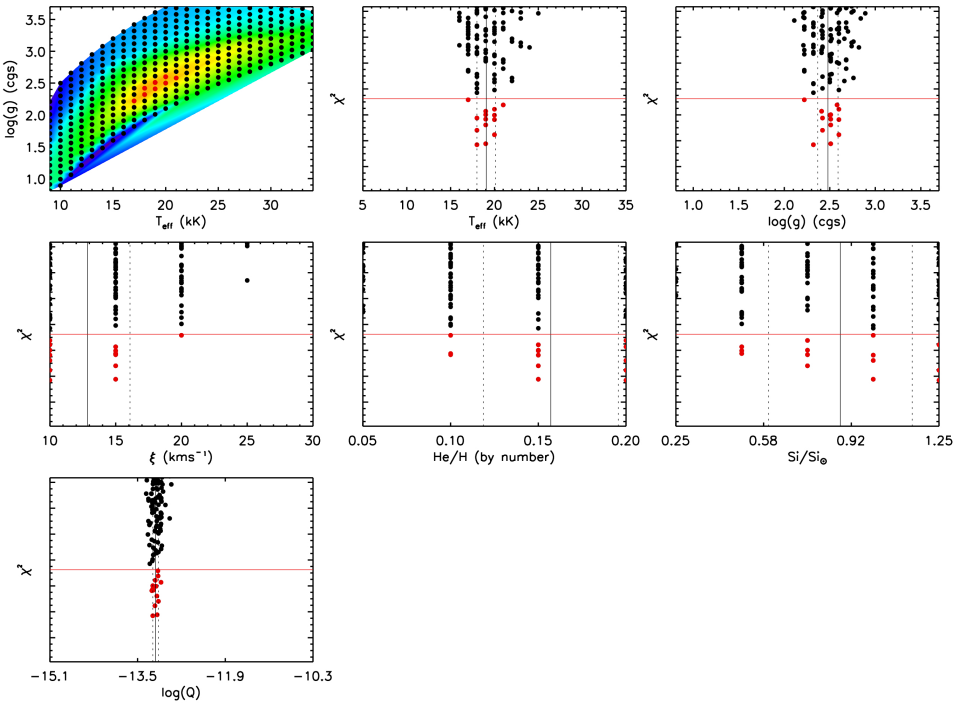

FIGURE 4.11— The top-left panel shows the χ^2 patterns obtained from the comparison of the transitions listed in Tab. 4.1 with the grid of models (black dots). Those models below the 15% threshold, defined in the text, are drawn in red dots. The rest of panels show the projection of the χ^2 distribution against the six stellar parameters considered in the study. The average value (solid black line) plus the standard deviations (dotted black lines) are also displayed in each chart.

analysis.

The whole process for a single star could take several hours (depending on computer CPU and memory). The match can be sped up by introducing restrictions to the stellar parameters. For instance, if the spectral type is known, it is not needed to sample the entire grid. The model can be limited in temperature and gravity, and even some microturbulence values can be dropped off from the analysis without loss of reliability in the result. The process can be accelerated even more parallelizing it through a system like CONDOR. An optimization of the χ^2 method would be also recommended. The implementation, for instance, of a gradient method to speed up the analysis will be contemplated in the future versions.

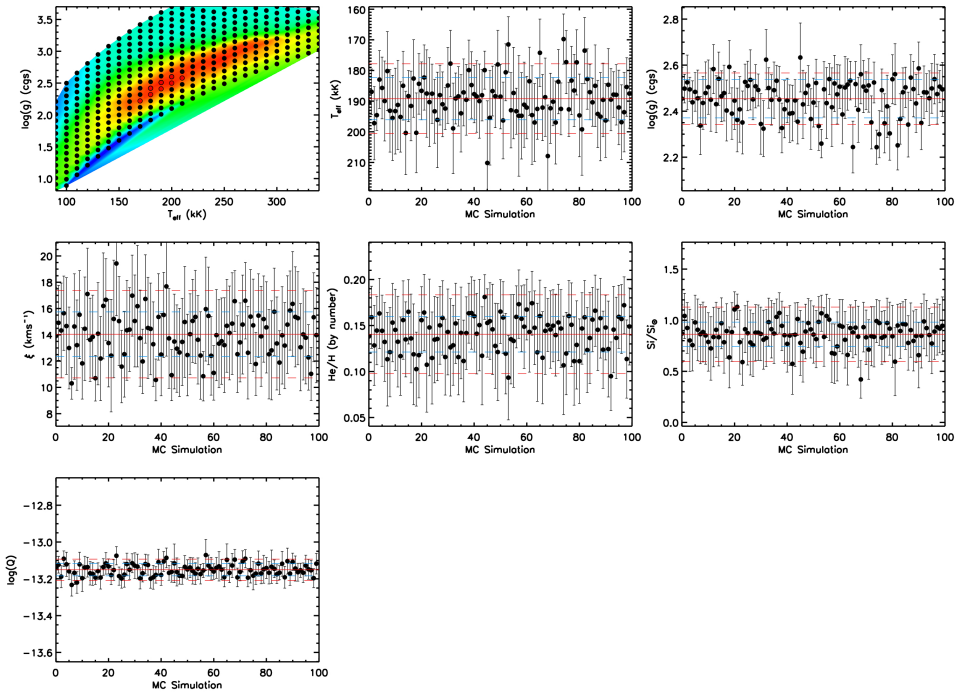

FIGURE 4.12— Stellar parameters determination in the galactic star HD 14818 ($R = 1000$ and $S/N = 100$). The top-left panel shows the χ^2 patterns obtained from the comparison of the transitions listed in Tab. 4.1 with the grid of models (black dots). Those models below the threshold marked by the $85\%\,\chi^2{}_{minimum}$ are drawn in red. The rest of panels show the Monte Carlo (MC) simulation and the values derived in each iteration (see text for more details). The error obtained from the standard deviation between the models considered is marked with red dashed lines while the dispersion in the MC simulation is drawn by blue dashed lines.

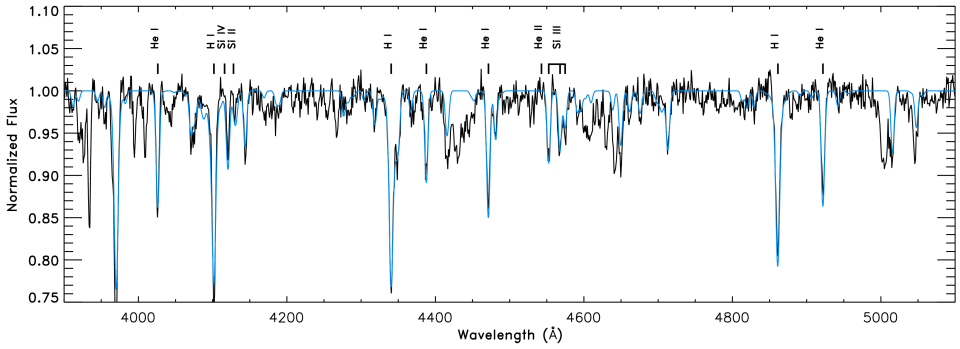

FIGURE 4.13— The comparison between the best model obtained through the methodology described for low resolution data and the HD 14818 spectrum (degraded to $R = 1000$ and $S/N = 100$) shows a good agreement. Those lines used as reference in the analysis (marked in the plot) are well reproduced. The rest of transitions, shown in the spectrum, were not modeled or did not belong to the star. As the interstellar band at ~ 4450 Å, which explains the strong discrepancies with the model.

Stellar Parameters: Tests

Before applying this method to real stars it is necessary to check its feasibility and the limitations of the stellar grid. In order to carry out these tests, we make a simulated analysis of three synthetic spectra created with FASTWIND and downgraded to $R = 1000$ with $S/N = 100$. The procedure was also tested on three Galactic supergiants, analyzed previously in the literature. The method was applied with and without H_α, to be consistent with our work on NGC 55 data (see chapter 5), and to evaluate its effect on the final result.

Comparison to Synthetic Spectra

The stellar parameters used in the synthetic test were randomly chosen within the grid, and do not necessarily represent a real star. Nonetheless, all of them were selected in the range of supergiant stars ($log\,(g_F) \sim 1.0 - 1.5$ *dex*, Eq. 4.1). No model in the grid has exactly the parameters used for the test models which leads to an interpolation between the available points.

Table 4.2 presents the input parameters of the synthetic spectra and the stellar parameters recovered by our method. Part of the information is lost when the quality is degraded, nevertheless the method recovers the input values within the errors. At this resolution different combinations of parameters, like microturbulence, silicon and helium abundance, can produce similar profiles which has a clear impact on the final uncertainties.

The spectra tested and the results with and without H_α are displayed in Fig. 4.14. In this test only elements included in the initial grid are considered and just the lines listed before are taken into account in the analysis.

The spectra calculated with the set of stellar parameters recovered through our technique show a remarkable good fit with the synthetic spectra analyzed (see Fig. 4.14). In the optical range between $4000 - 5000$ $\AA$ the impact of H_α in the analysis is almost null. The large differences are observed in the cooler object around the Si II $4128 - 4120$ $\AA$ transitions, although at this resolution them are negligible. The wind parameters and the H_α are well reproduced (of course with H_α included in the calculation). The largest discrepancy is around 0.08 *dex* in the model with an effective temperature of 30900 K, but at low resolution the impact is negligible as it is shown in Fig. 4.14.

Even with the lack of H_α in the analysis, and relying on the rest of Balmer lines (mainly H_β), the wind parameter is rather constrained. Only the hotter synthetic spectra (30900 K) show well reach large differences when H_α is not included, with a shift respect to the input value of 0.20 *dex*. In the other two examples analyzed, the differences with the input value do not go up to 0.05 *dex*. Although, this mismatch is

	T309G329			T265G280			T134G166		
	Input	Method	Method+H_α	Input	Method	Method+H_α	Input	Method	Method+H_α
T_{eff} (k)	30900	30776 ± 760	30848 ± 1083	26500	26097 ± 810	25780 ± 1088	13400	13275 ± 601	13201 ± 500
$log\,(g)$ (cgs)	3.29	3.25 ± 0.08	3.26 ± 0.08	2.80	2.74 ± 0.11	2.72 ± 0.11	1.66	1.65 ± 0.17	1.66 ± 0.07
v_{micro} (kms^{-1})	14.0	13.6 ± 3.3	14.4 ± 4.1	17.0	17.5 ± 4.0	17.9 ± 5.9	20.0	22.5 ± 5.3	19.6 ± 3.4
He/H	0.10	0.12 ± 0.03	0.13 ± 0.04	0.12	0.15 ± 0.04	0.14 ± 0.05	0.16	0.15 ± 0.04	0.16 ± 0.04
$Si/Si_\odot$	1.00	1.01 ± 0.25	0.94 ± 0.24	0.75	0.78 ± 0.30	0.66 ± 0.30	0.80	0.97 ± 0.23	0.81 ± 0.23
$log\,(Q)$	-12.70	-12.90 ± 0.35	-12.62 ± 0.20	-12.30	-12.30 ± 0.20	-12.31 ± 0.20	-12.20	-12.24 ± 0.20	-12.19 ± 0.20

TABLE 4.2— Results of the analyses of three synthetic spectra calculated with FASTWIND (parameters listed under column *'Input'*) degraded to $R = 1000$ and $S/N = 100$. The resulting parameters are gathered in column *'Method'*. The process was repeated including H_α, to estimate the effect of its absence on the parameters (*'Method+H_α'*).

	HD 209975			HD 38771			HD 14818		
	R04	Method	Method+H_α	U04	Method	Method+H_α	U04	Method	Method+H_α
T_{eff} (k)	32000	32723 ± 1004	32321 ± 1558	26500	27155 ± 1611	26876 ± 2055	20100	18319 ± 672	18905 ± 1290
$log\,(g)$ (cgs)	3.20	3.36 ± 0.09	3.32 ± 0.08	2.90	3.11 ± 0.10	3.11 ± 0.11	2.40	2.51 ± 0.11	2.45 ± 0.14
v_{micro} (kms^{-1})	10.0*	14.7 ± 5.3	14.4 ± 5.0	18.0	14.5 ± 4.6	14.1 ± 4.3	17.0	15.9 ± 3.9	13.9 ± 3.7
He/H	0.10*	0.11 ± 0.04	0.11 ± 0.04	0.10	0.15 ± 0.04	0.16 ± 0.04	0.15	0.11 ± 0.04	0.14 ± 0.05
$Si/Si_\odot$	1.00*	0.85 ± 0.30	1.08 ± 0.24	1.00*	0.91 ± 0.29	0.95 ± 0.26	1.00*	0.87 ± 0.30	0.87 ± 0.29
$log\,(Q)$	-12.67	-12.69 ± 0.38	-12.45 ± 0.20	-12.67	-13.01 ± 0.29	-12.93 ± 0.25	-13.22	-13.03 ± 0.20	-13.15 ± 0.20

TABLE 4.3— Results of the procedure for three Galactic stars degraded to $R = 1000$ and $S/N = 100$. The results, summarized in this table, with the errors (*'Method'*) are compared with analyses performed (though with different observational data) by Repolust et al. (2004) (*R04*) and Urbaneja (2004) (*U04*). The column *'Method+H_α'* gives the values returned with the incorporation of H_α. The parameters marked with '*' were kept fixed by the authors during their studies.

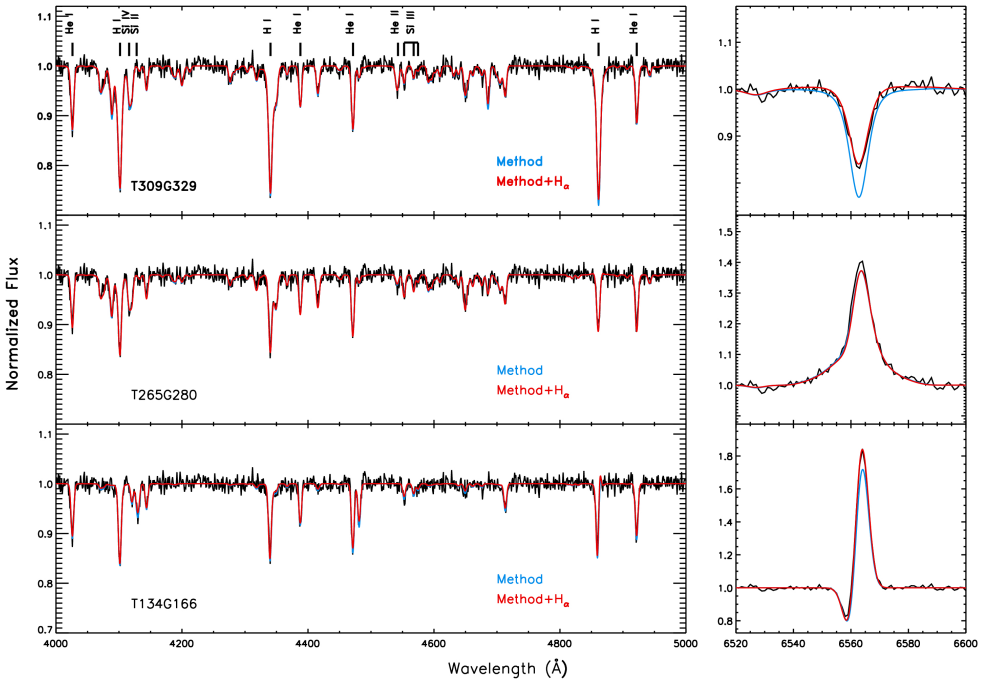

FIGURE 4.14— Synthetic spectra built for the χ^2-method test (black). The results presented in Tab. 4.2 using H_α (red) and leaving it out (blue) are displayed. The figure shows the optical range, $4000-5000$ Å and the H_α area. The match between the profiles is quite good in the $4000-5000$ Å range, the accuracy in the wind will be constrained by the available H_α information.

appreciable in the Fig. 4.14 we would like to remark that the method does not provide absurd result for any the objects.

Comparison to Galactic Stars

From the IACOB spectroscopic database (see section 3.5.1) we selected a sample of three Galactic stars, widely studied in the literature, for testing the method on real stars originally observed at high resolution and S/N. The objects were degraded to $R = 1000$, $S/N = 100$ and sampled them similarly to the NGC 55 spectra ($\sim 1\AA/pix$).

Table 4.3 shows the comparison between our results and the works by Repolust et al. (2004) and Urbaneja (2004). We have selected these studies because of similarities with ours. Both use FASTWIND as the source stellar code, although there are some differences with our work. For instance, Repolust et al. (2004) keep the microturbulence fixed to 10 kms^{-1}, considering it as a secondary parameter in their

study. HD 14818 was analysed by Urbaneja (2004) through a FASTWIND version that did not include line blanketing treatment, which explains the slightly higher temperature compared with this work.

The three stars analyzed are represented in Fig. 4.15, together with the models calculated using the parameters in Tab. 4.3. This second test also shows a good agreement between the values given by the low resolution method and previous studies at high resolution. There are important differences in $log(Q)$ for the three stars when H_α is not included in the analysis. Similarly to previous tests, inclusion of H_α results in a better estimation of the Q-parameter. The examples show as a variation in $\sim 0.1\ dex$ can introduce substantial changes in H_α. We must note that H_α profiles is also strongly dependent of effective temperature and surface gravity. Thus, changes in these variables modify its shape with the consequent modification of the best Q-parameter recovered. The errors in the stellar parameters will propagate to $log(Q)$ as well. The differences found for this transition with respect to the work by other authors on the same stars could be, mainly, due to the use of different observational campaigns (H_α is variable in this kind of stars, Markova et al. 2005) or differences inherited of employing different stellar code versions.

Similarly to the first tests, the match of the main lines used in the optical range ($4000 - 5000\ \AA$), marked in the figures, is excellent at this resolution. The differences produced when H_α is included are negligible for most parameters. The agreement with the profiles obtained using the parameters of other authors is also rather good, in spite of the stellar parameters differences gathered in Tab. 4.3. This fact hints to a degeneration of the stellar parameters, recovering almost similar profiles at low resolution. That should be kept in mind in any quantitative analysis, specially at low resolution.

Accuracy in $\mathrm{Si}/\mathrm{Si}_\odot$ *Determination*

The silicon abundance can be constrained using this initial procedure without a detailed analysis. The question is how truthful is this first value without an isolated silicon study. To check this, a straightforward test was implemented. Several models with different effective temperatures for the five silicon available abundances (see section 4.1) were degraded to a quality similar to the spectra analyzed before and the stellar parameters were recovered through the same technique.

A weak point of this test lies in the fact that the method does not need to interpolate between other stellar parameters since the model already exists in the grid and obviously the minimum χ^2 is given by itself. However, the test will allow us to estimate rapidly how accurate is the silicon estimation derived in this first step.

Figure 4.16 shows the ratio between the input abundances used in the model and those recovered by the χ^2-method. A first glance reveals that at low temperatures

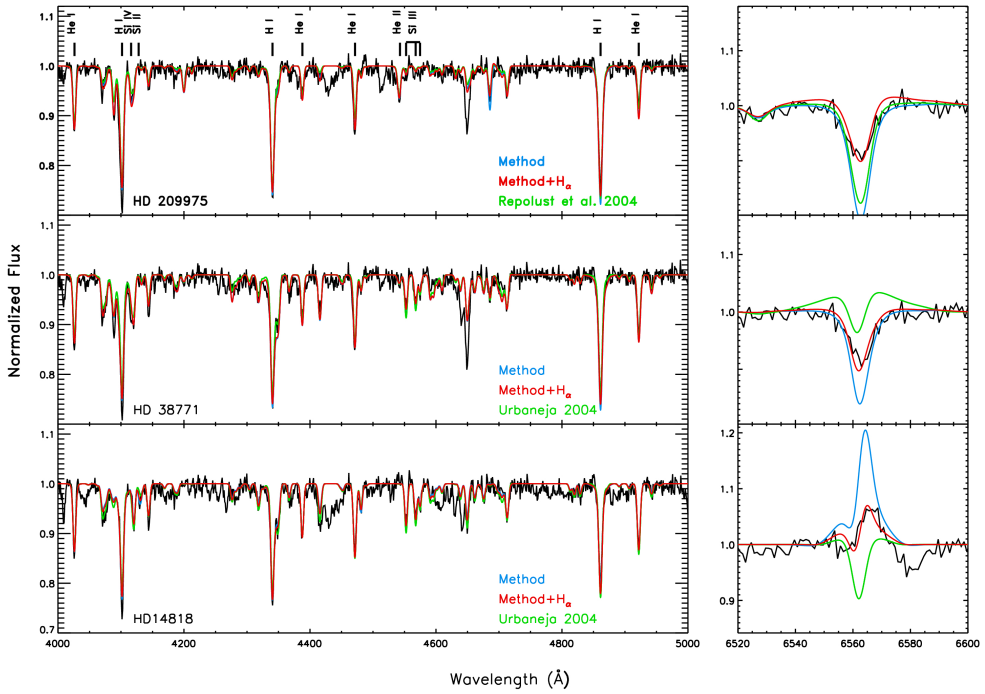

FIGURE 4.15— Test of the χ^2 method over three Galactic stars degraded to $R = 1000$ and $S/N = 100$ (black). The synthetic spectra obtained with H_α (red) and without it (blue) are plotted together with results suggested by other authors (green). As in Fig. 4.13, several features (not used in the analyses) are not well reproduced. Model atoms of carbon and nitrogen are not taken into account in this test, thus those transitions are not modeled plus the interstellar band at ~ 4450 Å, which does not belong to the stellar spectrum. The rest of features show a remarkable fit, again the correct wind parameter constraining will depend of the information kept in H_α.

and silicon abundances the method has difficulties. However, the errors always bracket the exact solution, without forgetting that a future detailed abundance analysis is recommended. At low temperatures (e. g. $\sim 10000 - 12000$ K) the Si III transitions have already faded (see section 3.4.1), and the chemical composition is only constrained by Si II $4128 - 4130$ Å. When we have a low silicon abundances recovering this parameter is a challenging task since Si II lines are weak and can be reproduced varying other input parameters. Moreover, these points are at the grid edge. Instead at higher temperatures a better estimation is obtained, because of Si III lines gain strength and the Si II/Si III ratios offer a better constraint.

Therefore, our first estimation has clear limitations in certain ranges of temperature, gravity and abundance, as shown in the figure. Nonetheless, this test brings us the certainty that the right value is within the error bars.

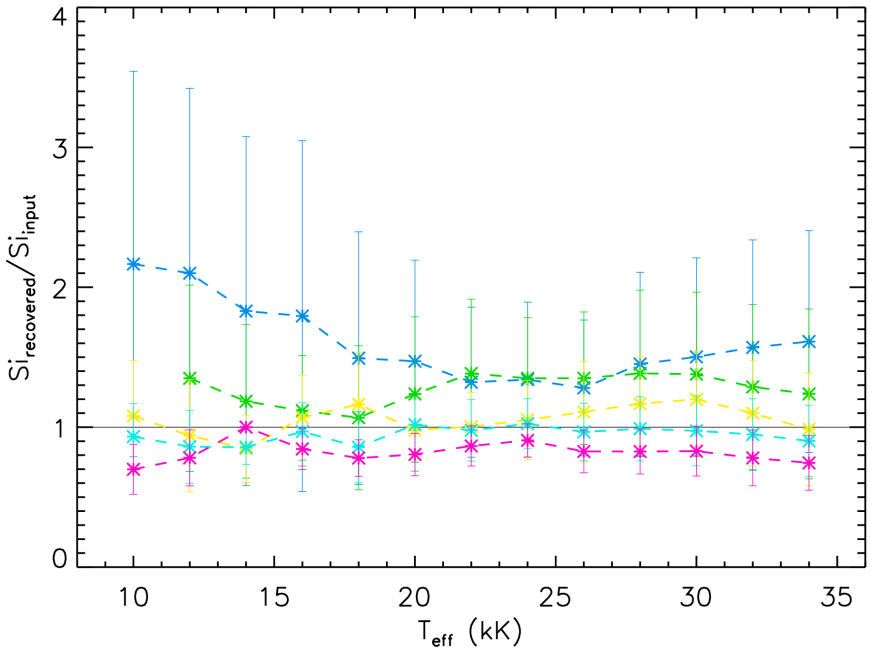

FIGURE 4.16— Check for the reliability of the silicon abundance first estimation obtained by χ^2-method. The technique was applied at different temperatures using the abundances available in the grid (marked in the plot with different colors). Results indicate that for very low silicon abundances and temperatures (where silicon lines are weak) deviation can be large, although still within the errors. The size of the error bars hint the inaccuracy in this parameter range.

Chemical Abundances

The chemical analysis, at this resolution, is not an easy task. The precision depends not only on the data quality but also on the atomic model accuracy and spectral type of the analyzed object.

Once the stellar parameters are defined, a new set of models is built for each star. The stellar parameters are fixed and different abundances are adopted in steps of 0.20 *dex*. This sub-grid is not only calculated for the best temperature and gravity, but also for the models at the edge of its error box, in order to estimate the uncertainties on the final abundance. This second analysis takes into account all the chemical species described in section 4.1.2.

Depending on the chemical element considered for the study, a particular set of lines were used to carry out the analysis, in a similar way to the work performed by Urbaneja et al. (2005a) and Evans et al. (2007). Briefly, the lines selected were:

Silicon		Carbon		Nitrogen		Oxygen		Magnesium	
Ion	$\lambda(\AA)$	**Ion**	$\lambda(\AA)$	**Ion**	$\lambda(\AA)$	**Ion**	$\lambda(\AA)$	**Ion**	$\lambda(\AA)$
Si IV	4116	C II	4267	N II	3995	O II	4076	Mg II	4481
Si III	4552	C II	3919	N II	5007	O II	4319		
Si III	4567	C II	3921	N II	5045	O II	4350		
Si III	4574					O II	4416		
Si II	4128					O II	4696		
Si II	4130								

TABLE 4.4— Selected lines for the chemical analysis at low-resolution spectra. The transitions chosen were taken from the optical wavelength range comprehended $\sim 3800-5100$ Å.

- **Silicon.-** The main transitions used were Si III $4552-4567-4574$ $\AA$, with Si II $4128-4130$ $\AA$ at low temperatures and Si IV 4116 $\AA$ at high temperatures. Bear in mind that transitions of Si II and Si IV, at this resolution, are blended with O II lines, so the latter must be included for reliable results.

- **Oxygen.-** Several O II transitions can be used. It has been already shown by Simon-Diaz (2005) that degree of accuracy in the oxygen atomic model varies from one multiplet to other, though at low resolution this lack of precision is less relevant. The analysis was based on the transitions around $4076-4319-4350-4416-4696$ $\AA$. At this resolution ($R = 1000$) they are, in fact, blends that must be handled with caution. For instance the line at 4076 $\AA$ can be overlapped with transitions of C II. Simón-Díaz et al. (2006) carried out a deep study about the reliability of the O II transitions for oxygen abundance analysis. However most of the transitions recommended by them are either too weak at this resolution and S/N or they are in the $4585-4680$ $\AA$ region, rich in transitions of other elements, blended at $R \sim 1000$. Nonetheless, the lines in this spectral window can be used as consistency check. Simón-Díaz et al. (2006)'s work was performed on dwarf stars and the lines that are reliable in this range of temperature and gravity do not necessarily behave correctly in the supergiant regime. A deeper study in this direction is recommended.

- **Nitrogen.-** The available wavelength range limits the number of useful N II transitions. Our study was centered on $3995-5007-5045$ $\AA$. Note that if nebular contamination is still present in the spectra, the O III 5007 $\AA$ transition will mask the correspondent nitrogen line. Around 4650 $\AA$ there are several important transitions of this element, but they are strongly blended and are only useful as a second criteria. At high temperatures, important N III lines are in

this region, though they are not correctly modeled, lacking correct dielectronic recombinations rates.

- **Carbon.-** Given the spectral quality and the wavelength range covered by our data ($\sim 4000 - 5000$ $\AA$) only the C II 4267 $\AA$ transition can be used. Notwithstanding, the modeling of this line has already been questioned in a previous study by Lennon et al. (2003) (see also references therein). Other lines are available at 3919 and 3921 $\AA$, however they are too weak in many cases. The transitions around 4650 $\AA$ can help, but in the same way as for oxygen and nitrogen, this part of the spectrum is strongly blended at this resolution. Nieva & Przybilla (2008) have developed a new updated carbon model for the stellar atmosphere code DETAIL which would be useful for a more trustworthy analysis of the C II 4267 $\AA$ transition, once it is adapted to FASTWIND's standards following a similar procedure as for the silicon atomic model described in chapter 3.

- **Magnesium.-** The abundance is based on the only line available in the wavelength range considered in our work, Mg II 4481 $\AA$.

A summary of the lines used in the chemical abundance analysis is gathered in Tab. 4.4.

The chemical analysis was carried out through two steps. Firstly, an automatic method was implemented by a χ^2 minimization technique but now centered on the line, listed in Tab. 4.4. Unfortunately, at low resolution and S/N the abundances of carbon and nitrogen are not reliable since the lines are weak. Therefore, a second step including a fine check made *by-eye* is performed. Of course, the automatic results for elements with strong and isolated lines, like silicon, are more reliable and straightforward.

Figure 4.17 shows an example of the first automatic step in HD 14818 for the silicon abundance, downgraded to $R = 1000$ resolution. For each one of the lines treated the method looks for the abundance that returns the minimum χ^2 between the models and the observed profiles. The final abundance is the result of averaging all lines included (if a transition produces an odd value compared with the mean by more than two sigmas, it is rejected).

Once this automatic estimations have been done, a set of three models with these abundances plus $\pm$ 0.20 *dex* is built. Through a final *by-eye* exploration we adjust the final values. Figure 4.18 illustrates this *by-eye* step on HD 14818, for which the analysis was focused on four different spectral ranges plotted in the figure. The best combination of elemental abundances (using the transitions commented before) was selected to reproduce the observed lines.

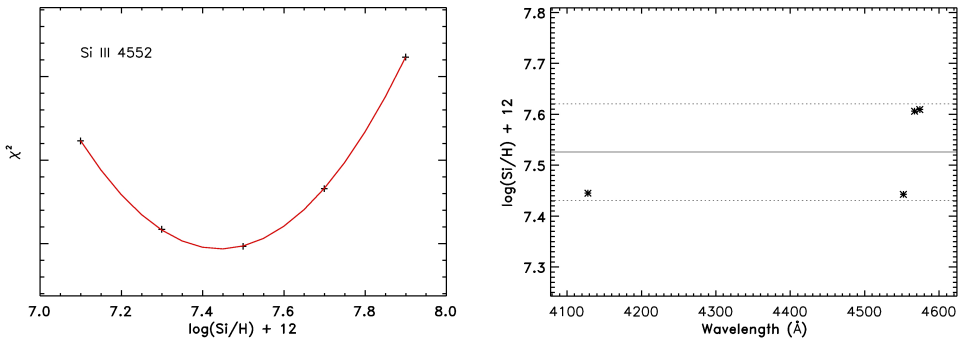

FIGURE 4.17— Example of the automatic chemical abundance procedure. The left chart shows the determination of the abundance by a minimization of the χ^2 distribution for the Si III 4552 $\AA$ profile. All the lines cited in the Tab. 4.4 go through this method. The final result for the silicon lines is plotted at the right side, where the mean value (solid line) and the standard deviation (dotted lines) are drawn.

Similarly to the stellar parameters, the spectral type affects the precision of the abundance analysis. For instance, in a star with effective temperature $\sim$ 12000 K some of the transitions considered before, like Si III, have disappeared or are too weak. Others, like Mg II, are stronger and can be used for an accurate abundance determination.

The HD 14818 final model is plotted over the observed data in Fig. 4.19. The good match between both shows the adequacy of the method even for the chemical analysis at this low resolution.

4.2.2 High Resolution: *Spectroscopy Synthesis Method + Curves of Growth*

The methodology described in the last section was focuses on low resolution spectra since it is aimed at our analysis in NGC 55 (see chapter 5), however it can be used as a powerful and faster way to perform a quantitative analysis at higher resolution too. Figure 4.8 offers a summary of the method. A detailed description is compiled now together with several examples, in a similar way to the previous sections. Following the same philosophy we are going to automatize as much as possible the quantitative analysis at higher resolution.

Stellar Parameters: How to Proceed...

Following the same scheme used at low resolution, a set of lines (Tab. 4.1) is compared with a model grid looking for the best match. Figure 4.20 displays an example of HD 31327 spectrum, identifying the transitions used for the study. The right-hand plot shows the H_β profile with the points used during the comparison with the stellar

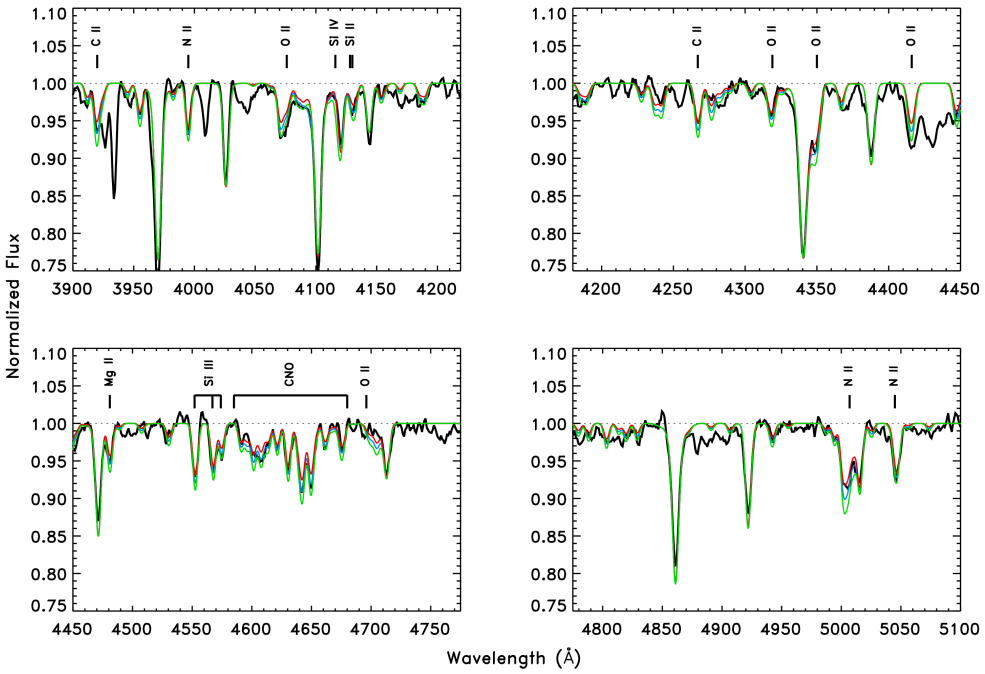

FIGURE 4.18— Visual chemical analysis for HD 14818 degraded to $R = 1000$ and $S/N = 100$. The study was performed on the transitions inside the four spectral ranges plotted in the figure. The best fit (blue) plus two models with the same parameters but with -0.20 (red) and $+0.2$ *dex* (green) in the abundances are displayed as well, together with the main transitions used. The area between $4585 - 4680$ *Å* is rich in transitions of carbon, nitrogen and oxygen (marked as *CNO* in the chart). Nonetheless, due to the low spectral resolution they were not used for the analysis but as consistency check. The spectrum reveals also several additional features that were not modeled, as the interstellar band at ~ 4440 *Å*

models (see below). A quick glance at Fig. 4.9 and Fig. 4.20 reveals the possibilities and accuracy that high resolution data provide. On the other hand, defects in the atomic models and in the atmosphere code that were negligible at low resolution become obvious. Now we are working with spectra of $R = 46000$ and $S/R \sim 150 - 300$.

At low-resolution it was possible to neglect the broadening caused by rotation or macroturbulence, since the instrumental profile dominates the profile shapes, but at $R = 46000$ this is no longer possible. Rotation and macroturbulence velocities were estimated through the Fourier transform technique described in Simón-Díaz & Herrero (2007) (and references therein). Once they are known synthetic profiles are convolved and compared with the observed spectra following the same χ^2-method described before.

Due to the large number of models in the grid, finding the best match can take

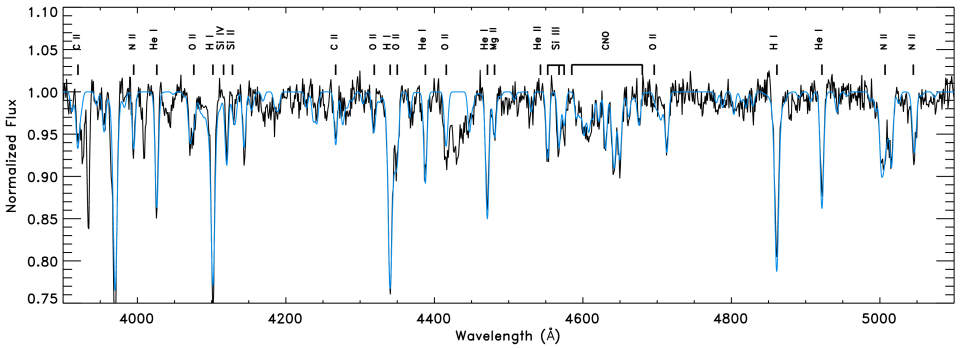

FIGURE 4.19— Spectrum of HD 14818 degraded to $R = 1000$ and $S/N = 100$ quality level (black) plus the best model obtained including all the chemical species used in the analysis (blue). All the main features employed in the stellar parameters and chemical analysis are marked.

several hours. This can be sped up in the same way as it was done at low resolution: if the spectral type is known, the study can be limited to a narrower temperature range; since a more accurate method is implemented for the microturbulence later, we can simplify the grid using only a discrete microturbulence grid, for instance $5-30$ values in steps of 5 $km\,s^{-1}$.

We are going to proceed with the quantitative analysis of HD 31327 as an example of the high resolution analysis.

The *'spectroscopy synthesis method'* described in the previous section was used as first step. Thus, a match with the grid was performed following Eq. 4.10. As in the low resolution case, the systematic errors associated with the continuum location were estimated using a Monte Carlo simulation. The final χ^2 patterns and the distribution recovered for each parameter using the Monte Carlo simulation are plotted in Fig. 4.21.

A comparison with the result of HD 14818 (see Fig. 4.12) reveals how at low resolution and $S/N = 100$ the errors derived from the grid (blue dashed lines) and the dispersion in the Monte Carlo simulation are of the same order for all parameters. In the analysis displayed in Fig. 4.21 (though in a different object) the error in some of the parameters are dominated by the grid limitation ($\sigma_{15\%}$ in Eq. 4.11) instead of the ones derived from the Monte Carlo (for instance, for the microturbulence). At high S/N the grid begins to be a bit coarse if high accuracy is desired. The deviations in parameters like the temperature and gravity are slightly reduced because of the improved data. Nonetheless, the grid still imposes the limit for parameters like microturbulence and helium abundance. This is not surprising since the helium, for instance, is limited to just four values (see Sec. 4.1).

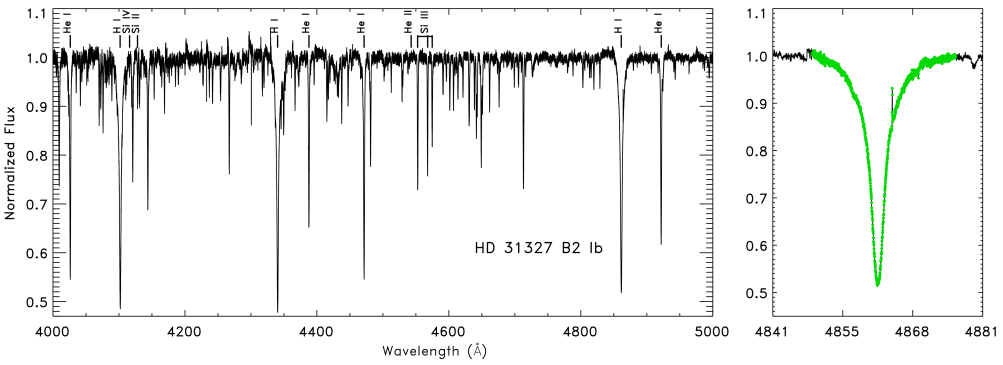

FIGURE 4.20— An example of a B-type supergiant, HD 31327 (B2 Ib), is shown. In the left the optical 4000 – 5000 $\AA$ region is plotted together with the main lines used for the analysis (see Tab. 4.1). The right-hand plot displays the points in H_β used for the *spectroscopy synthesis method* (see text for more details). Albeit H_α is not shown in the plot, it is available for the analysis.

This technique already produces stellar parameters that, depending of the accuracy desired, could be sufficient, even without a more detailed analysis of the ionization balances available in the spectra. Before proceeding with the analysis through a standard methodology (e. g. McErlean et al. 1999) it is possible to refine the results building a sub-grid around the values. Thus, a more accurate estimation of the mass loss rate can be obtained before proceeding with the temperature and gravity analysis.

Some authors have shown that the impact of parameters like the microturbulence on the ionization balance ratios (main temperature indicators) are small (Villamariz & Herrero 2000; Urbaneja 2004), but the role of the wind is not fully negligible. When it is strong enough, it affects the silicon and, mainly, the helium ionization balances. Starting from a reliable set of initial stellar parameters makes the final analysis easier and avoids undesired systematic effects.

The effective temperature will be estimated from the ionization balance between different ions of the same element present in the spectrum. In massive blue stars the main diagnostics are silicon or helium ions. Thus, in the O-type stars domain the temperature is fitted with He II/He I ratio. Around B0-type the ratio between Si IV/Si III is also available, while when temperature decreases the Si III/Si II balance provides the main reference. In late B-type stars only Si II remains and the silicon ionization balance cannot be used. In A-type stars an alternative way comes from the Balmer jump or the magnesium ionization balance (Kudritzki et al. 2008; Urbaneja et al. 2008).

The surface gravity will be constrained by the Balmer lines wings. A large gravity also implies a large density, which favors Stark broadening of Balmer lines. McErlean et al. (1999) showed that the the gravity determination is unaffected

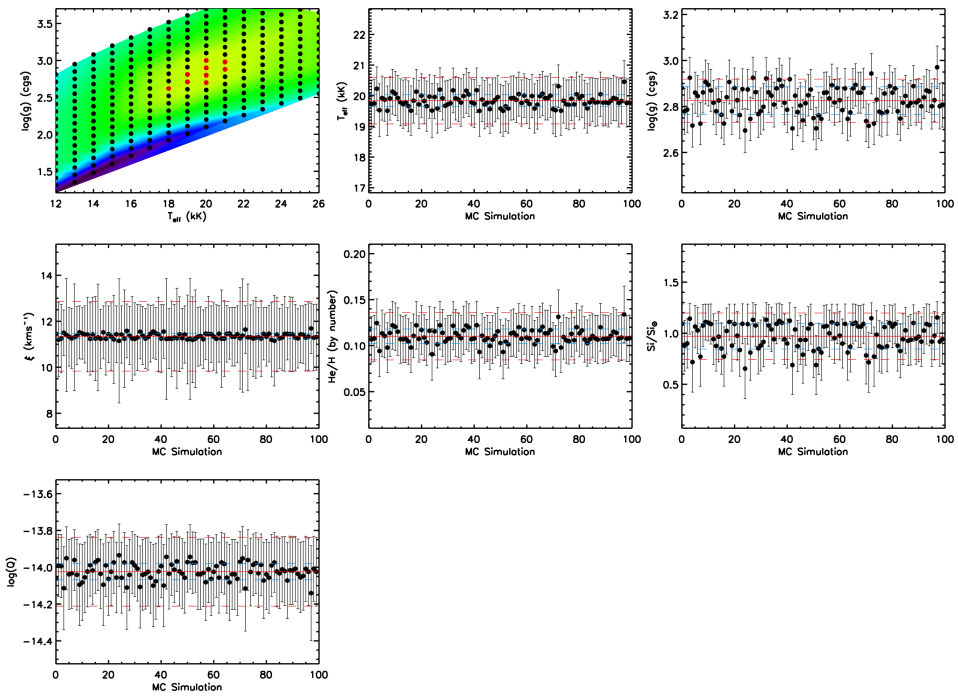

FIGURE 4.21— χ^2 distribution for HD 31327 together with the Monte Carlo (MC) simulations for each stellar parameters and iteration. See Fig. 4.12 for a full description of the figure.

by microturbulence. On the contrary, the stellar wind can strongly affect the gravity determination. It must be remembered that strong variations in metallicity, microturbulence or in the wind parameters could alter the stellar atmosphere, changing the temperature and density structure as well. Hence, the starting values for the stellar parameters provided by the previous step are fundamental.

To carry out the second step in the quantitative analysis a sub-grid was created, with nine temperatures and nine gravities around the values provides from the χ^2-method. The steps followed during the analysis of HD 31327 are described in detail:

- **Balmer Wings.-** The gravity was determined as a function of H_γ and H_δ wings. For each effective temperature, a match between the Balmer wings and synthetic models with different gravities was made. An optimum gravity was calculated per temperature following a χ^2-minimum scheme. According to spectral S/N the continuum was shifted and the χ^2 distribution was re-calculated. The differences give us an estimation of the error in surface gravity. Figure 4.22 illustrates this procedure using the wings of H_γ for HD 31327. Only wavelengths

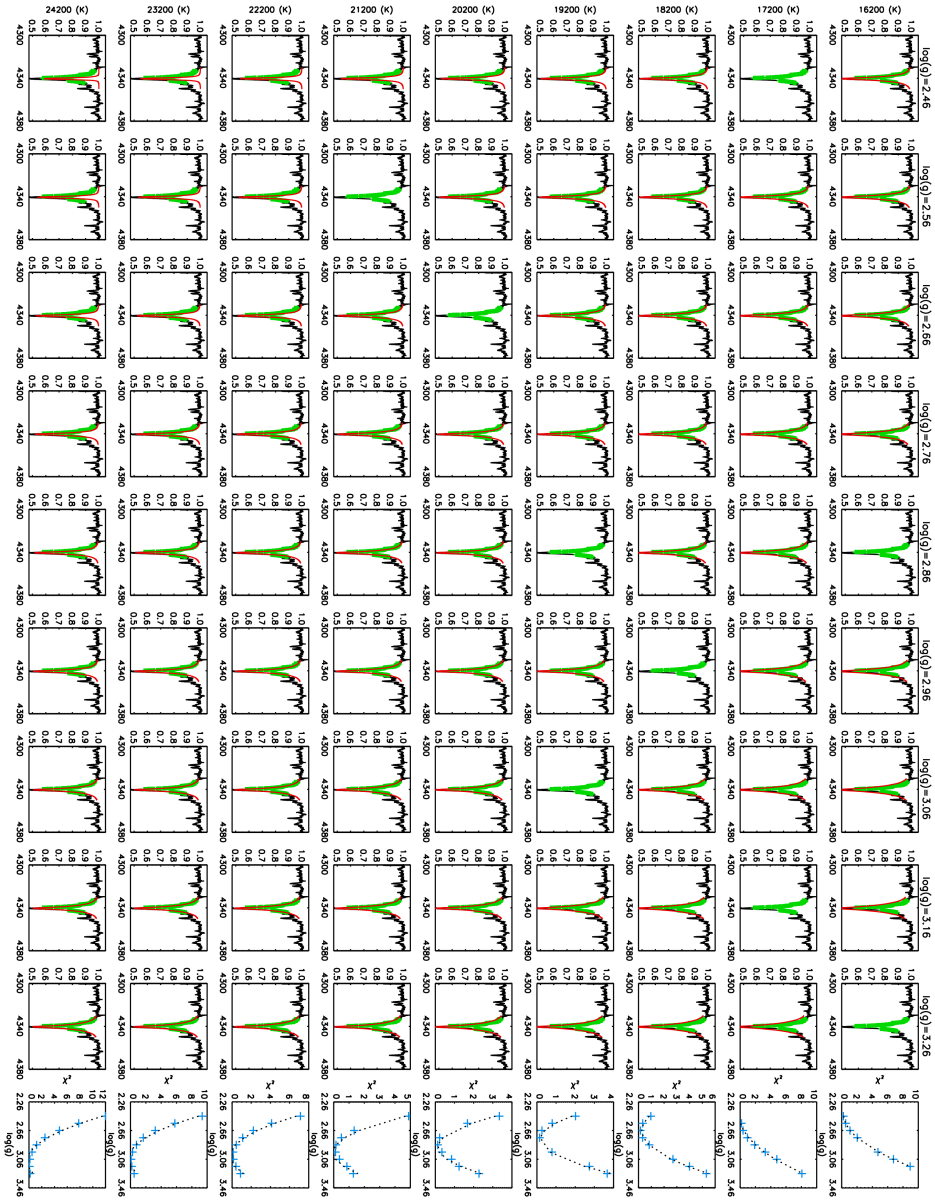

FIGURE 4.22— The wings of H_γ (green dots), avoiding blends, are compared to the sub-grid models created for the analysis (red profiles). Those cases for which no synthetic profile is drawn correspond to models that did not fulfill the convergence criteria. For each temperature the gravity that provides the minimum χ^2 in the Balmer wings is calculated and its error is estimated according to S/N. The χ^2 distribution (blue crosses) is plotted in the rightest column of the figure per temperature.

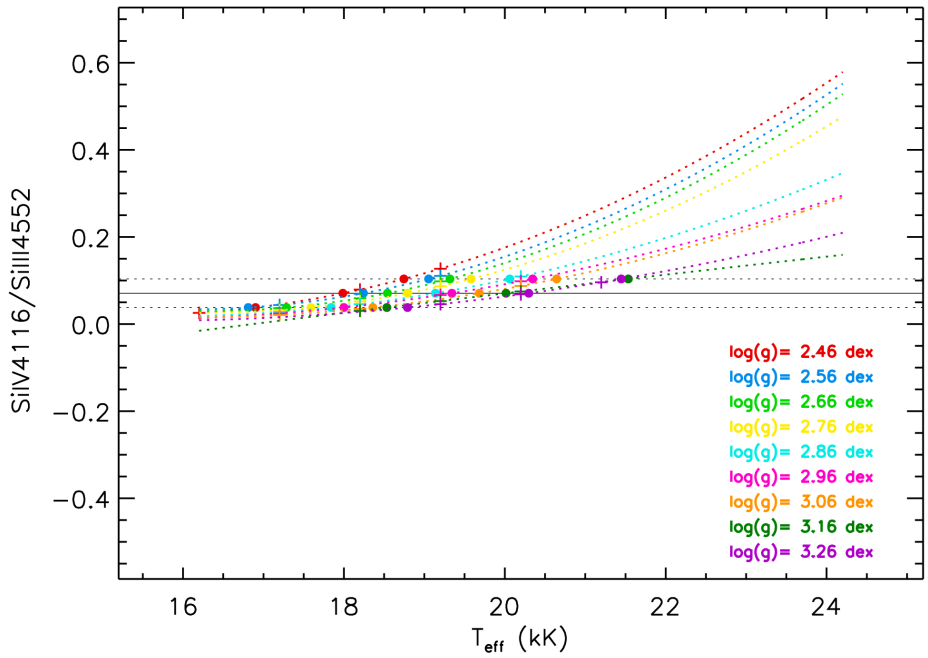

FIGURE 4.23— The observed ratio of Si IV4116/Si II4552 (solid black line) and its error (dotted black lines) are compared with synthetic values. Each one of the nine gravities, represented by crosses of different colors (see figure for color codification), gives an optimum effective temperature (for each gravity) with the corresponding error. The crossing of the polynomial regressions (dotted color lines) and the observed equivalent width and its errors are marked by filled color circles.

in the wings are compared with the models (red profiles). Those charts that do not show synthetic profiles correspond to models that do not fulfill the FASTWIND convergence criteria. Points that deviate significantly from the rest of the points are erased from the minimum χ^2 determination.

- **Ionization Balance.-** The new sub-grid gives the ionization balance for all the equivalent width ratios available. A direct comparison with observations together with their errors provides the best temperature for each gravity. Figure 4.23 displays the Si IV4116 / Si III4552 ratio in HD 31327.

  Firstly it is required to obtain the equivalent width of the lines involved. That was made by fitting a gaussian to the observed profiles by means of nonlinear least square method (a good approximation for metallic transitions). When they were blended, a gaussian for each of the components was used. The S/N determines the uncertainties following the work of Villamariz (2000).

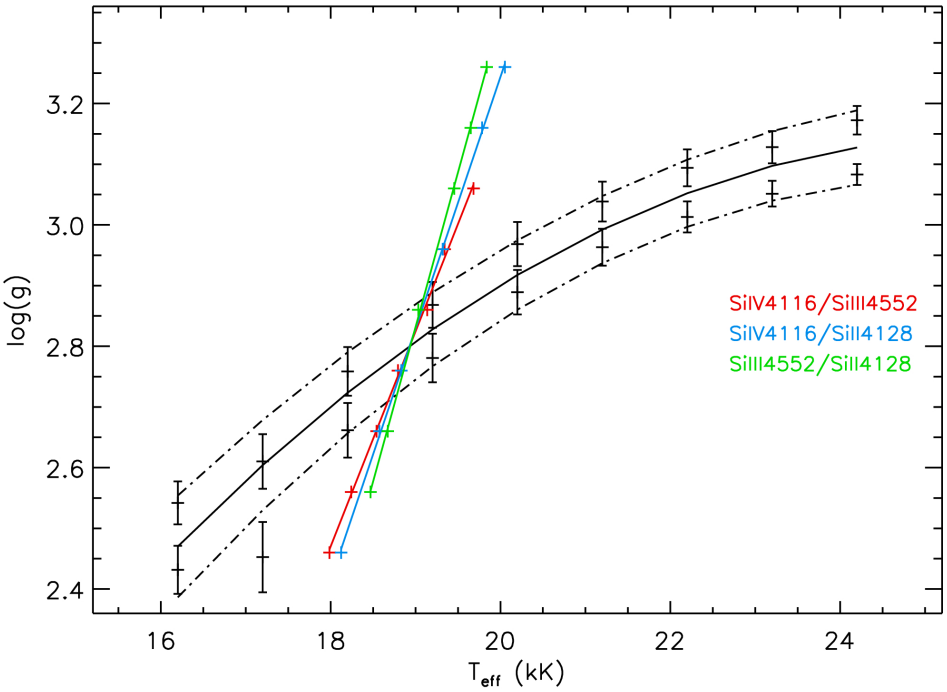

FIGURE 4.24— The trends obtained from the Balmer wings and the ones provided by the ionization balance (in this case from silicon transitions) are plotted together, looking for the intersection between them that gives the best $T_{eff} - log\,(g)$ for HD 31327. For this star three silicon ratios are available (marked in the plot with different colors). This example shows a remarkable consistent match between the three ratios drawn. The gravity was calculated according to H_γ and H_δ (dashed black lines) and the average relationship was used (solid black line).

- **T$_{eff}$–$log\,(g)$.-** Finally the trends from the last two steps are merged, searching for the pair $T_{eff} - log\,(g)$ that better reproduces the observed spectral features described before.

  In Fig. 4.24 both relationships, obtained in the previous steps, are fitted for HD 31327. In this particular example there are measurements of Si IV 4116 $\AA$, Si III 4552 $\AA$ and Si II 4128 $\AA$. Their ratios are drawn in the figure following the color codification described in it.

  The intersection of the best fit for each balance ratio with the average $T_{eff} - log\,(g)$ relationship derived from the Balmer line wings, H_γ and H_δ (solid black lines in Fig. 4.24) gives the best $T_{eff} - log\,(g)$ pair. The differences between the ratios (not in this particular example where the match is quite good) can be attributed to problems with the atomic models implemented, as it was already

commented in section 3.5.2.

It is possible to do a last iteration with the Q-parameter to get the best fit for H_α and the new $T_{eff} - log\,(g)$ set by introducing a refinement in the mass loss rate according to possible changes in temperature and gravity. If there is a difference larger than $0.2\ dex$ between the final $log\,(Q)$ and the initial estimation, the temperature and gravity should be re-calculated to avoid any systematic dependence with the stellar wind.

Stellar Parameters: Tests

With the goal of testing the methodology for the quantitative analysis at high resolution, the technique was applied to four Galactic stars from the IACOB database. The stellar parameters recover by our method and the values obtained in previous studies are compiled in Tab. 4.5. Figure 4.25 shows the best match between the observed spectra and the simulation obtained. We have only compared with one of the studies performed on these objects, a detailed summary of the most recent quantitative studies on them can be consulted in Tab. 3.3.

The figure displays a good match in the main lines used in the analysis (marked in the plot). The differences observed in the optical range between 4000 and 5000 $\AA$ are small, mainly within the S/N. Looking in detail the spectra, the model derived for HD 14818 shows certain issues, lacking a good match around Si II $4128 - 14130\ \AA$. During the test of the new silicon atomic model in chapter 3 we already pointed out these problems for this star. However, they were not found in HD 31327, which shows a remarkable fit.

The result obtained in HD 204172 does not give a good match of the Si III 4552 triplet, the strengths of the silicon lines are too weak. This problem is solved during the subsequent detailed chemical analysis (see below). This star was used to test the silicon atomic model in section 3.5. The result obtained there reproduces correctly the silicon transitions (see Fig. 3.25) after a detailed analysis.

The synthetic profiles derived by our method for H_α are well reproduced for the three stars analyzed. In spite of the issues commented for HD 14818, our technique is able to match approximately the observed H_α P-cygni profile.

The process was carried out automatically so far, once the lines required for the analysis and the wavelength range for the comparison with the grid were established. The agreement found for these stars hints to the strong possibilities of analyzing large samples with minimum human effort in a short period of time, and obtaining accurate results.

Chemical Abundances

Once the stellar parameters are defined, the chemical abundances plus the microturbulence are the last magnitudes in the stellar atmosphere characterization. Due to the

	HD 209975		HD 204172		HD 31327		HD 14818	
	R04	HR Method	S08	HR Method	M99	HR Method	U04	HR Method
$T_{eff}\ (k)$	32000	32291±566	28500	30059±840	21500	18951±809	20100	19932±1007
$log\,(g)\ (cgs)$	3.20	3.41±0.06	3.13	3.25±0.03	2.90	2.81±0.08	2.40	2.52±0.08
$v_{micro}\ (km\,s^{-1})$	10.0*	17.0±2.40	15.0*	16.4±4.10	15	11.3±2.00	17.0	17.6±3.00
He/H	0.10*	0.10±0.03	0.20*	0.08±0.03	–	0.11±0.03	0.15	0.09±0.03
$Si/Si_{\odot}$	1.00*	1.04±0.26	1.00*	0.69±0.25	–	0.97±0.26	1.00*	0.64±0.27
$log\,(Q)$	−12.67	-12.52±0.08	–	-12.60±0.08	–	-13.74±0.23	−13.22	-13.18±0.05

TABLE 4.5— The technique developed for quantitative analyses at high resolution was tested on four Galactic stars. The results recovered are summarized under the label *'HR Method'*. The stellar parameters were compared with previous studies of these objects: Searle et al. (2008) (S08), McErlean et al. (1999) (M99), Urbaneja (2004) (U04) and Repolust et al. (2004) (R04). HD 14818 has been analyzed by several authors. A detailed summary is listed in Tab. 3.3. The parameters marked with '*' were fixed by the authors.

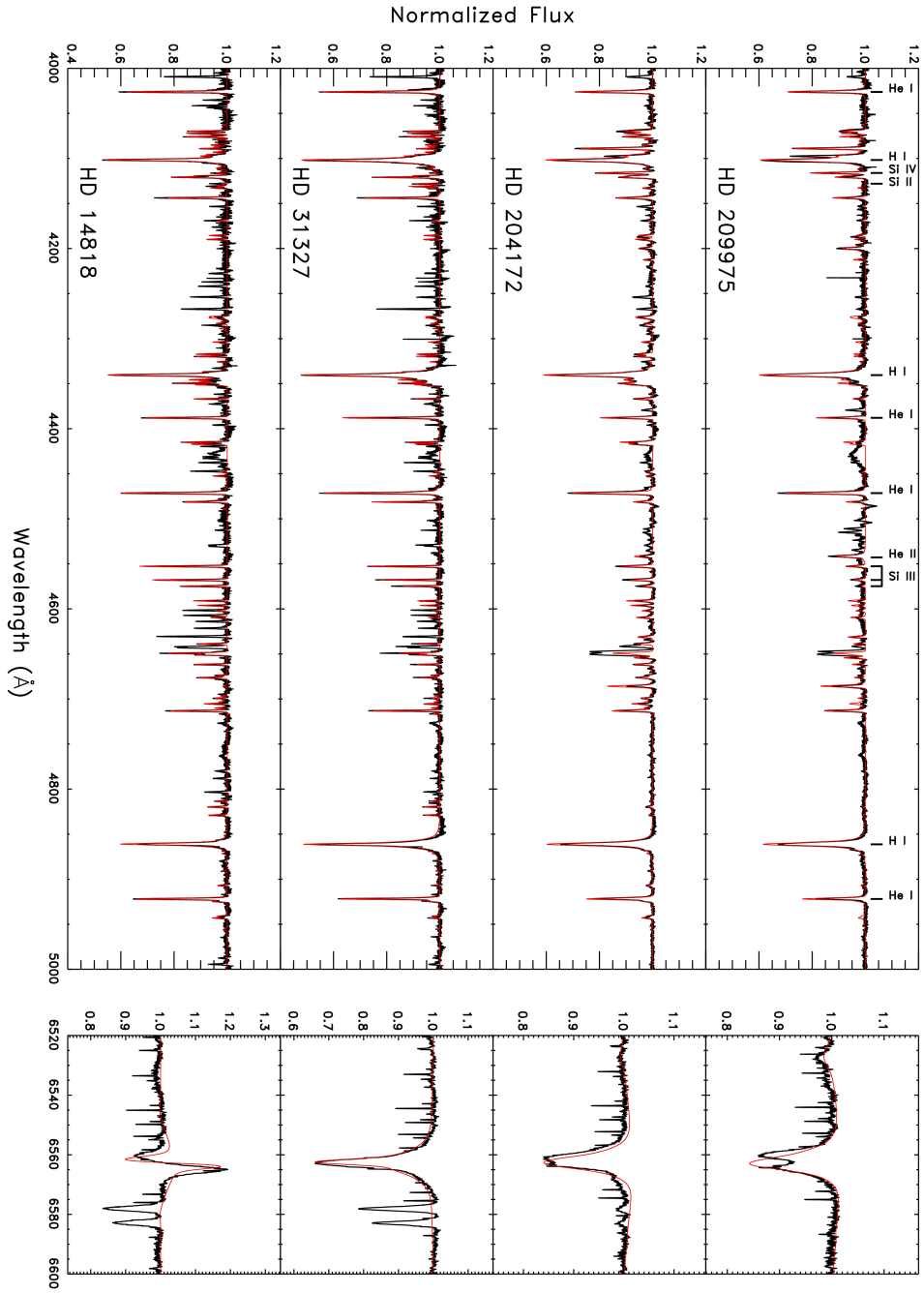

FIGURE 4.25— Comparison between the four Galactic stars analyzed with our methodology for high resolution data (black) together with synthetic spectra generated by the stellar parameters derived by us. The match of the model is rather good for the features used in the analysis (marked in the plot). The technique also recovers with certain accuracy the H_α profiles.

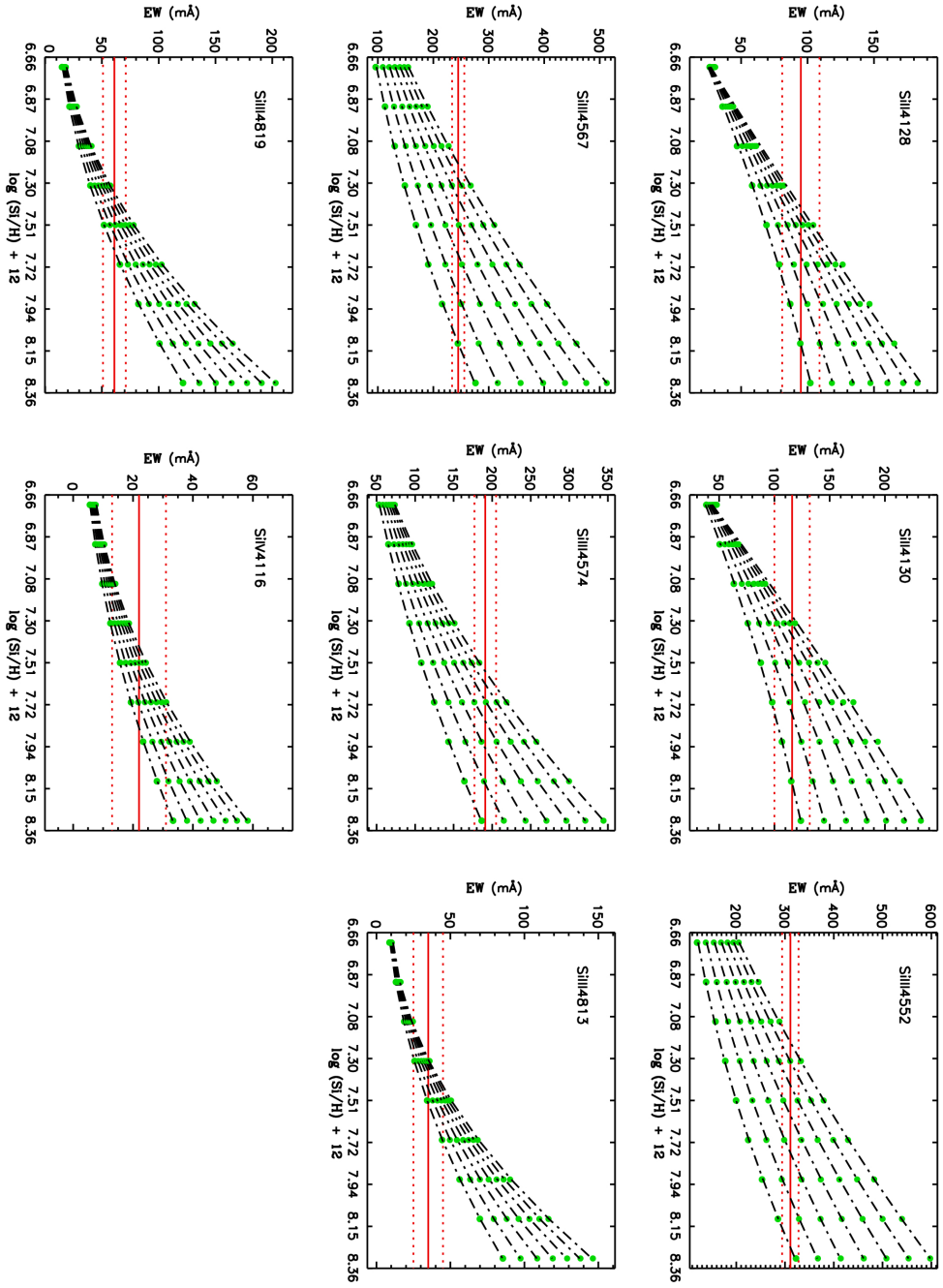

FIGURE 4.26— First step in the abundance-microturbulence analysis. We are looking for the abundance that reproduces the observed EW plus its errors (solid red lines and dotted red lines respectively) line by line. This example corresponds to silicon abundance analysis of HD 31327. The synthetic EW are represented by green dots for the seven microturbulences considered (dotted-dashed black lines).

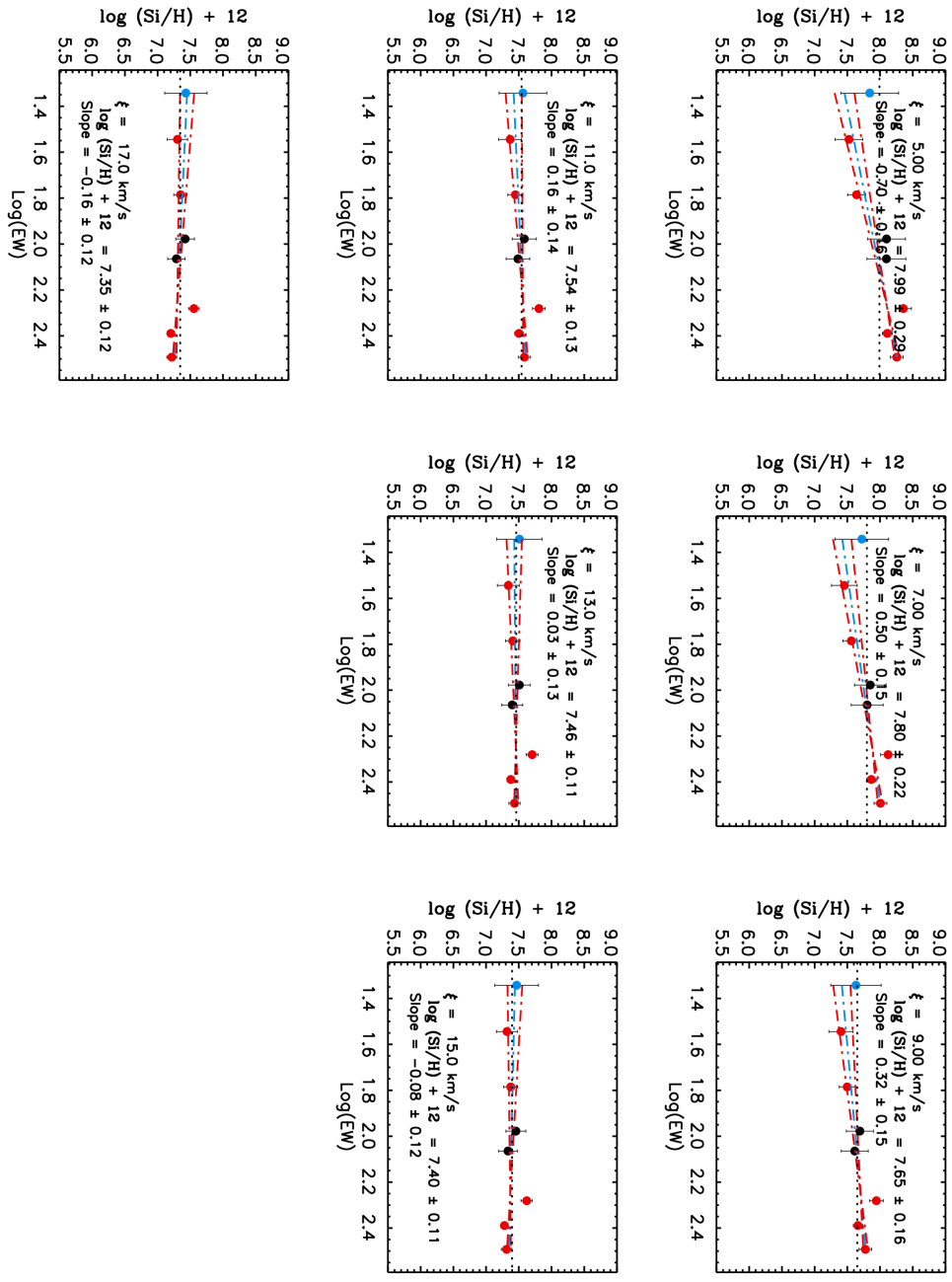

FIGURE 4.27— Once the abundance is determined for each line and microtubulence as it was shown in Fig. 4.26, the mean abundance (dotted black line) and the slope of the best fit together with their errors (dashed blue and red line respectively) are stored for each microturbulence. The silicon ions represented in the plot are coded with different colors (Si II, black; Si III, red; Si IV, blue). In this example the three silicon ionization stages show a fair behaviour with the microturbulence (ξ).

role played by the microturbulence in the line formation (a parameter imposed *ad doc* artificially to reproduce weak and strong lines at the same time) it must be taken as a free variable in the chemical analysis.

This abundance-microturbulence analysis is based on the *'curve of growth'* method (Gray 1976). Using the best set of parameters calculated so far in the analysis a new grid of models is built for each star, now with the chemical abundances and the microturbulence velocity as the only free parameters. In total, we used nine different abundances in steps of 0.20 dex and seven values of the microturbulence, centered on the best estimations from the previous steps.

The method was implemented by Urbaneja (2004) in three main steps plus one more for the individual analysis line by line. Briefly, the method follows the next strategy:

- For each of the lines and microturbulence velocities considered, the abundances that best reproduce the observed equivalent widths (EW) are calculated together with their errors, derived from the uncertainties in the EW. Figure 4.26 displays this first step in the silicon abundance determination for HD 31327. Initially all the silicon lines that are strong enough to be measured are included. Later, those that show an odd behavior are discarded.

- Using the values obtained in the first step, the slope of the EW–abundance relationship and the mean abundance of the best fit is calculated for each microturbulence (see Fig. 4.27). Those transitions with abundances far from the regular trend defined by the majority are rejected, probably due to a bad EW measurement or the lack of accuracy in the atomic model. With some exceptions, like Si IV 4089 $\AA$ that blends with O II, the trend is smoothly followed by the three ionization states (in this example).

- In first approximation, all the silicon transitions shall give the same abundance. Thus, we look for the microturbulence that returns the zero slope in the best fit assessed in the second step. Once this velocity is fixed, the relationship between the mean abundance and the microturbulence derived in the second step is used to obtain the final abundance. Figure 4.28 shows this last step in HD 31327.

Instead of using the average abundance of the lines considered, it is possible to derive it for each individual transition, using the microturbulence from the previous steps as reference. This allows the detections of possible issues with some of the lines included. Figure 4.29 displays the abundance as a function of the microturbulence line by line in HD 31327. This star shows a common behavior for all considered lines, only Si III 4574 $\AA$ deviates from the regular trend. This fair match is not always found, as it

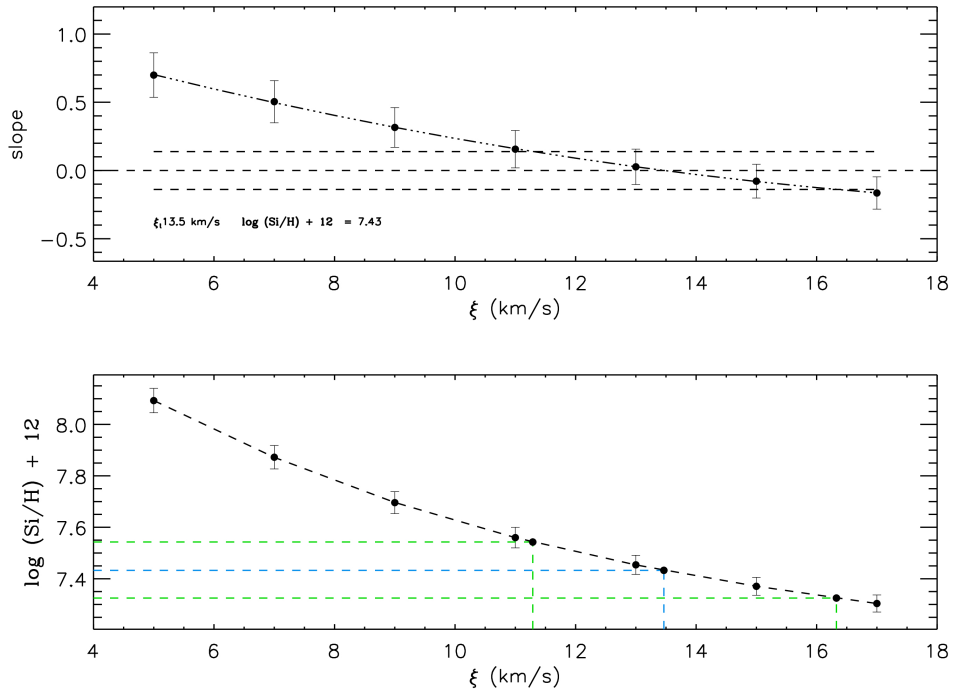

FIGURE 4.28— Eventually the microturbulence with a zero slope is calculated (top panel), given the pair abundance-microtubulence (bottom panel) together with their errors (blue and green dotted lines respectively).

is shown in section 3.5.2, where some stars display a larger scatter in the abundances derived line by line.

When the final microturbulence or silicon abundance differ in more than 5 kms^{-1} and 0.2 *dex*, respectively, from the ones used in the previous steps of the analysis, the determination of the temperature and gravity should be repeated.

4.2.3 Issues in the Quantitative Analysis

The methods presented in this chapter can constraint well enough the main stellar atmosphere parameters with errors according to the spectral quality. Nonetheless the method contains several caveats that must be taken into account. Some of the limitations are intrinsic to the technique, that bases the analysis on a fixed grid. Others, instead, are due to the atomic and stellar models used for calculation. Lefever et al. (2007) already noted some of these limitations in their work. The lower resolution of our spectra adds some extra difficulties. They can be summarized as follows:

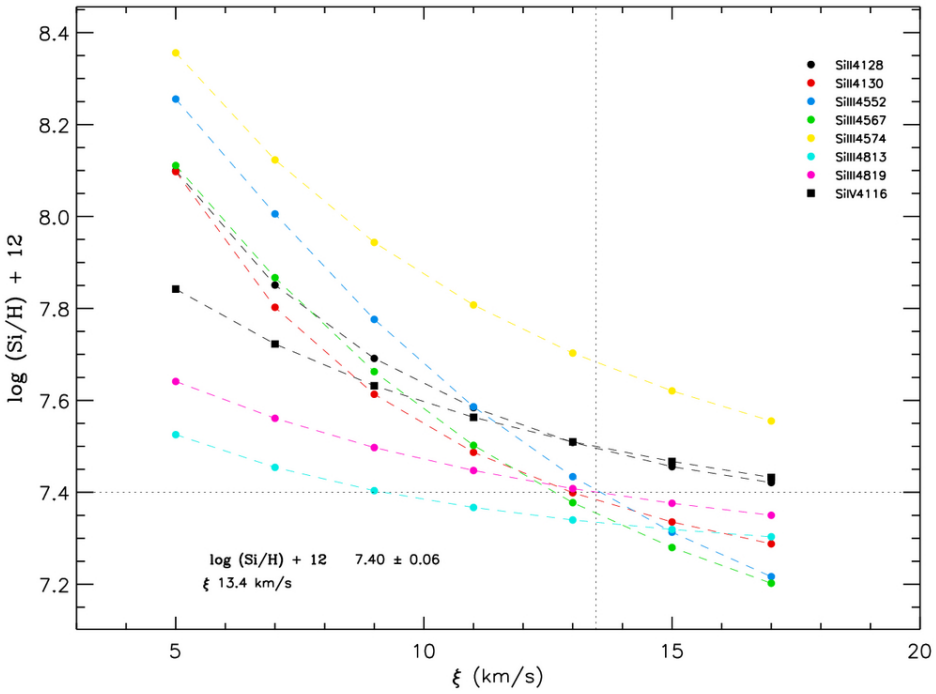

FIGURE 4.29— Silicon abundances line by line in HD 31327. This example shows a nice match between the different trends, only Si III 4574 Å displays differences from the common behavior.

- **Limitations inherited from the atmosphere code and atomic model:** the stellar and atomic models stand on certain approximations and some transitions will be better treated than others (see chapter 2 and 3). This results in areas of the parameter space where uncertainties can be larger.

- **The grid is based on a discreet set of points in the stellar parameters space**, then the parameters derived and their errors are the product of a interpolation between the points available in the parameters mesh. The method cannot extrapolate out of this space of variables. Any result at the edge of the grid can not be trusted, and a new grid around these values should be generated.

- **Lack of H_α.** It is impossible to give an accuracy estimation for the wind parameters without H_α and when there are no signs in H_β (if only the optical spectral range is available). The tests can only suggest an estimation of $log\,(Q)$, based on the rest of the Balmer lines. The incorporation of H_α in the analyses brings a more trustful result for the stellar wind, with a minor impact on the other

stellar parameters. The wind law used in the grid does not take into account any kind of clumping treatment.

- **Spectral type dependence of the results.** Since metallicity is determined from the transitions of silicon available, when these lines are not present or are too weak the value must be taken as an estimate. In a similar way, this affects the temperature: without silicon lines the stellar parameters are fixed chiefly from hydrogen and helium lines only, and the constraints the temperature will be looser.

- **Low resolution.** Data with low resolution ($R \sim 1000-2000$) show degeneration among the stellar parameters. Different combinations of microturbulence, helium and silicon abundances can produce the same profiles, increasing the uncertainties. In fact, this limitation is present in any quantitative analysis, but it is attenuated with high S/N data.

- **Chemical analysis.** The option of handling it with an automatic technique is limited at low S/N. However, a first estimation can be performed and it can be completed with a visual inspection.

In spite of all these drawbacks, the different tests indicate that the method is reliable and errors can be properly estimated, resulting in standard values (see for instance Figs. 4.15, 4.14 and 4.25 at high resolution analysis). The accuracy is therefore as good as spectral fitting *'by-eye'*, with the clear advantage of using a systematic and mostly repeatable method; a great improvement in the analysis of large samples.

4.2.4 High Resolution versus Low Resolution

A comparison between the results obtained at low and high resolution with several analyses compiled from the literature is mandatory. We have performed such a comparison for HD 14818 which has been used as a reference in the tests at low and high resolution in this work (see sections 4.2.1 and 4.2.2). From the literature we have chosen the quantitative studies developed by Kudritzki et al. (1999) (K99), Urbaneja (2004) (U04), Crowther et al. (2006) (C06) and Searle et al. (2008) (S08). That comparison with other authors must be carried out with caution, since they are based on different stellar codes, or older FASTWIND versions, as in the Urbaneja (2004) case. As we mentioned above, the differences in the Q-parameter obtained could also be attributed to different observational campaigns and the well-known H_α variability or differences in the stellar codes. Table 4.6 collects the stellar parameters of the different tests performed so far and compares then with the values from these

	HD 14818					
	S08	C06	U04	K99	Low-Resolution	High-Resolution
T_{eff} (k)	18000	18500	20100	20000	18905 ± 1290	19932±1007
$log(g)$ (cgs)	2.38	2.40	2.40	2.40	2.45 ± 0.14	2.52±0.08
v_{micro} (kms^{-1})	15	20	17	–	13.9 ± 3.7	17.6±3.00
He/H	0.20*	0.20*	0.15	0.10*	0.14 ± 0.05	0.09±0.03
$Si/Si_{\odot}$	1.00*	1.00*	0.87	1.00*	0.87 ± 0.29	0.64±0.27
$log(Q)$	-12.76	-12.88	−13.22	-13.31	-13.15 ± 0.20	-13.18±0.05
Stellar code	CMFGEN	CMFGEN	FW V8.0	FW V2.0	FW V9.0	FW V9.0

TABLE 4.6— Comparison of the stellar parameters derived using the methods described in this chapter for the Galactic star HD 14818 with those obtained by other authors: Searle et al. (2008) (S08), Crowther et al. (2006) (C06), Urbaneja (2004) (U04) and Kudritzki et al. (1999) (K99). They use different stellar codes, atomic models, etc. which accounts for part of the differences. The table also illustrates the stellar code employed and the version in the case of FASTWIND (FW). The parameters marked with '*' were fixed by the authors.

authors. The computing time of codes like CMFGEN forces to fix certain parameters (marked with '*' in Tab. 4.6) during the analysis.

The stellar parameters derived in our work are in good agreement, within the uncertainties, with the values suggested by other authors, in spite the heterogeneity of quantitative analyses. Note that the studies performed by Urbaneja (2004) and Kudritzki et al. (1999) (the latter based on the previous work by McErlean et al. 1999) did not include a blanketing treatment in the stellar atmosphere structure, which explains the slightly higher temperatures compared with our results. On the other hand, the values derived by Searle et al. (2008) and Crowther et al. (2006) predict lower temperatures. Both are based on the stellar code CMFGEN, with the restrictions already discussed (see section 2.2). Changes up to $1000 - 2000$ K are found between different stellar codes and can be traced back to differences in the codes.

Although compatible, the results obtained at high and low resolution show some differences in some of the stellar parameters. These are explained by the techniques used and the lost of information when resolution is degraded. Nevertheless, both solutions provide a good fit to the observed spectrum

4.2.5 Completing the Fundamental Parameters: Radius, Luminosity and Mass

The rest of physical properties of a star, like radius, luminosity or mass, can be determined once the stellar parameters are known, together with the apparent photometric magnitude and its distance. In addition, we will have to determine the reddening from our theoretical spectrum.

The distance is the most difficult parameter that has to be obtained. The basic way for its determination relies on trigonometric parallaxes, but they are limited in the distance covered by the projects developed so far. The Hipparcos mission (ESA 1997) is the most successful project in this field. The future mission Gaia (Perryman et al.

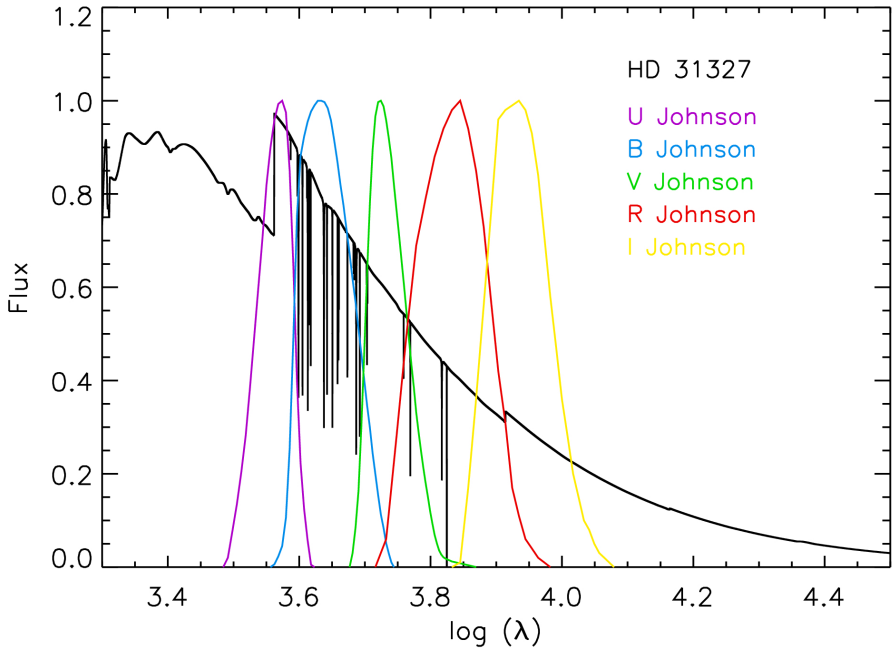

FIGURE 4.30— Flux distribution for HD 31327 according to the stellar parameters derived in previous sections. The function profile (E_λ) used for the Johnson photometry system are also drawn in different colors. The flux was normalized to clarify the comparison.

2001) will be fundamental for getting better estimations. Nonetheless, remote objects in our Galaxy are still affected by a lack of accuracy, which translates to the physical parameters. In other galaxies the relative error in the distance, usually measured by Cepheids or similar variable objects, is smaller, though the error in the zero point (LMC distance) is still present.

The stellar atmosphere model provides the emitted stellar flux (F_λ). This information can be used to obtain the magnitudes (m_λ) of the star by:

$$m_\lambda = -2.5\,log\left(\frac{1}{d^2}\int_0^\infty R_*^2 F_\lambda E_\lambda d\lambda\right) + const. \tag{4.12}$$

where d is the distance to the star and E_λ the transmission function of the filter used. Figure 4.30 shows the mock flux emitted by HD 31327 according to the stellar parameters determined previously in this chapter. The transmission functions for the standard Johnson filters system are also displayed.

The observed magnitude must be corrected due to interactions with the interstellar

medium. Thus, part of the radiation will be altered and reddened. This extinction effect produces a color excess in the observations, $E(X-Y)$:

$$E(X-Y) = (X-Y) - (X-Y)_0 \tag{4.13}$$

$(X-Y)_0$ is the color unaffected by the extinction, obtained from the simulated stellar flux derived from the best atmosphere model (see Fig. 4.30). Some studies related to the parametrization of the Galactic extinction have been performed by Seaton (1979) and Howarth (1983). The visual extinction (A_v) and color excess in the Johnson system are linked, in the Milky Way, by Cardelli et al. (1989) (see also Fitzpatrick 1999):

$$A_v = 3.1\,E(B-V) \tag{4.14}$$

The difference between the absolute ($d = 10\ pc$) and the observed apparent magnitude gives the distance of the stars by the so-called distance modulus (the extinction correction, A_λ, must be included in its calculation).

$$(m_\lambda - M_\lambda) = 5\,log\,(d) - 5 + A_\lambda \tag{4.15}$$

notwithstanding it would be only possible if the radius used in Eq. 4.12 is the right one.

The flux distribution also allows us to derive the bolometric correction (*BC*), establishing a relationship between the visual magnitude, for instance, and the bolometric one:

$$BC = M_{bol} - M_v \tag{4.16}$$

measuring the flux contribution outside the visual band. This correction brings a way for deriving the stellar physical parameters, once M_v and the distance are known. The bolometric magnitude definition gives the stellar luminosity through:

$$M_{bol} = -2.5\,log\,\frac{L}{L_\odot} + M_{bol\odot} \tag{4.17}$$

with $M_{bol\odot} = 4.74$. Once the luminosity is known, we can easily estimate the stellar radius by:

$$L = 4\pi R_*^2 \sigma T_{eff}^4 \tag{4.18}$$

Finally the spectroscopic mass is obtained through:

$$\frac{M}{M_\odot} = \frac{g}{2.736 \times 10^4} \left(\frac{R}{R_\odot}\right)^2 \tag{4.19}$$

being the solar surface gravity equal to 4.4371 *dex* in cgs units.

A complementary method for mass determination is through evolutionary models (e. g. Meynet & Maeder 2003). Placing the stars in the HR diagram allows a direct comparison between the stellar parameters and the evolutionary tracks which provide this information. This second technique relies on a good representation of the processes for stellar evolution.

4.2.6 Other Automatic Methods

Large databases demand the implementation of automatic techniques to carry out a quantitative analysis. Trying to avoid a standard visual methodology, several authors have implemented their own automatic procedures focused on their own work. We would like to remark briefly three of them focused on the massive blue stars field. They are not the only ones but likely the most representatives:

- The large B-type database provided by the GAUDI (Ground-based Asteroseismology Uniform Database Interface, Solano et al. 2005) archive created the need for an automatic analysis method. Lefever (2007) developed an homogeneous and robust grid-based method called *AnalyseBstar*. It follows an iterative scheme, in which fundamental parameters are calculated in certain order: (1) temperature, silicon abundance and microturbulence; (2) macroturbulence velocity; (3) surface gravity; (4) wind parameters. Each of them based on different lines available in the stellar spectrum. Starting from an initial guess, it converges searching for the parameters set that best reproduces the observed data.

  An alternative method was proposed by Lefever (2007), through a loglikelihood function constructed from a comparison of the EW of several lines, previously selected. This method gives all the parameters at once, avoiding the iterative process, although it is also less accurate that the previous one.

  The philosophy of our method, described before, takes an approach similar to this last one. However, our technique uses profiles instead of EW. At low-resolution ($R = 1000 - 2000$) and S/N (~ 75) it is the most accurate way since it is hard obtain a good EW estimation.

- To analyze the VLT-FLAMES survey (Evans et al. 2005b,a) of O- and B-type stars in the Milky Way and the Magellanic Clouds an automatic fitting method was designed by Mokiem et al. (2005), a genetic algorithm based on the optimization PIKAIA code by Charbonneau (1995).

  The advantage of this method lies in the *freedom* of a large number of parameters, that can be varied or fixed for each individual object according to

the characteristics of the problem. However, this means more calculation time. The algorithm is inspired in the notion of evolution by *natural selection* (Darwin 1859) implemented in a numerical fashion. The final solution is obtained from subsequent generations starting from a set of randomly initial values. The best match of each generation will be favored against the *weaker* descendants. The crossover of the best models together with the introduction of *mutation* allows to explore different regions of the parameter space, avoiding local solutions.

The method needs around 7000 models for the analysis of a single star, which is completely unfeasible for a single machine (to this date). That was solved parallelizing the routine. Even so, the method takes a few days for completing an object at the La Palma Mare Nostrum super-computer node, sensibly longer than our method. The method is implemented, so far, only for the hydrogen and helium analysis. The incorporation of more atoms for the study of cooler stars or performing chemical analyses will increase enormously the computational time.

The low resolution and the need to account for different chemical elements in the process to determine the chemical abundances makes unfeasible this kind of technique in our work.

- The analysis of late B-type stars is a tricky task since the effective temperature cannot be determined by any ionization balance. In these cases Kudritzki et al. (2008) suggested to use the Balmer jump as a temperature diagnostic. Urbaneja et al. (2008) decided to use an automatized numerical fit between data and synthetic spectra in their work on late B- and early A-type stars in the WLM galaxy. The algorithm follows an iterative process using the so-called *principal component analysis* (PCA).

  The goal of the method is determining temperature, surface gravity, metallicity and color excess. Starting with an initial temperature and metallicity it looks for the best gravity; then a new metallicity is obtained for this pair temperature–gravity. Eventually, the temperature and color excess are calculated in a similar way keeping the other two parameters fixed. The whole process is repeated for different initial temperatures, obtaining a set of parameters that leads to the final solution.

  This method was designed to constrain the temperature from the Balmer jump. Nonetheless, the same idea can be applied to other transitions (according to the spectral type) to constraint effective temperature with a similar accuracy.

  While this method is designed to recover the four parameters mentioned before, our work requires a detailed analysis of the entire set of stellar parameters. However, the same technique could be applied if the spectrum contains the required information.

To date the automatic method implemented by us is the best option for carrying out a complete analysis at low resolution in a short period of time with enough accuracy.

4.3 Summary

To Accomplish an automatic and reliable quantitative analysis is nowadays a fundamental task. The last generation of instruments brings the option of obtaining large databases in a relatively straightforward way and this kind of techniques are needed. In this chapter we have tackled that issue with the implementation of several automatic quantitative analysis procedures.

As a cornerstone of our method, a new grid of FASTWIND models has been calculated. We have looked for an efficient way for the stellar parameters selection, focusing on the area of blue supergiant stars. Thus, we count on a complete model data-set for evolved stars with masses between $8-60\,M_{\odot}$, for a wide range of microturbulences, helium abundances, metallicities and different mass loss rates.

Using this new grid we have implemented an automatic method based on χ^2-minimization. Depending on spectral resolution we have shown the different ways followed, searching for the most accurate one, as a function of data quality. The different tests carried out have shown the reliability of the techniques suggested and the limitations in the final stellar parameters derived. The final comparisons, either at low or high resolution, have displayed an excellent match to the Galactic stars used, and with synthetic test models at the low resolution.

The option of parallelizing not only the models grid construction but also the χ^2 comparison method through CONDOR has hugely accelerated both processes. The grid was forged in several weeks instead of months, the expected computational time on a small network (even years with a single computer). Besides, out χ^2-method goes from several hours for the comparison of a single star with ~ 100000 models (depending of the restrictions and the degree of freedom) to less than a hour. The software developed by us uses CONDOR in an efficient way and will form an excellent tool for carrying out the quantitative analyses of large samples in short periods of time.

Once we have tested the method and checked its reliability, in the next chapter we are going to use it for analyzing a large sample of low resolution spectra obtained in NGC 55. Due to their properties and the complete analysis desired, the low resolution methodology described in this chapter is the best option so far to carry out an objective quantitative analysis avoiding human interaction as much as possible. We have already shown that this is possible even with $R = 1000$ data, though the chemical determination still needs a more direct intervention.

5

Massive Blue Stars in NGC 55

Miguelito: "I have come to the conclusion
that there are more stars than we need."
To which Mafalda retorts,
"Than we need for what?"
Quino

THE quantitative spectroscopy of massive blue stars at the distance of NGC 55 pushes the last generation instruments and analysis techniques to their limits. Nonetheless, we have already shown in chapter 4 that it is possible to determine stellar parameters and abundances from low resolution and S/N spectra, such as those obtained when observing stars as far as NGC 55.

This chapter gathers the process followed for the analysis of an ample set of massive blue stars which belongs to NGC 55. Starting from the candidate selection, we describe the spectroscopic data reduction, spectral classification and eventually the quantitative analysis using the techniques described in chapter 4 for low resolution data.

5.1 The Sculptor Group Galaxy NGC 55

The Sculptor Group is located on the frontier of the Local Group (Puche & Carignan 1988). These galaxies are distributed along a filament at distances between ~ 1.6 and 4.0 Mpc; while NGC 247 (one of the main galaxies in the group) is located at $\sim 4Mpc$ other galaxies, such as NGC 300, are closer to us and therefore easier to work with. The system is completed with a set of irregular dwarf galaxies plus several large objects, including NGC 55, the target of this study. A detailed description of the

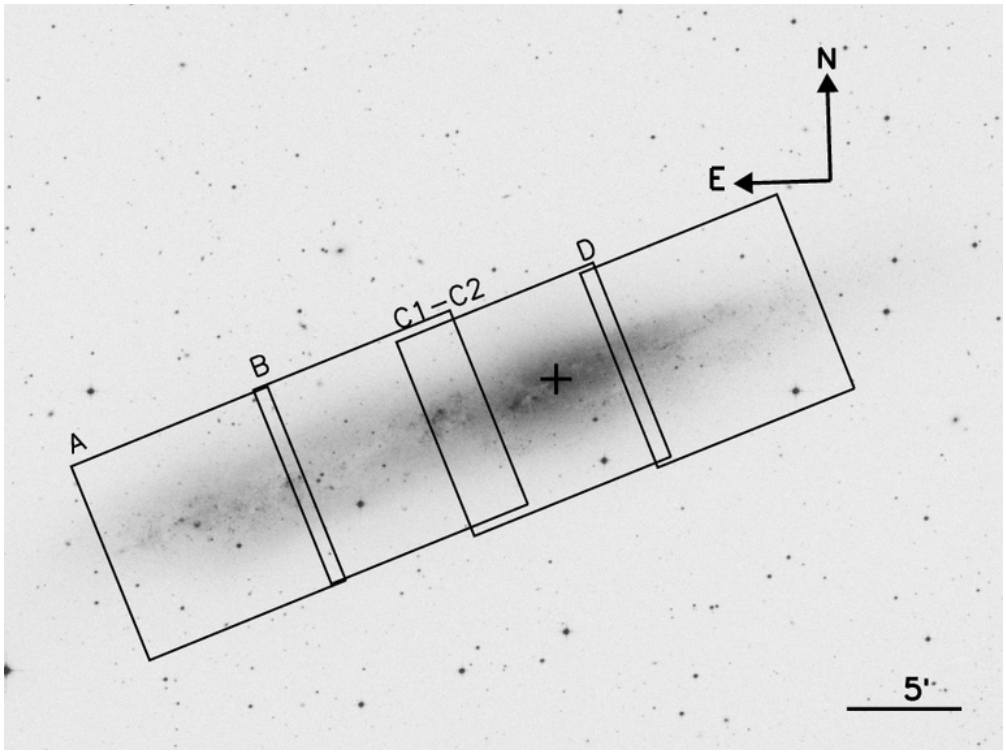

FIGURE 5.1— NGC 55 optical image obtained from the *DSS* archive ($http://archive.stsci.edu/cgi-bin/dss\_form$). The observed fields are also displayed (see text for details). Each square represents approximately the FORS2 field of view ($6'.8 \times 6'.8$) in MXU mode.

Sculptor Group dwarfs can be found in the work by Miller (1996).

At a distance of $\sim 1.9 Mpc$ (Pietrzyński et al. 2006; Gieren et al. 2008), NGC 55 presents an almost *edge-on* orientation with respect to the line of sight ($\sim 81^\circ$, Hummel et al. 1986), hiding its morphological classification. Sandage & Tammann (1987) suggested to classify it as spiral (Sc), notwithstanding de Vaucouleurs (1961) remarked the similarities between NGC 55 and the Large Magellanic Cloud (LMC) classifying it as an SBm(s) instead. The optical appearance of NGC 55 makes unlikely the Sc option since it does not present a clear bulge. The galaxy shows a projected size in the sky about $32' \times 5'$ in the optical range (see Fig. 5.1).

Different studies point to a metal content that resembles that of the LMC. Davidge (2005) estimated a [Fe /H]$= -0.3$ in the thin disk, very similar to the values provided by Luck et al. (1998) for the LMC. The oxygen abundances derived by Webster & Smith (1983) in several H II regions are also in agreement with the LMC value (Kurt & Dufour 1998; Tüllmann et al. 2003). This study did not find any significant

NGC 55		
RA (J2000)	$00^h:14^m:53.6^s$	Two Micron All Sky Survey team (2003)
DEC (J2000)	$-39^\circ:11':47.9''$	Two Micron All Sky Survey team (2003)
Distance	$1.94\,Mpc$	Gieren et al. (2008)
Inclination	81°	Hummel et al. (1986)
Mv	-7.95	Mateo (1998), references therein.
B-V	0.50	Mateo (1998), references therein.
$< E\,(B-V) >$	0.127	Gieren et al. (2008)
E(B-V)$_{foreground}$	0.013	Schlegel et al. (1998)
12+log (O /H)	8.40	Tüllmann et al. (2003)
Redshift	0.000430	Koribalski et al. (2004)
Radial Velocity	$129\,km\,s^{-1}$	Koribalski et al. (2004)

TABLE 5.1— NGC 55 fundamental parameters.

variation of the oxygen abundance across the galaxy. A metallic radial gradient could be interpreted as indicator of spiral structure (see the recent work of U et al. 2009 on M 33). For NGC 55, however, the metallicity does not point to strong evidence regarding its morphology. The main properties of NGC 55 are summarized in Tab. 5.1.

NGC 55 has been the subject of numerous studies covering a wide wavelength range. Due to its high inclination angle it is a perfect laboratory for studies related to galactic stratification through the disk and the halo. The analyses performed so far cover an ample range of topics as well, for instance: the gas distribution observed in X-rays (Oshima et al. 2002) supports the idea that the hot gas expelled by supernova explosions and stellar winds is the origin of the extraplanar hot gas (Otte & Dettmar 1999); or the red star population from the thin disk to the halo, based on infrared colors, revealing signatures of large-scale star formation in recent epochs in the plane (Davidge 2005). Puche et al. (1991) analyzed the galactic dynamics by means of H I clouds, determining the rotational curve of NGC 55 and finding an unsymmetrical distribution with respect to the light pattern and a possible warp of the H I plane in the northwest side. The dust emission in the far-infrared has provided important information about sources at the galactic center (Engelbracht et al. 2004), likely related with the bar suggested by de Vaucouleurs (1961). Also several studies in H II regions (Webster & Smith 1983) have been performed, chiefly in central regions, where intense stellar activity is revealed by bubbles and filaments produced by strong stellar winds and supernova explosions (Tüllmann et al. 2003).

Precisely, this intense stellar activity hints at an important population of massive

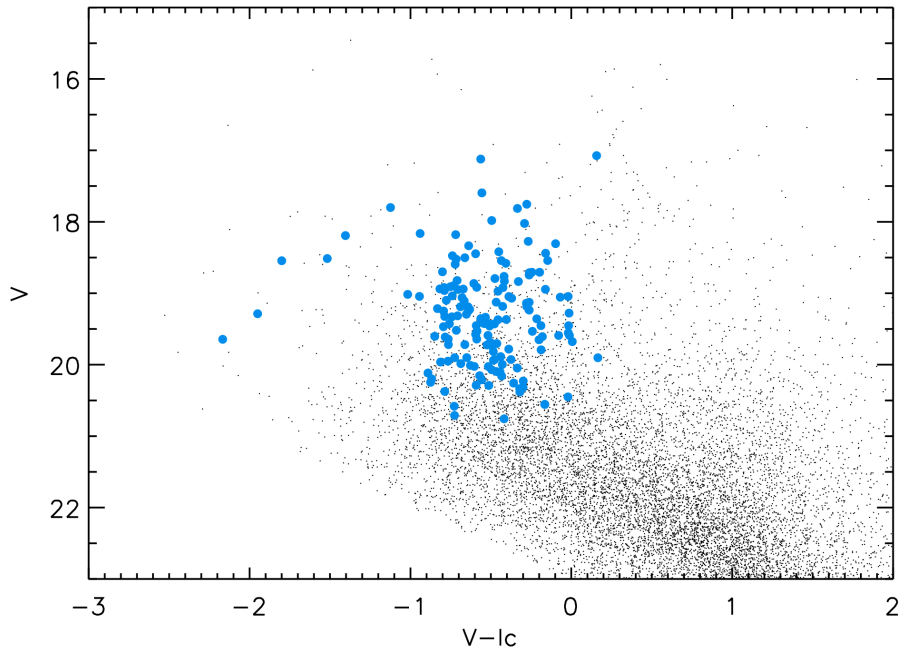

FIGURE 5.2— Color-magnitude diagram of NGC 55. The targets selected for the spectroscopic study presented in this work are marked with blue dots.

blue stars (Gieren et al. 2005), which is going to be the subject to our study. The quantitative studies of the young population will bring not only information about the evolution and characteristic of the stars themselves but also clues about the dynamical and chemical composition of NGC 55 by means of additional species not available from studies of H II regions.

5.2 Observations and Data Reduction

The observations of NGC 55 are part of the ongoing ARAUCARIA project (P. I.: Dr. W. Gieren)[1] whose results have been reported in Pietrzyński et al. (2006). The project is focused on the characterization of different standard candles (variables stars, red clump giants and blue supergiants) in the Local Group and nearby galaxies. The project aims to provide accurate distance diagnostics and analyze their poorly-known dependencies with environment (metallicity or age of the stellar population).

From the ARAUCARIA project efforts, a first list of blue star candidates was built

[1] http://ezzelino.ifa.hawaii.edu/∼bresolin/Araucaria/index.html

from existing V- and Ic-band photometry in NGC 55. The images were obtained with the Warsaw 1.3 m telescope at Las Campanas Observatory, equipped with a CCD $8k \times 8k$ mosaic which covers a field of view of $\sim 35' \times 35'$, with a plate scale of $\sim 0.25''/pix$.

Magnitude and color were the main criteria for candidate selection. B and early-A supergiants with $M_v \lesssim -6.5$ have an apparent magnitude $V \lesssim 20$ at the distance of NGC 55 ($m - M = 26.43$, Gieren et al. 2008). As we will show in the next section, low resolution spectroscopy of objects with magnitude $V \sim 20$ is feasible with 8-m class telescopes in a reasonable amount of time. NGC 55 has a high galactic latitude ($b = -75°$), therefore the foreground reddening is low ($E(B-V) = 0.013$, Schlegel et al. 1998). Nonetheless, the internal reddening of the galaxy may not be so negligible since NGC 55 is almost *edge-on*. In fact, it has been estimated from a multiwavelength analysis by Gieren et al. (2008) to be $E(B-V) = 0.127$ on average. Figure 5.2 shows the color-magnitude diagram from which targets were selected. The spatial location of the 204 selected objects is shown in Fig. 5.3.

The final list of candidates was forged by careful examination of existing images in order to reject objects with nearby companions (real or projected) and to avoid overlap with H II regions. Because of the large inclination angle of the galaxy, this was not always possible. We cannot role out the possibility that the targets are in fact unresolved binaries. Multiplicity is also an issue in the Milky Way studies of massive blue stars. According to Mason et al. (1998), 72.2% of O-type stars in clusters are in binary systems, while the rate is 19.4% for field stars. In addition, the low spectral resolution of our data will further hamper the detection of spectroscopic binaries.

5.2.1 Multi-Object Spectroscopy: FORS2

The spectra were obtained with FORS2[2] (FOcal Reducer and low dispersion Spectrograph, Appenzeller et al. 1998) at the Very Large Telescope (VLT) at Cerro Paranal (Chile). The spectrograph was designed for the optical and near ultraviolet spectral range, between $\sim 330 - 1100$ nm with a scale of 0".2 $pixel$ (in the standard collimator configuration). The detector is a mosaic of two $2k \times 4k$ MIT CCDs with a gap of 4" between them and a pixel size of $15 \times 15\,\mu m$. Both have high response in the red part of the spectrum (600 nm), but suffer from strong fringing above 650 nm. The efficiency drops significantly in the blue part, below 400 nm.

The instrument offers different observation modes, direct imaging, longslit or multi-object spectroscopy mode, the latter either through movable slits (MOS) or using carved masks (MXU). Our study looks for large star samples using the minimum observational time, therefore the MOS mode was discarded since it is limited to 19 objects per exposition. Thus, we relied on the MXU mode with a total field of view of

[2] http://www.eso.org/sci/facilities/paranal/instruments/fors/

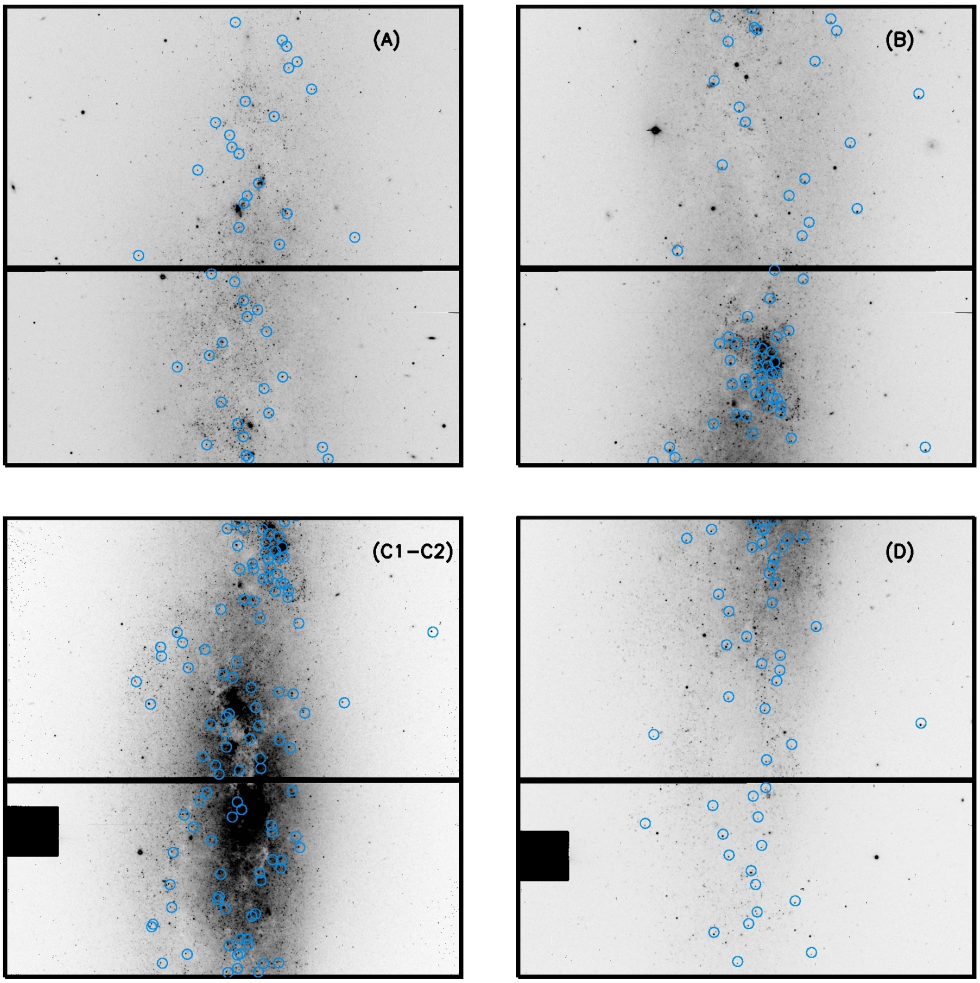

FIGURE 5.3— Location of the target stars on NGC 55 FORS2 V-band images. They spread over the galaxy providing information from different points. Each of the quadrants covers only a portion of $\sim 6'.8 \times 6'.8$ in the galaxy. They relative position of each observed field is shown on Fig. 5.1.

$6'.8 \times 6'.8$, which means that four pointings were necessary to cover the whole galaxy, as it is shown in Fig. 5.1. One mask per field was built with FIMS (FORS Instrumental Mask Simulator), except for the central pointing where the number of candidates to massive blue stars is expected to be larger and two masks were used, around $40-50$ objects were observed in each pointing. Figure 5.4 shows a mask design for one of the central pointings on NGC 55,created by the instrumental mask simulator FIMS, plus the final observed multi-spectra from this mask. Each slit was carved with a width of

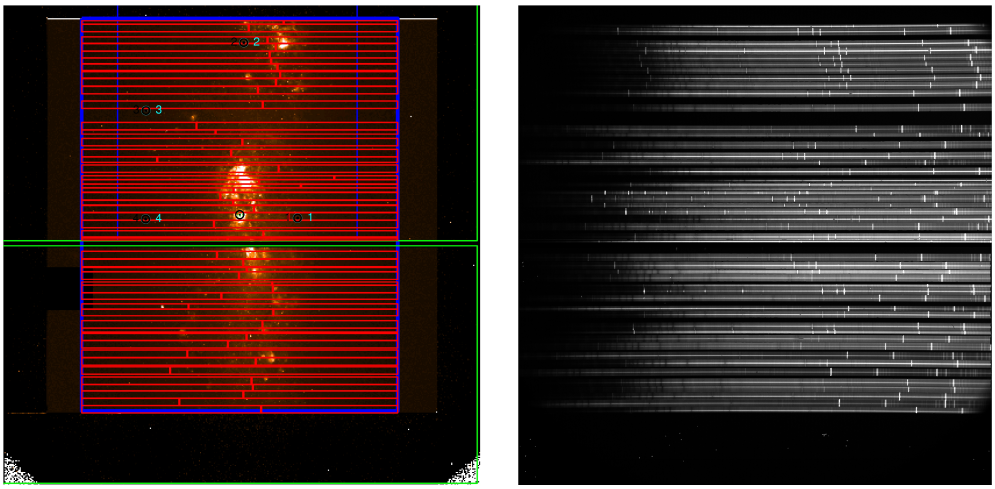

FIGURE 5.4— Mask design for FORS2 on NGC 55. The left panel shows the mask simulation created with FIMS on a central NGC 55 FORS2 image. The image displays how efficient the selection was done, using almost the entire CCD available. The right panel presents the multi-spectra observed through this mask.

1 arc-second.

FORS2 offers an ample set of grisms covering different spectral ranges and resolutions. At the time of the observations, the best option for our proposes was the 600B grism, which provided the highest resolving power for this study ($\lambda/\Delta\lambda = 780$) in the wavelength range of interest ($3100 - 6210$ $\AA$). The observations, performed in November 2004, are summarised in Table 5.2.

Field (1)	RA (J2000) (2)	DEC (J2000) (3)	T_{exp} (s) (4)	Date (5)
A	00:15:55.0	-39:16:13.0	10800	2004-11-07
B	00:15:22.9	-39:13:54.6	13500	2004-11-10
C1	00:14:57.6	-39:12:28.5	10800	2004-11-06
C2	00:14:57.6	-39:12:28.5	10800	2004-11-06
D	00:14:25.5	-39:10:21.4	16200	2004-11-07/10

TABLE 5.2— Summary of our VLT-FORS2 NGC 55 observations. The columns list: (1) the observed field (see Fig. 5.1); (2) and (3) center field coordinates; (4) total exposure time; and (5) date of the observations.

5.2.2 Data Reduction

Since no specific pipeline for FORS2 data existed, we used the routines developed by Demarco et al. (2005), optimized for FORS2 data and improved by us. The reduction process is outlined in Fig. 5.5. A general description of CCD reduction using IRAF[3] can be consulted in Massey et al. (1992) and Massey (1997).

The next example describes the reduction of the C2 field, at the center of NGC 55 (see Fig. 5.1). The designed mask allows us to obtain 55 objects in a single exposure in MXU mode. The steps we have followed, and summarized in Fig. 5.5, are:

- **a)** The pipeline extracts all the slits and works with them separately. The code then follows the standard steps for long slit spectral reduction, using IRAF tasks: bias and flat-field correction. Additionally the IRAF tasks are complemented by several modules programed in IDL[4] and Linux shell languages.

  We updated the pipeline by Demarco et al. (2005) introducing an efficient algorithm for cosmic rays subtraction developed by van Dokkum (2001) (LA-Cosmic[5]), based on the laplacian edge detection technique. A second upgrade was the implementation of a new module to normalize flat-field images prior to performing its correction, an important step if flux calibration is desired.

- **b) and c)** The 1-D spectra were obtained from the 2-D images through the IRAF task *apall*. The procedure performs the spectral extraction, sky subtraction and a correct object tracing along the spectral direction, taking into account the deformation of the projected slits on the CCD. Panel *a)* in Fig. 5.5 shows this slit distortion, introduced by the instrument and corrected by the *apall* tracing. The scale used for this example hides the effect, but the deformations are not negligible and they increase towards the CCD mosaic edges.

  The aperture used and the range selected for evaluating the sky background are crucial (see *b)* in Fig. 5.5). If the aperture for the target is too small some stellar flux is lost, which is critical for the final S/N of faint objects. On the other hand, if it is too large it will also include sky counts, increasing the noise of the extracted stellar spectra.

  Sky subtraction was a laborious task due to surrounding nebular emission, which is particularly strong in the central regions of the galaxy. The apertures considered and the way to treat the background in IRAF (mean, median or

[3]IRAF is distributed by the National Optical Astronomy Observatory, which is operated by the Association of Universities for Research in Astronomy, Inc., under cooperative agreement with the National Science Foundation.

[4]http://www.ittvis.com/

[5]http://www.astro.yale.edu/dokkum/lacosmic/

polynomial fit) will affect the accuracy of sky subtraction, but also the final spectral S/N. We found that the nebular emission in the slit (see panel *a)* in Fig. 5.5) is usually not homogeneous. Given the high inclination of the galaxy, the likely reason is that photons from a large number of H II regions (with different radial velocities) are integrated along the line of sight. The contamination is more severe for young stars, which are additionally still embedded in the dense regions where they were born. Interstellar absorption lines (Ca II $3933-3968\,\AA$) can also contaminate the spectrum (Hartmann 1904). Despite all our efforts, it was impossible to remove completely the nebular contamination in many objects due to the spectral resolution and faint magnitudes. Nevertheless, in most of them the nebular lines do not compromise the spectral classification and the final quantitative analysis.

- **d)** After extracting the spectra, wavelength calibration was carried out with the IRAF procedure *identify*. The arc lamp reference spectra (in our case a combination of He Ar +Hg Cd) were reduced following a), b) and c) steps, and wavelength calibrated. The derived pixel-wavelength relationship was them applied to the stellar spectra.

- **e)** The individual spectra were finally rectified to the local continuum (normalized) and all the exposures were combined (weighted according to their count number) with IDL routines developed by our group.

- **f)** The final products are wavelength-calibrated normalized spectra for all slits in the masks.

Finally, the complete observed sample consist of 204 spectra with a S/N of ~ 75 on average.

5.3 Spectral Classification

The morphological analysis of stellar spectra is a crucial first step in studying the population of massive stars in a galaxy, since it provides confirmation of the massive nature of objects selected from photometry and clues about the stellar parameters of the stars. Unfortunately, while we can know the spectral classification of cooler objects from photometric colors, this is impossible for objects with higher temperatures like A-, B- or O-type stars. The reason is that the energy distribution of hotter types displays very similar slope in the optical range. Consequently these stars have very similar colors which cannot be differentiated unless accurate photometry (exceeding current observing capabilities) is used (Maíz-Apellániz 2004). Spectral information is needed to unequivocally identify O-, B- and A-stars.

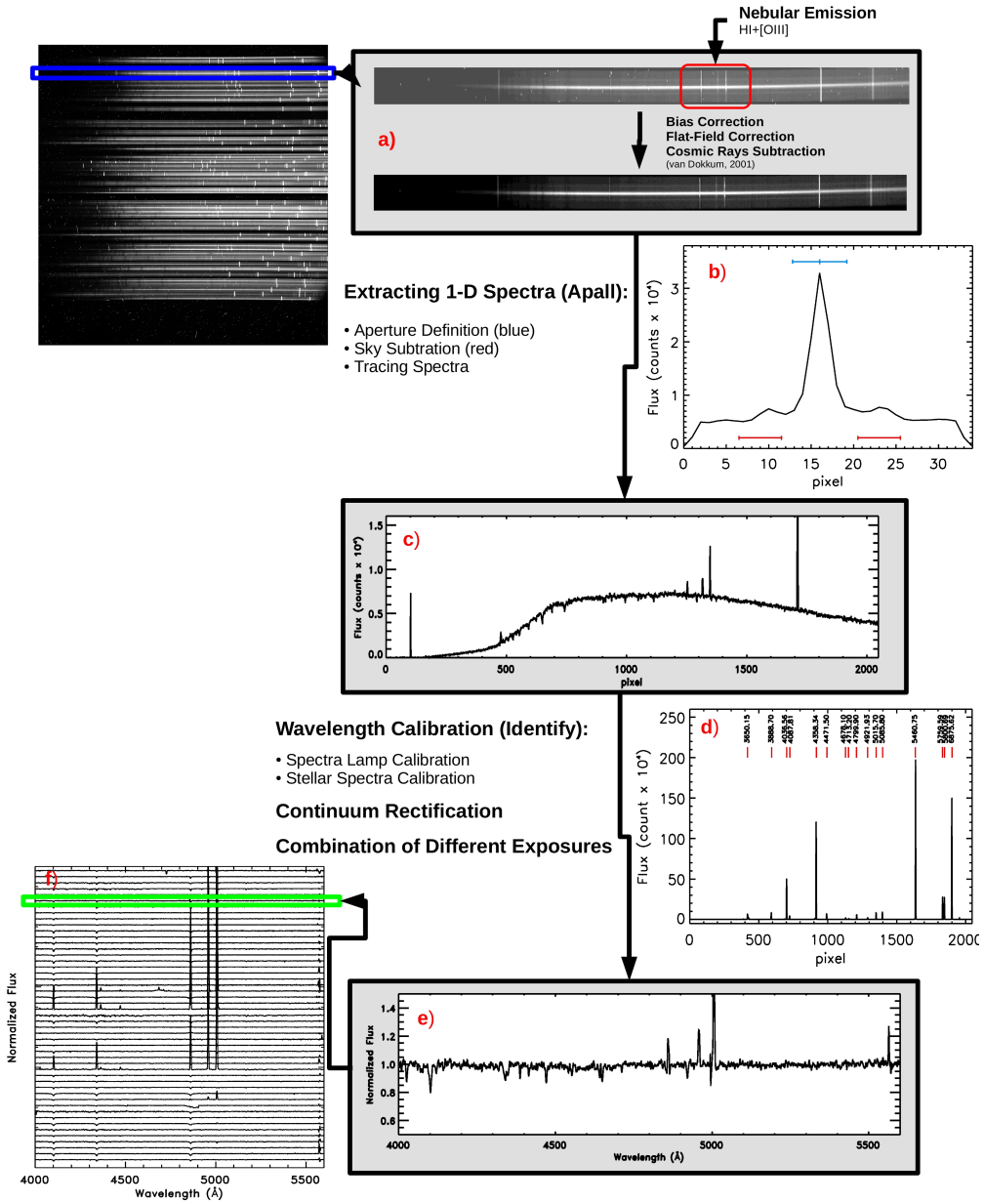

FIGURE 5.5— Summary of the steps followed for spectral reduction. See text for a compete description.

5.3.1 Classification Criteria for Massive Blue Stars

The criteria developed by Morgan et al. (1943) (forged in the Harvard classification system), together with subsequent refinements by Walborn & Fitzpatrick (1990) and Lennon et al. (1992), are the bases for the spectral classification of Galactic stars. Once out of the Milky Way, environmental factors such as metallicity will alter the strength of diagnostic lines and therefore mislead the classification. In newly explored galaxies where the metallicity is not accurately known, we have to be cautious and use appropriate standards since the chemical composition of the studied stars may differ from all the existing templates. In the light of this, we also supported our study in the works by Fitzpatrick (1991) on the LMC and Lennon (1997) and Evans & Howarth (2003) on the Small Magellanic Cloud (SMC).

In this section, we summarize the criteria used for the classification of massive blue stars. It has to be noted here that the criteria are developed for a given spectral resolution. A change in resolution may alter this criteria.

O-type Stars

The O-type classification is centered in the criteria proposed by Walborn & Fitzpatrick (1990) based on the standard stars in their atlas.

The spectra of this kind of stars are dominated by H I, He I and He II transitions plus some features of other metallic lines (for example Si IV or N III transitions). A summary of the main spectral type indicators is gathered in Tab. 5.3.

The principal criteria are defined as a function of He II/He I ratios, the most relevant being He II 4541 $\AA$/He I 4471 $\AA$ and He II 4200 $\AA$/He I+II 4026 $\AA$. In late O-types it is also possible to use He II 4541 $\AA$/He I 4387 $\AA$ and He II 4541 $\AA$/He I 4144 $\AA$, although they are also sensitive to luminosity. Walborn (1971) defined the additional O9.7 type using the ratio between He II 4541 $\AA$ and Si III 4552 $\AA$. This is the sort of criteria that should be handled cautiously when applied to stars of various metallicities. A weaker silicon line can be interpreted as higher temperature, while it may be caused by poorer metal content.

Additional *'f'* notation is used if there are emission nitrogen lines in the spectrum. Walborn & Fitzpatrick (1990) elaborated it paying more attention to other line strengths: *'((f))'* weak N III 4634 – 4640 – 4642 $\AA$ emission lines; *'f*'* N IV 4058 $\AA$ is stronger than N III 4640 $\AA$; and *'f+'* if, besides the nitrogen lines, Si IV 4116 $\AA$ is found in emission.

Walborn & Fitzpatrick (1990) based the luminosity classification of O stars on certain helium and metallic lines. OV stars present a strong absorption of He II 4686 $\AA$, sometimes together with weak N III 4634 – 4640 – 4642 $\AA$ absorption lines. As we move to the supergiant class, He II 4686 $\AA$ loses strength in absorption and shifts to emission; the nitrogen lines follow a similar behavior, but are weaker. A note of

caution must be taken due to the He II 4686 $\AA$ line, since it strongly depends on the stellar wind. The aforementioned Si IV transition can be used as a second indicator, mainly in the O8-O9 types. These criteria are presented in Tab. 5.4. O3 stars present strong emissions of N IV 4058 $\AA$ and absorptions at N V $4604-4620\,\AA$ which strength decreases when the luminosity class increases from dwarf to supergiants.

B-type Stars

For B-type stars we use again the criteria proposed by Walborn & Fitzpatrick (1990) together with the atlases built by Lennon et al. (1992) for the Milky Way, Fitzpatrick (1991) for the LMC and Lennon (1997) for the SMC. Because stars of a wide range of metallicities are used as reference, the metallicity effects must be carefully handled here.

Stars are mainly classified using the silicon transitions in this temperature range. The different ionization balances between Si IV, Si III and Si II will define the spectral type. Additional transitions in the spectra will be helpful to distinguish closer types. For instance, the rests of He II lines disappear around B0-1 when O II reaches its maximum strength. The transition of Mg II 4481 $\AA$ is first seen around B1 types. For late-B stars the ratio Mg II 4481 $\AA$/He I 4471 $\AA$ is a clear reference for the spectral type. Table 5.5 sorts the main criteria used for B-type stars.

There are several luminosity class indicators for early B-types (B0-2). For example, the strength of Si IV 4089 $\AA$ compared with the nearby He I 4025, 4121 ,4144 $\AA$ lines, and the Si IV 4116 $\AA$/He I 4121 $\AA$ ratio. At B0 the He II 4686 $\AA$ absorption is weak, but it can still be used in the same way as in O-types. In the B1-2 spectral types the relative strength between Si III 4552 $\AA$/He I 4387 $\AA$ is also a good reference (see Tab. 5.6).

An additional diagnosis for luminosity class is provided by the wings of Balmer lines. Their equivalent widths and gravity are linked through the Stark broadening (see section 4.2.2). Consequently, dwarf stars show broader Balmer lines than supergiants. This effect was quantified by Azzopardi (1987) and is used in this work as additional luminosity diagnostic.

A- and later type Stars

We have followed the study presented by Evans & Howarth (2003) in the SMC for the classification of A-type stars. Their work is based on the Ca II resonance transitions (Ca II K 3933 $\AA$ and Ca II H 3968 $\AA$). The ratios of Ca II K line with H_δ and H_ε+Ca II H indicate the spectral type for A-stars (Cannon & Pickering 1924). However, these criteria may be affected by interstellar contamination, metallicity or rapid stellar rotation (see Evans & Howarth 2003 for more details).

The ratio between Ca I 4226 $\AA$ and Mg II 4481 $\AA$ constitutes an additional indicator

Type	He II 4541 Å/He I 4471 Å	He II 4200Å/He I+II 4026Å	He II 4541 Å/He I 4387 Å	He II 4200Å/He I 4144 Å	Secondary Criteria
O3	He II>>He I	He II>He I+II	No He I	No He I	
O6	He II>He I	He II>He I+II	No He I	No He I	
O7	He II=He I	He II/He I+II>0.7	He II>>He I	He II>>He I	
O8	He II<He I	He II/He I+II>0.7	He II>>He I	He II>He I	
O9	He II<<He I	He II/He I+II<0.5	He II≥ He I	He II≥ He I	
O9.5	He II<<He I	He II<<He I+II	He II<He I	He II≤ He I	He II4541 Å >Si III4552 Å
O9.7	He II<<He I	He II 4200 Å Almost vanished	He II<He I	He II<He I	He II4541 Å ≤Si III4552 Å

TABLE 5.3— Spectral subtype definitions for O-type stars.

Type	Luminosity Class	He II 4686 Å	Si IV 4089 Å/He I 4121 Å	Secondary Criteria
O3	I	Emission	—	N IV 4058 Å in emission, N V 4604 Å >He II 4541 Å
	III	He II 4686 Å <He II 4541 Å	—	N IV 4058 Å in emission (weaker), N V 4604 Å <He II 4541 Å
	V	He II 4686 Å =He II 4541 Å	—	Neither N IV nor N V
O6	I	Emission	—	N III 4634 Å in emission
	III	He II 4686 Å <He II 4541 Å	—	No N III
	V	He II 4686 Å =He II 4541 Å	—	No N III
O8	I	There is no emission	Si IV>He I	N III 4634 Å in emission
	III	He II 4686 Å ≥ He II 4541 Å	Si IV≥ He I	No N III
	V	He II 4686 Å >He II 4541 Å	Si IV=He I	No N III
O9	I	There is no emission	Si IV>He I	—
	III	He II 4686 Å >He II 4541 Å	Si IV≥ He I	—
	V	He II 4686 Å >He II 4541 Å	Si IV=He I	—

TABLE 5.4— Luminosity Class criteria for O-type stars.

Type	Si IV 4089Å/Si III 4552Å	Mg II 4481Å/He I 4471Å	Si III 4552Å/Si II 4128Å	Si III 4552Å/Mg II 4481Å	Si II 4128Å/He I 4121Å	Si IV 4089Å/O II+C III 4070Å	Si III 4089Å/O II+C III 4650Å
B0	Si IV>Si III	—	—	—	—	Si IV>O II+C III	O II+C III>>Si III
B0.5	Si IV=Si III	—	—	—	—	Si IV>O II+C III	O II+C III>Si III
B1	Si IV<Si III	Mg II<<He I	—	Mg II<<Si III	—	Si IV=O II+C III	O II+C III≥ Si III
B1.5	Si IV<Si III	Mg II<<He I	Si III>>Si II	Mg II/Si III= 0.5	Si II<<He I	Si IV<O II+C III	O II+C III=Si III
B2	Si IV<<Si III	Mg II<<He I	Si III>Si II	Mg II/Si III> 0.5	Si II/He I< 0.5	Si IV<<O II+C III	O II+C III=Si III
B2.5	—	Mg II<He I	Si III>Si II	Mg II=Si III	Si II/He I= 0.5	—	O II+C III=Si III
B3	—	Mg II/He I< 0.5	Si III=Si II	Mg II>Si III	Si II/He I> 0.5	—	O II+C III<Si III
B5	—	Mg II/He I≤ 0.5	—	—	Si II/He I< 0.8	—	—
B7	—	Mg II/He I≥ 0.7	—	—	Si I=He I	—	—
B8	—	Mg II=He I	—	—	Si II>He I	—	—
B9	—	Mg II>He I	—	—	Si II>He I	—	—

TABLE 5.5— Spectral classification criteria for B-type stars.

Type	Luminosity Class	He II 4686Å/He II 4713Å	Si IV 4089Å/He I 4121Å	Si III 4552Å/He I 4387Å
B0	I	He II<He I	Si IV>He I	Si III<He I
	III	He II≤He I	Si IV≥He I	Si III<He I
	V	He II>He I	Si IV=He I	Si III<<He I
B1	I	—	Si IV≤He I	Si III/He I= 0.5
	III	—	Si IV<He I	Si III/He I< 0.5
	V	—	Si IV<<He I	Si III<<He I
B2	I	—	Si IV<<He I	Si III/He I= 0.5
	III	—	No Si IV	Si III/He I< 0.5
	V	—	No Si IV	Si III<<He I
B3 and later	Balmer lines width			

TABLE 5.6— Luminosity classification criteria for early-B type stars.

Type	CaK /He+CaH	Mg II 4481/He I 4471	Mg II 4481/Fe II 4471	Mg II 4481/Fe II 4549 – 4584	Si II 4128/Fe II 4233 – 4173	G-Band ∼ 4300/Fe II 4233 – 4173
A0	< 0.33	He I/Mg II≤ 0.5	Fe II<<Mg II	Fe II<<Mg II	Si II>Fe II	—
A2	0.33 – 0.53	He I<<Mg II	Fe II/Mg II< 0.5	Fe II/Mg II= 0.5	Si II≥ Fe II	Fe II>>G-Band
A3	0.53 – 0.75	—	Fe II/Mg II≥ 0.5	Fe II/Mg II> 0.5	Si II=Fe II	Fe II≥ G-Band
A5	0.75 – 0.85	—	Fe II/Mg II> 0.5	Fe II=Mg II	Si II<Fe II	Fe II≤ G-Band
A7	0.85 – 0.95	—	Fe II=Mg II	Fe II=Mg II	Si II<Fe II	Fe II<G-Band
F0	> 0.95	—	Fe II>Mg II	Fe II>Mg II	Si II<Fe II	Fe II<G-Band

TABLE 5.7— Spectral classification criteria for A-type stars.

(Yamashita & Nariai 1977), nonetheless the weakness of Ca I makes it only useful with high S/N data. At this temperature range, stars begin to show a rich variety of Fe II lines and the molecular band of CH (G-band) at ~ 4300 Å. These were used as secondary criteria together with the Si II $4128 - 4130$ Å transitions (see Tab. 5.7).

The luminosity class was estimated from the wing of the Balmer series, similarly to B-type stars.

For stars with spectral types later than F-type[6] we followed the criteria of Jaschek & Jaschek (1990). Basically, these stars are characterized by the relative strength of metallic lines and the G-band compared to H_γ.

Exotic Stars

Objects with peculiar spectral features, such as very broad emission or P-Cygni profiles were classified as Wolf-Rayet (WR) stars or Luminous Blue Variable candidates (LBVc). They are not easy to label due to the their complex morphology and variety of particular exceptional cases, chiefly in the case of LBV stars (Massey et al. 2007).

The WR classification was performed following two different schema, depending on whether the spectrum showed emission in nitrogen lines (WN) or in carbon transitions (WC). We used the criteria of by Smith et al. (1996) for WN, based on helium and nitrogen lines. The WC stars were classified according to the work of Crowther et al. (1998) (though finally our sample does not contain this sort of objects).

We have included in the LBVc category all the stars whose spectra exhibit P-Cygni profiles of the Balmer series or helium transitions, emission in metallic lines (mainly Fe II) or any other unusual spectral features. For confirmation we have compared with spectra published by Walborn & Fitzpatrick (2000); Abbott et al. (2004); Schild et al. (2003); Bohannan & Walborn (1989).

5.3.2 Results for NGC 55 Objects

As we pointed out in our description of NGC 55 (section 5.1), previous work indicated a metallicity close to the LMC. We have first performed the spectral classification of our sample with the criteria explained in section 5.3, and then compared with stellar templates from the LMC. Even though the metallicities of both galaxies are similar, we have been careful with criteria involving helium or hydrogen lines and metallic transitions. Criteria that only use metallic lines, for instance Si III / Si IV, were preferred when available. The resolution and quality of the spectra prevented us from doing a fine luminosity classification. Besides, the lack of Hα spectra and nebular contamination impairs further distinction. Additional diagnostic metallic lines

[6] These objects were not used for quantitative spectroscopic analysis. However, they were classified for completeness.

Field	O-Type	B-Type	A-Type	WR-LBVc	Total
A	5	20	13	1	39
B	4	7	7	3	21
C1-C2	4	34	30	3	71
D	1	14	18	0	33
Total	14	75	68	7	164

TABLE 5.8— Number of NGC 55 massive blue stars found in each field, sorted by spectral type.

for luminosity class of B- and A-types exist, but the variations are too small given the NGC 55 metallicity, and cannot be detected at the S/N and resolution of the spectra.

We have provided a classification for 204 spectra, out of which 164 correspond to stars belonging to NGC 55, and have spectral types earlier than F0. The rest of the objects include F- and G-supergiants (23 stars), H II regions (4 spectra) and a sample of Galactic B-, A-, F-, and G-dwarfs (13 stars) plus a white dwarf. The number of massive blue stars, sorted by spectral types, found in NGC 55 is provided in Table 5.8. The complete catalog is available the appendix A. The catalog provides coordinates, V-magnitude V-Ic color, spectral type, galactocentric distance, radial velocity and comments regarding the quality and peculiarities (see below) of the resulting spectra for all the stars included in the observations. A portion of the total database is shown as an illustration in Tab. 5.9, including some objects presented in this section. Table A.1 list the set of early-type stars (earlier than F0) found in NGC 55, F- and G-stars are compiled in Tab. A.2, for completeness. Finally, Tab. A.3 lists dwarf stars together with a Galactic white dwarf found in the sample.

The accuracy of the classification depends on several factors. It is essential to have spectra of sufficiently high S/N to detect spectral indicators and compare their relative strengths. Faint stars have been assigned only a rough classification. A good subtraction of cosmic rays and a complete sky subtraction are key points too. The latter was not always possible, leaving the Balmer lines (main luminosity class indicators in B- and A-types) contaminated by nebular emission at their cores. However, the impact on the luminosity classification was negligible in most cases, since we could still use the Balmer line wings and alternative metallic diagnostic lines were not affected. We have marked the spectra with remaining nebular contamination in the Balmer lines or in the [O III] lines (about 46% of the sample) with the comment *'neb.'* in Tabs. 5.9, A.1, A.2 and A.3.

OBA-type Stars

We have found a total of 14 O-type stars in our sample. Fig. 5.6 shows a subset of these objects. The largest fraction of the observed stars (75 of them) are B-type, some

ID (1)	RA(J2000) (2)	DEC(J2000) (3)	V (4)	V-Ic (5)	Spec. Type (6)	Rg (7)	v_r (8)	S/N (9)	Notes (10)
D_36	0:14:35.07	-39:11:20.04	19.189	-0.689	B9I	-278.26	78 (11,7)	70	
C2_8	0:14:43.87	-39:12:29.51	19.294	-0.652	A0I	-147.56	95 (16,8)	69	
C1_18	0:14:55.94	-39:11:21.84	19.316	-0.707	WN8	-37.95	124 (-,1)	30	neb.
C1_30	0:14:59.91	-39:12:11.88	18.921	-0.425	LBVc	95.62	158 (10,3)	28	
C1_37	0:15:02.50	-39:13:58.44	19.642	-0.588	A7II	153.43	146 (20,4)	55	
C1_51	0:15:14.70	-39:12:54.36	18.306	-0.098	Ofpe/WN9	319.21	187 (28,2)	57	neb.
B_12	0:15:16.68	-39:13:26.40	19.108	-0.666	Of/WN	351.60	176 (28,2)	90	neb.
B_13	0:15:18.63	-39:13:12.72	18.543	-0.435	LBVc/WN11	379.26	274 (25,3)	103	
B_34	0:15:37.73	-39:13:49.08	19.533	-0.242	LBVc/WN11	667.26	216 (19,3)	35	
B_36	0:15:40.62	-39:13:40.07	19.782	-0.389	O8I	709.64	171 (12,5)	55	
A_5	0:15:40.83	-39:15:09.72	20.071	-0.495	A3I	722.43	260 (18,7)	58	
A_8	0:15:44.18	-39:14:58.20	19.792	-0.188	O9.7I	770.70	304 (27,9)	62	
A_11	0:15:45.17	-39:15:56.15	18.706	-0.245	B5I	793.59	209 (25,11)	130	
A_29	0:15:57.97	-39:15:33.84	19.575	-0.595	O5If+	980.35	210 (25,3)	62	neb.
A_34	0:16:01.17	-39:16:34.67	20.247	-0.875	B0I	1036.66	215 (22,10)	68	
A_42	0:16:09.69	-39:16:13.44	19.453	-0.189	LBVc	1160.17	175 (20,4)	75	

TABLE 5.9— A subset of our catalog of massive blue stars in NGC 55. Different columns include: (1) our identification number; (2) and (3) coordinates; (4) and (5) apparent magnitude and color, the comparison with the synthetic magnitudes shows several problems with the observed ones (see section 5.5.6 for details); (6) spectral type derived in this work; (7) galactocentric distance (arc-sec); (8) radial velocity (kms^{-1}) measured in this work, together with the standard deviation and the number of lines used, *'(1σ,n_lines)'*; (9) S/N of the observed spectra; (10) notes.The complete catalogue is available in Tab. A.1.

examples are presented in Fig. 5.7. We have classified 68 stars as A-type (see Fig. 5.8). Our target selection criteria favors the brightest objects in NGC 55, and consequently the sample is biased towards A-type supergiants, the stars with the brightest intrinsic V-magnitudes. In all the example plots, we have marked the most important lines used for spectral classification.

Twelve stars display the typical absorption lines of B- or A-type stars but broad emission in the Balmer lines wings (see for instance C1_32 in Fig. B.5). These might have a nebular origin, nevertheless the width of the wings suggests that they are dominated by stellar emission. A possible explanation for these features is a strong wind, but we might also be witnessing a Be star or even an outburst stage of LBV where other distinctive features (like emission in Fe II lines) are masked by the low spectral resolution (see Walborn & Fitzpatrick 2000). A_42 (see Fig. 5.9) might be an extreme case, where the Balmer lines are completely in emission. We have marked these objects with *'Str. winds?'* in the catalogs.

WRs & LBV candidates

There are seven NGC 55 massive blue stars in the sample that do not belong to the O-, B- or A-spectral bins. These objects are classified as candidate WR or LBV stars. In

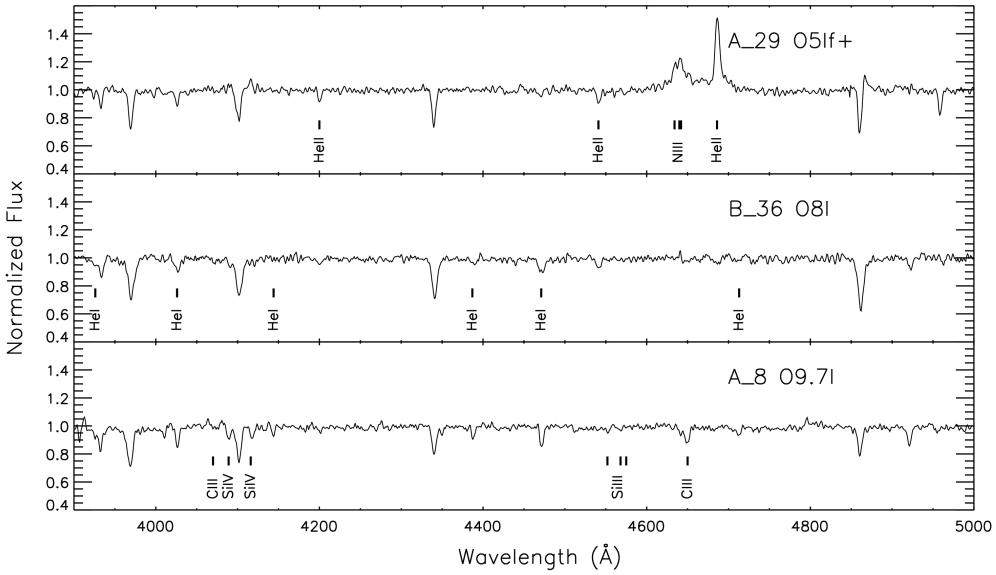

FIGURE 5.6— VLT-FORS2 spectra for a sample of O-type supergiants in NGC 55. The most relevant transitions for spectral classification are shown in the charts. The stars display He I and He II lines; the latter get weaker as we move towards colder types. The labels of Balmer lines have been omitted for clarity.

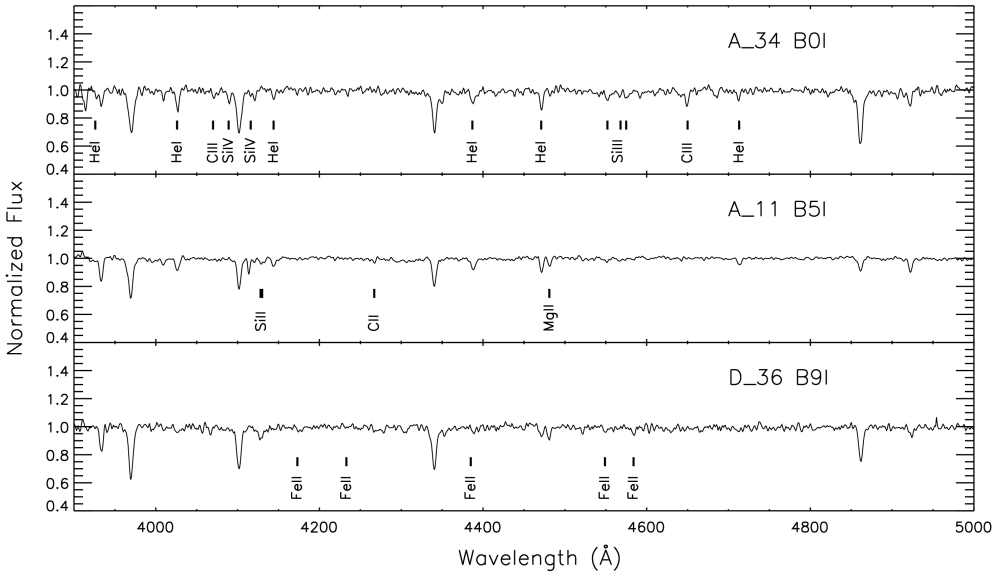

FIGURE 5.7— Optical spectra of B-type supergiants in NGC 55. No He II transitions are seen in the spectra, but He I is still strong in the B0-type. At this temperature range metallic lines start to be relevant. Transitions of carbon, oxygen, silicon and magnesium can be observed, B9-types even display iron lines.

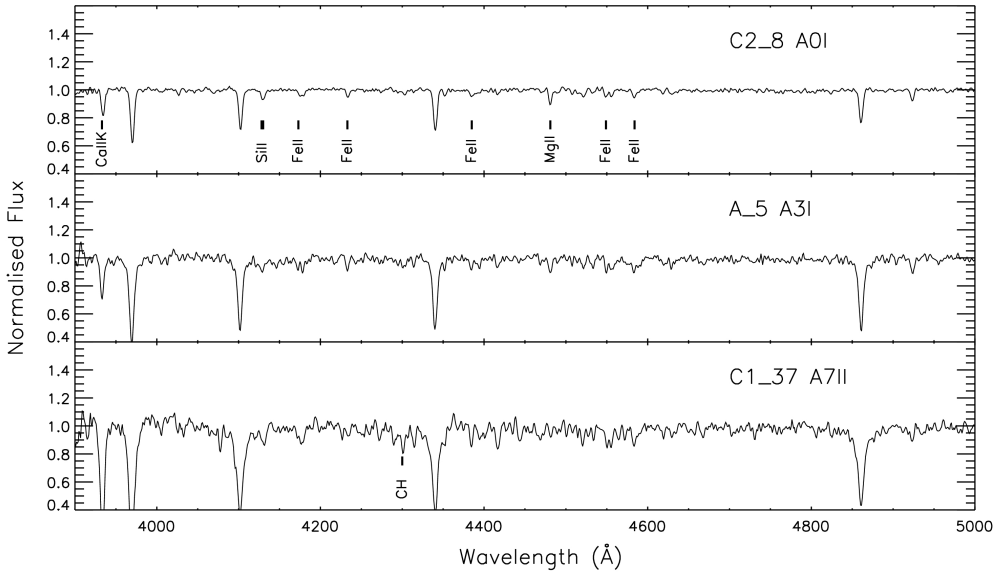

FIGURE 5.8— VLT-FORS2 spectra of A-supergiants in NGC 55. No He I lines are detected, while H I lines become prominent. In the A7 stars the continuum is dominated by many metallic lines. At these temperatures the CH molecular band appears in the optical spectrum at $\sim 4300\,\AA$.

the latters the classification is particularly tricky (as it was commented before), since LBVs undergo different stages during their evolution whose timing and sequence are not understood yet. We looked for similarities of our observations with the spectra of known LBVs or LBV candidates. The objects with positive indentification are marked as LBVc in Tabs. 5.9 and A.1.

Figure 5.9 presents the spectra of the peculiar emission line stars. C1_18 shows the typical features of a WN8 star, namely intense emission lines of He II4686$\AA$ and N III4640$\AA$. Comparison with the templates of Walborn & Fitzpatrick (2000) renders C1_30 an iron star and an LBV candidate. Its spectrum is rich in emission lines of hydrogen, helium and iron. Its overall morphology is very similar to that of the LBV '$\eta-$Carinae', considered by Walborn & Fitzpatrick (2000) *'the mother of all iron stars'*. B_13 displays H I and He I P-Cygni profiles with strong emission in the hydrogen lines, resembling the morphology of He3-519, a possible LBVc or WN1 (Walborn & Fitzpatrick 2000). B_34 falls into the same category, although its P Cygni profiles of He I are weaker, and the Balmer lines show nebular contamination. The spectrum of A_42 presents strong broad emission of the Balmer lines that might be due to strong stellar winds. This is an A-star according to its Mg II, Si II and Ca II lines, but its spectrum also shows transitions of Fe II in emission. That peculiarity hints to

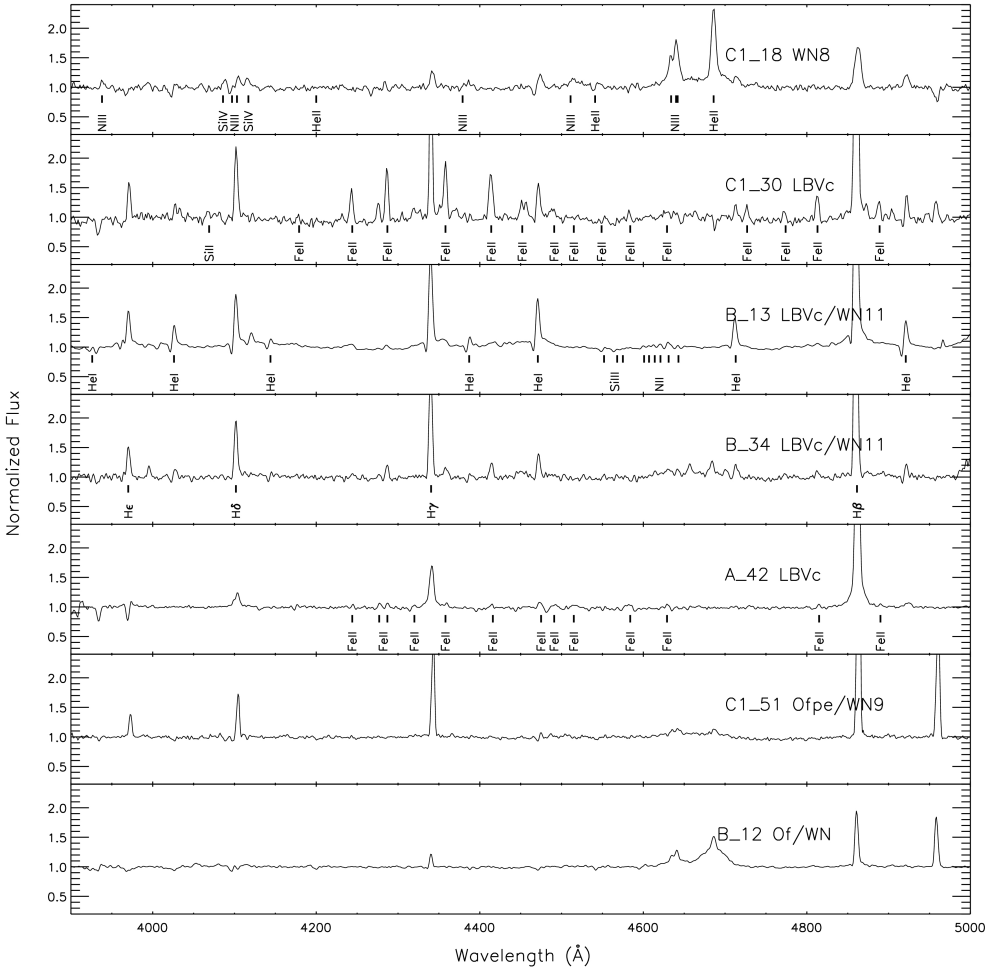

FIGURE 5.9— *Exotic* stars found in our survey of NGC 55. The intense emission (some times P-Cygni profiles) of the Balmer lines indicates a strong stellar wind. Numerous Fe II transitions are distinctive for LBVc, and the strong emission of N III 4640 Å plus He II 4686 *Å* are typical in the spectra of WR.

an LBVc. C1_51 resembles the Ofpn/WN9 objects in Walborn & Fitzpatrick (2000), see also the digital atlas of Bohannan & Walborn (1989). B_12 has typical features of Of stars with N III in emision and He II 4686 *Å* in emission as well. However, we have classified this star as Of/WN due to the broad emission of He II 4686*Å*. Finally, C1_43 (not included in Fig. 5.9) shows features that might be interpreted as Fe II in emission, but the S/N of its spectrum is too poor to be conclusive.

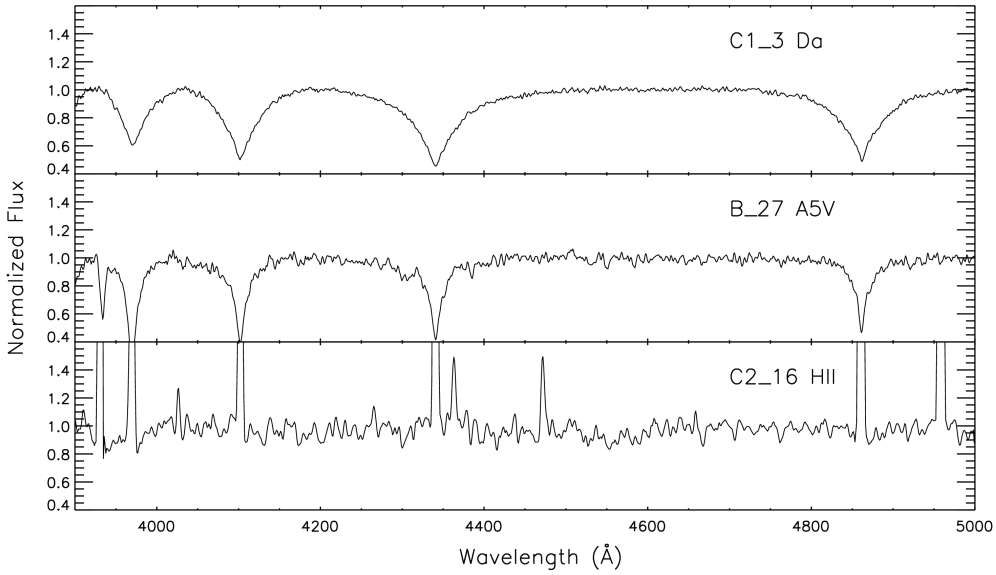

FIGURE 5.10— Examples of *unwanted* detections: a white dwarf (top), an A5V from the Milky Way (middle) and an example of spectra dominated by H II emission (bottom).

Contamination of the Sample

Examples of *undesired* objects that entered our sample are shown in Fig. 5.10. It includes what we have classified as an H II region: a poor S/N spectrum that displays only emission lines (it could be the composition of several regions). Figure 5.10 also includes a low luminosity class A-type star, which was discarded as NGC 55 member. At the distance of NGC 55 a V-class star would be too faint to be observed, so these are likely foreground Milky Way stars. Although their radial velocities concur with the projected position on NGC 55, they are also consistent with the velocity of stars from the halo (Brown et al. 2006).

5.4 Radial Velocity Distribution

Radial velocities were determined from the Doppler wavelength shift of strong absorption lines (Balmer lines, He I, He II and metallic transitions of Mg II and Si III), together with the standard deviation and the number of lines used (dependent on both the spectral type of the star, and the data quality). The values, compiled in Tab. 5.9 and appendix A, were calculated in the heliocentric system. The sampling of the spectra (~ 1 *Å*) introuces a limit on the accuracy of $\sim 35\ km\,s^{-1}$, we adopt this conservative value as an average uncertainty of the sample.

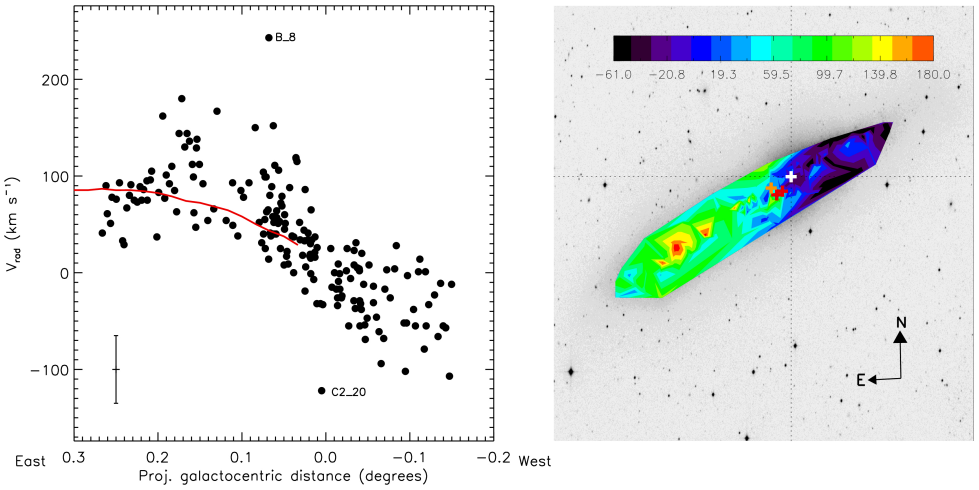

FIGURE 5.11— Left panel: stellar radial velocities of NGC 55 massive blue stars as a function of the projected galactocentric distance (the systemic velocity of NGC 55, $\sim 124\ kms^{-1}$, has been subtracted). The galaxy's rotation curve derived by Puche et al. (1991) from neutral hydrogen (solid red line) is included for comparison, showing good agreement with our results.The average error considered of $\pm 35\ kms^{-1}$ is plotted in the bottom-left corner. The two objects (C2_20 and B_8) found with a particular velocity, compared with the general behavior, are also marked. Right panel: A rough 2D dynamical map of NGC 55. The dynamical center (orange cross) is shifted to the south east compared with the optical one (white cross), and fits well the $24\,\mu m$ sources found by Engelbracht et al. (2004) (red crosses).

The resulting radial velocities are plotted in Fig. 5.11 as a function of the projected galactocentric distance, which is calculated with respect to the optical center of NGC 55 (α=00h14m53.60s δ=$-$39d11m47.9s [J2000], Two Micron All Sky Survey team 2003). We have also plotted the rotation curve derived from H I observations by Puche et al. (1991). The left pannel of Fig. 5.11 shows how the radial velocities derived from the stellar population trace the rotation of the galaxy, even in its outer parts simililarly to what was found by Evans et al. (2007) in NGC 3109. The systemic velocity of NGC 55 is $\sim 124\ kms^{-1}$, very similar to the 129 kms^{-1} obtained by Koribalski et al. (2004).

The radial velocity 2-D map distribution is shown in the right panel of Fig. 5.11. The dynamical center is located at α=00h15m02.37s δ=$-$39d12m18.61s, slightly shifted from the optical one, 2.25′ at the southest. Our calculated position for the center matches that of the centroid of H I determined by Puche et al. (1991), within the uncertainties of both works. It also correlates fairly well with two sources detected by Engelbracht et al. (2004) at $24\,\mu m$, in an optical obscured area near the center, likely related to the bar suggested by de Vaucouleurs (1961). However, the number of objects we handle is too small for an accurate dynamical study.

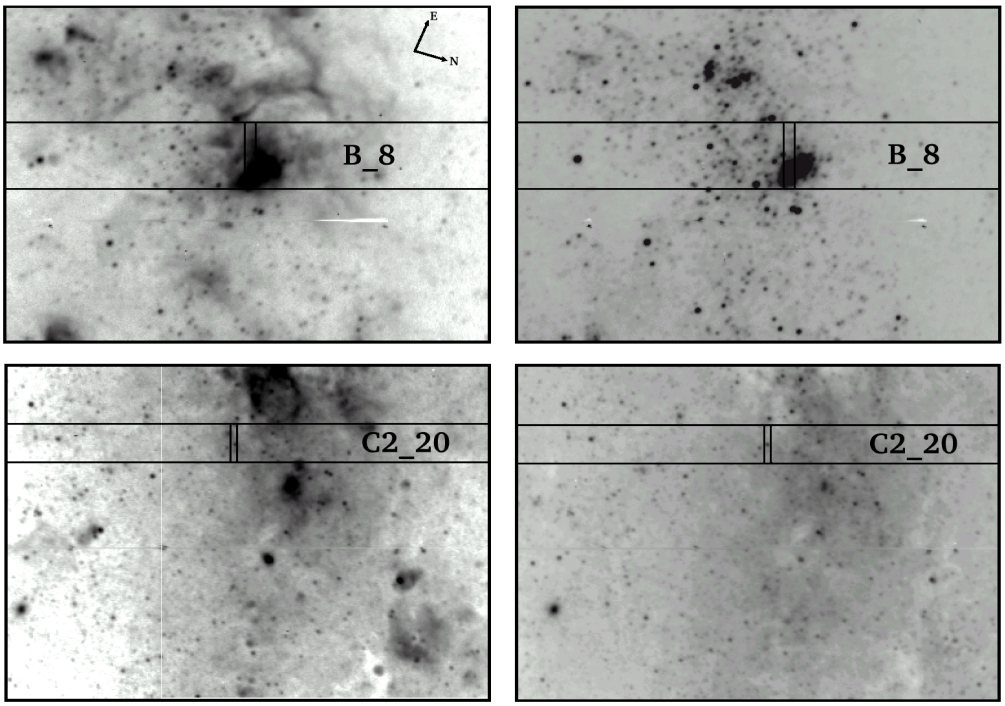

FIGURE 5.12— V-band (right) and Hα (left) images taken with FORS2. The position of the slits used to get the spectrum of B_8 (top) and C2_20 (bottom) are marked on the image. B_8 is close to a large H II structure which explains the discrepancy in the velocity measured, while C2_20 is located near the center of NGC 55 and apparently isolated.

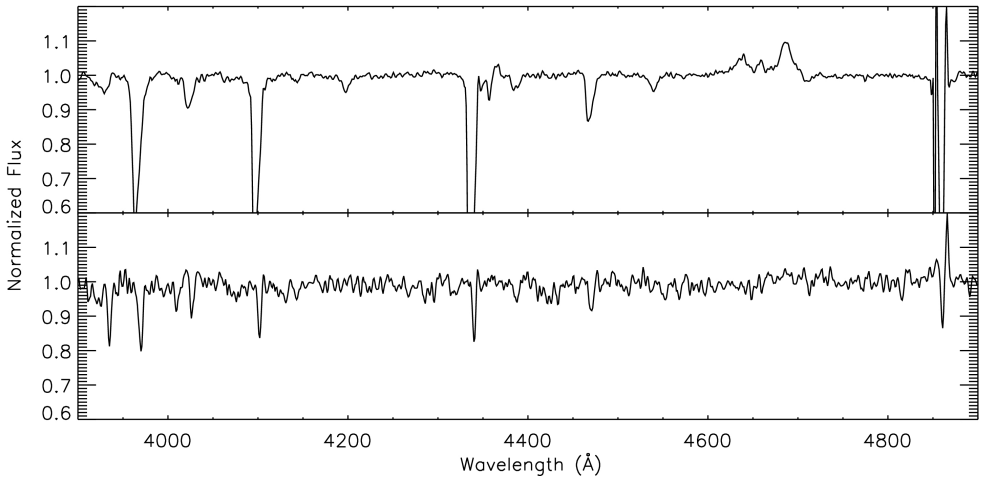

FIGURE 5.13— Spectra of objects with anomalous radial velocity in our NGC 55 sample. The broad profiles in B_8 hint to a cluster instead of a individual star spectrum, nonetheless the features are characteristics of O-type stars. C2_20 does not show any clear reason for its radial velocity, nevertheless the spectral S/N is low.

The error bars of the results and the high inclination angle of NGC 55 prevent us from going into further detail, such as substructures in the galaxy. Note, however, that there seems to be an additional off-set trend in the rotation curve (see Fig. 5.11). In addition, two objects deviate completely from the normal behavior. C2_20 (B2I) has a very small radial velocity while B_8 (O9If) presents a high radial velocity, compared to the expected value at their galactic position.

B_8 is located in a crowded region with nebulosity, clearly seen in the Hα image (see Fig. 5.12). This object presents the typical absorption lines of an O-type star, but we suspect it is in fact a group of stars. Its bright magnitude compared to other O-stars and the shape of the line profiles agree with this hypothesis (see Fig. 5.13). In addition, the spectrum is clearly affected by the nebular emission around the object.

The spectrum of C2_20 exhibits no hint as to the reason for its small radial velocity. Arguably, it might be a Galactic star. However, this would be inconsistent with its classification as a supergiant since it would be brighter. Moreover, it is in the center of NGC 55 and close to different clusters which show evidence of intense stellar activity. Therefore, we cannot exclude the possibility that it has been ejected by a nearby supernova explosion or is a binary. Any of these hypotheses could explain its peculiar radial velocity, although we must be cautious with this object due to the moderate S/N of its spectrum (Fig. 5.13).

5.5 Quantitative Analysis

The quantitative spectroscopic analysis of our complete sample of massive blue stars in NGC 55 would require a large amount of manpower and computational resources. However, the technique described in chapter 4 simplifies the process. Even though the method has some caveats, it is the most efficient for low resolution spectra (see section 4.2.6).

We have analyzed all the objects with spectral type comprised between O8 and B9, and luminosity class I or II included in our sample. These are the typical spectral types with physical properties presumably included in the parameter space of our grid (see section 4.1). In total, 75 stars have been analized in NGC 55. Their S/N quality is rather heterogeneous, which propagates to the error bars. The candidates selected are listed in Tab. 5.10.

5.5.1 Stellar Parameters

The stars were analyzed following the method described in section 4.2.1. The derived stellar parameters, including errors, are provided in Tab. 5.11. To illustrate the quality of the analysis, Figs. 5.14 – 5.15 show the comparison of the observed optical spectra with the best solution obtained by our algorithm for a sub-sample of twelve stars. The comparison of the best-fitting model and the observed data can be found in the

TABLE 5.10— O8-B9 supergiants selected for the quantitative analysis. A description of each column is provided in Tab. 5.9.

ID (1)	RA(J2000) (2)	DEC(J2000) (3)	V (4)	V-Ic (5)	Spec. Type (6)	Rg (7)	v_r (8)	S/N (9)
D_1	0:14:08.97	-39:09:20.88	20.212	-0.557	B9I	-671.79	112 (27,6)	43
D_4	0:14:12.11	-39:09:23.41	19.724	-0.524	B9I	-625.02	69 (17,8)	60
D_5	0:14:13.22	-39:09:19.79	19.963	-0.813	B3I	-608.56	113 (25,7)	44
D_9	0:14:16.74	-39:10:02.28	19.355	-0.563	B5I	-554.71	91 (18,8)	93
D_11	0:14:18.14	-39:10:14.16	18.447	-0.595	B3I	-533.37	45 (18,9)	199
D_14	0:14:20.02	-39:10:32.15	20.582	-0.728	B2.5I	-504.73	125 (6,2)	30
D_13	0:14:20.39	-39:09:49.32	20.375	-0.787	B1I	-500.77	138 (35,3)	42
D_16	0:14:22.80	-39:09:51.83	20.199	-0.868	B0.5II	-464.75	86 (17,7)	30
D_23	0:14:24.92	-39:10:00.11	19.330	-0.743	B2.5II	-432.89	121 (31,6)	58
D_28	0:14:28.63	-39:10:53.04	19.613	-0.784	B0.5I	-375.37	128 (34,8)	32
D_27	0:14:28.73	-39:10:17.76	19.191	-0.642	B2I	-375.34	152 (39,7)	76
D_31	0:14:32.04	-39:10:34.68	19.951	-0.767	B2I	-325.28	127 (45,4)	29
D_36	0:14:35.07	-39:11:20.04	19.189	-0.689	B9I	-278.26	78 (11,7)	70
D_42	0:14:40.33	-39:10:57.35	18.700	-0.801	B1.5I	-200.63	112 (12,6)	53
C1_5	0:14:42.10	-39:12:40.32	19.249	-0.794	B2.5I	-174.61	128 (21,11)	82
C1_4	0:14:43.39	-39:11:20.04	18.863	-0.606	B1.5I	-153.82	147 (15,8)	71
C2_5	0:14:43.57	-39:11:14.29	19.215	-0.832	B3I	-151.41	132 (13,8)	55
C1_9	0:14:45.54	-39:12:38.17	18.939	-0.817	B1I	-123.77	118 (20,8)	86
C1_8	0:14:45.70	-39:11:52.08	18.920	-0.791	B8I	-118.58	149 (18,8)	72
C2_14	0:14:48.05	-39:12:45.72	19.044	-0.944	B8I	88.67	130 (21,9)	112
C2_11	0:14:48.33	-39:11:20.75	18.545	-1.800	O8I	-80.41	98 (9,3)	67
C1_15	0:14:50.50	-39:12:36.35	19.642	-0.765	B8I	53.31	158 (26,6)	69
C1_13	0:14:51.86	-39:10:57.35	18.948	-0.706	B1I	-37.92	115 (20,8)	60
C2_18	0:14:52.32	-39:12:05.76	19.453	-0.591	B2.5II	21.52	92 (19,10)	42
C2_17	0:14:52.76	-39:11:29.04	18.748	-0.902	B0.5I	-16.32	149 (21,8)	51
C2_21	0:14:53.46	-39:12:35.64	19.719	-0.662	B2I	26.30	145 (22,7)	30
C2_20	0:14:53.58	-39:12:06.11	18.745	-0.262	B2I	10.01	2 (11,6)	65
C2_29	0:14:56.75	-39:11:56.40	18.335	-0.638	B8I	47.50	150 (19,5)	63
C1_32	0:14:58.59	-39:13:52.68	17.122	-0.563	B9I	102.93	161 (10,7)	241
C2_36	0:15:02.11	-39:11:35.87	19.325	-0.787	B8I	127.83	142 (32,5)	28
C1_34	0:15:02.58	-39:12:30.60	18.962	-0.789	B8I	137.00	176 (12,7)	69
C1_38	0:15:03.16	-39:14:02.03	19.603	-0.849	B0I	163.24	175 (20,4)	38
C2_43	0:15:04.19	-39:13:22.80	19.985	-0.687	B9II	168.27	212 (19,6)	30
C1_40	0:15:08.71	-39:12:09.73	20.010	-0.627	B1.5I	227.06	184 (24,8)	59
C2_46	0:15:09.18	-39:12:55.44	18.941	-0.672	B1I	237.18	196 (26,6)	75
C2_47	0:15:10.45	-39:12:39.97	19.459	-0.508	B9I	254.68	230 (18,8)	43
C2_48	0:15:11.24	-39:12:38.17	19.371	-0.456	B5I	266.36	188 (40,6)	58
C1_44	0:15:11.29	-39:12:34.55	19.037	-0.740	B0I	266.90	181 (42,5)	79
C1_45	0:15:11.31	-39:12:50.40	19.607	-0.180	B1I	268.32	179 (20,9)	38
C2_49	0:15:11.82	-39:12:43.92	20.154	-0.570	B1I	275.40	235 (17,5)	33
C2_50	0:15:12.18	-39:12:52.56	20.159	-0.433	B1I	281.50	276 (11,6)	34
C2_51	0:15:12.68	-39:12:56.51	19.719	-0.764	B9I	289.24	213 (24,7)	61
C1_48	0:15:13.11	-39:12:47.16	19.519	-0.715	B0.5I	294.93	164 (24,6)	30

C2_54	0:15:14.34	-39:13:27.84	19.435	-0.497	B9I	317.20	223 (9,8)	51
C1_53	0:15:14.64	-39:13:36.12	19.816	-0.485	B2.5I	322.60	164 (16,4)	45
B_9	0:15:14.66	-39:13:03.72	19.416	-0.524	B5I	319.34	223 (28,6)	57
C2_55	0:15:15.95	-39:12:54.36	19.185	-0.277	B5I	337.85	228 (26,8)	39
B_11	0:15:16.74	-39:12:46.08	19.001	0.206	B1I	349.09	155 (17,9)	61
B_22	0:15:19.73	-39:14:48.12	18.274	-0.268	B2.5I	408.46	202 (22,9)	143
B_23	0:15:24.24	-39:13:04.79	19.531	-0.586	B2I	462.36	209 (22,10)	77
B_26	0:15:26.91	-39:13:28.92	20.116	-0.891	O9I	504.13	217 (36,8)	52
B_30	0:15:31.27	-39:14:30.12	19.591	-0.012	B9I	575.47	291 (27,5)	74
B_31	0:15:32.22	-39:14:40.20	19.429	-0.478	B2.5I	590.90	190 (23,8)	95
B_35	0:15:36.86	-39:15:10.79	20.291	-0.513	B1.5I	663.87	236 (30,4)	30
A_1	0:15:38.52	-39:14:49.21	19.099	-0.777	B1I	685.46	262 (17,8)	110
A_2	0:15:38.64	-39:14:52.43	19.227	-0.632	B1.5I	687.62	253 (25,8)	77
A_7	0:15:41.99	-39:15:30.95	19.901	-0.650	B2I	742.73	254 (25,10)	73
A_8	0:15:44.18	-39:14:58.20	19.792	-0.188	O9.7I	770.70	304 (27,9)	62
A_11	0:15:45.17	-39:15:56.15	18.706	-0.245	B5I	793.59	209 (25,11)	130
A_14	0:15:49.14	-39:15:35.64	19.139	-0.279	B9I	849.33	225 (8,7)	115
A_15	0:15:49.93	-39:15:28.80	18.794	-0.475	B3I	860.21	201 (20,8)	154
A_16	0:15:50.25	-39:15:43.92	19.590	-0.518	B0.5I	867.08	286 (19,6)	121
A_25	0:15:50.78	-39:17:29.40	19.687	-0.504	B8I	893.29	229 (17,10)	86
A_17	0:15:51.42	-39:15:57.60	20.336	-0.321	B1I	886.44	207 (25,8)	79
A_26	0:15:55.45	-39:15:30.60	19.236	-0.262	B2.5I	942.47	220 (17,11)	96
A_30	0:15:57.58	-39:16:14.51	19.468	-0.795	O9I	980.26	199 (73,4)	44
A_27	0:15:58.03	-39:14:27.60	19.928	-0.477	B2I	973.83	199 (29,8)	66
A_31	0:15:58.22	-39:16:14.16	20.288	-0.592	O9I	989.71	213 (27,7)	46
A_34	0:16:01.17	-39:16:34.67	20.247	-0.875	B0I	1036.66	215 (22,10)	68
A_36	0:16:02.33	-39:16:48.72	20.758	-0.418	B2I	1056.24	191 (24,7)	39
A_37	0:16:02.90	-39:17:04.91	20.024	-0.603	B0.5I	1067.34	153 (22,5)	71
A_39	0:16:05.30	-39:16:45.84	20.451	-0.021	B5I	1099.75	217 (24,7)	51
A_40	0:16:08.02	-39:15:52.20	19.938	-0.484	B5I	1132.32	200 (22,10)	67
A_41	0:16:09.00	-39:16:18.84	20.114	-0.445	B1I	1150.65	202 (24,8)	52
A_45	0:16:10.98	-39:17:19.68	20.710	-0.726	B0I	1189.70	165 (28,9)	44

appendices for the complete sample analyzed (see Figs. B.1–B.13). It can be seen in these figures that the final best fitting models match fairly well the observations.

The right side of these figures display χ^2 isocontours in the $T_{eff} - log\,(g)$ plane, a measurement of the resemblance of the models to the observations as defined in section 4.2.1. The entire $T_{eff} - log\,(g)$ mesh is represented by black dots, those models that provide the best fit (i. e. their χ^2-value fulfill the criteria imposed, see section 4.2.1) are marked with red dots.

The impact of the S/N can be gauged from these plots. For stars like A_11 and B_31, the models that would reproduce the observations are a smaller set than in the case of C1_45. The better data quality is clearly reflected in the range of stellar parameters compatible with the observed data, following the criteria suggested in this work. Note how the wide range of temperatures and gravities covered by the grid

prevented, in these twelve examples, the presence of results near the borders of the model grid. The method cannot be extrapolated beyond these boundaries, therefore values derived for objects close to these limits must be re-analyzed with the appropiate set of parameters. In the full analysis gathered in appendix B, several objects are close these critical edges. For instance, the results obtained for C1_32 and B_30 (see Figs. B.5 and B.9 respectively) suggest lower surface gravities. These objects show emissions in the Balmer lines, that could indicate strong winds or even an LBV stage. Instead in C2_11 (Fig. B.4) the limit is imposed by the temperature, our χ^2-method hints a larger effective temperature than the maximum available in the grid.

We would like to remind the reader that the Q-parameter, without H_α, is only a rough indication of the stellar wind, and it is only weakly constrained by the rest of Balmer lines in the spectra, mainly H_β (see section 4.2.3 for a detailed summary of the main caveats derived from the χ^2-method and the observed data).

The silicon abundances, shown in Tab. 5.11, are obtained during the first step, based on a coarse set of values, just four points in the grid (see the grid description in section 4.1). These first estimations are improved later on, along with abundances for other species, in the detailed chemical study.

5.5.2 Chemical Composition

The chemical abundances derived from stellar spectra of massive blue stars constitute a powerful tool to study the galactic chemical evolution of NGC 55. The technique followed, described in chapter 4, is not straightforward at low resolution and a careful examination is essential for an accurate determination. Obviously in extreme cases where the quality is low the accuracy will be lower as well, for instance for D_14 (see Fig. B.1).

An error of 0.25 *dex* was adopted as an average of the different uncertainties estimated, taking into account the S/N ratio of each spectrum, and the results obtained in the automatic first step, where errors in gravity and temperature were included into the analysis (see section 4.2.1).

Table 5.12 compiles the abundance obtained for each star. In the low temperature regime (around 15000 K) we have omitted the carbon, oxygen and nitrogen analyses since their transitions, in the studied spectral range, start to be too faint. Similarly, the magnesium abundance was not estimated for hotter objects ($T_{eff} \gtrsim 25000\ K$).

Systematic Effects

The effective temperature may play correlate with systematic errors in the chemical abundances determination. Thus, the magnesium abundance, for instance, is easily obtained at lower temperature ($\sim$ 12000) since the Mg II 4481 $\AA$ is stronger than at high temperatures, therefore it could introduce systematic effects in the results. We

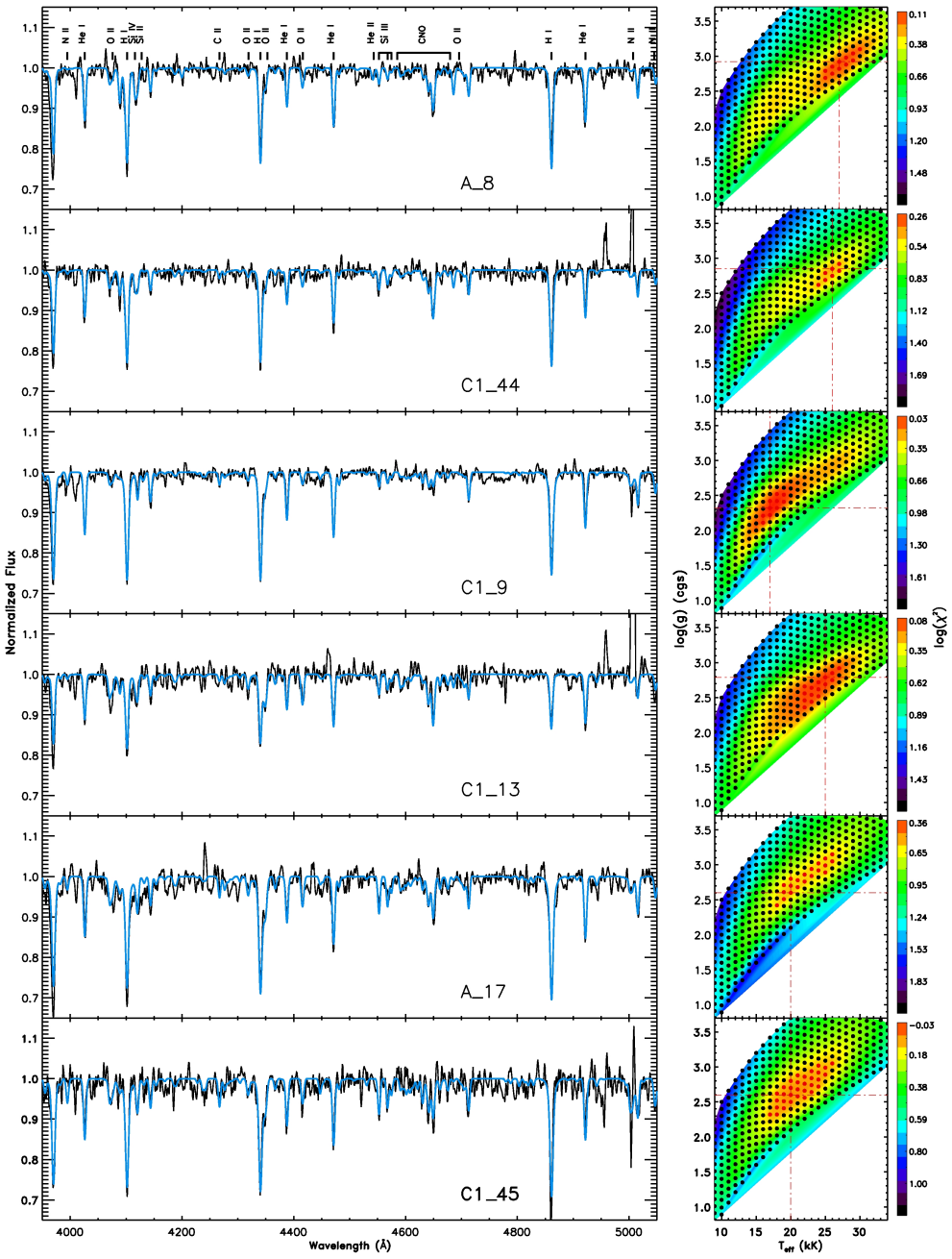

FIGURE 5.14— Left panel: NGC 55 spectra (black) plus best fit model (blue) obtained by our automatic method together with a subsequent detailed abundance analysis. The main transitions used in the study are marked in the top chart. Right panel: χ^2 difference between observations and the entire grid models in the $T_{eff} - log\,(g)$ parameter space. $log\,(\chi^2)$ has been color-coded from red (minimum, better fit) to blue (maximum). Black dots represent all the grid models; the models whose parameters have been averaged to produce the stellar parameters are marked with red dots.

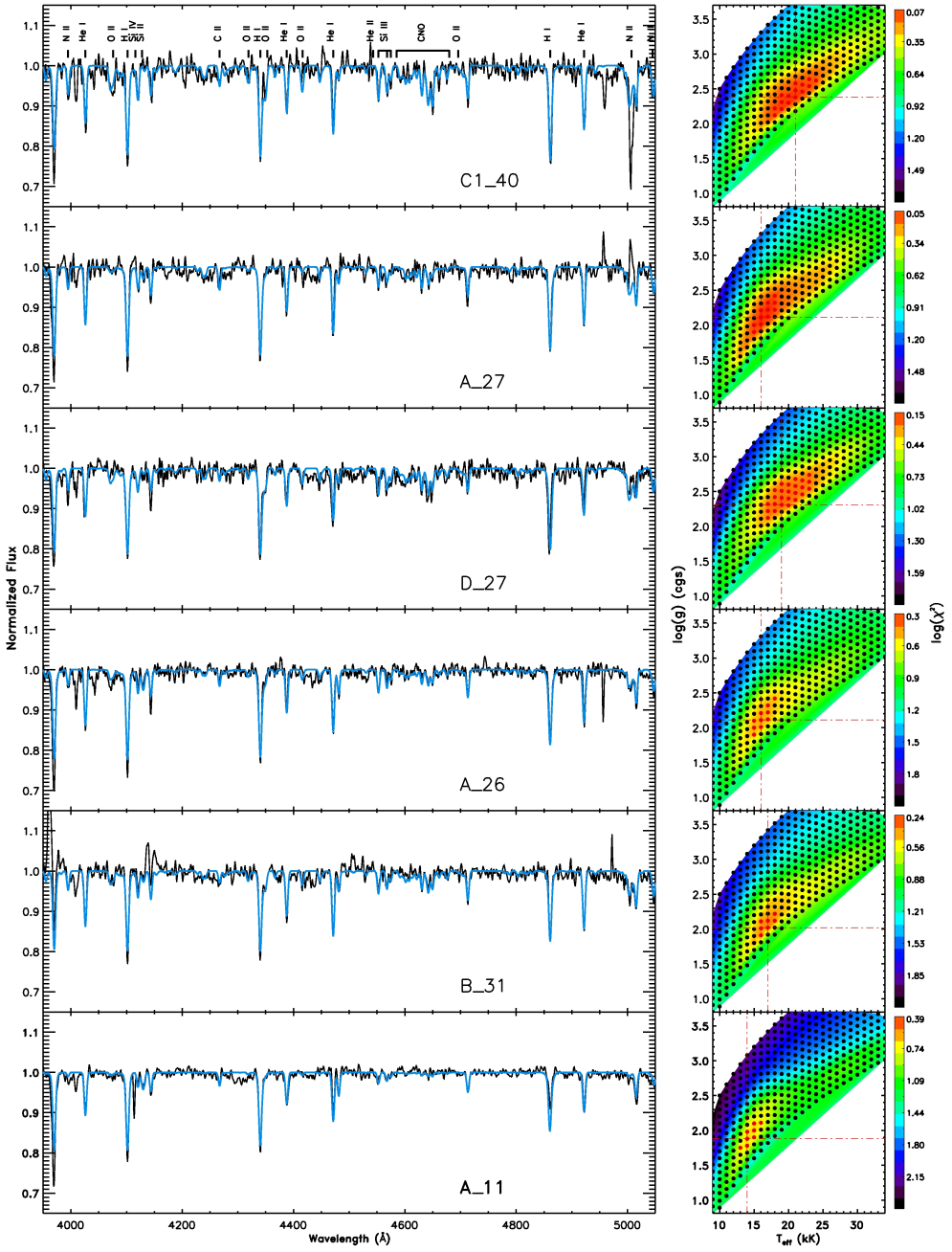

FIGURE 5.15— Figure 5.14, continued.

TABLE 5.11— Stellar parameters derived for the NGC 55 sample enclosed in Tab. 5.10. Different columns include: (1) identification number; (2) effective temperature; (3) surface gravity; (4) microturbulence; (5) helium abundance with respect to hydrogen (number density ratio); (6) first silicon abundance estimation (see text for additional details) ; (7) wind Q-parameter (see Eq. 4.6).

ID (1)	T_{eff} (K) (2)	$log(g)$ (cgs) (3)	ξ (kms^{-1}) (4)	He /H (5)	$Si/Si_{\odot}$ (6)	$log(Q)$ (7)
D_1	13851 ± 3115	2.20 ± 0.49	11.8 ± 3.3	0.09 ± 0.05	0.60 ± 0.34	-13.70 ± 0.46
D_4	11591 ± 1775	1.69 ± 0.35	14.7 ± 5.2	0.10 ± 0.05	0.58 ± 0.35	-13.15 ± 0.35
D_5	17628 ± 2666	2.43 ± 0.26	15.7 ± 5.5	0.09 ± 0.04	0.65 ± 0.36	-13.57 ± 0.33
D_9	13366 ± 1161	1.84 ± 0.21	11.3 ± 2.6	0.11 ± 0.05	0.35 ± 0.18	-13.07 ± 0.20
D_11	14391 ± 747	1.87 ± 0.13	11.6 ± 2.9	0.14 ± 0.05	0.61 ± 0.31	-12.37 ± 0.20
D_14	22622 ± 4077	3.01 ± 0.37	20.1 ± 6.9	0.13 ± 0.05	0.76 ± 0.35	-13.93 ± 0.54
D_13	23819 ± 4202	2.62 ± 0.24	18.5 ± 6.5	0.09 ± 0.05	0.40 ± 0.23	-13.00 ± 0.44
D_16	19602 ± 3512	2.38 ± 0.34	18.8 ± 6.8	0.12 ± 0.05	0.65 ± 0.34	-12.90 ± 0.42
D_23	16303 ± 1624	2.33 ± 0.25	13.3 ± 4.4	0.10 ± 0.05	0.74 ± 0.36	-13.08 ± 0.22
D_28	25978 ± 2122	2.79 ± 0.22	20.5 ± 6.5	0.13 ± 0.05	0.80 ± 0.33	-12.72 ± 0.46
D_27	19406 ± 1614	2.41 ± 0.15	14.4 ± 4.6	0.10 ± 0.05	0.48 ± 0.29	-13.18 ± 0.20
D_31	25366 ± 5901	2.82 ± 0.45	17.1 ± 6.7	0.11 ± 0.05	0.58 ± 0.34	-13.10 ± 0.58
D_36	11556 ± 1289	1.69 ± 0.29	15.2 ± 5.0	0.10 ± 0.05	0.65 ± 0.36	-13.04 ± 0.30
D_42	18112 ± 2223	2.25 ± 0.25	17.2 ± 5.9	0.13 ± 0.05	0.44 ± 0.27	-12.72 ± 0.41
C1_5	15670 ± 1444	2.14 ± 0.19	16.8 ± 5.9	0.13 ± 0.05	0.36 ± 0.20	-12.98 ± 0.31
C1_4	17815 ± 1854	2.27 ± 0.20	14.0 ± 4.0	0.14 ± 0.05	0.75 ± 0.35	-12.81 ± 0.20
C2_5	15226 ± 1464	2.03 ± 0.25	15.9 ± 5.7	0.13 ± 0.05	0.53 ± 0.32	-12.69 ± 0.20
C1_9	17450 ± 1464	2.37 ± 0.18	11.8 ± 3.3	0.15 ± 0.05	0.32 ± 0.15	-13.37 ± 0.27
C1_8	12096 ± 1128	1.62 ± 0.26	15.8 ± 6.0	0.11 ± 0.05	0.55 ± 0.34	-12.91 ± 0.21
C2_14	12445 ± 896	1.67 ± 0.21	17.8 ± 5.1	0.11 ± 0.06	0.58 ± 0.34	-12.88 ± 0.20
C2_11	32763 ± 1157	3.26 ± 0.16	12.9 ± 4.4	0.13 ± 0.05	0.68 ± 0.34	-12.75 ± 0.51
C1_15	13163 ± 1854	1.96 ± 0.33	12.5 ± 3.5	0.09 ± 0.05	0.73 ± 0.36	-13.13 ± 0.30
C1_13	24257 ± 1438	2.69 ± 0.15	17.7 ± 5.7	0.15 ± 0.05	0.57 ± 0.28	-12.60 ± 0.20
C2_18	16514 ± 2458	2.28 ± 0.34	14.1 ± 5.0	0.10 ± 0.05	0.63 ± 0.35	-13.32 ± 0.33
C2_17	23568 ± 4632	2.77 ± 0.28	15.8 ± 5.5	0.15 ± 0.05	0.50 ± 0.30	-13.42 ± 0.43
C2_21	20135 ± 2981	2.56 ± 0.29	17.4 ± 6.4	0.13 ± 0.05	0.70 ± 0.35	-13.23 ± 0.50
C2_20	15381 ± 2092	1.89 ± 0.27	15.5 ± 5.5	0.11 ± 0.05	0.74 ± 0.34	-12.38 ± 0.22
C2_29	13901 ± 2435	1.68 ± 0.29	17.3 ± 6.6	0.12 ± 0.05	0.59 ± 0.33	-12.39 ± 0.22
C1_32	10357 ± 698	1.02 ± 0.15	19.8 ± 6.1	0.12 ± 0.06	0.37 ± 0.17	-12.12 ± 0.20
C2_36	11475 ± 1746	1.54 ± 0.38	24.2 ± 5.4	0.12 ± 0.06	0.90 ± 0.31	-12.76 ± 0.32
C1_34	12944 ± 2120	1.75 ± 0.41	12.5 ± 4.1	0.08 ± 0.05	0.72 ± 0.35	-12.52 ± 0.20
C1_38	21525 ± 4051	2.56 ± 0.25	17.9 ± 6.3	0.13 ± 0.05	0.47 ± 0.29	-12.93 ± 0.37
C2_43	11729 ± 2218	1.92 ± 0.46	14.1 ± 5.1	0.11 ± 0.06	0.59 ± 0.35	-13.62 ± 0.45
C1_40	20342 ± 1806	2.41 ± 0.14	23.4 ± 5.3	0.14 ± 0.05	0.35 ± 0.18	-13.19 ± 0.21
C2_46	20538 ± 1974	2.45 ± 0.18	13.4 ± 4.3	0.12 ± 0.05	0.51 ± 0.29	-12.85 ± 0.22
C2_47	14321 ± 2083	1.97 ± 0.32	14.5 ± 5.7	0.12 ± 0.06	0.57 ± 0.34	-12.90 ± 0.31
C2_48	13972 ± 1820	1.87 ± 0.30	14.7 ± 5.8	0.11 ± 0.05	0.55 ± 0.33	-12.68 ± 0.24
C1_44	26182 ± 1484	2.83 ± 0.15	17.8 ± 6.3	0.10 ± 0.05	0.43 ± 0.25	-12.93 ± 0.30
C1_45	21484 ± 2553	2.73 ± 0.24	19.0 ± 6.1	0.12 ± 0.05	0.54 ± 0.31	-13.65 ± 0.36

C2_49	23337 ± 2792	3.02 ± 0.20	25.2 ± 5.2	0.07 ± 0.03	0.52 ± 0.30	-14.12 ± 0.44
C2_50	23334 ± 3953	2.79 ± 0.23	16.6 ± 6.0	0.08 ± 0.04	0.45 ± 0.27	-13.47 ± 0.53
C2_51	12045 ± 1548	1.64 ± 0.34	17.1 ± 6.4	0.10 ± 0.05	0.64 ± 0.36	-12.76 ± 0.31
C1_48	25873 ± 4157	3.07 ± 0.27	23.4 ± 6.0	0.14 ± 0.05	0.63 ± 0.34	-13.74 ± 0.54
C2_54	10949 ± 1532	1.52 ± 0.36	23.2 ± 5.5	0.12 ± 0.06	0.60 ± 0.35	-12.97 ± 0.35
C1_53	18242 ± 2043	2.54 ± 0.26	16.4 ± 5.8	0.10 ± 0.05	0.60 ± 0.34	-13.73 ± 0.35
B_9	17211 ± 4814	2.28 ± 0.37	15.6 ± 6.0	0.11 ± 0.05	0.32 ± 0.15	-13.51 ± 0.35
C2_55	14207 ± 2331	1.85 ± 0.33	17.3 ± 6.4	0.13 ± 0.05	0.62 ± 0.35	-12.63 ± 0.32
B_11	14364 ± 1882	2.65 ± 0.37	26.8 ± 3.9	0.13 ± 0.06	0.48 ± 0.28	-14.02 ± 0.23
B_22	17030 ± 2097	2.02 ± 0.23	13.7 ± 4.2	0.16 ± 0.04	0.49 ± 0.30	-12.31 ± 0.20
B_23	17291 ± 939	2.29 ± 0.15	19.0 ± 5.6	0.10 ± 0.05	0.52 ± 0.28	-13.20 ± 0.20
B_26	31050 ± 2979	3.38 ± 0.19	15.1 ± 5.7	0.13 ± 0.05	0.53 ± 0.32	-13.56 ± 0.59
B_30	25061 ± 3072	2.54 ± 0.20	14.2 ± 5.0	0.14 ± 0.05	0.65 ± 0.35	-11.78 ± 0.22
B_31	16680 ± 889	2.09 ± 0.13	20.4 ± 5.6	0.14 ± 0.05	0.30 ± 0.12	-12.83 ± 0.20
B_35	22276 ± 4164	2.71 ± 0.36	16.1 ± 6.2	0.16 ± 0.05	0.71 ± 0.35	-12.99 ± 0.51
A_1	20081 ± 1486	2.46 ± 0.11	17.9 ± 4.3	0.16 ± 0.04	0.45 ± 0.24	-12.72 ± 0.20
A_2	19598 ± 1721	2.62 ± 0.14	28.0 ± 2.8	0.06 ± 0.03	0.32 ± 0.14	-14.05 ± 0.25
A_7	17426 ± 1088	2.22 ± 0.16	23.9 ± 5.2	0.12 ± 0.05	0.44 ± 0.23	-12.71 ± 0.20
A_8	27719 ± 1246	2.91 ± 0.13	20.3 ± 5.8	0.14 ± 0.05	0.43 ± 0.25	-12.79 ± 0.33
A_11	14425 ± 979	1.94 ± 0.18	11.8 ± 3.7	0.10 ± 0.05	0.59 ± 0.33	-12.64 ± 0.20
A_14	11803 ± 925	1.59 ± 0.24	16.9 ± 4.6	0.10 ± 0.05	0.82 ± 0.32	-12.63 ± 0.22
A_15	14848 ± 865	1.91 ± 0.13	11.1 ± 2.6	0.12 ± 0.04	0.34 ± 0.17	-12.80 ± 0.20
A_16	23611 ± 1085	2.63 ± 0.14	18.9 ± 3.9	0.16 ± 0.04	0.54 ± 0.16	-12.88 ± 0.35
A_25	12934 ± 1323	1.87 ± 0.27	14.1 ± 4.7	0.09 ± 0.05	0.61 ± 0.35	-13.09 ± 0.24
A_17	22524 ± 2357	2.85 ± 0.16	20.7 ± 5.3	0.10 ± 0.04	0.32 ± 0.15	-13.90 ± 0.33
A_26	16070 ± 962	2.15 ± 0.17	17.1 ± 6.5	0.12 ± 0.05	0.47 ± 0.27	-12.86 ± 0.20
A_30	14322 ± 2396	2.42 ± 0.36	19.1 ± 7.1	0.13 ± 0.06	0.52 ± 0.31	-13.94 ± 0.37
A_27	16274 ± 1110	2.13 ± 0.19	20.4 ± 5.7	0.12 ± 0.05	0.35 ± 0.19	-12.90 ± 0.20
A_31	28952 ± 1815	2.96 ± 0.15	20.4 ± 6.5	0.16 ± 0.04	0.67 ± 0.34	-12.62 ± 0.40
A_34	25143 ± 3475	3.06 ± 0.20	15.7 ± 5.5	0.08 ± 0.04	0.33 ± 0.17	-14.00 ± 0.44
A_36	17390 ± 3151	2.47 ± 0.32	15.8 ± 5.7	0.15 ± 0.05	0.68 ± 0.36	-13.34 ± 0.46
A_37	26218 ± 1770	2.83 ± 0.19	16.0 ± 5.8	0.16 ± 0.04	0.54 ± 0.31	-12.86 ± 0.50
A_39	13884 ± 1767	1.95 ± 0.29	15.8 ± 6.1	0.12 ± 0.05	0.63 ± 0.35	-12.76 ± 0.26
A_40	13259 ± 1040	1.89 ± 0.23	16.8 ± 6.1	0.12 ± 0.05	0.55 ± 0.34	-12.84 ± 0.25
A_41	21850 ± 3962	2.52 ± 0.29	17.4 ± 5.8	0.17 ± 0.03	0.56 ± 0.32	-12.87 ± 0.39
A_45	24645 ± 2720	3.02 ± 0.22	15.9 ± 5.6	0.12 ± 0.05	0.73 ± 0.35	-13.72 ± 0.44

TABLE 5.12— Stellar abundances determined for the NGC 55 sample listed in Tab. 5.10. The abundances are defined as $\varepsilon_x = log(X/H) + 12$ (by number). Different columns include: (1) identification number; (2) silicon; (3) carbon; (4) nitrogen; (5) oxygen; (6) magnesium; (7) global metallicity ($Z/Z_\odot$), defined as a results of Si , Mg and O respect to solar values (Asplund et al. 2009); (8) [N /O] ratio; (9) notes, We have marked in the last column with '*' those objects for which temperature was derived with an error smaller than $\pm 2000\ K$. The solar values suggested by Asplund et al. (2009) are gathered in the first row for comparison ($\odot$).

ID	ε_{Si}	ε_C	ε_N	ε_O	ε_{Mg}	$Z/Z_\odot$	$[N/O]$	Notes
(1)	(2)	(3)	(4)	(5)	(6)	(7)	(8)	(9)
$\odot$	7.51	8.43	7.83	8.69	7.60	1.00	–	–
D_1	6.85	–	–	–	7.08	–	–	–
D_4	6.95	–	–	–	6.98	–	–	*
D_5	7.15	7.32	8.02	8.33	7.28	0.44	0.55	–
D_9	6.85	–	–	–	6.88	–	–	*
D_11	7.05	–	–	–	7.08	–	–	*
D_14	7.25	8.22	7.62	8.33	7.28	0.45	0.15	–
D_13	7.25	8.02	7.42	7.93	7.28	0.22	0.35	–
D_16	7.05	8.02	7.52	8.43	7.28	0.53	-0.05	–
D_23	7.45	7.52	8.12	8.73	7.28	1.04	0.25	*
D_28	7.65	8.22	7.82	8.33	–	0.59	0.35	–
D_27	7.01	7.37	8.28	8.26	7.27	0.38	0.88	*
D_31	7.25	8.22	7.62	7.93	–	0.23	0.55	–
D_36	7.25	–	–	–	6.98	–	–	*
D_42	7.05	7.62	7.72	8.13	7.08	0.28	0.45	–
C1_5	6.85	7.52	7.62	8.53	6.78	0.63	-0.05	*
C1_4	7.05	7.52	7.62	8.63	7.28	0.81	-0.15	*
C2_5	7.45	8.02	7.62	8.53	7.38	0.70	-0.05	*
C1_9	6.80	7.23	7.95	8.66	6.80	0.84	0.15	*
C1_8	7.25	–	–	–	7.28	–	–	*
C2_14	7.25	–	–	–	7.08	–	–	*
C2_11	7.05	8.22	7.62	8.13	–	0.27	0.35	*
C1_15	7.05	–	–	–	6.98	–	–	*
C1_13	7.07	7.60	7.63	8.45	6.92	0.54	0.04	*
C2_18	7.25	7.52	7.62	8.53	7.38	0.68	-0.05	–
C2_17	7.05	8.02	7.92	8.13	7.08	0.28	0.65	–
C2_21	7.35	8.42	7.22	6.93	7.48	0.11	1.15	–
C2_20	7.35	7.92	7.82	8.73	7.38	1.04	-0.05	–

C2_29	7.45	–	–	–	7.78	–	–	–
C1_32	7.35	–	–	–	7.28	–	–	*
C2_36	7.45	–	–	–	7.48	–	–	*
C1_34	7.25	–	–	–	7.28	–	–	–
C1_38	6.85	7.82	7.82	8.23	6.98	0.33	0.45	–
C2_43	6.85	–	–	–	6.78	–	–	–
C1_40	6.92	7.79	8.30	8.39	7.25	0.48	0.77	*
C2_46	7.05	7.92	8.02	8.43	7.28	0.53	0.45	*
C2_47	7.15	–	–	–	7.38	–	–	–
C2_48	7.05	–	–	–	7.08	–	–	*
C1_44	7.08	7.71	7.56	8.07	–	0.25	0.35	*
C1_45	7.13	8.07	8.17	8.34	7.00	0.43	0.69	–
C2_49	7.15	7.92	7.42	8.53	7.18	0.66	-0.25	–
C2_50	7.25	8.22	7.52	8.03	6.98	0.24	0.35	–
C2_51	7.05	–	–	–	7.08	–	–	*
C1_48	7.25	8.02	7.72	8.13	–	0.31	0.45	–
C2_54	6.95	–	–	–	6.98	–	–	*
C1_53	7.25	7.52	8.22	8.63	7.28	0.82	0.45	–
B_9	6.95	8.22	7.62	8.33	7.08	0.42	0.15	–
C2_55	7.35	–	–	–	7.28	–	–	–
B_11	6.75	–	–	–	6.78	–	–	*
B_22	6.95	7.82	8.12	8.53	7.18	0.65	0.45	–
B_23	7.25	7.52	8.12	8.53	7.28	0.67	0.45	*
B_26	7.25	7.92	6.92	5.93	–	0.07	1.85	–
B_30	7.25	8.22	7.62	7.93	–	0.22	0.55	–
B_31	7.10	7.22	8.25	8.59	7.26	0.75	0.52	*
B_35	7.05	8.22	7.82	8.33	7.18	0.43	0.35	–
A_1	7.05	7.52	8.32	8.43	7.08	0.52	0.75	*
A_2	7.05	7.52	7.92	8.53	7.08	0.64	0.25	*
A_7	7.45	7.42	8.32	8.33	7.58	0.50	0.85	*
A_8	7.18	7.27	7.33	8.28	–	0.40	-0.09	*
A_11	7.17	–	–	–	7.20	–	–	*
A_14	7.45	–	–	–	7.48	–	–	*
A_15	6.95	–	–	–	6.98	–	–	*
A_16	7.35	7.82	7.42	8.13	7.28	0.31	0.15	*
A_25	7.05	–	–	–	6.98	–	–	*
A_17	7.06	7.77	7.64	8.37	7.02	0.46	0.13	–
A_26	7.43	7.48	8.22	8.60	7.33	0.79	0.48	*
A_30	6.95	–	–	–	6.98	–	–	–
A_27	7.04	7.77	8.52	8.07	6.98	0.25	1.31	*

A_31	7.25	8.22	6.72	6.73	–	0.08	0.85	*
A_34	7.05	7.52	7.22	8.23	–	0.34	-0.15	–
A_36	7.25	7.32	7.62	8.53	7.28	0.67	-0.05	–
A_37	7.05	7.32	7.82	7.73	–	0.14	0.95	*
A_39	7.25	–	–	–	7.28	–	–	*
A_40	7.15	–	–	–	7.08	–	–	*
A_41	6.95	8.02	7.42	8.23	7.08	0.34	0.05	–
A_45	6.95	7.82	7.87	8.33	6.98	0.41	0.40	–

have a similar situation with other elements as a result of the temperature. At low S/N these effects can be enhanced.

Figure 5.16 displays the trend between the different elements analyzed in this study and the effective temperture. Silicon and magnesium show a flat distribution; the scattering that both elements exhibit is within errors. Instead, the nitrogen, oxygen and carbon (the latter at a lower level) do hint a trend with the effective temperature. However, we are aware that these chemical species are affected by the stellar evolution, additionally to any sort of systematics.

The spatial distribution of the effective temperature across NGC 55 is shown in Fig. 5.17, with the purpose of cheking on possible correlations between the chemical patterns along the galaxy and this parameter. We have studied objects with temperatures between 10000 K and almost 33000 K, without finding a clear spatial trend. Only a few particular *spots* stand out in the diagram, probably related with our selection criterion (O8-B9 supergiant) and the lower number of points, not statistically respresentative of the area.

5.5.3 Comments on individual targets

Figures 5.14 and 5.15 show the final results for the twelve stars used as examples. The entire studied sample plus the best models fitted, including all the chemical species analized, are compiled in Figs. B.1–B.13.

A detailed description of the analysis of each star would be excessive and probably tedious for the reader. Nonetheless a brief enumeration of the main issues found for the examples presented in Figs. 5.14 and 5.15 is provided here. These objects can be considered representative of the common issues encountered in the whole analysis.

- **A_8 .-** It is an O9.7 I star whose main features are well represented by the calculated atmosphere model. At this temperature ($\sim$ 28000 K) the Mg II line has vanished and the Si III lines are weak. The Si IV 4089 $\AA$ line, blended with O II, is well reproduced. The apparent slight discrepancy around the O II 4079 $\AA$ line is most likely due to the normalization. Note also that the O II 4414 – 16 $\AA$

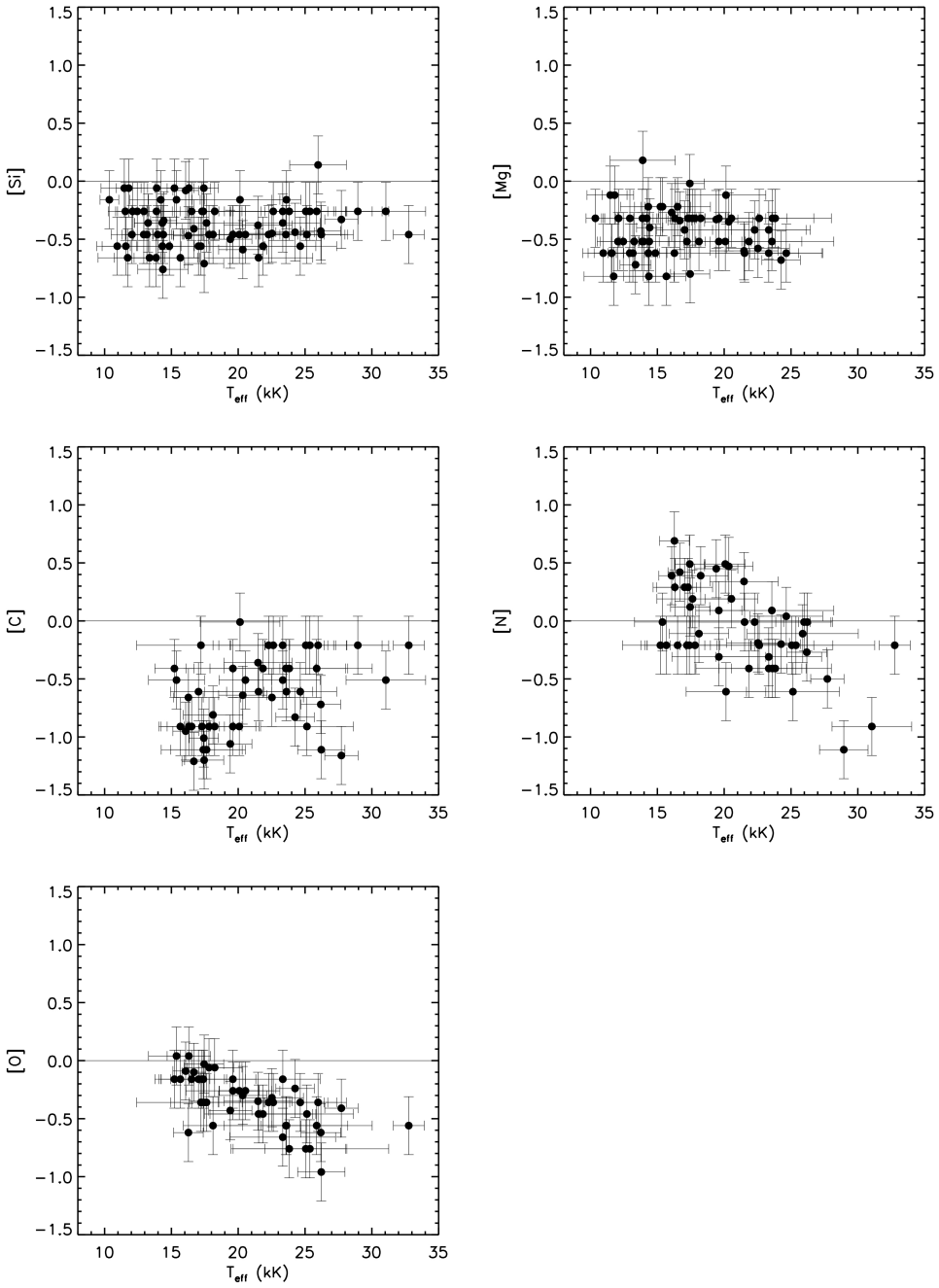

FIGURE 5.16— Distribution of the chemical abundances measured, listed in Tab 5.12, against the effective temperature. The abundances are defined respect to the solar values compiled by Asplund et al. (2009) ($[X] = log\,(X/H) - log\,(X/H)_{\odot}$).

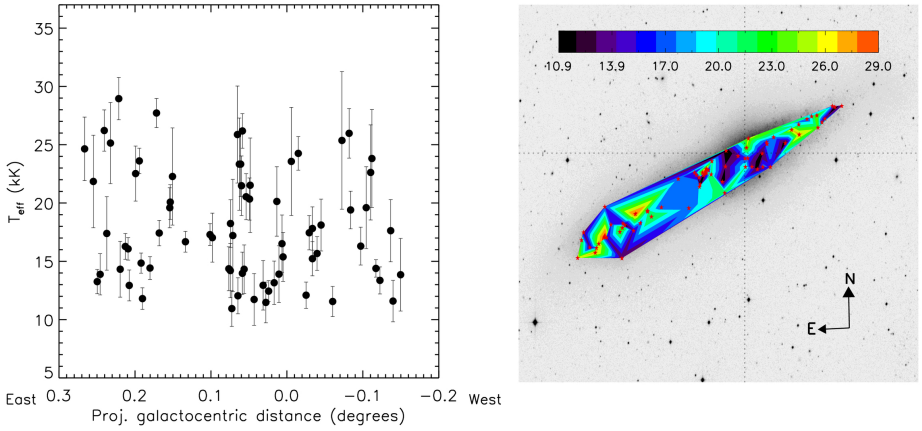

FIGURE 5.17— Spatial distribution of effective temperature across NGC 55. The left panel shows the temperature distribution versus the projected galactocentric distance. The right panel displays a rough 2-D map over a NGC 55 image taken from the DSS archive. The galactic center is marked by dotted lines and the objects included are indicated by red stars.

blend is stronger in the model than the observed profile. He II 4686 $\AA$ shows also a clear mismatch probably due to wind effects which could not be characterized since we lack H_α.

- **C1_44 .-** The bulk of the lines are well represented by our best fitting model with the exception of some transitions: He II 4686 $\AA$, possibly affected by the stellar wind; Si IV 4089 $\AA$, blended with O II and Si IV. Consequently, these lines were not used to find the best models. The doublet of O II at 4416 $\AA$ is also poorly represented, although this is likely not an abundance issue since the rest of oxygen lines are well fitted. Finally, the transition of N II 5007 $\AA$ is filled by the nebular contamination ([O III] 5007 $\AA$).

- **C1_9 .-** The final model shows a good match to most of the considered transitions. The lines of silicon, magnesium and oxygen are not particularly strong at this temperature but they are well reproduced. Note that the derived temperature corresponds to a B2-2.5 I star rather than B1 I.

- **C1_13 .-** The model matches nicely the spectra of this B1 supergiant. The blends of O II 4079 $\AA$ and 4319 $\AA$ show the largest difference, but still within the required limit of ± 0.25 *dex*. Some contamination by nebular emission is seen in the N II 5007 $\AA$ line. The Mg II is weak, as expected for this temperature.

- **A_17 .-** Its spectrum differs from the model at the continuum around H I 4120 $\AA$, likely due to the rectification. The stellar parameters and abundances derived

reproduce well the rest of the spectrum.

- **C1_45 .-** This star has the lowest S/N ratio of the examples and this is clearly reflected by the errors derived for the stellar parameters: Fig. 5.15, right panel, shows a large set of compatible models in the $T_{eff} - log(g)$ plane. Despite the low quality, the model corresponding to our solution reproduces well the main features of the spectrum. The observed N II 3995 $\AA$ line is not well represented by the model, and the transition at 5007 $\AA$ is, again, masked by nebular contamination.

- **C1_40 .-** Our model provides a fair match to this B1.5 supergiant, although with some issues at $\sim$ 4079 $\AA$. We suspect that this may be related to cosmic rays not correctly subtracted. The temperature, slightly lower than in the previous B1, stars makes the magnesium abundance determination easier. An evident oversubtraction of O III $4959 - 5007$ $\AA$ nebular lines is affecting the N II blend at $\sim$ 5007 $\AA$.

- **A_27 .-** There is a mismatch around the O III 5007 $\AA$ line, but the transitions of the rest of the chemical elements are well reproduced.

- **D_27 .-** The line of He I at 4144 $\AA$ is not well fitted. Note, however that it was not included in the analysis because its broadening is not well known. The features around 4670 $\AA$ show a slight discrepancy (within the error) which could be attributed to the continuum rectification.

- **A_26 .-** The model shows a good agreement with the observed spectrum, its better S/N ratio results in smaller errors. The oxygen lines, weak at this temperature, are well represented by the model. The only exception is the O II 4079 $\AA$ line, which is so close to the H I wing that the rectification must be taken with care. In contrast with the oxygen lines, Mg II and Si III are stronger. The synthetic and observed spectra again disagree at He I 4144 $\AA$.

- **B_31 .-** This B2.5 supergiant star is nicely reproduced by our model. We obtained a good estimation for temperature and gravity as it is shown in Fig. 5.15. All the main features are reproduced except He I 4144 $\AA$.

- **A_11 .-** Its spectrum has the best S/N ratio of this sub-sample, and this can be seen in the derived uncertainties. Its effective temperature suggests a spectral type a bit earlier. At these cool temperatures ($\sim$ 14000 K) the transitions of O II, N II and C II are very weak or even completely vanished. We can only provide upper limits for their abundances. The Si III lines are weak but instead the transitions of Si II (although blended with O II lines) gain strength together with the magnesium line.

In the subsequent analyses four stars have been removed since the stellar parameters derived lie too close to the grid edges. As we commented before, their results are not reliable, though the values obtained can be consulted in Tabs 5.11 and 5.12. These stars are: C2_11 (Fig. B.4), C1_32 (Fig. B.5), B_26 (Fig. B.9) and B_30 (Fig. B.9). It would be interesting to go deeper in future analyses on C1_32 and B_30, they could hint evolved stages close to an LBV phase.

The sample includes objects for which the analysis is higtly unreliable due to the low S/N of the spectra (reflected in a wide $T_{eff} - log\,g$ range of possible models), but the bulk of the χ^2 distribution is included into the grid boundaries and what is reflected in the erros obtained (e. g. C1_48, Fig B.8), hence they are kept in the study.

5.5.4 Chemical Spatial Distribution

Previous studies suggest a similar metallicity for NGC 55 and the LMC (Webster & Smith 1983; Davidge 2005). The mean abundance derived for silicon, oxygen and magnesium, more reliable than the nitrogen and carbon abundances (since they may be more affected by evolutionary effects than oxygen), has a relative average with respect to the solar values of $-0.36\,dex$, quite near to the $-0.3\,dex$ derived by Davidge (2005). The solar references were taken from Asplund et al. (2009).

Although the orientation of NGC 55 together with its shape makes its morphologic classification and any chemical pattern difficult to analyze, we have measured the distribution of silicon, oxygen and magnesium along the galaxy. The left panel in Fig. 5.18 shows the behavior of their measured abundances as a function of projected galactocentric distance, as well as the global metallicity derived from them. We have fitted the results to a first order polynomial to check for a systematic variation.

$$\begin{aligned} [X] &= log\,(X/H) - log\,(X/H)_{\odot} \\ [X] &= a\,(\rho/\rho_o) + b \end{aligned} \tag{5.1}$$

where X is each one of the elements considered and ρ the projected galactocentric distance ($\rho_o = 15'$, approximately the optical radius of NGC 55).

All of them exhibit a basically flat distribution and almost null gradient. The values obtained from the linear regression described by Eq. 5.1 are gathered in Tab. 5.13. Webster & Smith (1983) analyzed the oxygen abundance of several H II regions in the galaxy without finding any sort of chemical gradient. Their results are in complete agreement with ours as it is shown in Fig. 5.18.

The large sample studied in this work allows us to go a little further tham a 1-D chemical distribution analysis across the galaxy. Clearly, it is not homogeneously radially distributed and it could mask shallow chemical tendencies or isolated interesting areas. The right panel in Fig. 5.18 shows 2-D distribution maps for the three species

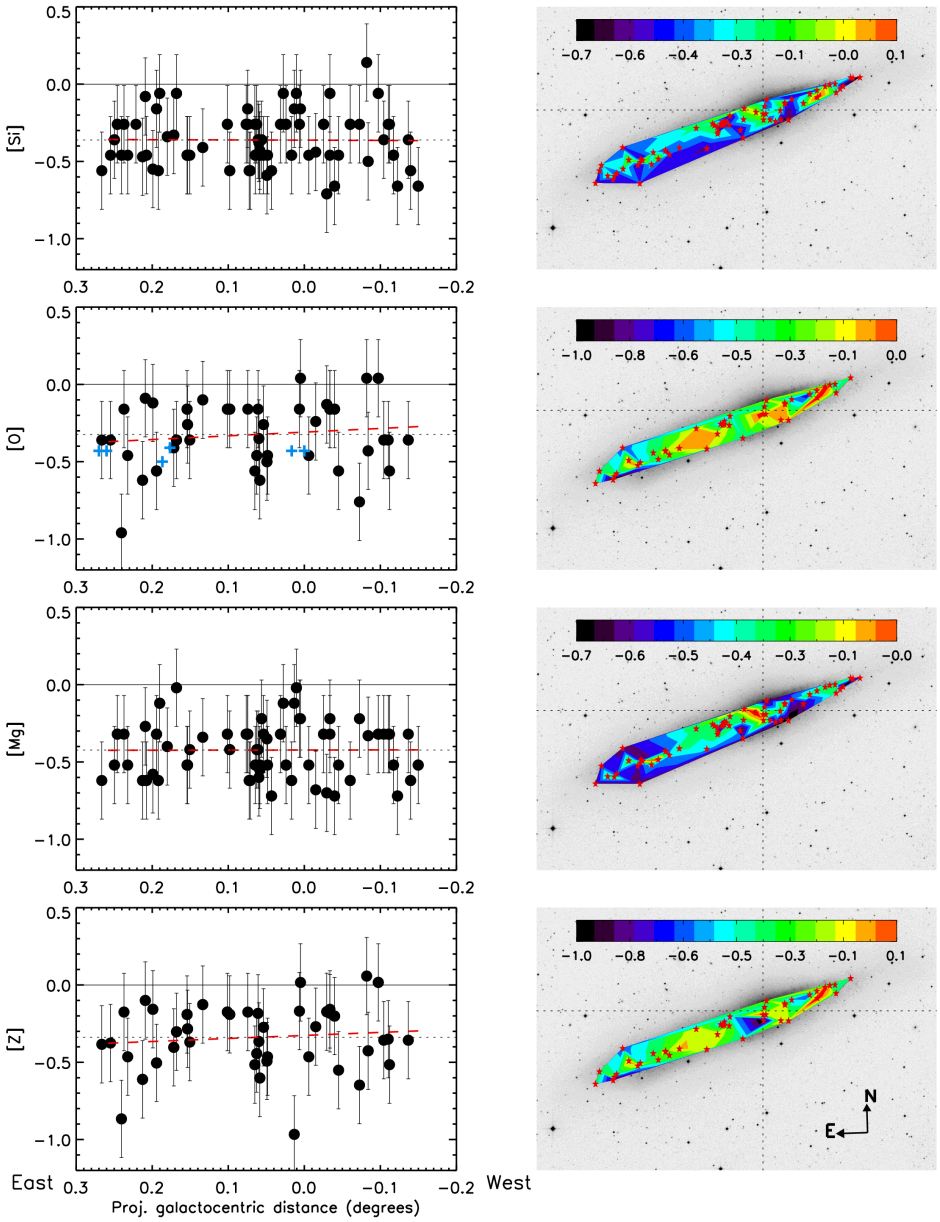

FIGURE 5.18— Chemical distribution along NGC 55. The left chart displays the distribution of the abundance of Si, Mg, O and Z with respect to solar values (Asplund et al. 2009) as a function of projected galactocentric distance. The mean value is marked with a dotted black line and the best linear regression to the points with a red dashed line. The right side of the figure shows a 2-D chemical map distribution following the color-code described in each chart. The positions of the objects analyzed are also marked (red stars). The [O] panel includes the values obtained by Webster & Smith (1983) for oxygen abundances using several H II regions in NGC 55 (blue crosses).

[X]	a	b
Si	0.02 ± 0.18	-0.36 ± 0.02
O	-0.23 ± 0.29	-0.31 ± 0.04
Mg	0.01 ± 0.20	-0.42 ± 0.02
Z	-0.20 ± 0.28	-0.33 ± 0.04

TABLE 5.13— Parameters of the linear regression to fit the silicon, magnesium and oxygen abundance distribution as a function of projected galactocentric distance (see Eq. 5.1).

considered plus the total metallicity (sum of these three elements). Although rather modestly, the three chemical probes show large abundances toward the north-west part, more marked in the [Si] distribution.

Altough roughly confirmed by the three elements, this fact could be considered as an artifact due to the large errors in the abundances, which prevent us from reaching a conclusive result.

5.5.5 CNO Evolution Status

Carbon, nitrogen and oxygen (to lesser extend) are indicators of evolutionary status in massive blue stars. The enrichment with CNO material processed from the inner layers does not occur only in the last stages of stellar evolution when the stars reach the red supergiant or WR phase. Mechanisms such as rotation and magnetic fields can contaminate the surface chemical composition as well, during the first evolutionary stages. Evolutionary models predict tight relationships between [N /O] and [N /C] that can be used to track the ageing of stars (Maeder & Meynet 2005).

Figure 5.19 shows the spatial distribution of the [N /O] ratio along NGC 55. It hints at a trend similar to what the individual chemical spatial patterns presented before, despite of the errors. The largest dispersion is found in the south-east side of the galaxy, while the north-west part reveals lower values and scattering. Being aware of the sample limits, that can be interpreted as the presence of a more evolved population in the east part compared to stars observed in the west, settled by less evolved objects according to the [N /O]. This is not unexpected since the north part is a very active region with a recent stellar population. Inhomogenities in the H I regions velocity pattern (Puche et al. 1991) in the north-west area together with the high stellar activity, X-ray emissions, and the apparent warp could suggest that the galaxy has suffered interaction with a companion (Oshima et al. 2002), which could have triggered the star formation. de Vaucouleurs (1961) referred to the posibility of a bar in this area, another important engine to start the formation of new massive blue stars in Magellanic-type galaxies (Elmegreen & Elmegreen 1980).

The linear relation expected from theoretical models between [N/C] and [N/O] is

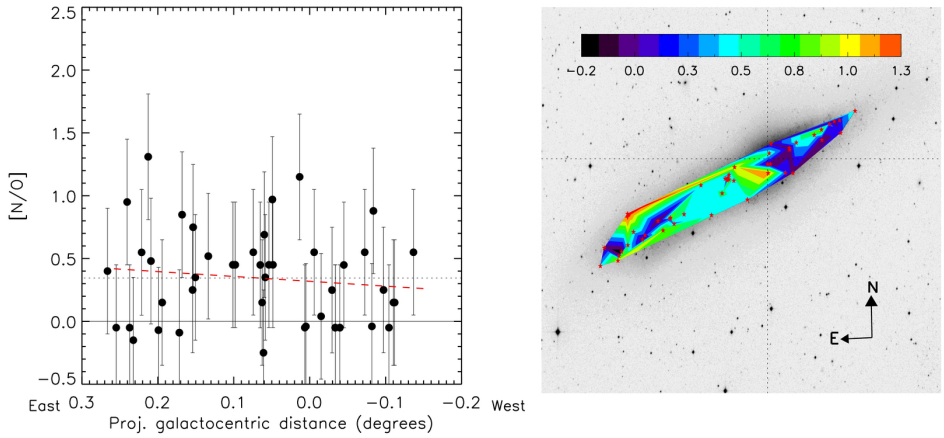

FIGURE 5.19— [N/O] ratio (by number) spatial distribution along NGC 55. Left panel shows the 1-D radial distribution, while the right side displays the 2-D distribution on a DSS NGC 55 image. The symbol and color codes follow the same rules described in Fig. 5.18

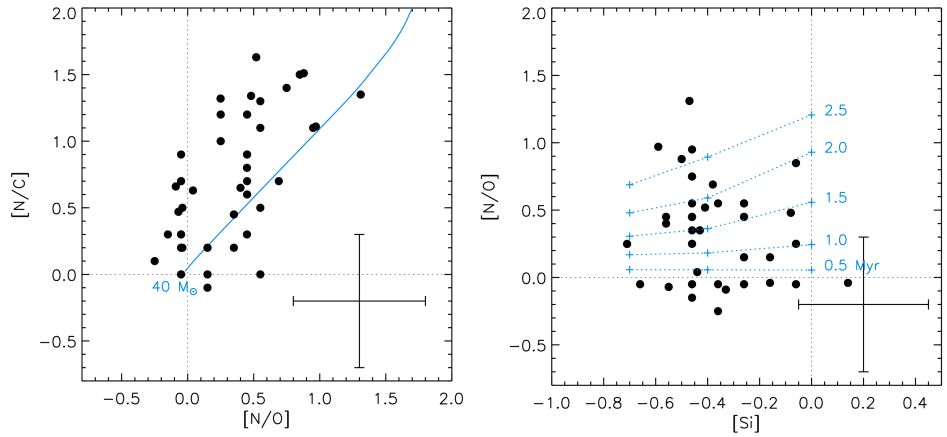

FIGURE 5.20— Left panel: [N/C] versus [N/O] ratios (by number). The blue line represents the ratio expected for a theoretical model with 40 $M_{\odot}$, rotational velocity (300 kms^{-1}) and LMC metallicity (Maeder & Meynet 2005). Right panel: [N/O] ratio as a function of silicon abundance, the [N/O] time scale for a 40 $M_{\odot}$ star for Galactic, LMC and SMC metallicities (blue crosses) is also displayed as reference at five different ages (blue dotted line). The average errors of both charts are plotted in the right-bottom corner.

also followed in NGC 55. Nevertheless there is a difference in the slope obtained by our analysis and the evolutionary tracks developed by Maeder & Meynet (2005) using rotation (300 $km\,s^{-1}$) for a 40 $M_{\odot}$ (the behavior is only weakly dependent on the mass) with LMC metallicity, as is is shown in Fig. 5.20, but there is agreement within the errors. Note also the problems with the C II abundance determination (see section 4.2.1). Deriving the carbon abundance just from C II 4217 $\AA$, which modeling has been questioned by other authors, may introduce the observed shift. This mismatch was also found in Galactic studies as remarked by Przybilla et al. (2010) (and references therein). The right panel of Fig. 5.20 displays the relation between the evolutionary state of our stars, indicated by [N/O], and the silicon abundance. The silicon was choosen as a reference of the star metallicity, since it almost does not suffer any enrichment due to processed material during these stages (Woosley et al. 2002). The time scale shown in the figure is the result of the evolution of a 40 $M_{\odot}$ star according to its metallicity. After the red supergiant phase an abrupt increment in surface [N/O] is expected since the star suffered a convective dredge-up. The typical [N/O] ratios estimated point out that they are still evolving towards the red supergiant area.

5.5.6 Fundamental Parameters

Parameters like extinction, mass, radius or luminosity can be calculated using the best fit models if the observed magnitudes and the distances are known (see section 4.2.5). The relation between Av and the color excess $E(V-Ic)$ (the only observed color) was calculated through the calibrations provided by Cardelli et al. (1989).

For almost all the objects a nonphysical value (negative) is found for Av. Either colors are contaminated by the nebular emission around the stars or the photometry calibration is biased. The first hypothesis was also suggeted by Evans et al. (2007) for two stars of their sample in NGC 3109. NGC 55 is further away than this galaxy and the high inclination contributes to the contamination by gas emission in the observations, however the fact that all the stars analyzed show this problem demands a revision of the photometry for riding out any kind of mislead.

Due to the problems with the extinction, we eventually used the mean value, $E(B-V)=0.127$, together with the distance proposed by Gieren et al. (2008). Based on those results, we have calculated masses, luminosities and radii of the stars acording to the observed V-magnitude and the synthetic photometry obtained from the best stellar model. Additionally, we have used an alternative way for determining these parameters, given by the FGLR (see Eq. 4.2 in section 4.1.1). As all the objects in the study are supergiants, the interpretation of Kudritzki et al. (2008) applies. In Table 5.14 we provide $log\,(L/L_{\odot})^{FGLR}$, $(R/R_{\odot})^{FGLR}$ and $(M/M_{\odot})^{FGLR}$ derived from the FGLR. Instead the values obtained by the observed photometry are marked by ^{PHOT} in Tab. 5.14.

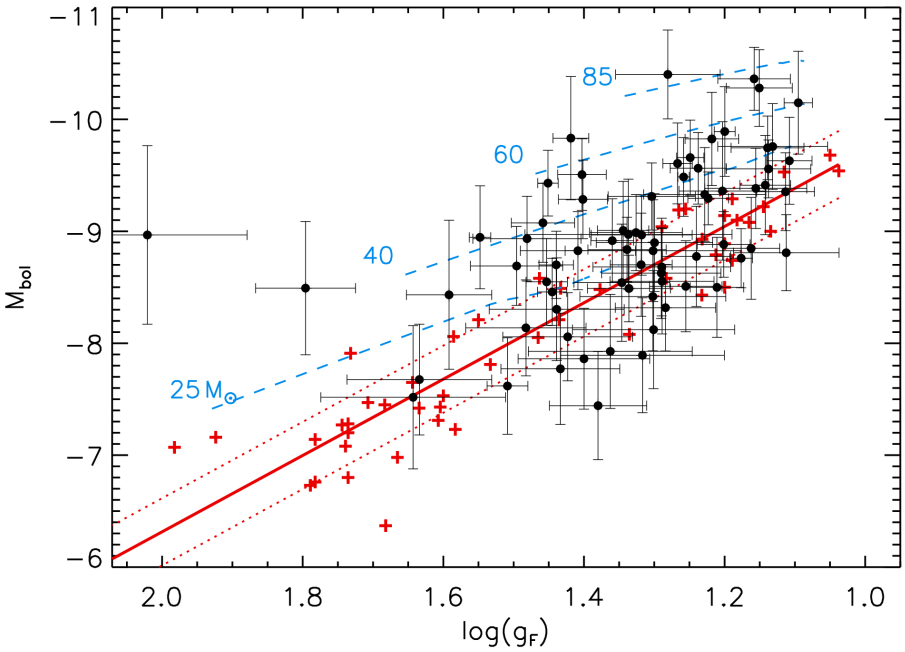

FIGURE 5.21— The M_{bol} for the NGC 55 sample (black dots) together with the points used by Kudritzki et al. (2008) (red crosses) to derive the relation represented by the red line plus an offset of ± 0.3 in M_{bol} (dotted red lines). Additionally, stellar evolutionary tracks with rotation (Meynet & Maeder 2003) are included (blue dashed lines). Evolution proceeds towards lower $log\,(g_F)$ values.

Figure 5.21 shows M_{bol} for our data, derived using the mean reddening and the distance calculated by Gieren et al. (2008). The points reveal a large dispersion compared with the results recovered by Kudritzki et al. (2008) and the linear regression derived. Our large error bars and the dispertion can be easily associated to the data quality and the photometry problems already mentioned. Another systematic uncertainty source may come from using an average value for $E(V-Ic)$. Looking at the optical NGC 55 image (see for instance Fig. 5.3) it is clear that adopting an homogeneous extinction distribution across the galaxy is a naive approach, but it is the only method we could use so far, introducing an undesired scatter in M_{bol}.

The general behavior of our results follows the trend marked by the FGLR estimated by Kudritzki et al. (2008) and the evolutionary tracks developed by Meynet & Maeder (2003, 2005) with rotation (300 kms^{-1}). Even in the upper part of the relation, toward lower gravities and higher luminosities, where the FGLRs predicted by the evolutionary tracks show a curvature and start to differ from the linear behavior

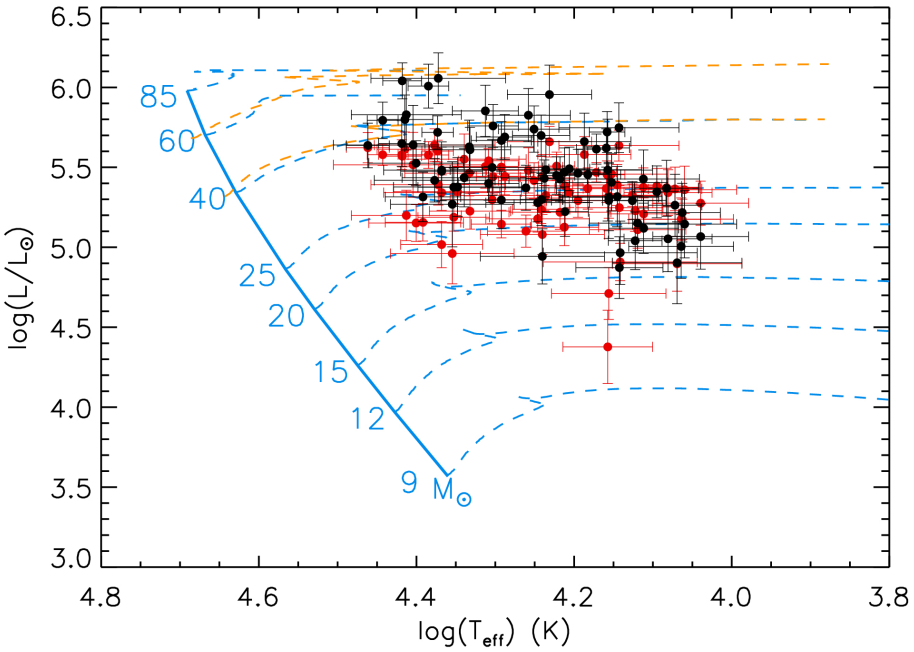

FIGURE 5.22— Distribution of the NGC 55 stars in the HR diagram. Both the values obtained with the observed photometry (black dots) and from the FGLR relationship (red dots) are plotted. The evolutionary tracks developed with rotation (300 kms^{-1}) at solar (blue, Meynet & Maeder 2003) and LMC (orange, Meynet & Maeder 2005) metallicity are also displayed.

of the spectral analysis (Urbaneja et al. 2008). However, more accurate estimations are needed to confirm this match with the theoretical evolution models. Two stars show strong discrepancies with the theoretical predictions at large $log\,(g_F)$ (Fig. 5.21), this likely is an artifact for using an average extinction correction.

Figure 5.22 displays the position of the stars obtained using both the photometry and FGLR method in the HR diagram. The evolutionary tracks generated by Meynet & Maeder (2003, 2005) (with rotation, 300 kms^{-1}, using Galactic and LMC metallicity) are also included. With the exception of some particular cases both estimations cover a similar region in the HR diagram with evolution masses beetween $\sim 20-50\ M_{\odot}$. Because of the errors carried from previous steps, performing a detailed comparison between the spectroscopic and evolutionary masses has not much relevance, since we can not add nothing new to the well-known mass discrepancy problem between these two dianostics of masses (Herrero et al. 1992). There are some extreme cases which may be interesting due to their high masses. We hope that once the photometry

problems are clarified, more information can be extracted from this sample.

5.6 Summary

We have presented a detailed description of the quantitative analysis of a sample of massive blue stars in NGC 55. So far, this conforms the largest set of OB-type supergiants analyzed at the NGC 55 distance. Thanks to their brightness and the last generation of multi-object spectrographs, we can acquire spectra with enough quality to carry out the study, using the techniques described in chapter 4.

As a previous step, we have presented the first census of massive blue stars in NGC 55. A careful qualitative analysis of the entire observed sample allows us to carry out the spectral classification of 204 stars, selecting the hotter objects (spectral type earlier than F0) and discarding cooler stars, H II regions, and foreground Milky Way objects. We have found 164 stars with spectral types earlier than F0, including a set of seven peculiar objects (WR and LBVc).

We have determined radial velocities from the observed spectra, finding a good agreement with the published rotation curve measured from neutral hydrogen (Puche et al. 1991). This study allowed us to detect objects with peculiar velocities that deserve a more detailed study. Although we are aware of the statistical limitations of our sample, we developed a 2-D kinematic map distribution of the galaxy, going beyond a simple radial profile. The velocity map hints at *'hot-spots'* in the velocity distribution related to different structures in the galaxy, including a possible bar.

From our catalog we have selected 75 supergiant stars with spectral types between O8 and B9. We have obtained the stellar parameters and chemical abundances according to their spectral type. The accuracy is constrained by the S/N of each individual spectrum. However, the final fit obtained shows a good agreement with the observed spectra in the optical range available to us.

The chemical composition derived from the blue stars analyzed shows a fair match with previous studies, pointing to a mean metallicity close to the LMC value. We have not found gradients in the radial chemical distributions of silicon, oxygen and magnesium. Analyzing the 2-D spatial chemical pattern a faint variation across the galactic plane can be observed. This fact suggests a 1-D distribution is a simple interpretation for the entire galaxy, given that the projection effect could mask any possible trends. However, the large error bars blur the results, and our sample is not large enough to get a conclusive evolution pattern for the galaxy. The errors, the spectral type, and the high projection of the galaxy introduce important uncertainties in our results should be kept in mind. A statistically weighted study is recommended.

The NGC 55 sample shows a good agreement between the observed spectra and the best stellar atmosphere models, within the limits of our S/N and resolution. The general distribution of our results on the FGLR relationship present a good match.

Even in the upper part of the relation our objects follow, on average, the trend marked by theoretical models. The nebular contamination in the observed photometry and the issues commented above, plus the use of an average extinction for the entire sample (which has also revealed as a naive approach known the irregular spatial dust distribution of NGC 55, Engelbracht et al. 2004) could explain part of the scatter shown in the FGLR distribution. The representation of our objects in the HR diagram shows a range of masses between $\sim 20-50\ M_{\odot}$, but these results must be improved by a reliable photometry.

We have shown in this chapter that it is possible to develop a detailed characterization of a large sample of massive blue stars and the host galaxy, not only its dynamics and extinction (with an accurate photometry), but also the chemical distribution and evolution. In spite of the low resolution, the tools built during this work have displayed their potential in an extragalactic quantitative spectral analysis.

TABLE 5.14— Fundamental parameters for the sample of stars analysed in NGC 55. The columns list: (1) star identification; (2) bolometric correction; (3) flux-weighted gravity (Eq. 4.2); (4), (5) and (6) luminosity, radius and mass derived from the observed photometry (*PHOT*); (7), (8) and (9) luminosity, radius and mass derived from flux-weighted gravity luminosity relationship (*FGLR*, Kudritzki et al. 2003).

ID	BC	$log\,(g_F)$	$log\,(L/L_\odot)^{PHOT}$	$R/R_\odot^{PHOT}$	$M/M_\odot^{PHOT}$	$log\,(L/L_\odot)^{FGLR}$	$R/R_\odot^{FGLR}$	$M/M_\odot^{FGLR}$
(1)	(2)	(3)	(4)	(5)	(6)	(7)	(8)	(9)
D_1	-1.04	1.63±0.10	4.97±0.20	53.0	16.2	4.91±0.12	49.5	14.2
D_4	-0.64	1.43±0.08	5.01±0.20	79.1	11.2	5.18±0.13	96.3	16.6
D_5	-1.57	1.45±0.02	5.28±0.12	46.9	21.6	5.18±0.08	41.7	17.1
D_9	-0.99	1.34±0.06	5.29±0.12	82.8	17.3	5.33±0.07	86.1	18.7
D_11	-1.16	1.24±0.04	5.72±0.13	117.	37.1	5.45±0.09	86.0	20.1
D_14	-2.16	1.59±0.06	5.27±0.27	28.1	29.6	4.96±0.19	19.7	14.6
D_13	-2.33	1.11±0.07	5.42±0.14	30.2	13.9	5.64±0.10	38.9	23.0
D_16	-1.85	1.21±0.04	5.30±0.18	38.7	13.1	5.50±0.15	49.0	21.1
D_23	-1.41	1.48±0.08	5.47±0.15	68.3	36.4	5.13±0.12	46.0	16.5
D_28	-2.52	1.13±0.08	5.80±0.15	39.3	34.8	5.61±0.11	31.7	22.7
D_27	-1.83	1.26±0.01	5.69±0.14	62.1	36.2	5.44±0.12	46.8	20.6
D_31	-2.46	1.20±0.06	5.64±0.25	34.3	28.4	5.52±0.20	29.7	21.4
D_36	-0.64	1.44±0.10	5.22±0.18	101.	18.5	5.18±0.13	96.8	16.8
D_42	-1.67	1.22±0.04	5.83±0.17	83.4	45.2	5.48±0.14	56.0	20.4
C1_5	-1.31	1.36±0.03	5.46±0.15	73.3	27.1	5.29±0.10	60.2	18.3
C1_4	-1.62	1.27±0.02	5.74±0.14	77.9	41.3	5.42±0.11	53.8	19.7
C2_5	-1.26	1.30±0.08	5.46±0.17	76.9	23.2	5.37±0.13	69.6	19.0
C1_9	-1.59	1.40±0.03	5.70±0.13	77.6	51.6	5.24±0.09	45.6	17.8
C1_8	-0.75	1.29±0.10	5.37±0.17	110.	18.6	5.37±0.12	110.	18.8
C2_14	-0.82	1.29±0.08	5.35±0.16	101.	17.7	5.38±0.11	106.	19.2
C1_15	-0.93	1.48±0.09	5.15±0.17	72.6	17.5	5.11±0.12	69.2	16.0
C1_13	-2.38	1.15±0.05	6.01±0.14	57.3	58.8	5.58±0.08	34.9	21.8

C2_18	-1.43	1.41±0.08	5.43±0.14	63.3	27.9	5.22±0.11	49.8	17.3
C2_17	-2.30	1.28±0.07	6.06±0.16	64.2	88.8	5.39±0.13	29.8	19.2
C2_21	-1.88	1.34±0.04	5.50±0.18	46.3	28.4	5.30±0.15	36.7	17.9
C2_20	-1.31	1.14±0.04	5.66±0.18	95.6	25.9	5.58±0.11	87.1	21.5
C2_29	-1.11	1.11±0.03	5.75±0.16	129.	29.3	5.64±0.10	113.	22.6
C2_36	-0.60	1.30±0.12	5.15±0.21	94.8	11.4	5.36±0.15	121.	18.7
C1_34	-0.94	1.30±0.13	5.43±0.18	103.	21.8	5.38±0.12	97.2	19.4
C1_38	-2.08	1.23±0.09	5.63±0.17	47.0	29.3	5.46±0.14	38.9	20.1
C2_43	-0.65	1.64±0.13	4.90±0.26	68.7	14.3	4.90±0.17	68.2	14.1
C1_40	-1.92	1.18±0.02	5.40±0.11	40.5	15.4	5.54±0.08	47.6	21.3
C2_46	-1.98	1.20±0.01	5.85±0.16	66.9	46.1	5.51±0.14	44.8	20.7
C2_47	-1.15	1.35±0.07	5.31±0.21	73.9	18.6	5.32±0.14	74.6	19.0
C2_48	-1.07	1.29±0.07	5.32±0.19	78.0	16.5	5.39±0.13	84.8	19.5
C1_44	-2.55	1.16±0.05	6.04±0.11	51.1	64.5	5.57±0.07	29.7	21.8
C1_45	-2.04	1.40±0.03	5.61±0.14	46.2	41.9	5.23±0.11	29.7	17.3
C2_49	-2.25	1.55±0.02	5.48±0.18	33.5	43.0	5.02±0.14	19.8	15.0
C2_50	-2.28	1.32±0.07	5.48±0.14	33.8	25.8	5.34±0.11	28.8	18.6
C2_51	-0.76	1.32±0.12	5.05±0.21	77.4	9.60	5.34±0.14	108.	18.6
C1_48	-2.50	1.42±0.03	5.83±0.22	41.0	72.1	5.20±0.16	19.8	16.9
C2_54	-0.51	1.36±0.12	5.07±0.20	95.2	11.0	5.28±0.14	121.	17.7
C1_53	-1.66	1.50±0.07	5.37±0.14	48.7	30.1	5.10±0.10	35.7	16.1
B_9	-1.54	1.34±0.15	5.49±0.20	62.3	27.1	5.32±0.11	51.8	18.7
C2_55	-1.11	1.24±0.05	5.41±0.18	83.5	18.1	5.46±0.12	88.7	20.4
B_11	-1.12	2.02±0.14	5.48±0.32	89.3	130.	4.38±0.23	25.0	10.2
B_22	-1.57	1.10±0.02	5.96±0.18	109.	45.8	5.66±0.10	77.9	23.2
B_23	-1.52	1.34±0.06	5.43±0.12	58.0	24.0	5.31±0.08	50.4	18.1
B_31	-1.46	1.20±0.04	5.45±0.12	63.7	18.2	5.51±0.09	68.1	20.9

B_35	-2.14	1.32±0.04	5.38±0.18	32.9	20.2	5.35±0.16	31.7	18.9
A_1	-1.91	1.25±0.02	5.76±0.13	62.8	41.5	5.44±0.11	43.6	20.0
A_2	-1.81	1.45±0.01	5.67±0.12	59.4	53.7	5.15±0.09	32.5	16.1
A_7	-1.56	1.26±0.05	5.30±0.16	49.1	14.6	5.44±0.13	57.7	20.2
A_8	-2.69	1.14±0.05	5.79±0.11	34.3	35.0	5.58±0.07	26.8	21.3
A_11	-1.17	1.30±0.06	5.62±0.12	103.	34.3	5.37±0.09	77.6	19.1
A_14	-0.71	1.30±0.10	5.26±0.19	102.	15.0	5.37±0.14	115.	19.0
A_15	-1.24	1.22±0.03	5.61±0.09	97.2	28.0	5.47±0.06	82.2	20.1
A_16	-2.30	1.14±0.06	5.72±0.10	43.4	29.3	5.60±0.07	37.9	22.4
A_25	-0.89	1.42±0.09	5.12±0.16	72.4	14.2	5.21±0.10	80.3	17.5
A_17	-2.19	1.44±0.02	5.38±0.12	32.1	26.7	5.19±0.09	25.9	17.3
A_26	-1.37	1.33±0.07	5.49±0.14	72.0	26.8	5.34±0.09	60.6	18.9
A_30	-1.11	1.80±0.07	5.29±0.24	72.2	50.1	4.71±0.16	36.9	13.1
A_27	-1.39	1.28±0.07	5.22±0.15	51.6	13.1	5.38±0.11	62.1	19.0
A_31	-2.79	1.11±0.04	5.64±0.14	26.2	23.0	5.62±0.09	25.8	22.2
A_34	-2.47	1.46±0.04	5.53±0.14	30.6	39.3	5.15±0.11	19.9	16.6
A_36	-1.53	1.51±0.03	4.94±0.17	32.7	11.5	5.08±0.13	38.3	15.8
A_37	-2.56	1.16±0.07	5.65±0.14	32.4	26.0	5.58±0.09	29.9	22.1
A_39	-1.04	1.38±0.07	4.87±0.19	47.4	7.30	5.25±0.14	72.9	17.3
A_40	-0.95	1.40±0.09	5.04±0.18	63.0	11.3	5.23±0.13	78.2	17.4
A_41	-2.11	1.16±0.04	5.44±0.18	36.5	16.1	5.55±0.16	41.7	21.1
A_45	-2.41	1.45±0.03	5.32±0.15	25.0	23.9	5.16±0.12	20.8	16.6

6

Conclusions and Future Research

What matters it how far we go? his scaly friend replied.
There is another shore, you know, upon the other side.
The further off from England the nearer is to France -
Then turn not pale, beloved snail, but come and join the dance.
A Whiting And A Snail, Lewis Carroll

THE theory of evolution of massive blue stars has many caveats. Nowadays standard scenarios give basic ideas about the processes that carry out a star through phases so active and complex as LBVs, nonetheless a detailed description is still lacking and important doubts are present. A better understanding requires better observational facts that can only be obtained through extensive quantitative analyses with state-of-the-art NLTE atmosphere models, updated model atoms, and data sets observed in different conditions (metallicity, age, etc.). The efforts invested in this thesis work have aimed at large improving our knowledge of massive blue stars through the adaptation of new atomic data, and the development of automatic techniques for the subsequent analysis of large samples, in this study belonging to NGC 55. We review here the conclusions reached in this thesis, and give a short list of items for future work.

Updating the Silicon Model Atom in FASTWIND

The role of accurate atomic data in the quantitative analysis of massive blue stars under NLTE conditions is indisputable. Recent data based on quantum mechanical techniques pushed the development of an updated silicon model atom (Si II, Si III and Si IV) for the stellar code DETAIL, trying to solve certain observational issues

attributed to a lack of accuracy in the previous model. In this work we have taken a new model designed by Dr. N. Przybilla and transferred into the format of the stellar code FASTWIND. The highlights of this process are:

- Both stellar codes, DETAIL and FASTWIND, follow a similar philosophy in the atomic data treatment, thus it was relatively straightforward to move it from one to another, without changing the source code. Only RBF transitions (with OP photoionization cross section data) required modifications for the stellar code.

- The new model resulting in a detailed level structure for Si III and Si IV, notwithstanding similar to the previous one in the case of Si II. Instead the treatment of the radiative and collisional processes have suffered substantial changes on the three ions.

- Comparison of synthetic profiles between both atomic versions showed the largest differences in the Si II lines studied. Variations in relevant transitions, such as Si III 4552 $\AA$ and Si IV 4116 $\AA$, were less pronounced with an estimated impact in the effective temperature around $\sim$ 500 and 1000 K. Instead, the differences shown in other lines (for instance Si II 3853 $\AA$) are remarkable. These transitions are usually weak in supergiants, but their role on the analysis of dwarf stars could be relevant as it was already pointed out by other authors.

- The quantitative comparison of six Galactic supergiant stars, using both model atoms, showed divergent results depending on the analyzed star. Four of them were cold enough for displaying Si II, Si III and Si IV transitions. While two of these stars showed a clear improvement in $T_{eff} - log\,(g)$ values obtained by different silicon ionization ratios, compared with the old model, the other two stars showed the opposite behavior. At higher temperatures (only Si III and Si IV are available), the rest of stars displayed a better match with the helium ionization ratio when the new silicon atomic model was used.

  A similar behavior is found for the silicon chemical determination. Only two of the six stars analyzed show better results with the previous old version (measured by the dispersion from different ionization stages); the lack of concordance in the ionization balances is propagated here as well. In spite of this result, in these two cases the abundance-microturbulence trend, followed for the lines considered using the old model, still shows inconsistencies.

  The Si III 4813 $\AA$ line shows a better correlation with the rest of the transitions through the new atomic model.

Automatic Analysis Techniques

The last generation of massive blue stars surveys demands systematic, objective and reproducible quantitative analyses, avoiding as much as possible visual techniques. To study hundreds of massive blue star spectra is challenging, but necessary. Following this idea:

- A new FASTWIND grid of models was implemented for the quantitative analysis of massive blue supegiant stars with spectral type between $\sim A1$ and $O8$. The stellar parameters included in the model atmosphere grid were selected in an efficient way, saving computational time and simplifying the match with the observed spectra.

- We have implemented a χ^2-method to determine the best stellar parameters (plus errors) that reproduce the observed spectrum. The technique was based on the direct comparison of several spectral windows centered on relevant lines (according to their spectral type) and the synthetic profiles generated by the stellar code FASTWIND. The different tests showed the reliability of the technique and the errors estimated. These tests have also underlined the caveats, which must be taken into account to avoid additional error sources.

- We have followed the standard *'Spectroscopy Synthesis Method'* procedure for the quantitative analyses at low resolution ($R \sim 700 - 2000$), avoiding *'by-eye'* techniques through the χ^2-method developed in this work, recovering the stellar parameters and their errors in a fast and efficient way.

  The different tests on synthetic models showed a good agreement between the input profiles and those recovered by our procedure. The study of Galactic stars degraded to low resolution and S/N gave similar results to those of the analyses of original spectra. However, the chemical abundances analysis was trickier. Due to the low quality of the data (resolution and S/N) and the intrinsic weakness of the some key lines at these temperatures, it was not possible to use a completely automatic method and a final *'by-eye'* refinement was employed.

- The technique was adapted to high resolution quantitative studies through a hybrid procedure. Starting with an initial guest of the stellar parameters by the *'Spectroscopy Synthesis Method'* (as at low resolution data), and accomplishing the final results by means of standard ways (i. e. ionization balances–Balmer wings and *'Curves of Growth'*). The different tests showed again the reliability of this technique. The whole process was done with a minimum of human interaction, and in a relatively small amount of time.

- The creation and improvements of several procedures, adapting the quantitative analysis under a distributed computation philosophy, have hugely sped up all the processes. The role of CONDOR has been revealed as an important step in the analyses, not only in the creation of new stellar grids, but also providing a faster path to the match the observed and synthetic profiles.

NGC 55 Quantitative Analysis

Extending massive blue star research out of the Milky Way is mandatory for a better understanding of the role played by environmental factors. Additionally, hot stars provide important tools for understanding the formation and chemical evolution of host galaxies, complementary to H II regions analyses. Even more, these objects have revealed themselves as potential standard candles with an accuracy similar to Cepheid variable stars. Using the tools designed in this work, we have performed a detailed analyses on a sub-set of the massive blue stellar population belonging to NGC 55. The main conclusions can be summarized as:

- We have presented the first census of massive blue stars observed in NGC 55. The spectral classification performed on 204 FORS2 spectra recovered 164 stars with spectral type earlier than F0-type. The catalog also encloses seven exotic stars, likely highly evolved massive blue star stages, such as WRs or LBV candidates.

- The wide range of objects analyzed allowed us to study, although only roughly, the kinematic distribution of the galaxy, obtaining a similar systemic velocity than studies based on neutral hydrogen. The 2-D map showed that the massive blue stars follow, in average, the galactic velocity pattern. The dynamical center fits well with the H I studies and IR sources detected in this area, likely related with the bar suggested by some authors. However the map was too rough for a detailed NGC 55 structural analysis.

- From the catalog presented, we selected 75 supergiants for the quantitative determination of their stellar parameters and chemical abundances, being the largest sample of blue massive stars analyzed at this distance. This study, gathering stars with temperatures between $\sim$ 12000 and 32000 K, has illustrated the potential and efficiency of the techniques developed in this work.

- The chemical composition analysis was demanding, but possible. The radial galactic distribution did not show any sort of trend, as previous authors argued. The silicon, magnesium, and oxygen 2-D chemical maps, though shallow, hinted at a variation toward the north-west of NGC 55, however the error bars are too

large and an artifact cannot be discard. In spite of their rudeness, the 2-D patterns illustrate the necessity of using them as an alternative to a simple 1-D radial distribution, which could *disguise* a more complex spatial distribution or hidden particular areas of interest (especially in irregular galaxies such as NGC 55).

- Nitrogen, carbon, and to lesser degree, oxygen abundances can be *'contaminated'* by stellar evolution. Thus, [N/C] and [N/O] ratios are commonly used as stellar aging diagnostics. The NGC 55's [N/O] ratio showed a large scatter in the south-east, decreasing northward. Nonetheless, the large errors and the lack of a statistical representation of the NGC 55 blue population (in spite of this, it is the largest set of objects analyzed at this distance so far) avoid to reach a clear conclusion about a possible evolution trend across the galaxy.

- Unfortunately, issues with the observed photometry hampered the derivation of radii and masses. Assuming an average extinction, we have obtained preliminary values for the physical stellar parameters. The study set the stars between $\sim 20-50\ M_{\odot}$. The position in the HR diagram, together with the [N/O] ratio, suggested that these stars are still evolving towards the red side of the diagram.

Future Perspectives

Certainly a long way is still ahead before reaching a deep knowledge of massive blue stars formation and evolution in different environments, and their impact on the interstellar medium. The techniques and tools developed in this thesis were carried out to help on this titanic, though fundamental, task. Several long term projects have already been proposed as a continuation of the work presented here, briefly:

Atomic Models

The introduction of new chemical species and the updating of some of the model atoms is mandatory for a reliable description of the stellar spectrum. As we have pointed out in this work, the carbon model has shown caveats, and a new version developed by Nieva (2007) seems to solve these discrepancies in dwarf and giant stars, where the model has been tested. Following a similar path as for the silicon model, we plan to incorporate the carbon model into FASTWIND with the help of Drs. F. Nieva and N. Przybilla. This will be indispensable to obtain trustworthy carbon abundances, strongly linked to the stellar chemical evolution.

Automatic Techniques

Introducing optimization procedures in the implementation of the χ^2-method is considered as the next main step in the improvement of the technique developed in this work. Although the method used gives reliable results, a more objective approach for the error determination is desired. This improvement could make the χ^2 determination even faster.

In spite of the good results recovered by the method, the necessity of using a *'by-eye'* refinement in the chemical determination at low resolution hinders our final goal of a full automatic analysis. The improvement of this part of the code will be contemplated in future versions. The possibility of obtaining all the stellar parameters plus the chemical abundances without human intervention and minimum computational effort will be priceless for future large surveys.

Galactic Massive Blue Stars

The tools developed in this work will play a fundamental role in the fast quantitative analyses of the IACOB spectroscopic database. The survey brings the opportunity of performing a detailed study on high resolution and S/N spectra, obtained homogeneously and in different time series. This efficient observation program and high quality data will allow us to get rid of some of the issues found in low resolution data, and study the time dependency of stellar parameters.

Extragalactic Massive Blue Stars

Once the NGC 55 photometry is revised, the analyses provided in this work will give a reliable estimation of masses, radii and luminosities, bringing a full characterization of the stars involved in the study. Additionally, the NGC 55 extinction distribution will be mapped through the color excess.

Extending our study to nearby galaxies in the Local Group and performing detailed quantitative analyses (following a similar path to that presented in this work on NGC 55) are fundamental steps in our extragalactic future perspectives. We already have spectroscopy data of massive blue stars in M 33 and IC 1613, two galaxies that are closer than NGC 55, and with a simpler projected morphological structure. The different metallic content, spatial distribution, and the important blue stellar population showed by both makes these systems perfect environments to apply the techniques developed in our work. Our group is also involved in *'The Tarantula Survey'* (Evans et al. 2010), forged with multi-epoch spectroscopy of over 1000 massive stars in the 30 Doradus region in the LMC.

A

NGC 55 Catalog

THIS appendix compiles the qualitative analysis developed on the NGC 55 sample studied in this work. The catalog presented forms the first census of massive blue stars in the galaxy. Additionally, it also includes objects cooler than F0-type and foreground stars from the Milky Way. Although they are not the aim of this study, we have provided a spectral classification for them as well for the completeness of the entire observed data set. A description of the spectral classification process and criteria can be consulted in chapter 5.

TABLE A.1— Blue massive stars observed in NGC 55 earlier than F0 type. The columns list: (1) star identification; (2) right ascension (hh:mm:ss); (3) declination (dd:mm:ss); (4) apparent V-magnitude; (5) V-Ic colour, the comparison with the synthetic magnitudes shows several problems with the observed ones (see section 5.5.6 for details) ; (6) spectral type; (7) projected galactocentric distance (arc-seconds); (8) radial velocity (km s^{-1}) measured in this work, together with the standard deviation obtained and the number of lines used, *'(1σ,n_lines)'*; (9) signal-to-noise ratio of the spectrum; (10) notes.

ID (1)	RA(J2000) (2)	DEC(J2000) (3)	V (4)	V-Ic (5)	SpT (6)	Rg (7)	v_r (8)	S/N (9)	Notes (10)
D_1	0:14:08.97	-39:09:20.88	20.212	-0.557	B9I	539.27	112 (27,6)	43	
D_3	0:14:10.51	-39:09:50.76	18.581	-0.407	A0I	514.45	67 (20,6)	117	Str. winds?
D_4	0:14:12.11	-39:09:23.41	19.724	-0.524	B9I	503.52	69 (17,8)	60	
D_5	0:14:13.22	-39:09:19.79	19.963	-0.813	B3I	492.25	113 (25,7)	44	
D_6	0:14:15.09	-39:08:50.28	19.367	-0.404	A3II	481.66	58 (9,5)	62	
D_7	0:14:15.24	-39:09:29.87	19.928	-0.375	A0I-II	466.83	101 (6,7)	52	
D_9	0:14:16.74	-39:10:02.28	19.355	-0.563	B5I	441.34	91 (18,8)	93	
D_12	0:14:16.84	-39:11:25.08	20.096	-0.466	A0I-II	427.94	125 (19,5)	45	

D_11	0:14:18.14	-39:10:14.16	18.447	-0.595	B3I	422.76	45 (18,9)	199	neb. Str. winds?
D_10	0:14:18.35	-39:09:37.08	20.026	-0.516	A2I	430.18	69 (19,6)	44	neb.
D_14	0:14:20.02	-39:10:32.15	20.582	-0.728	B2.5I	397.66	125 (6,2)	30	neb.
D_13	0:14:20.39	-39:09:49.32	20.375	-0.787	B1I	403.89	138 (35,3)	42	
D_15	0:14:21.82	-39:10:00.11	20.258	-0.359	A0I	384.87	69 (7,5)	43	
D_16	0:14:22.80	-39:09:51.83	20.199	-0.868	B0.5II	376.42	86 (17,7)	30	neb.
D_25	0:14:23.76	-39:11:45.95	20.162	-0.449	A5II	346.89	72 (7,3)	38	
D_23	0:14:24.92	-39:10:00.11	19.330	-0.743	B2.5II	350.42	121 (31,6)	58	
D_24	0:14:26.77	-39:09:43.20	20.593	-0.455	A3II	335.94	72 (-,1)	16	neb.
D_28	0:14:28.63	-39:10:53.04	19.613	-0.784	B0.5I	295.43	128 (34,8)	32	neb.
D_27	0:14:28.73	-39:10:17.76	19.191	-0.642	B2I	302.86	152 (39,7)	76	
D_29	0:14:31.14	-39:10:16.32	18.972	-0.456	A3I	276.72	98 (29,6)	84	
D_26	0:14:31.87	-39:07:57.73	17.669	-0.073	A5I	341.81	22 (16,7)	174	
D_31	0:14:32.04	-39:10:34.68	19.951	-0.767	B2I	261.14	127 (45,4)	29	
D_32	0:14:33.14	-39:10:21.36	19.733	-0.567	A2I	253.13	107 (5,3)	40	
D_36	0:14:35.07	-39:11:20.04	19.189	-0.689	B9I	217.22	78 (11,7)	70	
D_38	0:14:36.07	-39:11:34.45	19.184	-0.427	A7II	204.24	110 (16,6)	49	
D_35	0:14:36.29	-39:09:59.40	18.506	-0.462	A3I	228.66	63 (14,3)	94	neb.
D_37	0:14:36.88	-39:10:45.12	19.926	-0.392	A3II	204.29	93 (25,4)	25	
D_39	0:14:38.46	-39:10:48.36	18.313	-0.453	A2I	185.83	132 (5,6)	100	
D_40	0:14:39.02	-39:10:57.00	19.903	0.165	A3III	177.00	77 (23,4)	27	
C2_2	0:14:39.42	-39:12:19.81	19.704	-0.463	A2II	167.89	70 (14,6)	55	
D_42	0:14:40.33	-39:10:57.35	18.700	-0.801	B1.5I	162.36	112 (12,6)	53	neb.
C1_1	0:14:40.51	-39:11:20.04	18.893	-0.732	A0I	154.72	144 (7,6)	100	
D_43	0:14:41.08	-39:11:12.84	19.454	-0.017	O9I	149.73	92 (6,3)	27	
C2_1	0:14:41.38	-39:10:53.76	19.249	-0.641	A0I	152.06	86 (12,7)	68	
C1_5	0:14:42.10	-39:12:40.32	19.249	-0.794	B2.5I	143.56	128 (21,11)	82	
D_45	0:14:42.25	-39:11:15.36	19.737	-0.493	A2I	135.92	129 (17,5)	45	neb.
D_46	0:14:42.58	-39:11:27.61	19.141	0.006	Late_AII	129.72	155 (27,3)	19	
C1_4	0:14:43.39	-39:11:20.04	18.863	-0.606	B1.5I	121.94	147 (15,8)	71	
C2_5	0:14:43.57	-39:11:14.29	19.215	-0.832	B3I	121.37	132 (13,8)	55	
C2_8	0:14:43.87	-39:12:29.51	19.294	-0.652	A0I	120.49	95 (16,8)	69	
C1_9	0:14:45.54	-39:12:38.17	18.939	-0.817	B1I	106.29	118 (20,8)	86	
C1_8	0:14:45.70	-39:11:52.08	18.920	-0.791	B8I	91.93	149 (18,8)	72	
C1_10	0:14:47.70	-39:11:57.48	17.982	-0.495	A2I	69.24	100 (11,8)	138	
C2_14	0:14:48.05	-39:12:45.72	19.044	-0.944	B8I	86.57	130 (21,9)	112	
C2_11	0:14:48.33	-39:11:20.75	18.545	-1.800	O8I	67.05	98 (9,3)	67	neb.
C2_12	0:14:48.84	-39:11:24.00	19.006	-0.064	A2III	60.32	107 (24,6)	73	neb.
C1_11	0:14:49.80	-39:11:07.43	19.444	-0.761	A3I	59.97	123 (18,6)	46	neb.
C2_15	0:14:50.00	-39:12:16.19	19.424	-0.542	A0I	50.46	98 (16,8)	83	
C2_13	0:14:50.21	-39:11:17.16	18.822	-0.710	A2I	50.04	90 (6,7)	89	
C1_15	0:14:50.50	-39:12:36.35	19.642	-0.765	B8I	60.31	158 (26,6)	69	neb.
C1_16	0:14:51.16	-39:12:47.88	18.917	-0.588	A5I	66.27	154 (16,8)	98	
C1_13	0:14:51.86	-39:10:57.35	18.948	-0.706	B1I	54.53	115 (20,8)	60	neb.
C2_16	0:14:52.28	-39:11:26.52	18.419	-0.451	HII	26.40	109 (11,3)	24	
C2_18	0:14:52.32	-39:12:05.76	19.453	-0.591	B2.5II	23.18	92 (19,10)	42	
C1_14	0:14:52.59	-39:11:04.21	18.503	-0.662	A5I	45.33	107 (7,7)	125	
C1_17	0:14:52.67	-39:12:38.88	18.830	-0.416	A3I	52.02	117 (13,7)	107	
C2_17	0:14:52.76	-39:11:29.04	18.748	-0.902	B0.5I	21.33	149 (21,8)	51	
C2_19	0:14:53.13	-39:12:00.00	19.070	-0.371	A3I	13.20	91 (22,6)	46	neb.
C2_21	0:14:53.46	-39:12:35.64	19.719	-0.662	B2I	47.67	145 (22,7)	30	neb.
C2_20	0:14:53.58	-39:12:06.11	18.745	-0.262	B2I	18.12	2 (11,6)	65	neb.
C2_22	0:14:55.19	-39:12:30.96	18.764	-0.418	A2I	46.77	140 (21,5)	48	neb. Str. winds?
C1_18	0:14:55.94	-39:11:21.84	19.316	-0.707	WN8	37.73	124 (-,1)	30	neb.
C2_29	0:14:56.75	-39:11:56.40	18.335	-0.638	B8I	37.57	150 (19,5)	63	neb.
C1_27	0:14:57.48	-39:12:00.00	19.274	-0.093	A2I	46.67	161 (23,4)	24	neb.

C2_33	0:14:58.50	-39:12:38.88	19.645	-2.167	O5III	76.38	165 (36,4)	42	neb.
C1_32	0:14:58.59	-39:13:52.68	17.122	-0.563	B9I	137.52	161 (10,7)	241	Str. winds?
C2_32	0:14:58.69	-39:12:15.12	18.164	-0.940	HII	65.09	139 (5,3)	28	
C2_34	0:14:58.73	-39:12:54.00	19.062	-0.679	A3III	88.95	210 (5,2)	41	neb.
C2_35	0:14:59.68	-39:12:42.84	18.193	-1.404	Early_OI	89.46	105 (31,3)	34	neb.
C2_40	0:14:59.90	-39:14:12.11	19.428	-0.758	A7II	161.65	133 (17,6)	39	
C1_30	0:14:59.91	-39:12:11.88	18.921	-0.425	LBV	77.14	158 (10,3)	28	LBV-Candidate
C1_31	0:15:00.01	-39:12:41.39	18.523	-0.716	Early_OI	91.67	157 (7,3)	40	neb.
C2_37	0:15:01.19	-39:12:20.16	18.909	-0.752	A0I	93.91	168 (24,5)	51	neb.
C2_36	0:15:02.11	-39:11:35.87	19.325	-0.787	B8I	99.66	142 (32,5)	28	
C1_36	0:15:02.36	-39:13:31.44	19.287	-1.950	HII	145.15	162 (21,3)	22	
C1_37	0:15:02.50	-39:13:58.44	19.642	-0.588	A7II	166.49	146 (20,4)	55	
C1_34	0:15:02.58	-39:12:30.60	18.962	-0.789	B8I	112.74	176 (12,7)	69	neb.
C2_41	0:15:02.82	-39:12:58.68	18.475	-0.739	B0.5III	128.38	243 (17,7)	82	neb.
C1_35	0:15:02.85	-39:12:49.67	19.336	-0.534	B5III	123.96	239 (24,6)	52	neb.
C2_39	0:15:02.98	-39:12:05.04	18.180	-0.719	A2I	110.36	158 (21,7)	112	
C1_38	0:15:03.16	-39:14:02.03	19.603	-0.849	B0I	174.11	175 (20,4)	38	neb.
C2_38	0:15:03.96	-39:11:04.92	18.586	-0.397	A3II	127.90	242 (38,7)	97	
C2_44	0:15:04.10	-39:13:44.40	19.902	-0.725	A2I	168.66	141 (17,5)	51	neb.
C2_42	0:15:04.15	-39:12:51.84	20.382	-0.320	A7II	138.26	124 (23,4)	30	neb.
C2_43	0:15:04.19	-39:13:22.80	19.985	-0.687	B9II	155.37	212 (19,6)	30	
C1_39	0:15:04.72	-39:13:52.32	18.514	-1.517	HII	179.34	132 (9,3)	22	
B_3	0:15:07.65	-39:13:21.71	20.556	-0.165	A2II	188.30	193 (16,7)	33	
C1_41	0:15:07.65	-39:13:21.71	20.556	-0.165	A3II	188.30	203 (27,6)	41	
C2_45	0:15:08.05	-39:12:45.01	20.229	-0.299	A3II	177.39	169 (23,7)	26	
C1_40	0:15:08.71	-39:12:09.73	20.010	-0.627	B1.5I	176.99	184 (24,8)	59	neb.
C1_42	0:15:09.00	-39:13:04.79	17.754	-0.277	A2I	194.79	149 (7,6)	137	Str. winds?
C2_46	0:15:09.18	-39:12:55.44	18.941	-0.672	B1I	193.26	196 (26,6)	75	neb.
C2_47	0:15:10.45	-39:12:39.97	19.459	-0.508	B9I	202.65	230 (18,8)	43	neb.
C1_43	0:15:10.86	-39:12:28.80	19.055	-0.069	A0I	204.75	175 (26,3)	57	Str. winds?
C1_46	0:15:11.18	-39:13:18.12	19.887	-0.439	B2III	223.35	164 (17,4)	27	neb.
C2_48	0:15:11.24	-39:12:38.17	19.371	-0.456	B5I	211.10	188 (40,6)	58	neb.
C1_44	0:15:11.29	-39:12:34.55	19.037	-0.740	B0I	210.84	181 (42,5)	79	neb.
C1_45	0:15:11.31	-39:12:50.40	19.607	-0.180	B1I	215.12	179 (20,9)	38	neb.
C2_49	0:15:11.82	-39:12:43.92	20.154	-0.570	B1I	219.06	235 (17,5)	33	neb.
C1_47	0:15:11.92	-39:13:08.76	18.023	-0.291	A0I	227.76	182 (20,7)	134	Str. winds?
C2_50	0:15:12.18	-39:12:52.56	20.159	-0.433	B1I	225.43	276 (11,6)	34	neb.
C2_51	0:15:12.68	-39:12:56.51	19.719	-0.764	B9I	232.14	213 (24,7)	61	neb.
C1_48	0:15:13.11	-39:12:47.16	19.519	-0.715	B0.5I	234.38	164 (24,6)	30	neb.
C1_49	0:15:13.14	-39:13:01.20	19.127	-0.262	A5I	238.65	165 (19,7)	92	
B_7	0:15:13.31	-39:12:43.56	17.595	-0.556	A0I	235.76	162 (15,5)	125	neb. Str. winds?
B_8	0:15:13.98	-39:12:48.25	15.874	-1.606	O9If	244.45	367 (1,2)	185	Cluster. neb.
C2_54	0:15:14.34	-39:13:27.84	19.435	-0.497	B9I	260.95	223 (9,8)	51	neb.
C1_53	0:15:14.64	-39:13:36.12	19.816	-0.485	B2.5I	267.42	164 (16,4)	45	neb.
B_9	0:15:14.66	-39:13:03.72	19.416	-0.524	B5I	256.26	223 (28,6)	57	neb.
C1_51	0:15:14.70	-39:12:54.36	18.306	-0.098	Ofpe/WN9	254.10	187 (28,2)	57	neb.
C1_52	0:15:14.79	-39:13:10.92	18.542	-0.147	A2I	259.91	149 (19,4)	107	neb. Str. winds?
C2_55	0:15:15.95	-39:12:54.36	19.185	-0.277	B5I	268.15	228 (26,8)	39	neb.
B_12	0:15:16.68	-39:13:26.40	19.108	-0.666	Of/WN	285.77	176 (28,2)	90	neb.
B_11	0:15:16.74	-39:12:46.08	19.001	0.206	B1I	275.19	155 (17,9)	61	neb.
B_13	0:15:18.63	-39:13:12.72	18.543	-0.435	LBV/WN11	303.05	274 (25,3)	103	LBV-Candidate
B_22	0:15:19.73	-39:14:48.12	18.274	-0.268	B2.5I	353.14	202 (22,9)	143	Str. winds?
B_15	0:15:20.89	-39:13:17.76	20.308	-0.161	A3I	329.69	217 (21,6)	29	neb.
B_23	0:15:24.24	-39:13:04.79	19.531	-0.586	B2I	364.36	209 (22,10)	77	
B_24	0:15:25.44	-39:13:03.00	20.318	-0.300	A5II	377.65	162 (21,7)	43	
B_26	0:15:26.91	-39:13:28.92	20.116	-0.891	O9I	400.15	217 (36,8)	52	

B_28	0:15:27.41	-39:14:36.60	19.591	-0.079	A0III	427.67	178 (23,7)	56	
B_25	0:15:27.78	-39:12:25.56	18.712	-0.261	A0III	399.10	173 (23,7)	74	
B_30	0:15:31.27	-39:14:30.12	19.591	-0.012	B9I	466.95	291 (27,5)	74	neb. Str. winds?
B_31	0:15:32.22	-39:14:40.20	19.429	-0.478	B2.5I	480.84	190 (23,8)	95	
B_33	0:15:33.53	-39:15:10.44	19.125	-0.467	O5If	506.40	178 (32,2)	94	neb.
B_35	0:15:36.86	-39:15:10.79	20.291	-0.513	B1.5I	542.23	236 (30,4)	30	neb.
B_34	0:15:37.73	-39:13:49.08	19.533	-0.242	LBV/WN11	527.09	216 (19,3)	35	LBV-Candidate
B_37	0:15:38.38	-39:15:29.88	19.651	-0.201	A2I	565.87	186 (10,2)	53	neb.
A_1	0:15:38.52	-39:14:49.21	19.099	-0.777	B1I	552.73	262 (17,8)	110	neb.
A_2	0:15:38.64	-39:14:52.43	19.227	-0.632	B1.5I	555.11	253 (25,8)	77	neb.
A_4	0:15:39.99	-39:15:00.71	19.604	-0.167	A5I	572.67	236 (20,6)	71	neb.
B_36	0:15:40.62	-39:13:40.07	19.782	-0.389	O8I	557.96	171 (12,5)	55	
A_5	0:15:40.83	-39:15:09.72	20.071	-0.495	A3I	584.92	260 (18,7)	58	
A_3	0:15:41.35	-39:13:48.73	19.623	-0.184	A2I	568.05	223 (40,5)	86	neb.
A_7	0:15:41.99	-39:15:30.95	19.901	-0.650	B2I	605.09	254 (25,10)	73	
A_6	0:15:42.47	-39:14:46.32	19.039	-0.199	A3I	595.43	268 (13,8)	86	
A_10	0:15:43.43	-39:16:20.28	18.836	-0.329	A0I	640.06	187 (10,8)	134	
A_8	0:15:44.18	-39:14:58.20	19.792	-0.188	O9.7I	617.97	304 (27,9)	62	
A_11	0:15:45.17	-39:15:56.15	18.706	-0.245	B5I	648.82	209 (25,11)	130	
A_9	0:15:45.56	-39:14:45.59	18.824	-0.175	A5I	629.58	268 (24,7)	84	
A_12	0:15:46.52	-39:15:48.96	18.594	-0.722	O5If	660.69	234 (21,6)	129	neb.
A_13	0:15:48.53	-39:15:14.04	20.310	-0.195	A5II	670.96	216 (21,6)	44	
A_14	0:15:49.14	-39:15:35.64	19.139	-0.279	B9I	684.59	225 (8,7)	115	neb.
A_15	0:15:49.93	-39:15:28.80	18.794	-0.475	B3I	691.04	201 (20,8)	154	neb. Str. winds?
A_16	0:15:50.25	-39:15:43.92	19.590	-0.518	B0.5I	699.52	286 (19,6)	121	neb.
A_25	0:15:50.78	-39:17:29.40	19.687	-0.504	B8I	747.25	229 (17,10)	86	
A_18	0:15:51.38	-39:16:20.28	19.555	-0.019	A7I	724.76	161 (21,5)	100	neb.
A_17	0:15:51.42	-39:15:57.60	20.336	-0.321	B1I	716.99	207 (25,8)	79	
A_26	0:15:55.45	-39:15:30.60	19.236	-0.262	B2.5I	752.66	220 (17,11)	96	
A_28	0:15:55.62	-39:16:11.27	20.047	-0.336	A2I	767.53	219 (16,7)	62	
A_30	0:15:57.58	-39:16:14.51	19.468	-0.795	O9I	790.06	199 (73,4)	44	neb.
A_29	0:15:57.97	-39:15:33.84	19.575	-0.595	O5If+	781.62	210 (25,3)	62	neb.
A_27	0:15:58.03	-39:14:27.60	19.928	-0.477	B2I	765.79	199 (29,8)	66	
A_31	0:15:58.22	-39:16:14.16	20.288	-0.592	O9I	796.94	213 (27,7)	46	neb.
A_33	0:15:58.83	-39:17:05.29	19.996	-0.429	A0I	821.98	199 (13,7)	75	
A_32	0:15:59.49	-39:16:08.40	17.813	-0.335	A7I	809.01	197 (25,3)	141	neb.
A_34	0:16:01.17	-39:16:34.67	20.247	-0.875	B0I	836.16	215 (22,10)	68	
A_35	0:16:01.49	-39:16:42.96	19.744	-0.490	B3III	842.52	204 (22,10)	80	
A_36	0:16:02.33	-39:16:48.72	20.758	-0.418	B2I	853.69	191 (24,7)	39	neb.
A_37	0:16:02.90	-39:17:04.91	20.024	-0.603	B0.5I	865.68	153 (22,5)	71	neb.
A_38	0:16:04.95	-39:16:15.96	18.706	-0.197	A0I	871.63	157 (13,8)	146	
A_39	0:16:05.30	-39:16:45.84	20.451	-0.021	B5I	885.11	217 (24,7)	51	
A_40	0:16:08.02	-39:15:52.20	19.938	-0.484	B5I	898.91	200 (22,10)	67	
A_41	0:16:09.00	-39:16:18.84	20.114	-0.445	B1I	917.39	202 (24,8)	52	neb.
A_42	0:16:09.69	-39:16:13.44	19.453	-0.189	LBV	923.49	175 (20,4)	75	LBV-Candidate
A_43	0:16:10.57	-39:16:27.48	19.358	-0.215	A2I	937.39	185 (14,8)	94	neb.
A_44	0:16:10.91	-39:16:33.25	20.103	-0.443	B3II	942.89	214 (26,8)	49	neb.
A_45	0:16:10.98	-39:17:19.68	20.710	-0.726	B0I	958.72	165 (28,9)	44	

TABLE A.2— F- and G-type stars observed in NGC 55. Columns are detailed in Table A.1.

ID (1)	RA(J2000) (2)	DEC(J2000) (3)	V (4)	V-Ic (5)	Spectral Type (6)	Rg (7)	v_r (8)	S/N (9)	Notes (10)
D_2	0:14:11.65	-39:08:19.69	20.461	-0.213	F0-2I	530.29	17 (13,3)	36	
D_33	0:14:32.48	-39:11:11.40	17.808	-0.223	F5I	248.23	56 (21,3)	166	neb.
D_34	0:14:33.65	-39:10:56.64	19.475	-0.051	F5I	237.53	30 (15,2)	46	neb.
D_41	0:14:39.70	-39:10:56.64	18.418	-0.024	F5-8I	169.55	55 (12,4)	76	
C2_6	0:14:41.86	-39:12:40.68	19.545	-0.088	F2-5I	146.29	69 (26,4)	68	
C1_2	0:14:42.13	-39:10:51.96	18.887	-0.383	F0-2I	144.64	126 (9,5)	64	
D_44	0:14:42.61	-39:10:39.01	19.163	0.253	G0-2I	145.19	95 (-,1)	25	
C2_4	0:14:43.18	-39:11:11.04	19.666	-0.387	F0-2I	126.65	87 (10,5)	39	neb.
C1_6	0:14:45.67	-39:11:14.64	17.392	-0.077	G0I	98.04	69 (25,3)	104	
C2_9	0:14:45.99	-39:11:51.72	19.459	-0.265	F2-5I	88.55	126 (23,3)	30	
C1_12	0:14:50.42	-39:11:09.25	18.345	-0.329	F5-8I	53.55	133 (14,3)	107	neb.
C1_25	0:14:56.02	-39:12:14.39	17.310	-0.287	F8I	38.57	92 (24,3)	109	neb.
C2_30	0:14:56.08	-39:12:50.40	19.480	-0.517	F0-2I	68.74	141 (26,6)	32	neb.
C1_28	0:14:57.43	-39:12:33.13	17.611	-0.410	F5I	63.39	189 (-,1)	158	neb.
C2_31	0:14:59.10	-39:11:37.32	18.107	-0.282	F8I	64.82	123 (14,4)	114	
C1_29	0:14:59.39	-39:11:49.19	18.230	-0.342	F8I	67.31	143 (25,3)	88	
B_4	0:15:10.36	-39:12:27.36	17.987	0.328	G0-2I	198.76	177 (33,2)	101	neb.
B_5	0:15:11.07	-39:12:54.71	18.759	0.134	F8I	213.76	164 (16,3)	76	neb.
B_6	0:15:11.58	-39:13:06.24	19.402	0.123	G0I	223.17	176 (34,3)	48	neb.
C1_50	0:15:12.90	-39:13:27.48	17.635	-0.006	F5-8I	245.42	138 (23,4)	162	
C2_52	0:15:13.51	-39:12:52.92	18.064	-0.261	F5I	240.38	204 (17,5)	87	
C2_53	0:15:13.88	-39:13:04.08	18.737	-0.102	F5I	247.72	189 (17,5)	81	
B_10	0:15:13.88	-39:13:41.87	19.274	0.180	F8I	261.81	179 (29,3)	57	neb.

TABLE A.3— Low luminosity class stars, likely members of the Milky Way halo. Columns are the same as in Table A.1.

ID (1)	RA(J2000) (2)	DEC(J2000) (3)	V (4)	V-Ic (5)	Spectral Type (6)	Rg (7)	v_r (8)	S/N (9)	Notes (10)
D_8	0:14:16.16	-39:09:38.16	18.945	-0.161	A5V	454.18	75 (16,3)	69	neb.
D_30	0:14:32.02	-39:10:17.03	19.746	0.139	G2-5V	266.85	34 (-,1)	36	
C1_3	0:14:40.77	-39:12:01.07	19.016	-1.017	Da	149.72	106 (29,3)	111	
C2_3	0:14:42.07	-39:11:17.16	19.045	-0.020	B2V	137.54	107 (7,5)	40	
C1_7	0:14:45.26	-39:11:42.36	18.455	-0.197	G0-2V	97.12	136 (38,2)	93	neb.
C2_7	0:14:45.38	-39:11:17.16	18.440	-0.160	B3V	100.41	79 (25,6)	55	neb.
C1_26	0:14:55.76	-39:12:36.72	19.046	-0.388	B8V	54.81	171 (20,6)	40	neb.
C1_33	0:15:03.24	-39:11:52.08	17.373	-0.056	G5V	112.13	74 (2,2)	131	
B_1	0:15:11.68	-39:10:10.57	18.120	0.191	G0-2V	231.65	160 (19,3)	117	
B_14	0:15:21.01	-39:12:50.05	19.677	0.006	B2V	324.62	179 (17,7)	75	neb.
B_27	0:15:28.60	-39:13:20.64	19.278	-0.014	A5V	417.28	228 (18,4)	43	
B_29	0:15:32.54	-39:12:52.56	19.572	0.326	F8V	457.24	157 (17,3)	55	
B_32	0:15:38.10	-39:12:08.64	18.438	0.212	G5V	517.71	20 (14,3)	67	

B

NGC 55 B-type Stars: Quantitative Analyses

THIS appendix displays the comparison between 75 observed supergiant blue stars belong to NGC 55, listed in Tab 5.10, with the best synthetic FASTWIND stellar model obtained. A dissertation of their quantitative analysis and a description of the observed data can be checked in chapter 5. Additionally, the models selected in the $T_{eff} - log(g)$ space of parameters are shown as a result of the techniques and criteria proposed in chapter 4. According to the signal-to-noise ratio of the data, the distribution of compatible models will change with clear repercussions on the stellar parameters and errors derived, gathered in Tab. 5.11.

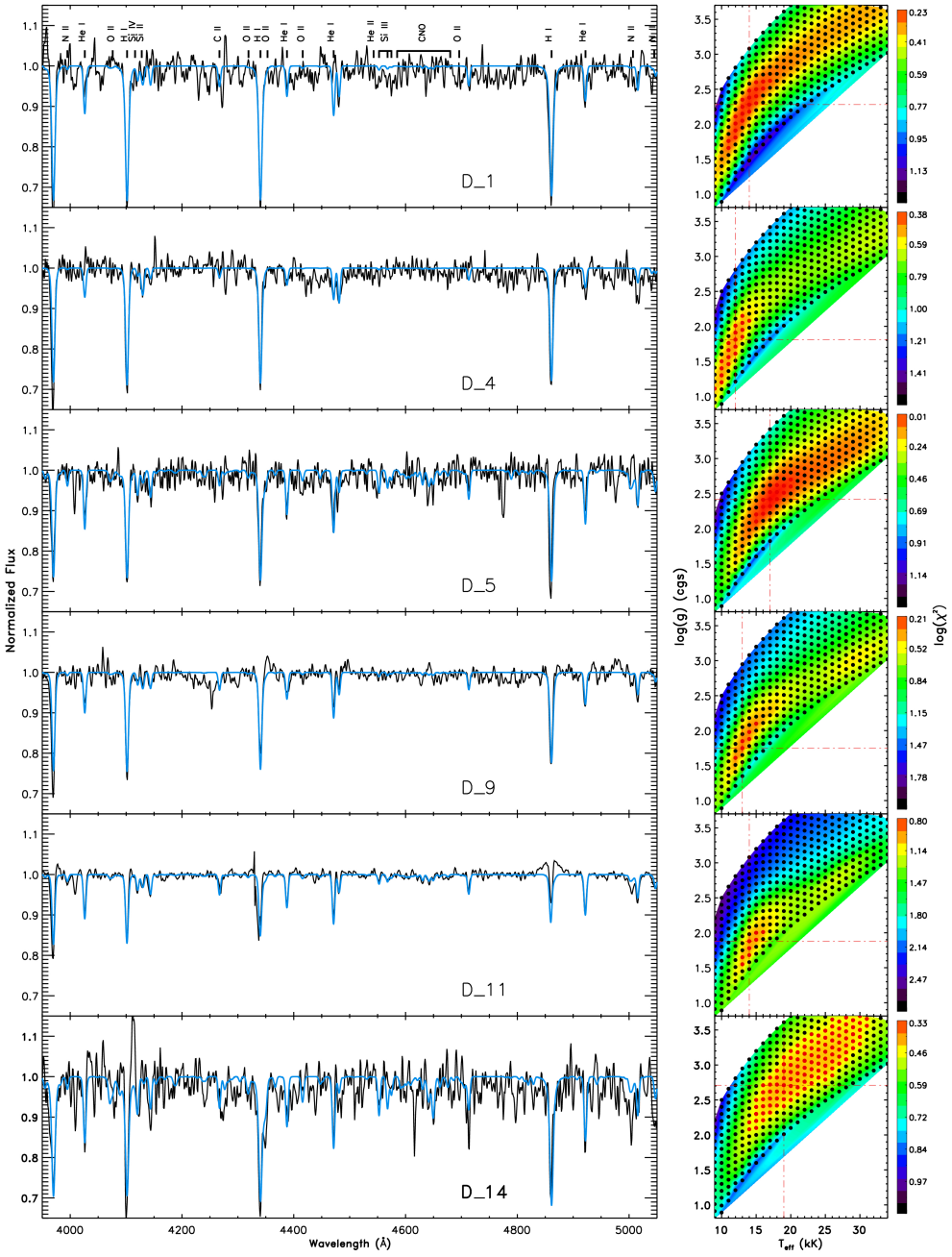

FIGURE B.1— Left panel: NGC 55 spectra (black) plus best fit model (blue) obtained by our automatic method together with a subsequent detailed abundance analysis. The main transitions used in the study are marked in the top chart. Right panel: χ^2 difference between observations and the entire grid models in the $T_{eff} - log\,(g)$ parameter space. $log\,(\chi^2)$ has been color-coded from red (minimum, better fit) to blue (maximum). Black dots represent all the grid models; the models whose parameters have been averaged to provide the stellar parameters are marked with red dots.

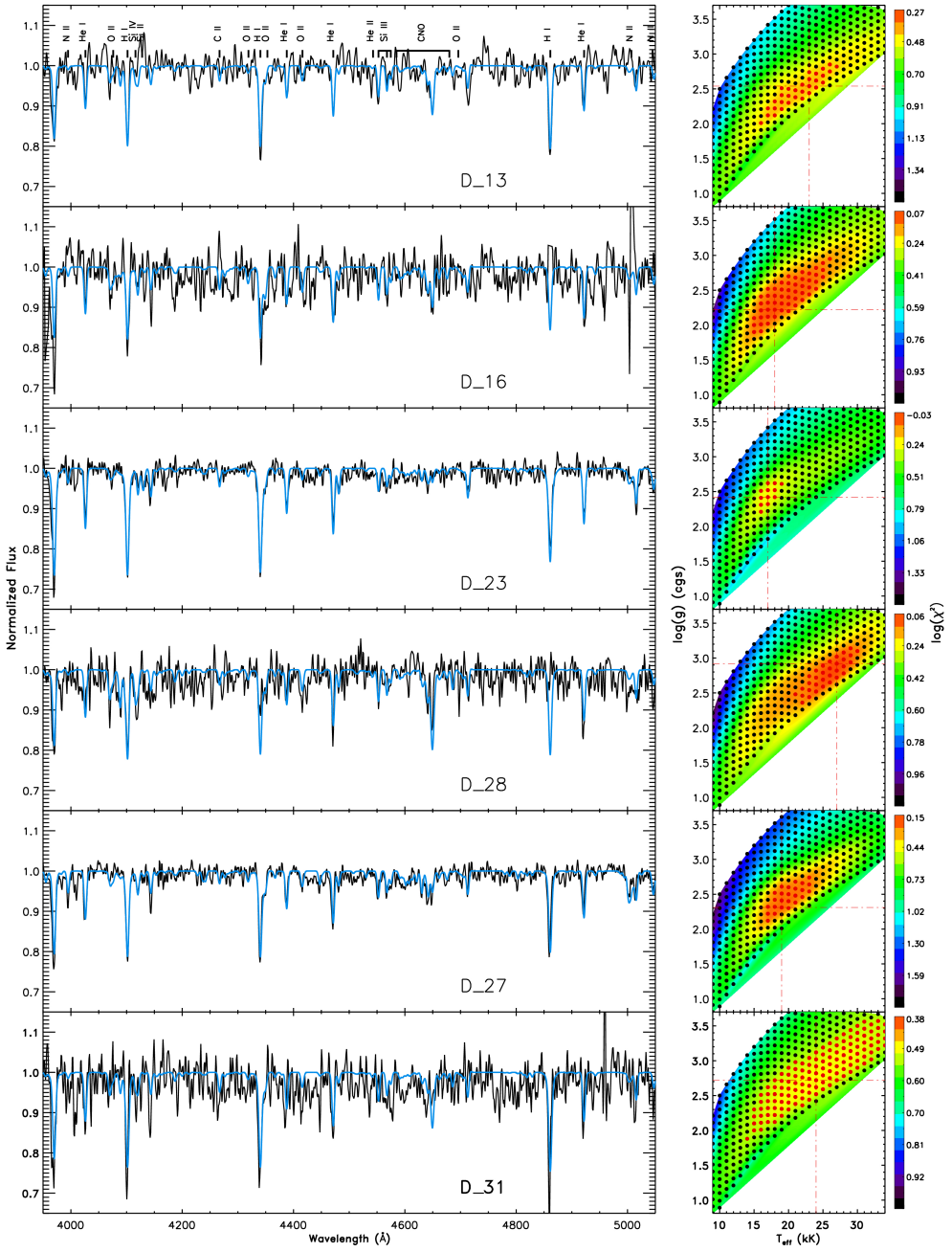

FIGURE B.2— Figure B.1, continued.

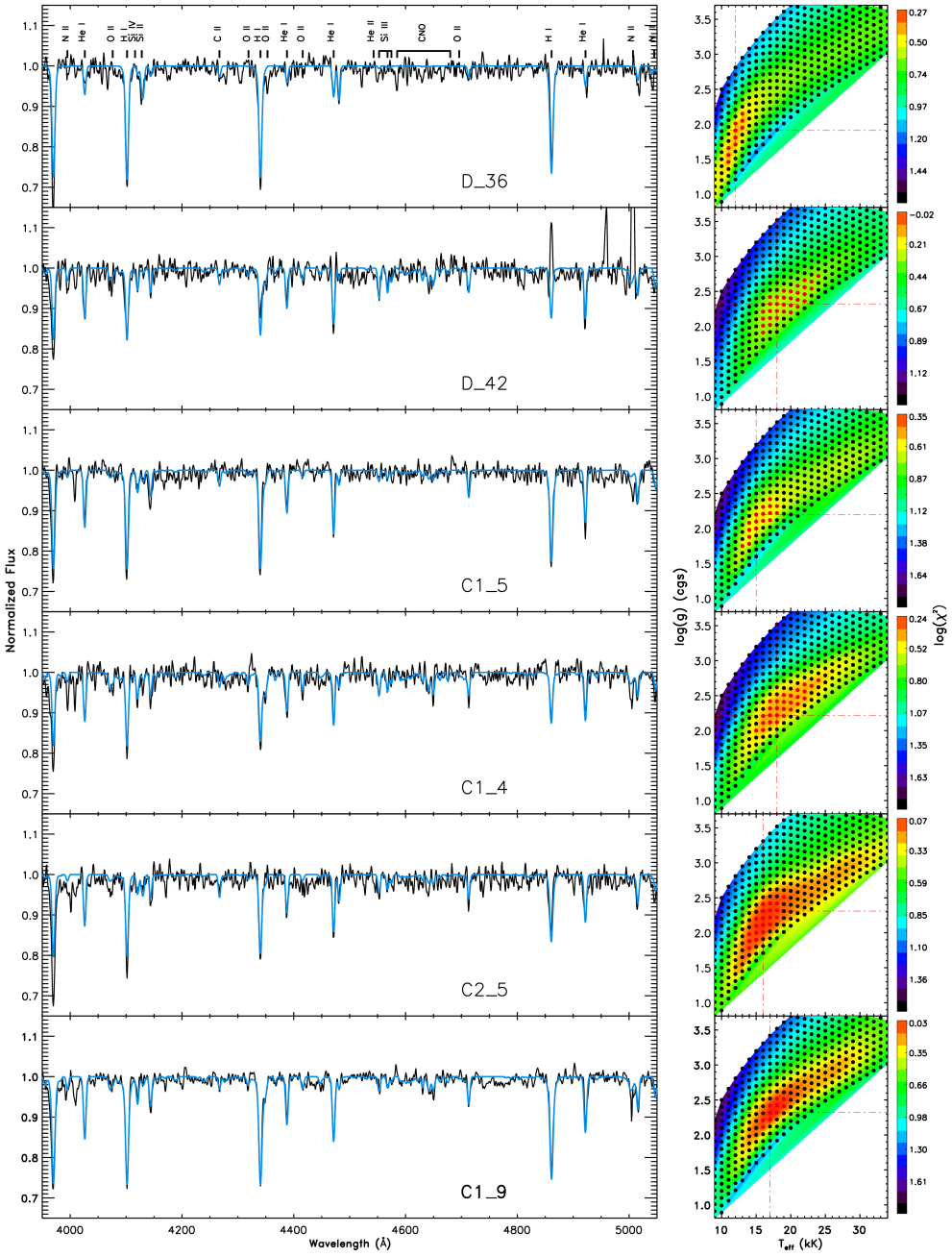

FIGURE B.3— Figure B.1, continued.

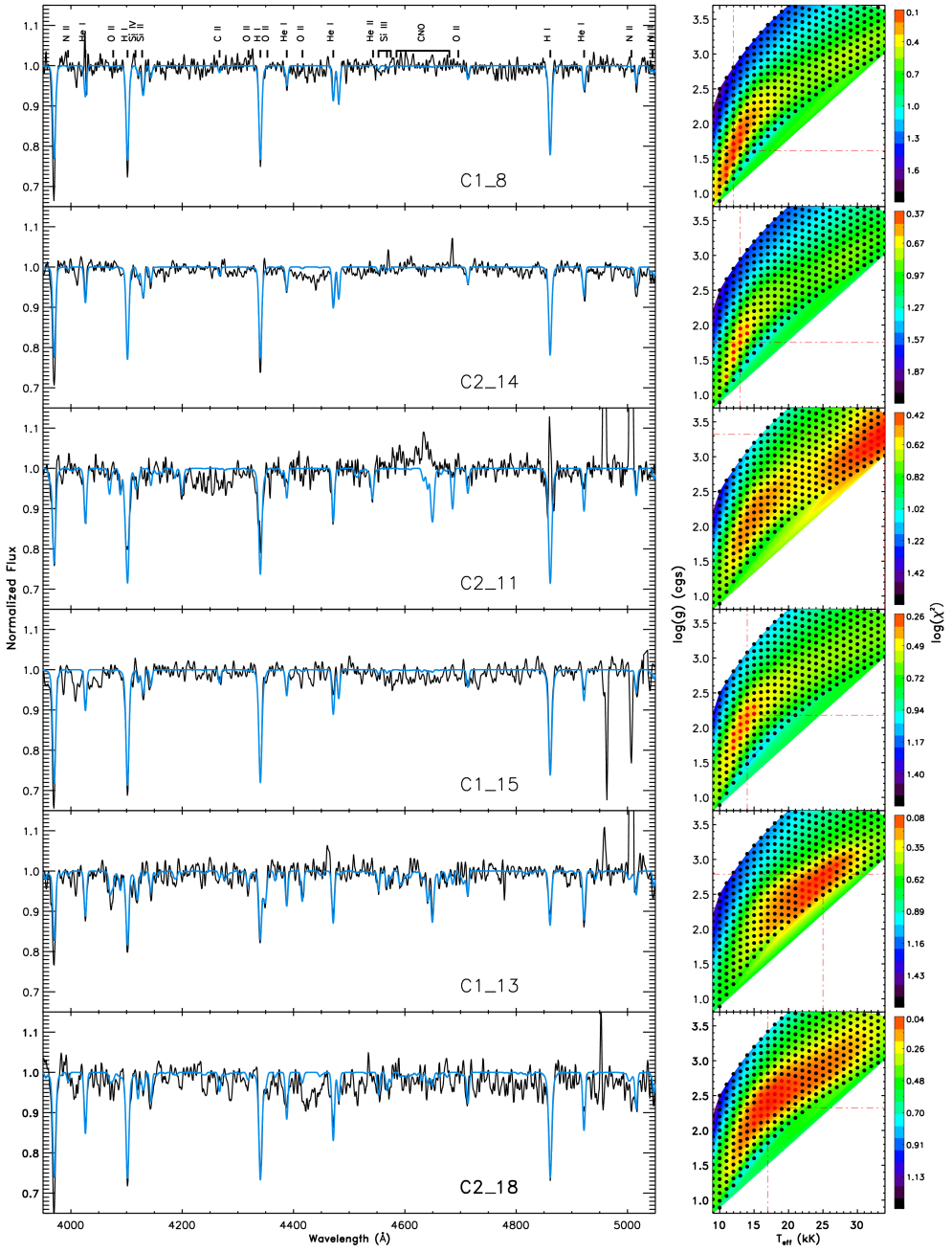

FIGURE B.4— Figure B.1, continued.

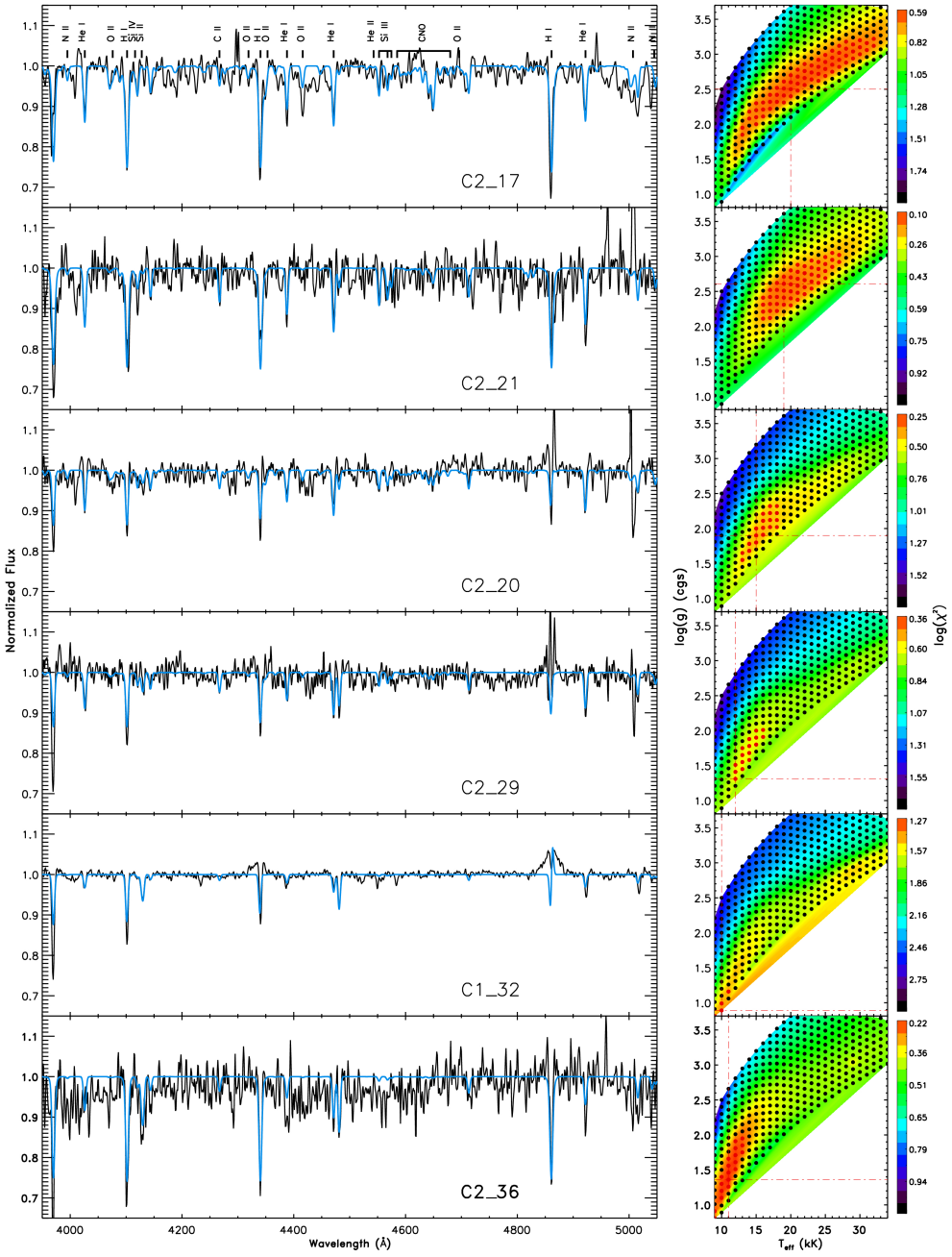

FIGURE B.5— Figure B.1, continued.

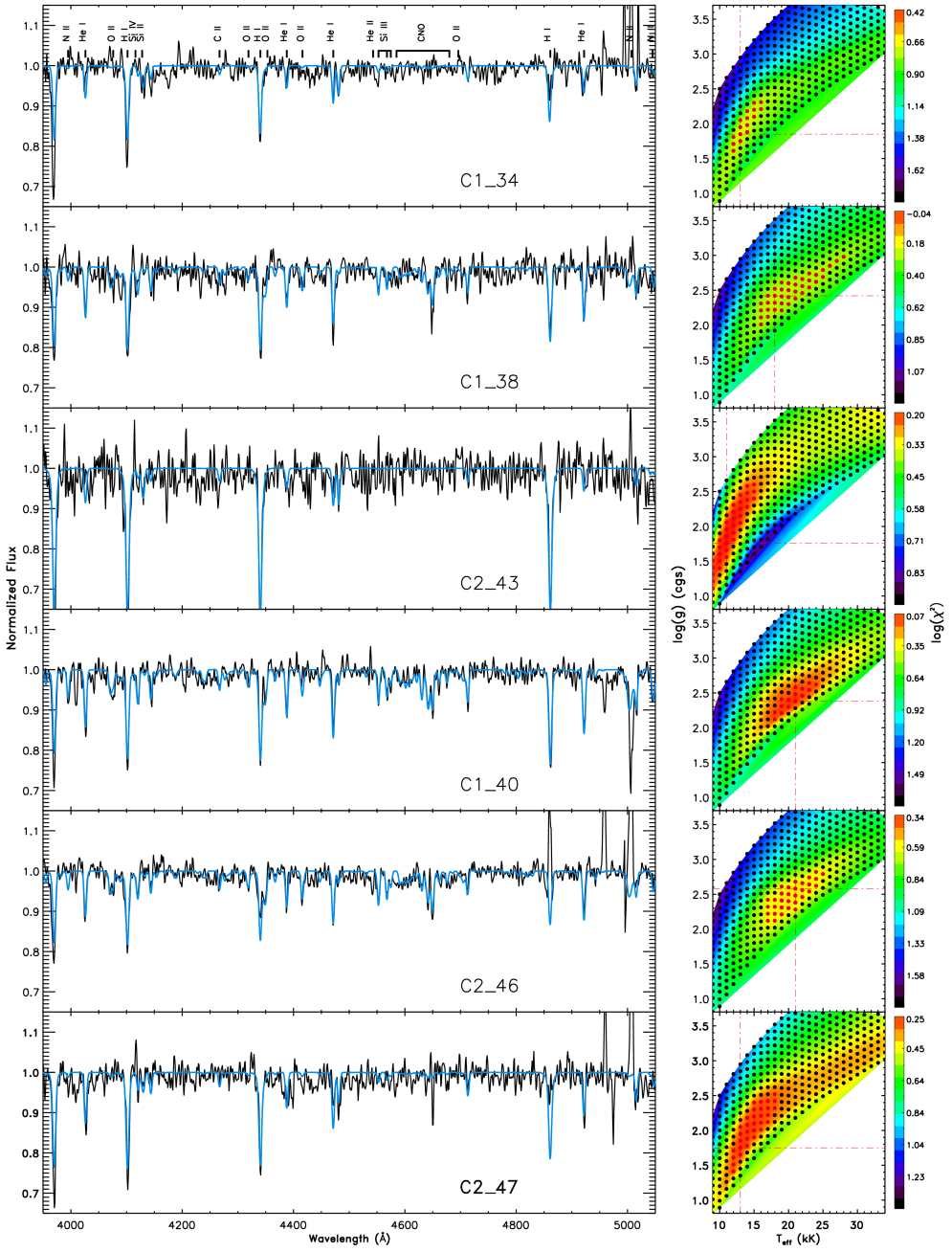

FIGURE B.6— Figure B.1, continued.

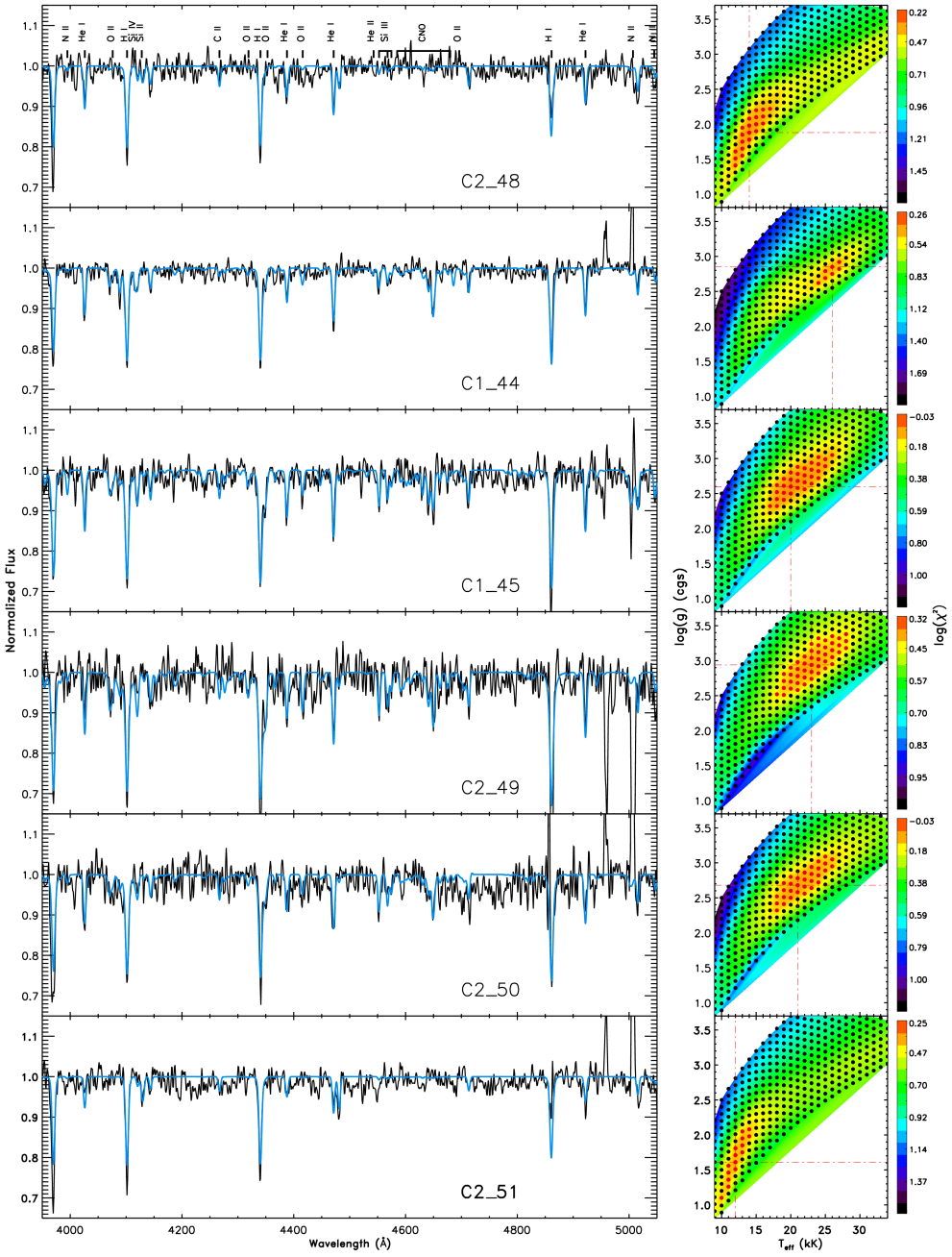

FIGURE B.7— Figure B.1, continued.

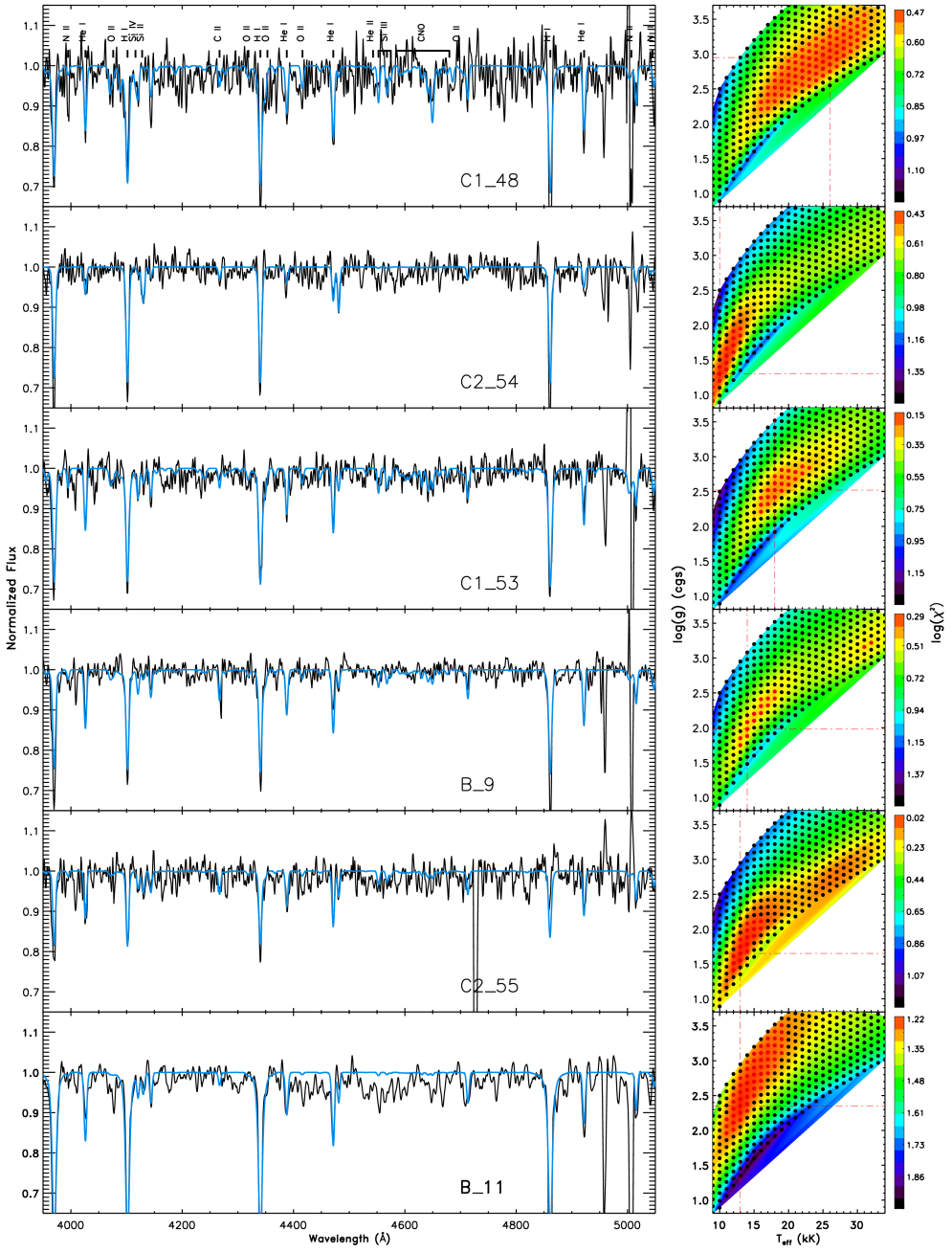

FIGURE B.8— Figure B.1, continued.

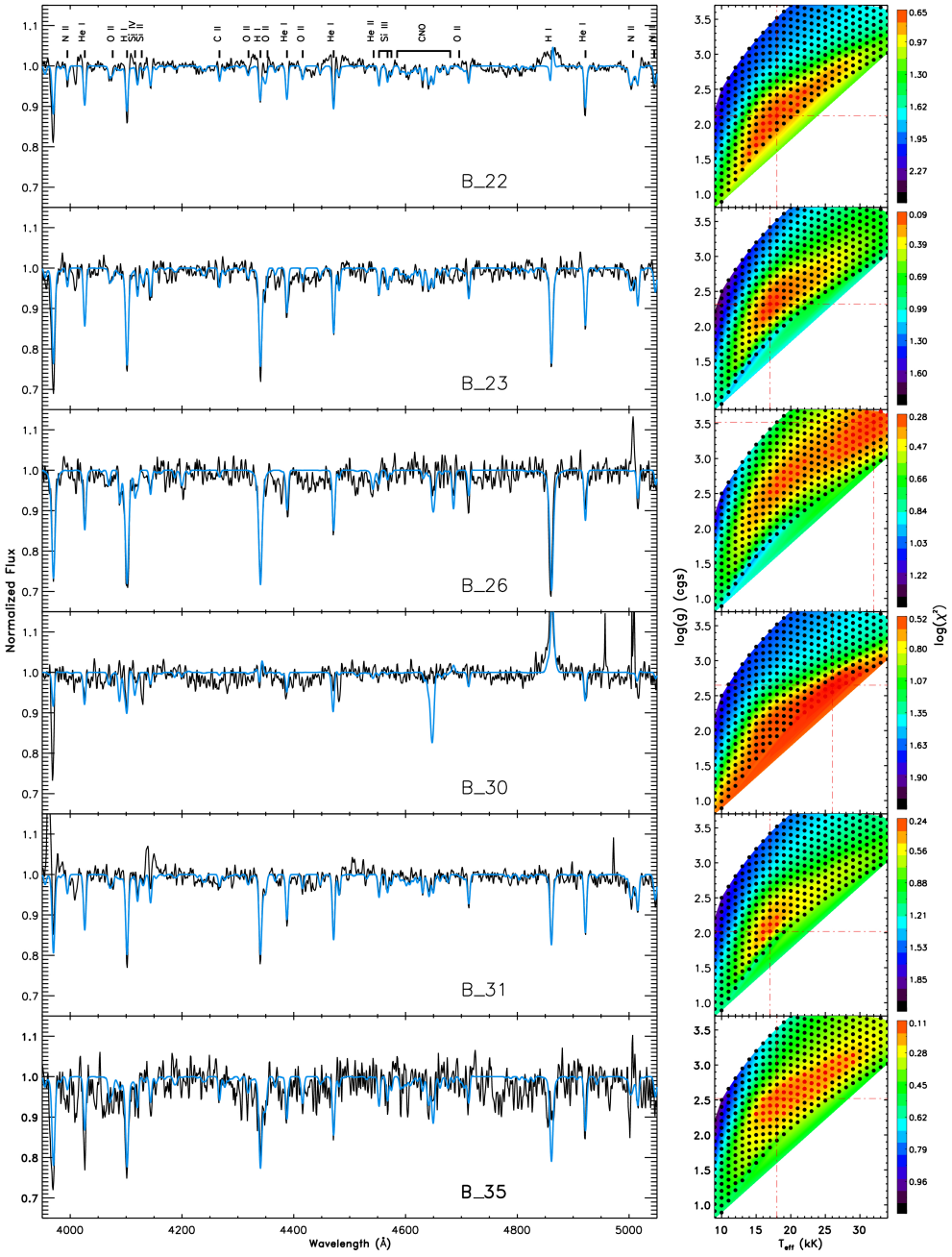

FIGURE B.9— Figure B.1, continued.

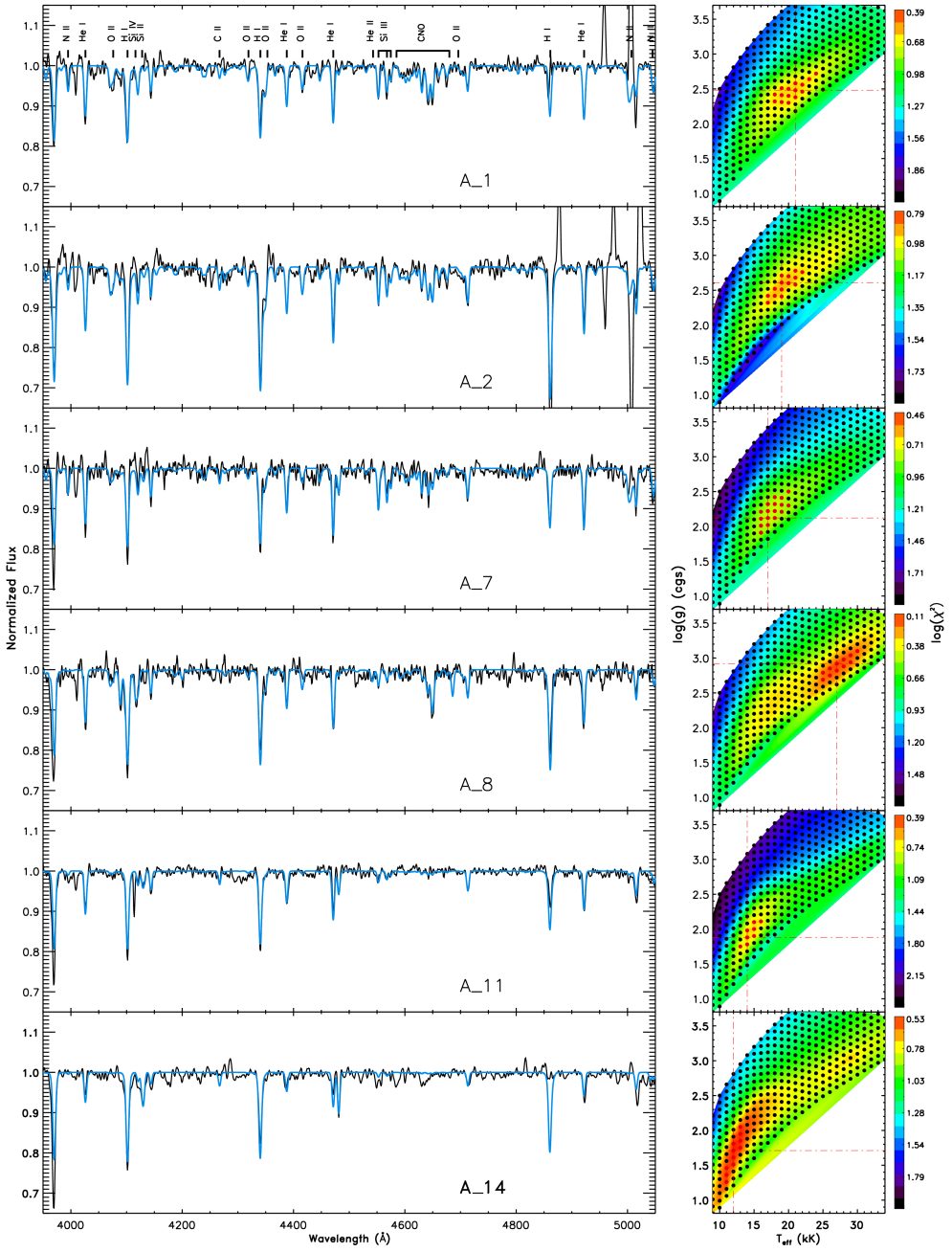

FIGURE B.10— Figure B.1, continued.

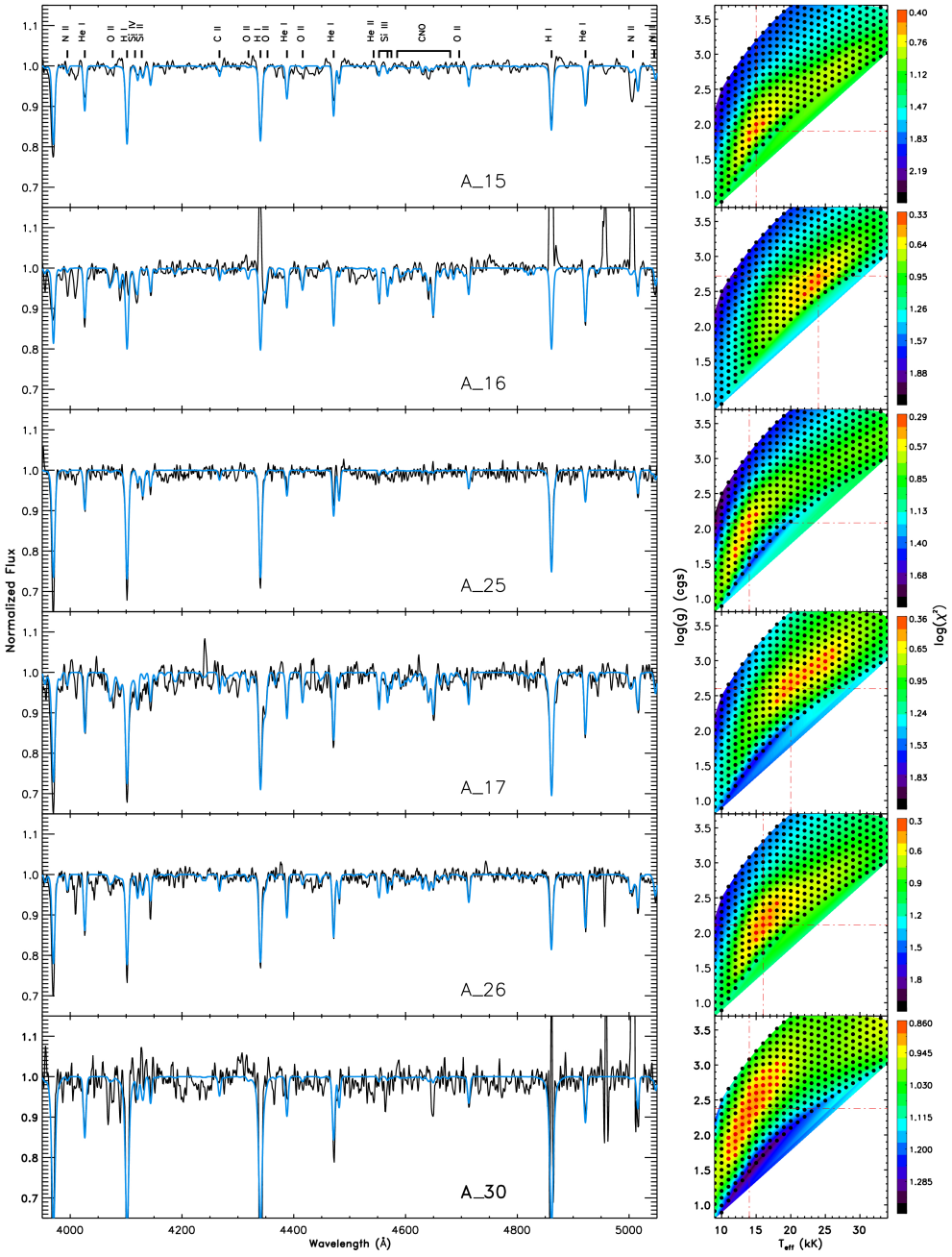

FIGURE B.11— Figure B.1, continued.

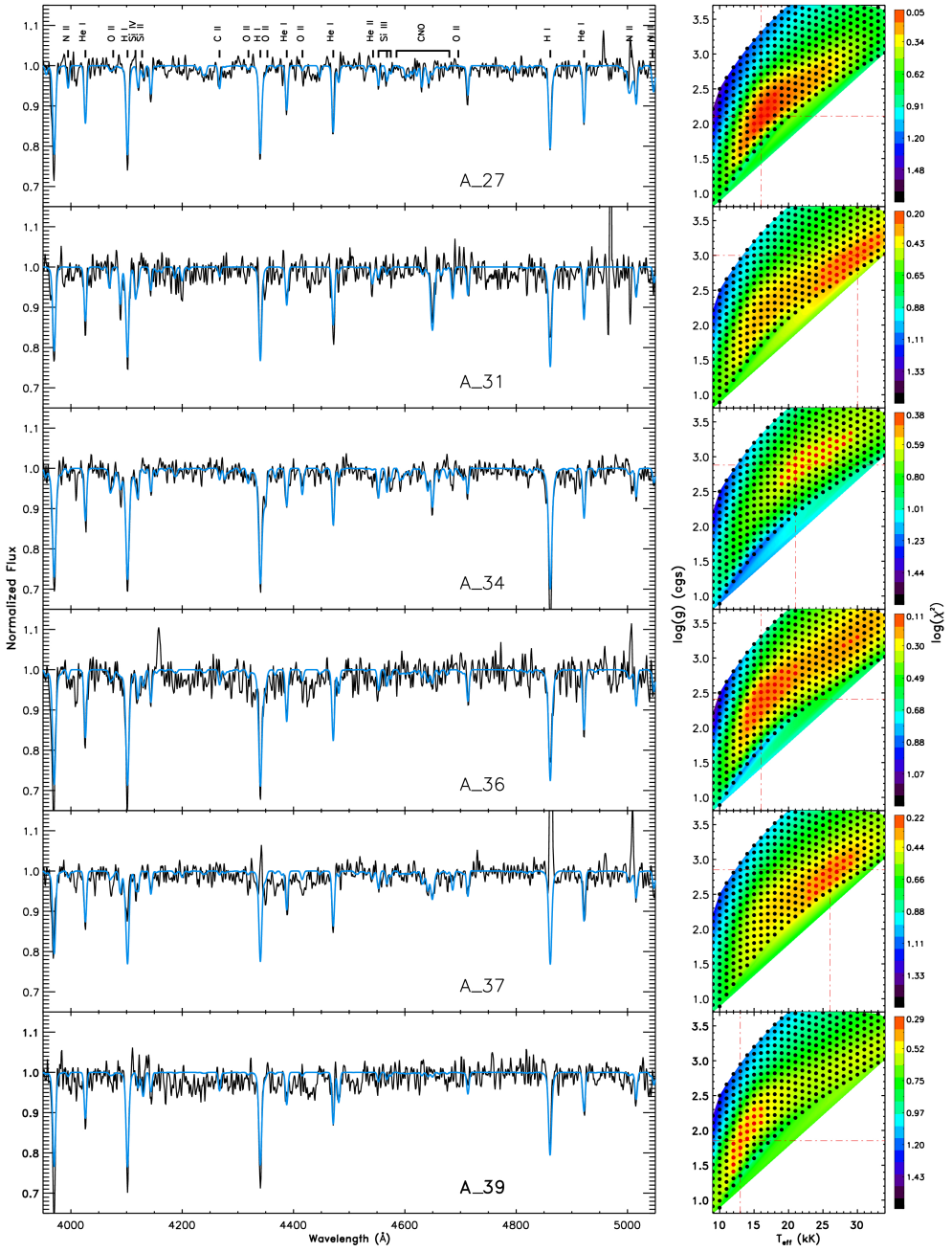

FIGURE B.12— Figure B.1, continued.

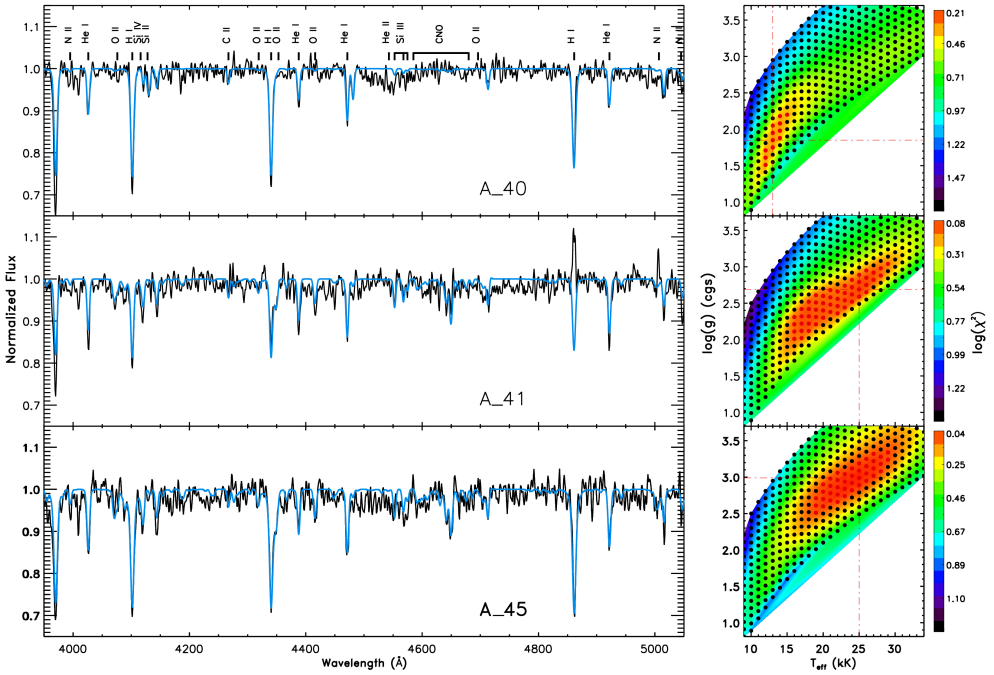

FIGURE B.13— Figure B.1, continued.

Bibliography

Abbott, D. C. 1982, ApJ, 259, 282

Abbott, J. B., Crowther, P. A., Drissen, L., et al. 2004, MNRAS, 350, 552

Allen, C. W. 1973, Astrophysical quantities, ed. Allen, C. W.

Allende Prieto, C., Lambert, D. L., Hubeny, I., & Lanz, T. 2003, ApJS, 147, 363

Appenzeller, I., Fricke, K., Fürtig, W., et al. 1998, The Messenger, 94, 1

Asplund, M., Grevesse, N., Sauval, A. J., & Scott, P. 2009, ARA&A, 47, 481

Auer, L., Bendicho, P. F., & Trujillo Bueno, J. 1994, A&A, 292, 599

Auer, L. H. & Mihalas, D. 1972, ApJS, 24, 193

Azzopardi, M. 1987, A&AS, 69, 421

Bautista, M. A., Romano, P., & Pradhan, A. K. 1998, ApJS, 118, 259

Becker, S. R. & Butler, K. 1988, A&A, 201, 232

Becker, S. R. & Butler, K. 1989, A&A, 209, 244

Becker, S. R. & Butler, K. 1990, A&A, 235, 326

Bianchi, L. & Garcia, M. 2002, ApJ, 581, 610

Bohannan, B. & Walborn, N. R. 1989, PASP, 101, 520

Bresolin, F., Gieren, W., Kudritzki, R., Pietrzyński, G., & Przybilla, N. 2002, ApJ, 567, 277

Bresolin, F., Kudritzki, R., Mendez, R. H., & Przybilla, N. 2001, ApJ, 548, L159

Bresolin, F., Pietrzyński, G., Urbaneja, M. A., et al. 2006, ApJ, 648, 1007

Bresolin, F., Urbaneja, M. A., Gieren, W., Pietrzyński, G., & Kudritzki, R. 2007, ApJ, 671, 2028

Brown, W. R., Geller, M. J., Kenyon, S. J., & Kurtz, M. J. 2006, ApJ, 647, 303

Butler, K. 1984, PhD thesis, Univ. College London

Butler, K. & Giddings, J. 1985, Newsletter on Analysis of Astronomical Spectra, Vol. 9 (Univ. London)

Cannon, A. J. & Pickering, E. C. 1924, Henry Draper (HD) catalog and HD extension

Cannon, C. J. 1973, ApJ, 185, 621

Cardelli, J. A., Clayton, G. C., & Mathis, J. S. 1989, ApJ, 345, 245

Castor, J. I., Abbott, D. C., & Klein, R. I. 1975, ApJ, 195, 157

Charbonneau, P. 1995, ApJS, 101, 309

Chiosi, C., Bertelli, G., & Bressan, A. 1992, ARA&A, 30, 235

Conti, P. S. 1976, Memoires of the Societe Royale des Sciences de Liege, 9, 193

Corbelli, E. & Salpeter, E. E. 1988, ApJ, 326, 551

Cowley, A. P., Dawson, P., & Hartwick, F. D. A. 1979, PASP, 91, 628

Crowther, P. A., De Marco, O., & Barlow, M. J. 1998, MNRAS, 296, 367

Crowther, P. A., Lennon, D. J., & Walborn, N. R. 2006, A&A, 446, 279

Cunha, K. & Lambert, D. L. 1992, ApJ, 399, 586

Darwin, C. 1859, The Origin of Species (Gramercy)

Davidge, T. J. 2005, ApJ, 622, 279

de Vaucouleurs, G. 1961, ApJ, 133, 405

Demarco, R., Rosati, P., Lidman, C., et al. 2005, A&A, 432, 381

Eber, F. 1987, PhD thesis, Munich: Ludwig-Maximillians-Univ.

Eber, F. & Butler, K. 1988, A&A, 202, 153

Eggenberger, P., Meynet, G., & Maeder, A. 2002, A&A, 386, 576

Eissner, W. 1974, J. Physique (Paris), C1, 3

Elmegreen, B. G. 1980, in Giant Molecular Clouds in the Galaxy, ed. P. M. Solomon & M. G. Edmunds, 255–264

Elmegreen, D. M. & Elmegreen, B. G. 1980, AJ, 85, 1325

Engelbracht, C. W., Gordon, K. D., Bendo, G. J., et al. 2004, ApJS, 154, 248

ESA. 1997, The Hipparcos and Tycho Catalogues, ESA SP-1200

Evans, C., Smartt, S., Lennon, D., et al. 2005a, The Messenger, 122, 36

Evans, C. J., Bastian, N., Beletsky, Y., et al. 2010, in IAU Symposium, Vol. 266, IAU Symposium, ed. R. de Grijs & J. R. D. Lépine, 35–40

Evans, C. J., Bresolin, F., Urbaneja, M. A., et al. 2007, ApJ, 659, 1198

Evans, C. J., Crowther, P. A., Fullerton, A. W., & Hillier, D. J. 2004, ApJ, 610, 1021

Evans, C. J. & Howarth, I. D. 2003, MNRAS, 345, 1223

Evans, C. J., Smartt, S. J., Lee, J., et al. 2005b, A&A, 437, 467

Figer, D. F. 2005, Nature, 434, 192

Fitzpatrick, E. L. 1991, PASP, 103, 1123

Fitzpatrick, E. L. 1999, PASP, 111, 63

Froese Fischer, C. & Tachiev, G. 2004, At. Data Nucl. Data Tables, 87, 1

Gabler, R., Gabler, A., Kudritzki, R. P., Puls, J., & Pauldrach, A. 1989, A&A, 226, 162

Garcia, M. & Bianchi, L. 2004, ApJ, 606, 497

Gieren, W., Pietrzynski, G., Bresolin, F., et al. 2005, The Messenger, 121, 23

Gieren, W., Pietrzyński, G., Soszyński, I., et al. 2008, ApJ, 672, 266

Gray, D. F. 1976, The observation and analysis of stellar photospheres, ed. Gray, D. F.

Griffin, D. C., Badnell, N. R., Pindzola, M. S., & Shaw, J. A. 1999, Journal of Physics B Atomic Molecular Physics, 32, 2139

Hamann, W. 1985, A&A, 148, 364

Hamann, W. & Schmutz, W. 1987, A&A, 174, 173

Harnden, Jr., F. R., Branduardi, G., Gorenstein, P., et al. 1979, ApJ, 234, L51

Hartmann, J. 1904, ApJ, 19, 268

Heger, A. & Langer, N. 2000, ApJ, 544, 1016

Herrero, A. 2003, in Astronomical Society of the Pacific Conference Series, Vol. 304, Astronomical Society of the Pacific Conference Series, ed. C. Charbonnel, D. Schaerer, & G. Meynet, 10–14

Herrero, A., Garcia, M., Uytterhoeven, K., et al. 2010, A&A, 513, A70+

Herrero, A., Kudritzki, R. P., Vilchez, J. M., et al. 1992, A&A, 261, 209

Herrero, A. & Najarro, F. 2005, in Massive Stars and High-Energy Emission in OB Associations, ed. G. Rauw, Y. Nazé, & R. Blomme Gosset, E., 21–29

Hillier, D. J. & Miller, D. L. 1998, ApJ, 496, 407

Howarth, I. D. 1983, MNRAS, 203, 301

Hubeny, I. 1988, Computer Physics Communications, 52, 103

Hubeny, I. & Lanz, T. 1995, ApJ, 439, 875

Hummel, E., Dettmar, R.-J., & Wielebinski, R. 1986, A&A, 166, 97

Hummer, D. G., Berrington, K. A., Eissner, W., et al. 1993, A&A, 279, 298

Humphreys, R. M. & Davidson, K. 1979, ApJ, 232, 409

Hunter, I., Brott, I., Lennon, D. J., et al. 2008a, ApJ, 676, L29

Hunter, I., Lennon, D. J., Dufton, P. L., et al. 2008b, A&A, 479, 541

Hunter, I., Lennon, D. J., Dufton, P. L., et al. 2009, A&A, 504, 211

Irrgang, A., Przybilla, N., Heber, U., Nieva, M. F., & Schuh, S. 2010, ApJ, 711, 138

Jaschek, C. & Jaschek, M. 1990, The Classification of Stars, ed. Jaschek, C. & Jaschek, M.

Jokuthy, A. 2002, PhD thesis, Univ. Munich

Kennicutt, Jr., R. C., Bresolin, F., & Garnett, D. R. 2003, ApJ, 591, 801

Kimura, E., Ohsaki, A., Nakazaki, S., & Itikawa, Y. 1998, A&AS, 132, 99

Koribalski, B. S., Staveley-Smith, L., Kilborn, V. A., et al. 2004, AJ, 128, 16

Korn, A. J., Keller, S. C., Kaufer, A., et al. 2002, A&A, 385, 143

Korn, A. J., Nieva, M. F., Daflon, S., & Cunha, K. 2005, ApJ, 633, 899

Kubát, J., Puls, J., & Pauldrach, A. W. A. 1999, A&A, 341, 587

Kudritzki, R. 2010, Astronomische Nachrichten, 331, 459

Kudritzki, R. P. 2002, ApJ, 577, 389

Kudritzki, R. P., Bresolin, F., & Przybilla, N. 2003, ApJ, 582, L83

Kudritzki, R.-P., Lennon, D. J., & Puls, J., eds. 1995, Quantitative Spectroscopy of Luminous Blue Stars in Distant Galaxies. ed. J. R. Walsh & I. J. Danziger, 246–+

Kudritzki, R.-P. & Puls, J. 2000, ARA&A, 38, 613

Kudritzki, R. P., Puls, J., Lennon, D. J., et al. 1999, A&A, 350, 970

Kudritzki, R.-P., Urbaneja, M. A., Bresolin, F., et al. 2008, ApJ, 681, 269

Kurt, C. M. & Dufour, R. J. 1998, 7, 202

Kurucz, R. 1993a, ATLAS9 Stellar Atmosphere Programs and 2 km/s grid. Kurucz CD-ROM No. 2-12. Cambridge, Mass.: Smithsonian Astrophysical Observatory, 1993., 2-12

Kurucz, R. 1993b, ATLAS9 Stellar Atmosphere Programs and 2 km/s grid. Kurucz CD-ROM No. 13. Cambridge, Mass.: Smithsonian Astrophysical Observatory, 1993., 13

Kurucz, R. L. 1992, Revista Mexicana de Astronomia y Astrofisica, vol. 23, 23, 45

Lamers, H. J. G. L. M., Snow, T. P., & Lindholm, D. M. 1995, ApJ, 455, 269

Langer, N. & Maeder, A. 1995, A&A, 295, 685

Lanz, T. & Hubeny, I. 2003, ApJS, 146, 417

Lanz, T. & Hubeny, I. 2007, ApJS, 169, 83

Larson, R. B. 2003, Reports on Progress in Physics, 66, 1651

Larson, R. B. 2010, Reports on Progress in Physics, 73, 014901

Lefever, K. 2007, PhD thesis, K. U. Leuven

Lefever, K., Puls, J., & Aerts, C. 2007, A&A, 463, 1093

Leitherer, C., Robert, C., & Drissen, L. 1992, ApJ, 401, 596

Lennon, D. J. 1997, A&A, 317, 871

Lennon, D. J., Dufton, P. L., & Crowley, C. 2003, A&A, 398, 455

Lennon, D. J., Dufton, P. L., & Fitzsimmons, A. 1992, A&AS, 94, 569

Lennon, D. J., Dufton, P. L., & Fitzsimmons, A. 1993, A&AS, 97, 559

Lennon, D. J., Lee, J., Dufton, P. L., & Ryans, R. S. I. 2005, A&A, 438, 265

Luck, R. E., Moffett, T. J., Barnes, III, T. G., & Gieren, W. P. 1998, AJ, 115, 605

Maeder, A. & Meynet, G. 2001, A&A, 373, 555

Maeder, A. & Meynet, G. 2005, A&A, 440, 1041

Maíz-Apellániz, J. 2004, PASP, 116, 859

Markova, N. & Puls, J. 2008, A&A, 478, 823

Markova, N., Puls, J., Scuderi, S., & Markov, H. 2005, A&A, 440, 1133

Martins, F., Schaerer, D., & Hillier, D. J. 2005, A&A, 436, 1049

Mason, B. D., Gies, D. R., Hartkopf, W. I., et al. 1998, AJ, 115, 821

Massey, P. 1997, A User's Guide to CCD Reduction with IRAF, ed. Massey, P.

Massey, P. 2003, ARA&A, 41, 15

Massey, P., McNeill, R. T., Olsen, K. A. G., et al. 2007, AJ, 134, 2474

Massey, P., Valdes, F., & Barnes, J. 1992, A User's Guide to Reducing Slit Spectra with IRAF , ed. Massey, P. Valdes, F. & Barnes, J.

Mateo, M. L. 1998, ARA&A, 36, 435

McErlean, N. D., Lennon, D. J., & Dufton, P. L. 1999, A&A, 349, 553

Meynet, G. & Maeder, A. 2003, A&A, 404, 975

Meynet, G. & Maeder, A. 2005, A&A, 429, 581

Mihalas, D. 1978, Stellar atmospheres /2nd edition/ (San Francisco, W. H. Freeman and Co., 1978. 650 p.)

Miller, B. W. 1996, AJ, 112, 991

Mokiem, M. R., de Koter, A., Puls, J., et al. 2005, A&A, 441, 711

Mokiem, M. R., de Koter, A., Vink, J. S., et al. 2007, A&A, 473, 603

Monteverde, M. I. & Herrero, A. 1998, Ap&SS, 263, 171

Monteverde, M. I., Herrero, A., & Lennon, D. J. 2000, ApJ, 545, 813

Moore, C. E. 1965, Selected tables of atomic spectra - A: Atomic energy levels - Second edition; B: Multiplet tables - SI II, SI III, SI IV. Data derived from the analyses of optical spectra, ed. Moore, C. E.

Morgan, W. W., Keenan, P. C., & Kellman, E. 1943, An atlas of stellar spectra, with an outline of spectral classification, ed. Morgan, W. W., Keenan, P. C., & Kellman, E.

Muschielok, B., Kudritzki, R. P., Appenzeller, I., et al. 1999, A&A, 352, L40

Nahar, S. N., Eissner, W., Chen, G., & Pradhan, A. K. 2003, A&A, 408, 789

Nahar, S. N. & Pradhan, A. K. 2003, ApJS, 149, 239

Najarro, F., Hillier, D. J., & Stahl, O. 1997, A&A, 326, 1117

Nieva, M. F. 2007, PhD thesis, Friedrich-Alexander University, Erlangen-Nuremberg

Nieva, M. F. & Przybilla, N. 2008, A&A, 481, 199

Oshima, T., Mitsuda, K., Ota, N., & Yamasaki, N. 2002, in 8th Asian-Pacific Regional Meeting, Volume II, ed. S. Ikeuchi, J. Hearnshaw, & T. Hanawa, 287–288

Otte, B. & Dettmar, R. 1999, A&A, 343, 705

Pagel, B. E. J., Edmunds, M. G., Blackwell, D. E., Chun, M. S., & Smith, G. 1979, MNRAS, 189, 95

Pauldrach, A. & Herrero, A. 1988, A&A, 199, 262

Pauldrach, A., Puls, J., & Kudritzki, R. P. 1986, A&A, 164, 86

Pauldrach, A. W. A., Hoffmann, T. L., & Lennon, M. 2001, A&A, 375, 161

Perryman, M. A. C., de Boer, K. S., Gilmore, G., et al. 2001, A&A, 369, 339

Pietrzyński, G., Gieren, W., Soszyński, I., et al. 2006, AJ, 132, 2556

Prinja, R. K., Barlow, M. J., & Howarth, I. D. 1990, ApJ, 361, 607

Przybilla, N. 2002, PhD thesis, Ludwing-Maximilians University, Munich

Przybilla, N., Butler, K., Becker, S. R., & Kudritzki, R. P. 2006, A&A, 445, 1099

Przybilla, N., Butler, K., & Kudritzki, R. P. 2001, A&A, 379, 936

Przybilla, N., Firnstein, M., Nieva, M. F., Meynet, G., & Maeder, A. 2010, ArXiv e-prints

Przybilla, N., Nieva, M., & Butler, K. 2008, ApJ, 688, L103

Puche, D. & Carignan, C. 1988, AJ, 95, 1025

Puche, D., Carignan, C., & Wainscoat, R. J. 1991, AJ, 101, 447

Puls, J. 1991, A&A, 248, 581

Puls, J., Kudritzki, R., Herrero, A., et al. 1996, A&A, 305, 171

Puls, J., Urbaneja, M. A., Venero, R., et al. 2005, A&A, 435, 669

Puls, J., Vink, J. S., & Najarro, F. 2008, A&A Rev., 16, 209

Ralchenko, Y., E., K. A., Reader, J., & NIST ASD Team. 2008, NIST Atomic Spectra Database (version 3.1.5), National Institute of Standards and Technology, Gaithersburg, MD.

Rauch, T. & Deetjen, J. L. 2003, in Astronomical Society of the Pacific Conference Series, Vol. 288, Stellar Atmosphere Modeling, ed. I. Hubeny, D. Mihalas, & K. Werner, 103–+

Rauw, G., Crowther, P. A., De Becker, M., et al. 2005, A&A, 432, 985

Repolust, T., Puls, J., & Herrero, A. 2004, A&A, 415, 349

Salpeter, E. E. 1955, ApJ, 121, 161

Sandage, A. & Tammann, G. A. 1987, A revised Shapley-Ames Catalog of bright galaxies, ed. Sandage, A. & Tammann, G. A.

Santolaya-Rey, A. E., Puls, J., & Herrero, A. 1997, A&A, 323, 488

Scharmer, G. B. 1981, ApJ, 249, 720

Schild, H., Crowther, P. A., Abbott, J. B., & Schmutz, W. 2003, A&A, 397, 859

Schlegel, D. J., Finkbeiner, D. P., & Davis, M. 1998, ApJ, 500, 525

Searle, S. C., Prinja, R. K., Massa, D., & Ryans, R. 2008, A&A, 481, 777

Seaton, M. J. 1962, in: Atomic and Molecular Processes, ed. Seaton, M. J. ((Acad. Press, New York and London)

Seaton, M. J. 1979, MNRAS, 187, 73P

Seaton, M. J. 1987, Journal of Physics B Atomic Molecular Physics, 20, 6363

Seaton, M. J., Yan, Y., Mihalas, D., & Pradhan, A. K. 1994, MNRAS, 266, 805

Simon-Diaz, S. 2005, PhD thesis, Universidad de La Laguna

Simón-Díaz, S. 2010, A&A, 510, A22+

Simón-Díaz, S. & Herrero, A. 2007, A&A, 468, 1063

Simón-Díaz, S., Herrero, A., Esteban, C., & Najarro, F. 2006, A&A, 448, 351

Smith, L. F., Shara, M. M., & Moffat, A. F. J. 1996, MNRAS, 281, 163

Solano, E., Catala, C., Garrido, R., et al. 2005, AJ, 129, 547

Stasińska, G. 2002, ArXiv Astrophysics e-prints

Stasińska, G. 2004, in Cosmochemistry. The melting pot of the elements, ed. C. Esteban, R. García López, A. Herrero, & F. Sánchez , 115–170

Sundqvist, J. O., Puls, J., & Feldmeier, A. 2010, A&A, 510, A11+

Takeda, Y. & Takada-Hidai, M. 1998, PASJ, 50, 629

Trundle, C., Dufton, P. L., Hunter, I., et al. 2007, A&A, 471, 625

Trundle, C., Dufton, P. L., Lennon, D. J., Smartt, S. J., & Urbaneja, M. A. 2002, A&A, 395, 519

Trundle, C. & Lennon, D. J. 2005, A&A, 434, 677

Trundle, C., Lennon, D. J., Puls, J., & Dufton, P. L. 2004, A&A, 417, 217

Tüllmann, R., Rosa, M. R., Elwert, T., et al. 2003, A&A, 412, 69

Two Micron All Sky Survey team. 2003, Extended objects. Final release.

U, V., Urbaneja, M. A., Kudritzki, R.-P., et al. 2009, ArXiv e-prints

Unsold, A. 1955, Physik der Sternatmospharen, MIT besonderer Berucksichtigung der Sonne., ed. Unsold, A.

Urbaneja, M. A. 2004, PhD thesis, Universidad de La Laguna

Urbaneja, M. A., Herrero, A., Bresolin, F., et al. 2005a, ApJ, 622, 862

Urbaneja, M. A., Herrero, A., Bresolin, F., et al. 2003, ApJ, 584, L73

Urbaneja, M. A., Herrero, A., Kudritzki, R.-P., et al. 2005b, ApJ, 635, 311

Urbaneja, M. A., Kudritzki, R.-P., Bresolin, F., et al. 2008, ApJ, 684, 118

van Dokkum, P. G. 2001, PASP, 113, 1420

van Regemorter, H. 1962, ApJ, 136, 906

Venn, K. A., Lennon, D. J., Kaufer, A., et al. 2001, ApJ, 547, 765

Venn, K. A., McCarthy, J. K., Lennon, D. J., et al. 2000, ApJ, 541, 610

Venn, K. A., Tolstoy, E., Kaufer, A., et al. 2003, AJ, 126, 1326

Vilchez, J. M., Pagel, B. E. J., Diaz, A. I., Terlevich, E., & Edmunds, M. G. 1988, MNRAS, 235, 633

Villamariz, M. R. 2000, PhD thesis, Universidad de La Laguna

Villamariz, M. R. & Herrero, A. 2000, A&A, 357, 597

Vink, J. S., de Koter, A., & Lamers, H. J. G. L. M. 1999, A&A, 350, 181

Vink, J. S., de Koter, A., & Lamers, H. J. G. L. M. 2001, A&A, 369, 574

Walborn, N. R. 1971, ApJS, 23, 257

Walborn, N. R. & Fitzpatrick, E. L. 1990, PASP, 102, 379

Walborn, N. R. & Fitzpatrick, E. L. 2000, PASP, 112, 50

Webster, B. L. & Smith, M. G. 1983, MNRAS, 204, 743

Woosley, S. E., Heger, A., & Weaver, T. A. 2002, Reviews of Modern Physics, 74, 1015

Yamashita, Y. & Nariai, K. 1977, An Atlas of representative stellar spectra, ed. Yamashita, Y. & Nariai, K.